ANALYSIS AND DESIGN OF NEW THREE-PHASE AC-DC RECTIFIER SYSTEMS WITH HIGHER FREQUENCY ISOLATION

A Dissertation

by

JOSE JUAN SANDOVAL

Submitted to the Office of Graduate and Professional Studies of
Texas A&M University
in partial fulfillment of the requirements for the degree of

DOCTOR OF PHILOSOPHY

Chair of Committee,	Prasad N. Enjeti
Committee Members,	Hamid A. Toliyat
	José Silva-Martinez
	Steven Taliaferro
Head of Department,	Miroslav M. Begovic

May 2017

Major Subject: Electrical Engineering

ABSTRACT

The field of power electronics finds extensive application within the energy industry. In particular, three-phase AC-DC conversion is employed in many high power applications that require integration with the utility grid such as electric vehicle charging, adjustable speed drive systems, telecommunication power supplies, and renewable energy systems. The power electronics industry is constantly pushing the limits of three-phase AC-DC converters in terms of power density, efficiency, and input current quality. Thus, the driving force behind this research is to analyze and design new three-phase AC-DC rectifier systems which exhibit high power density and efficiency while complying with input current harmonic standards.

Without losing generality, a particular application is suggested for each of the proposed three-phase AC-DC rectifier systems to demonstrate their value within the energy industry. In the first study, a push-pull based three-phase AC-DC rectifier with medium frequency galvanic isolation is proposed. The unique features of this topology include the simplicity of its modulation scheme, its minimized active switch count and its high power density. It is shown that operating at medium frequency of 600 Hz, the transformer size is 1/3 of the equivalent 60 Hz design. A 10 kW design example is shown to achieve 96.5% efficiency.

In the second study, a full-bridge based three-phase AC-DC rectifier with high frequency galvanic isolation (20 kHz) is implemented to further improve power density and transformer utilization. Galvanic isolation is provided through a three-phase, five-

limb ferrite core transformer. By operating at 20 kHz, the transformer size is reduced twenty-one times compared to the 60 Hz design. The output DC voltage is regulated with simple duty cycle control without affecting the low order harmonics in the input current making this topology suitable for electric vehicle charging applications.

In the third study, a three-phase AC-DC PWM rectifier is proposed. The converter is modulated using programmed PWM switching functions. It is shown that selected harmonics are eliminated from the utility input current. The main advantages of this topology include the absence of electrolytic capacitors, good input current quality, and high power density.

In the final study, a three-phase AC-DC rectifier with bidirectional power flow capability is proposed. The converter operates in soft switching conditions, improving the system's efficiency. The utility input current exhibits unity power factor and low total harmonic distortion. High power density is achieved by employing high frequency isolation and by avoiding electrolytic capacitors in the front-end.

The analysis and design principles of each topology are accompanied with mathematical modeling and detailed simulation results. Additionally, finite element analysis (FEA) software such as Ansys Maxwell is used to assess the performance of the medium and high frequency transformers. Furthermore, experimental results - on scaled down laboratory prototypes- are presented to validate the performance of the proposed systems. Overall, the results obtained indicate that the proposed topologies offer advantages in terms of power density, simplicity, and input current quality compared to conventional and state of the art three-phase AC-DC systems.

I dedicate this dissertation to Christ, with Him everything is possible.
I also dedicate this dissertation to my lovely wife,
to my parents, and to my brothers and sisters.

ACKNOWLEDGEMENTS

My time at Texas A&M University as a graduate student has been edifying; I have grown intellectually and spiritually. Growing in both of these aspects of my life has brought me immense joy, and has helped me to achieve one of my most challenging goals; completing a doctorate degree. I could not have done this by myself. Many persons have helped me to cultivate the intellectual and spiritual virtues I deem essential for completing my Ph. D degree; to these persons I extend my sincere gratitude.

I will always be grateful to my committee chair Dr. Prasad Enjeti for his guidance and support throughout my graduate studies. I owe much of my intellectual growth to Dr. Enjeti. Working with him has made the Ph.D experience very pleasant. I am thankful for his dedication as both a professor and researcher. I appreciate the many hours he has spent with me discussing my research, as well as both my professional and personal life. I also want to thank Dr. Hamid Toliyat, Dr. José Silva-Martinez, and Dr. Steven Taliaferro for being members in my Ph. D committee. I also had the privilege of growing intellectually from the courses they teach at Texas A&M University.

My classes and research work would have been much more difficult without the assistance of the students in the Power Electronics and Power Quality research group. I thank (in no particular order) Somasundaram Essakiappan, Harish Krishnamoorthy, Pawan Garg, Michael Daniel, Jorge Ramos-Ruiz, Erick Pool, Taeyong Kang, Bahaa Hafez, Ahmed Morsy, Messad Albader, Sinan Al-Obaidi, Ahmed Allehyani, Weiran

Dai, and Alejandra Sandoval for discussing power electronics, along many other things, with me and for making the lab a pleasant working environment.

I will also be forever grateful to St. Mary's Catholic Center, where I have grown spiritually in my Catholic faith. At St. Mary's I have always felt at home and has definitely helped me grow as a student, classmate, teaching assistant, son, brother, and husband. Growing in my faith helped me pursue the excellence and perseverance needed to obtain a Ph. D. I thank (in no particular order) Bishop David Konderla, Fr. Brian McMaster, Fr. Jonathan, Fr. Remo, Fr. Adam McDonald, and Fr. Hai Nguyen for their words during Mass and for the friendship we share in Christ. I also want to thank all the past and current members of Pescadores and all the members of the Hispanic Community for sharing their love for Christ with me.

My Ph. D would not have been possible without the support of my parents and my wife. I thank my parents for their guidance and for teaching me that education is essential for growth as a human being. I am also forever grateful to my wife, Karen Fuentes-Sandoval, for her patience and for always looking after what is best for me. I also thank Karen for trusting in me, for loving me, and for helping me to grow, with her, in virtue every day.

All virtues whether intellectual or spiritual come from God. Thank you Lord for everything, for the gift of life, for Your mercy, for placing me in Texas A&M University, and for all the persons You have placed in my path so that I could grow as a human being and so that I could know that You love me.

CONTRIBUTORS AND FUNDING SOURCES

The work in this dissertation was guided by the dissertation committee consisting of Professor Prasad Enjeti, Professor Hamid Toliyat and Professor José Silva-Martinez from the Electrical and Computer Engineering Department, and Professor Steven Taliaferro from the Mathematics Department.

The development and design of the medium and high frequency transformers was done in collaboration with Dr. Ira Pitel from Magna-Power Inc. The construction of the transformers was done at Magna-Power Inc. All other work for the dissertation was completed by the student.

My graduate studies were funded in part by the Bill Gates and Melinda Gates foundation, which awarded me the Gates Millennium Scholarship. I also had the opportunity to fund my graduate studies through a teaching assistantship. I would like to thank Dr. James, Dr. Miller, and Dr. Peterson for giving me the opportunity to work for their Engineering Ethics course. My graduate studies were also funded in part by the Department of Electrical and Computer Engineering which awarded me the Thomas Powell' 62 Fellowship and the Graduate Merit Scholarship. The last year of my graduate studies was supported by a Dissertation Fellowship from Texas A&M University.

TABLE OF CONTENTS

Page

LIST OF FIGURES

Page

LIST OF TABLES

Page

1. INTRODUCTION

1.1 Introduction to Three-Phase AC-DC Rectifier Systems

Electrical energy conversion through power electronic converters makes it possible to integrate many systems with the utility grid. Power electronic converters condition and process electrical energy in such a way that is beneficial to the end user. The input side of an off-line power electronic converter, simplified to a black box in Figure 1-1, is the utility grid at line frequency (50/60 Hz). The output characteristics of the power electronic converter such as voltage, current, frequency, and number of phases are dictated by the load requirements. Within the power electronic converter box the following components are usually found: semiconductor switching devices (IGBTs, diodes, MOSFETs, etc.), inductors and capacitors that are used as energy storage devices or for filtering purposes, heatsinks for cooling, and power transformers for isolation.

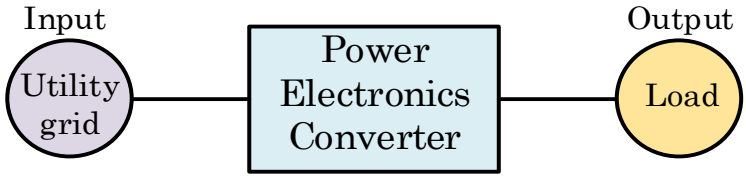

Figure 1-1: Block diagram of a power electronic converter

An AC-DC power electronic converter is classified as a *rectifier* if it delivers a DC output from an AC input [1]. The AC input for the rectifier is usually a single-phase voltage source or a three-phase voltage source. For high power applications, three-phase AC-DC conversion is more convenient as opposed to single-phase AC-DC conversion

[2, 3]. Based on the load requirements and the design criteria, the three-phase rectifier system might require multiple conversion stages to achieve overall AC-DC conversion. For instance, as shown in Figure 1-2, the first power electronic converter could be used to transform the utility grid three-phase voltages into another set of three-phase voltages with different magnitude and frequency. Meanwhile, the second power electronic converter in Figure 1-2 could be used to convert the new set of three-phase voltages into a DC output. Usually when power conversion is done in multiple stages there is an energy storage element such as a capacitor to decouple the systems.

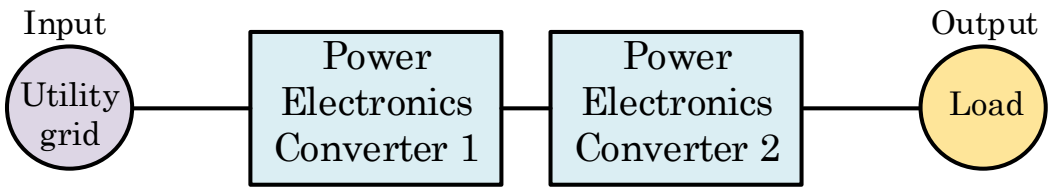

Figure 1-2: AC-DC rectifier system with multiple conversion stages

1.2 Utility Grid Applications with Three-Phase AC-DC Rectifier Systems

A prediction on the worldwide use of AC-DC converters is given in Figure 1-3. As shown in this figure, the market for AC-DC converters grows annually [4]. In particular, three-phase AC-DC rectifier systems find widespread application within the energy industry. For example, in traditional applications such as adjustable speed drive systems, a three-phase AC-DC rectifier is utilized as the front-end power electronic converter. As shown in Figure 1-4, three-phase AC-DC conversion also plays a significant role in emerging and developing applications such as electric vehicle

charging, battery energy storage systems, server power supplies, and data centers [5], [6], [7], [8].

This widespread applicability of AC-DC converters encourages the development of new three-phase AC-DC converters which overcome the limitations of conventional three-phase AC-DC conversion schemes. Furthermore, the constant push within the industry towards smaller sizes and higher efficiencies in high power applications opens up a wide window of research opportunities within three-phase AC-DC rectifier systems.

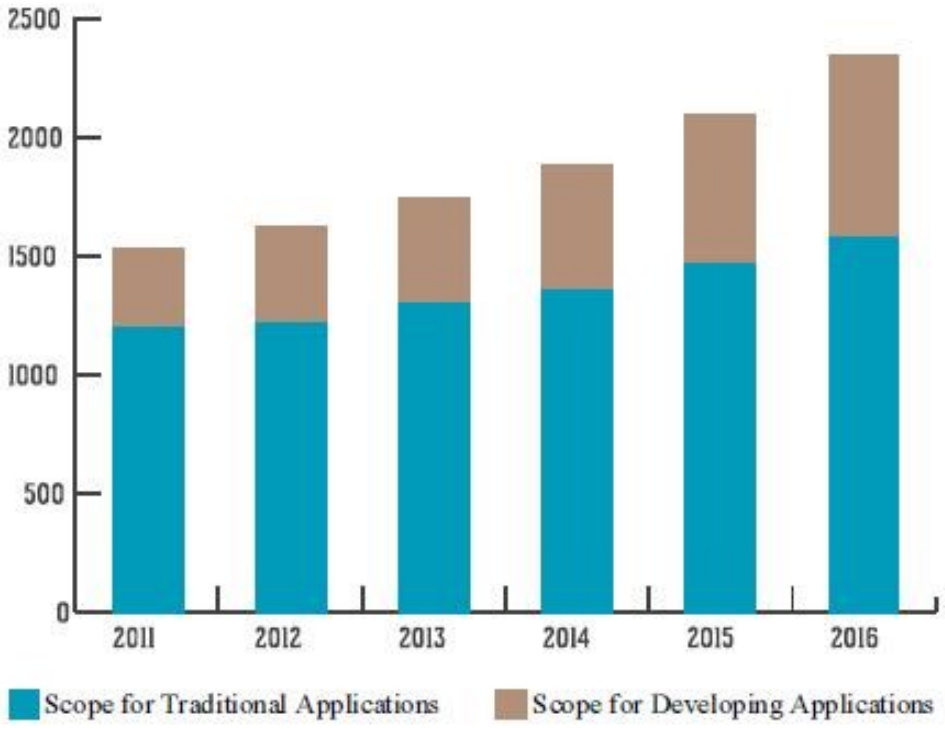

Figure 1-3: Industry outlook for AC-DC converters (in million units). Reprinted from [4].

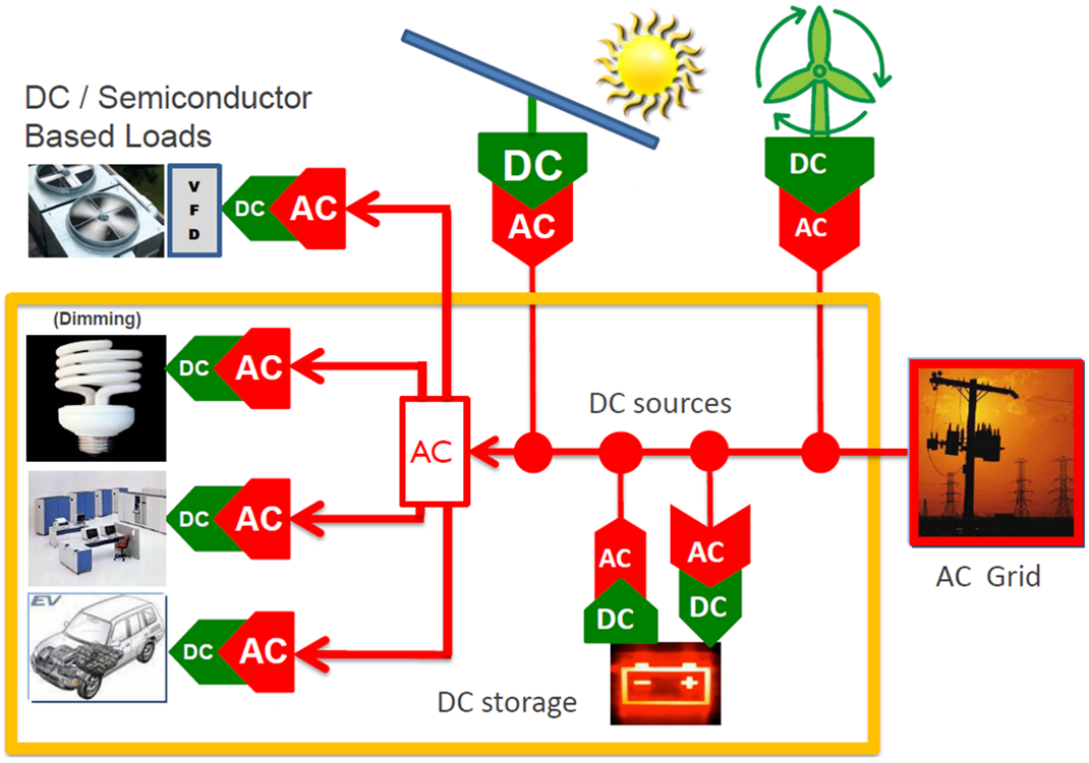

Figure 1-4: Three-phase AC-DC conversion applicable in EV charging, adjustable speed drive systems, DC energy storage, and data-centers. Reprinted from [8].

1.3 Performance Indices for Three-Phase AC-DC Rectifier Systems

The design of three-phase AC-DC rectifier systems tied to the utility grid must take into account the following parameters: utility input current quality, power density (i.e. size and weight), efficiency, cost, and reliability. It is worth noting that in this dissertation, the reliability of the proposed three-phase AC-DC converters is not fully discussed.

1.3.1 Input Current Quality

The current drawn from the utility grid by the three-phase rectifier must be of high quality. Input current quality is assessed in terms of power factor (PF) and total

harmonic distortion (THD). Independent of the application, the input current typically requires a PF close to unity and a THD of less than 5% [9]. The PF of a system drawing non-sinusoidal currents is characterized by two components, the distortion factor (DF) and the displacement power factor (DPF), and is defined in (1.1). The THD is an index that describes the non-sinusoidal nature of a waveform due to its harmonics and is calculated by (1.2). In addition, standards such as IEEE-519 and IEC61000-3-4 place limitations on the magnitudes of the current harmonic components drawn by systems connected to the utility grid [10], [11].

$$PF = DF \cdot DPF = \frac{I_1}{I_{rms}} \cdot \cos\phi \tag{1.1}$$

$$THD = \frac{\sqrt{\sum_{n=2}^{\infty} I_n^2}}{I_1} \tag{1.2}$$

1.3.2 Power Density

The power density of a power electronic converter is a measure of its size and weight. In this dissertation, the power density of a power electronic converter is defined as in (1.3); it is the ratio between the total power processed by the converter and the total volume it occupies. It is desirable for a power electronic converter to have high power density especially in high power utility connected systems because it leads to lower costs in terms of installation and maintenance, enables compact designs, and reduces weight and footprint [12].

$$Power\ Density = \frac{Total\ power\ processed\ (W)}{Total\ Volume\ (dm^3)} \tag{1.3}$$

The components that have a strong impact in the power density of a converter include the total capacitor volume compromised of EMI filter capacitors and DC link capacitors, the cooling system which primarily consists of heatsinks, and the magnetic components such as inductors and transformers [13]. The volume breakdown of power electronic converters for various switching frequencies is shown in Figure 1-5. It is evident that roughly 60-70% of the volume for a given converter is occupied by the magnetic components [13]. For instance, the volume of a voltage source inverter (VSI) operating at a switching frequency of 4 kHz is roughly 5 dm^3 with its magnetic components occupying a volume of 4.2 dm^3.

In addition, safety standards mandate the use of galvanic isolation – between input and output – in applications such as those mentioned in subsection 1.2. Therefore, it is common for AC-DC rectifier systems to employ galvanic isolation through transformers. By nature, transformers are made of magnetic material and also contribute significantly to the size of power converters. Inductors and transformers also have a strong impact on the weight of converters. Reducing the size and weight of these magnetic components is an important theme in this dissertation because it would result in the benefits outlined previously.

After magnetic components, DC link capacitors are the components which affect power electronic converters the most in terms of size and weight. Thus, approaches that reduce the number or eliminate the use of DC link capacitors are also desirable.

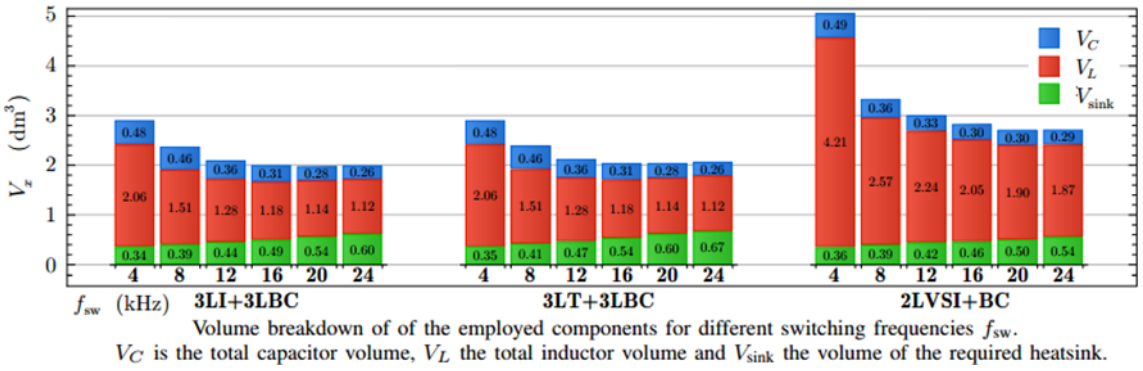

Figure 1-5: Volume occupied by components in power electronic converters for different switching frequencies [13]. © 2013 IEEE

1.3.3 Efficiency

Along with having high input current quality and high power density, high efficiency is desired for three-phase AC-DC converters. Efficiencies of 95% or higher are desired. Within a power electronic converter, power losses come primarily from the semiconductor devices and from its magnetic components.

The semiconductor device losses account for both switching losses and conduction losses. Switching losses occur due to the non-ideal nature of the semiconductor devices; the active switching devices are not able to turn ON and OFF instantaneously as shown in Figure 1-6. During switching transitions, power loss occurs and is proportional to the switching frequency. Higher switching frequencies imply higher switching losses. Switching losses can be minimized by employing components and control techniques that enable soft switching (i.e. zero voltage switching (ZVS) or zero current switching (ZCS)). Achieving ZVS and ZCS enables the use of higher switching frequencies in converters without compromising the system's efficiency. The conduction losses of a semiconductor device occur during the ON state of the device due

to forward voltage drops as shown in Figure 1-6. Furthermore, reducing the number of conversion stages within a power electronic converter is desirable because higher efficiencies can be obtained.

The magnetic components in a power electronic converter (i.e. inductors and transformers) also incur power losses. Ohmic losses are present due to the windings around the magnetic cores. Moreover, the magnetic structures themselves suffer from core losses which encompass eddy current loss and hysteresis loss. Thus, appropriate selection of the magnetic materials for inductors and transformers is critical when designing three-phase AC-DC rectifier systems.

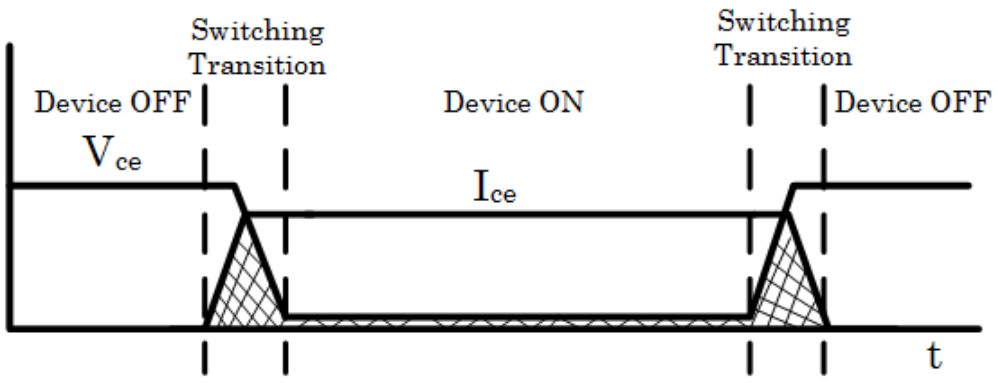

Figure 1-6: Semiconductor power losses. Switching losses occur during switching transitions and conduction loss occurs due to device forward voltage drop.

1.3.4 Cost and Reliability

Logically, it is desired by the designer and user to keep the cost of a three-phase AC-DC rectifier system as low as possible. In general, maintaining simplicity helps to reduce cost while complexity increases cost. Having a low semiconductor device count

helps to maintain simplicity. The voltage and current ratings of the semiconductor devices also affects their cost. The magnetic material chosen for inductors and transformers also impact the cost of a rectifier system. Magnetic cores that are more efficient tend to be more expensive.

In power electronics, reliability is defined as the probability of a converter not failing within a desired timeframe under certain operating conditions [14]. Within a power electronic converter, the components most prone to failure are the power semiconductor devices and electrolytic capacitors [15]. Failure of these components usually results in shutdown of the power electronic converter. This shut-down is undesired as it increases the cost of operation. Metrics such as failure rate, meant time between failure, and average downtime are used to assess the reliability of power electronic converters. Although the reliability of the proposed rectifiers in this dissertation is not investigated thoroughly, the use of electrolytic capacitors is avoided.

1.4 Medium or High Frequency Isolation

From the discussed performance indices it is clear that in general the power electronics industry is moving towards compact, high efficient and cost-effective systems; three-phase AC-DC rectifier systems are not an exception.

A well-known method to reduce the size and weight of a converter is to increase the operation frequency of transformers and inductors. Increasing the operation frequency through power semiconductor devices (e.g. IGBTs, MOSFETs) allows a reduction in size of the transformer and inductor cores resulting in improved power

density [16], [17], [18]. The volume of magnetic cores can be reduced when operated at frequencies higher than utility line frequency (50/60 Hz) [12], [19]. This inverse relation between magnetic core area and frequency can be observed from (1.4) and applies to magnetic cores excited with sinusoidal waveforms [20]. In (1.4), A refers to the cross-sectional area of the core in m^2, B_{max} refers to the peak magnetic flux density, f is the core's frequency of operation, E_{rms} is the voltage induced in the winding, and N is the number of turns in the winding.

$$A = \frac{E_{rms}}{\sqrt{2}\pi \cdot f \cdot N \cdot B_{\max}} \tag{1.4}$$

While improving power density, the use of higher frequencies also impacts the efficiency three-phase AC-DC rectifier systems. At higher frequencies, magnetic core losses tend to increase and can compromise the system efficiency if the core's operating conditions are not designed properly [21, 22]. Proper selection of the magnetic core material is also essential to achieve high power density while simultaneously maintaining high system efficiency. The core materials commonly used for high power applications are silicon-steel, ferrite, amorphous materials and nanocrystalline materials with each having its merits and limitations [23, 24].

Silicon-steel cores can be operated at relatively high magnetic flux densities (i.e. 1.6T) but are limited to medium frequency operation (i.e. 400 Hz- 2 kHz) because they exhibit high core loss at higher frequencies [23]. Compared to silicon-steel cores, amorphous cores can be operated at higher frequencies (i.e. 5 kHz - 8 kHz) but are more expensive. Meanwhile, ferrite cores are more expensive than both silicon-steel and

amorphous material cores and have relatively low magnetic flux density (i.e. 0.5T) but exhibit high efficiency at frequencies greater than tens of kilohertz. Nanocrystalline cores can operate at relatively high magnetic flux densities (i.e. 1.4T) and also have the lowest core losses among the mentioned magnetic materials [23]. The main limitation of nanocrystalline cores is that they are the most expensive among the mentioned materials.

In this dissertation, the proposed three-phase rectifier systems employ transformers that operate at a frequency higher than the line frequency (50/60 Hz). Thus to avoid a conceptual issue the terms medium frequency and high frequency must be defined. In this dissertation the term medium frequency applies to the range 400 Hz – 2 kHz, while the term high frequency applies to frequencies greater than 5 kHz.

1.5 Conventional and State of the Art Three-Phase AC-DC Rectifier Systems

Three-phase AC-DC rectifier systems can be classified as passive systems, hybrid systems, and active systems [9]. Many such systems have been proposed in the literature and an overview is given in this sub-section. Moreover, the limitations of conventional and state of the art three-phase rectifier systems are discussed.

1.5.1 Passive Systems

A passive system is characterized by the absence of controllable semiconductor devices (IGBTs, MOSFETs, SCRs, etc.). The semiconductor devices in these systems commutate purely from the input source voltages. Furthermore, passive systems lack the ability of output voltage regulation. Examples of passive rectifier systems include diode bridge rectifiers and multi-pulse rectifiers.

1.5.1.1 Diode Bridge Rectifier

A conventional three-phase AC-DC rectifier that is widely used in industry interfaces a six-pulse rectifier with the utility grid as shown in Figure 1-7. This uncontrolled six pulse rectifier draws an input current with low order harmonics (i.e. 5^{th}, 7^{th}, 11^{th}, 13^{th}, etc.) accounting for a THD of at least 31% [1]. Since the input current has low order harmonics, the input filter must be large in size compromising the power density of the system. The diodes in the three-phase rectifier can be replaced with SCRs to provide output voltage regulation (albeit this SCR would not be classified as a passive system), but this further exacerbates the input current quality.

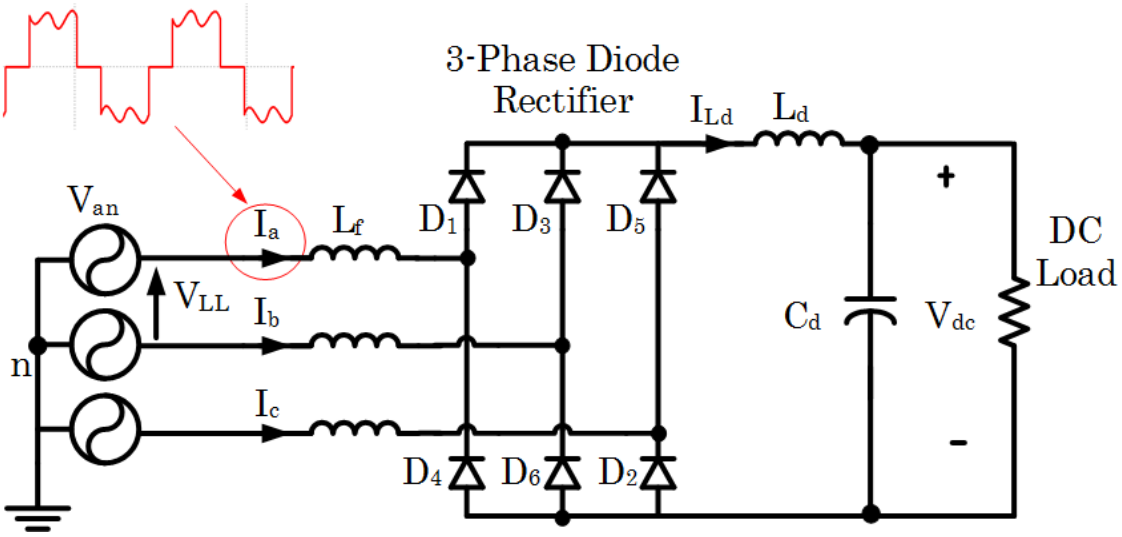

Figure 1-7: Uncontrolled six-pulse three-phase AC-DC Rectifier. Input currents contain low order harmonics

1.5.1.2 Multi-pulse Rectifier Schemes

Methods to improve the input current quality include the use of phase shifting transformers and multi-pulse rectifiers. Using a 12-pulse arrangement as shown in

Figure 1-8, the topology naturally eliminates the 5^{th}, 7^{th}, 17^{th}, etc. low order harmonics from the line input current. The harmonics present in the line input current are the 11^{th}, 13^{th}, 23^{rd}, 25^{th}, etc. This kind of arrangement is typical in industrial motor drives [25]. The input current quality can be further improved by adding more windings to the transformers and six-pulse diode rectifiers in the output. In general, the harmonics present in the input current are given by (1.5), where h represents the harmonic order, n is any integer and p is the number of pulses in the rectifier.

$$h = n \cdot p \pm 1 \tag{1.5}$$

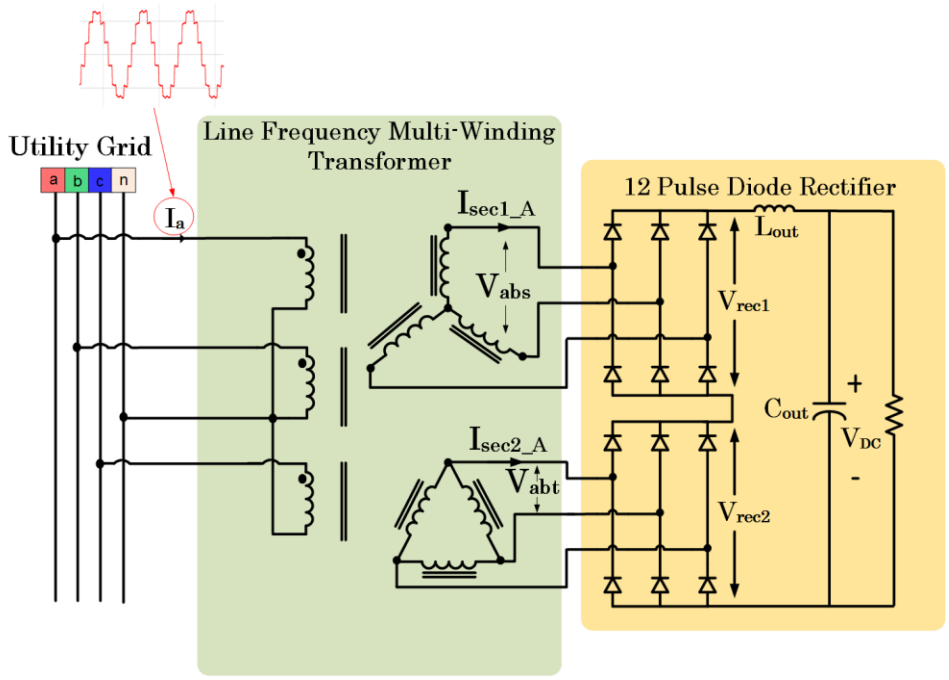

Figure 1-8: Multi-pulse three-phase AC-DC rectifier with phase-shifting transformer to eliminate low order harmonics

Despite the improvement in input current quality, the transformers employed for phase shifting operate at line frequency (50/60 Hz) and are thus large in size and weight,

compromising the power density of the system. A reduction in size and weight is achieved by employing the half-power 12-pulse approach as explained in [26]. As shown in Figure 1-9, this approach takes advantage of the fact that the star-connected secondary windings in the conventional 12-pulse approach do not have a phase shift compared to the utility grid voltages. Therefore, instead of using a star-connected set of windings, a set of reactors is interfaced between the utility grid and one of the six-pulse rectifiers in the output. However, the delta-connected windings and the new set of reactors operate at line frequency and thus size and weight remain a concern. Furthermore, in this approach electrical isolation between the input source and the load is lost.

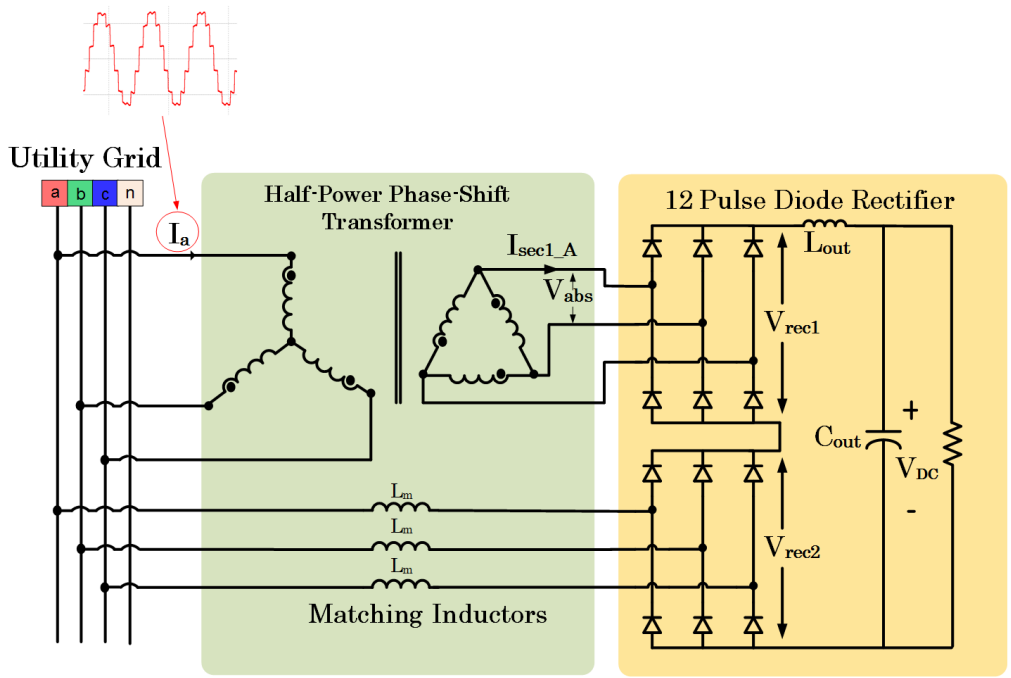

Figure 1-9: Half-power 12-pulse topology. This topology reduces size of conventional line frequency 12-pulse rectifier but loses galvanic isolation

The size and weight of multi-pulse rectifiers have been reduced by employing multi-winding autotransformers with reduced kVA ratings [27-29] . A 12-pulse rectifier approach employing autotransformer connection is shown in Figure 1-10 [27]. As shown in this figure galvanic isolation between the utility grid and the load is lost. Furthermore, since these autotransformers operate at line frequency the power density of these systems remain a concern.

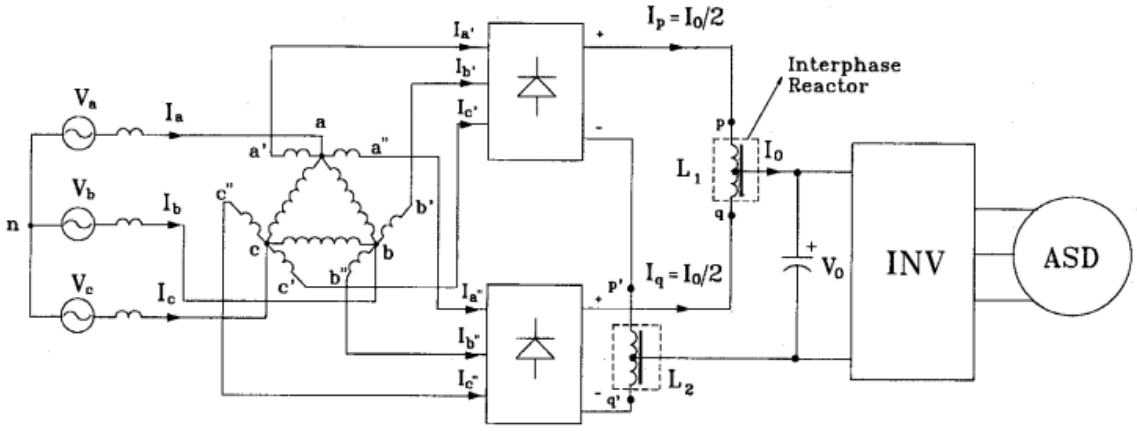

Figure 1-10: Multi-pulse rectifier with autotransformer connection. © 1996 IEEE

1.5.2 Hybrid Systems

A hybrid three-phase AC-DC rectifier system usually involves a combination of passive semiconductor devices (commutating at line frequency) and active semiconductor devices. A relevant feature of hybrid systems is output voltage regulation. A typical hybrid system is shown in Figure 1-11. When electrical isolation and output voltage regulation are required, the DC link produced by the six-pulse rectifier is interfaced to a DC-DC converter which is then connected to a high frequency

transformer. The secondary side of the transformer is then connected to a single-phase diode rectifier to produce the overall DC output. Although this topology provides isolation and output voltage regulation, it still draws an input current with low order harmonics requiring a large input filter large. In addition the configuration has multiple conversion stages (ac-dc-ac-dc) to the detriment of the system's efficiency.

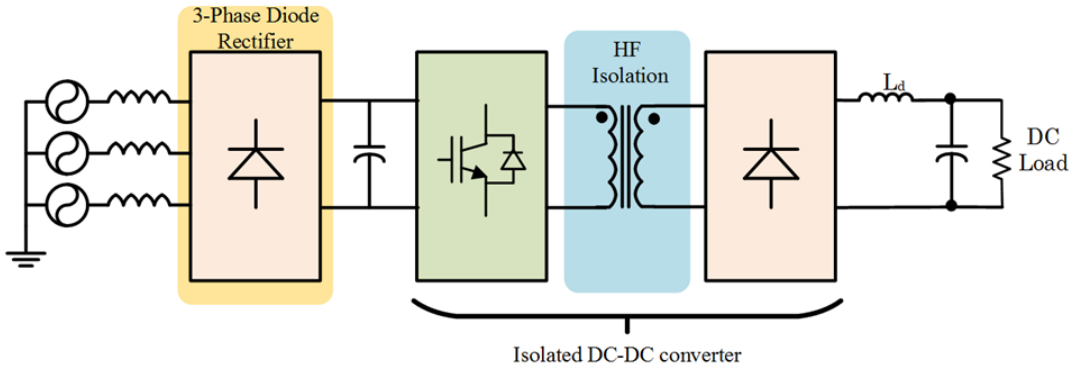

Figure 1-11: Three-phase isolated AC-DC converter with multiple conversion stages.

Other hybrid systems employ active semiconductor devices to emulate the inductor in the DC side of the diode bridge as shown in Figure 1-12 [30]. The reasoning behind this approach is that a reduction in size is achieved by eliminating the inductor, but no improvement is made to the input current quality. Other three-phase rectifier which uses the emulating inductor concept are proposed in [31, 32] . However, the current still exhibits low order harmonics (5^{th}, 7^{th}, 11^{th}, 13^{th}, etc.). This emulating inductor concept can also be extended to multi-pulse rectifiers.

Another hybrid system employing multi-pulse rectifiers and boost converters on the output for voltage regulation is shown in Figure 1-13 [33]. In this topology, a good

input current quality is achieved even when the input line voltages are distorted. Nevertheless, this topology employs line frequency magnetics and size remains a concern. In addition, this topology is not isolated.

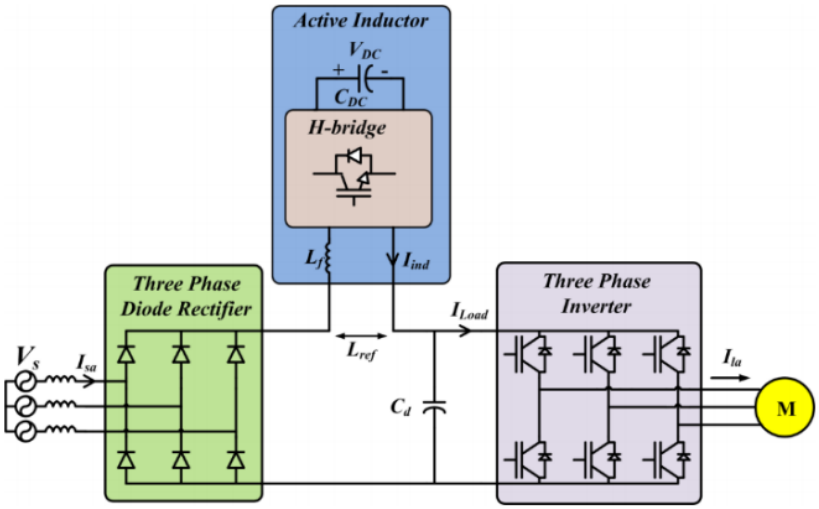

Figure 1-12: Active inductor topology [30]. © 2014 IEEE

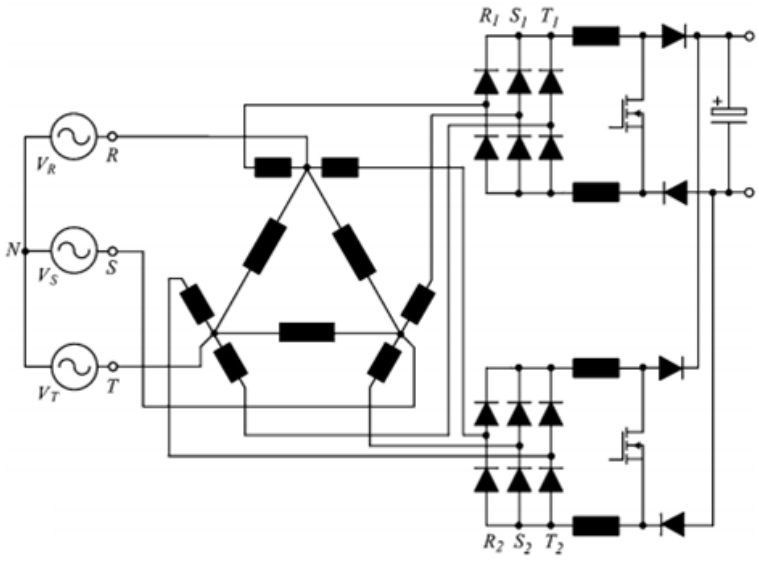

Figure 1-13: Boost type 12-pulse converter with autotransformer connection. © 2011 IEEE

1.5.3 Active Systems

A distinguishing feature of active systems is the sinusoidal nature of the line input currents. One such active method is the phase modular approach shown in Figure 1-14. In this approach, the well-known single-phase boost power factor correction (PFC) module is used for three-phase applications [34], [35]. Each module has a single-phase rectifier followed by a boost converter which allows the input current to be nearly sinusoidal and in phase with the utility line-to-neutral voltages. The electrolytic DC capacitors connected at the output of each boost converter has to suppress twice the line frequency ripple and is thus large in size. Furthermore, if isolation is required an additional full bridge converter must be added to produce an AC voltage at high frequency. At the secondary side of the transformer, a single-phase rectifier must be used to produce an overall DC output voltage. Thus, this converter requires multiple components and multiple conversion stages (i.e. ac-dc-ac-dc) contributing to complexity. Moreover, the control and modulation schemes are relatively complicated. In addition, significant sensing effort is required for proper operation.

Another active system was introduced in [36]. This scheme, shown in Figure 1-15, employs an autotransformer and multi-pulse rectifiers whose outputs are actively switched to produce an input current with low distortion at rated loads. Although low distortion is achieved, the autotransformers operate at line frequency and the overall size continues to be of concern. Furthermore, this autotransformer based multi-pulse rectifiers lack isolation between the input source and output load to detriment of safety.

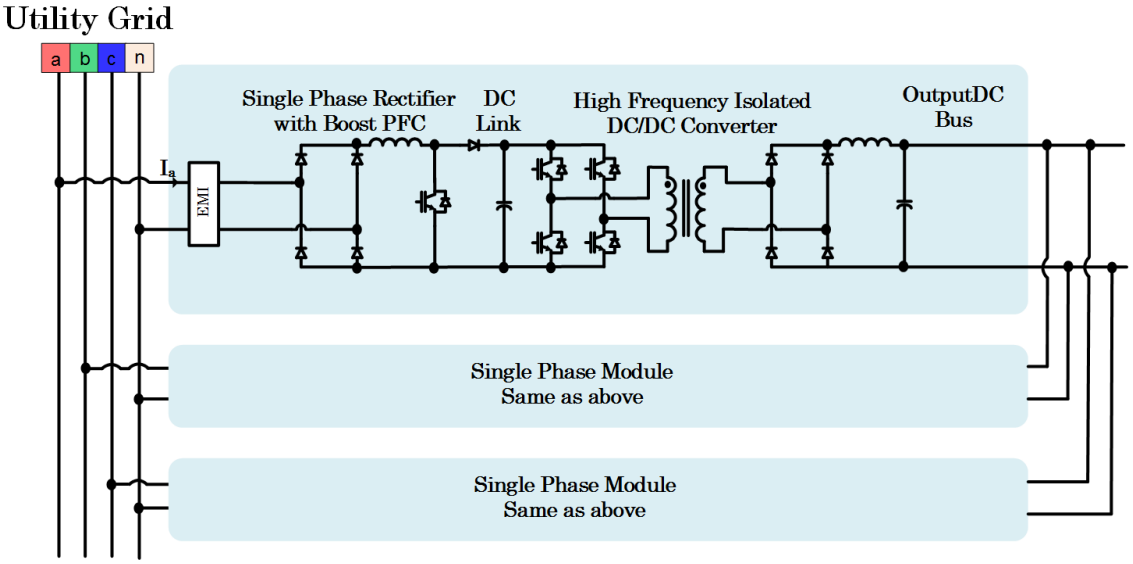

Figure 1-14: Modular three-phase AC-DC rectifier system.

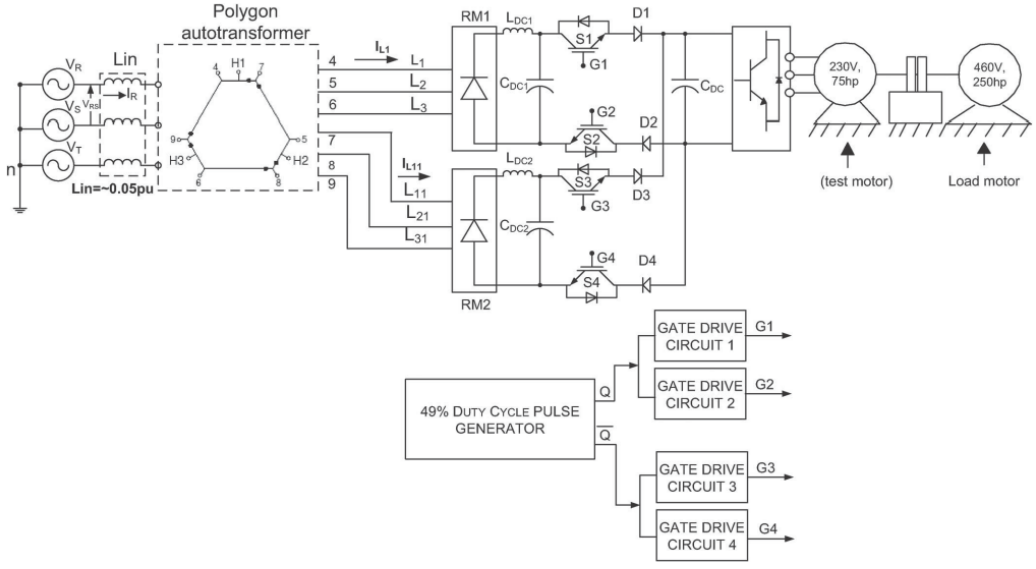

Figure 1-15: 12-pulse autotransformer rectifier for variable frequency drives. © 2015 IEEE

Other popular active rectifier systems include the three-level Vienna rectifier [37], and the six-switch PWM rectifier [38]. The Vienna rectifier has good

characteristics such as sinusoidal input current, output voltage regulation, and low voltage stress on the semiconductor devices. In comparison, the six-switch PWM rectifier has higher voltage stress but offers bidirectional power flow capability. However, these systems require an electrolytic capacitor for a DC link and also require additional conversion stages in applications requiring galvanic isolation. The shortcomings discussed in this subsection make it evident that there is room for improvement in three-phase AC-DC rectifier systems.

1.6 Research Objective

Driven by the trends and needs in the power electronics industry, the primary objective of the work in this dissertation is to analyze, design, simulate and test new three-phase AC-DC rectifier systems which employ medium or high frequency transformer isolation. These new three-phase isolated AC-DC rectifier systems overcome the limitations of conventional systems in terms of power density, simplicity, efficiency, and input current quality. Four different three-phase AC-DC rectifier systems are proposed in this dissertation. Without losing generality, a particular application is suggested for each topology to demonstrate their merit within the energy industry.

First, a push-pull based three-phase AC-DC rectifier with medium frequency isolation is proposed. The unique features of this topology include the simplicity of its modulation scheme, its minimized active switch count and its high power density.

In the second proposed three-phase AC-DC rectifier, power density and transformer utilization are further improved. A full bridge based three-phase AC-DC

rectifier with high frequency isolation is implemented. The output DC voltage is regulated with simple duty cycle control without affecting the low order harmonics in the input current making this topology suitable for telecommunication and electric vehicle charging applications. In addition this topology eliminates the use of electrolytic capacitors in the front-end.

In the third study, a PWM rectifier with selective harmonic elimination techniques is presented. A high frequency transformer is employed for isolation. The utility input current is programmed to have desired harmonic content by selecting appropriate unipolar switching functions. Thus, the input current THD is improved. The output voltage is regulated by the modulation index. Similar to the second study, this topology eliminates the use of electrolytic capacitors in the front-end.

In the final study of this dissertation, an active rectifier system based on a matrix converter is proposed. A unique feature of this system is its bidirectional power flow capability. Furthermore, a series resonant tank is employed to achieve soft switching conditions. In both the rectifier and inverter mode, the system achieves sinusoidal input current quality.

Detailed mathematical analysis and design examples are presented for each topology. The design of the medium and high frequency transformers is validated using Ansys Maxwell FEA simulations. Furthermore, the validity of the three-phase AC-DC rectifier systems is supported with detailed simulation results and experimental results on laboratory scaled-down prototypes.

1.7 Outline of Dissertation

This dissertation is divided into seven sections. Section 1 introduces three-phase AC-DC rectifier systems and their relevance is emphasized by describing their role in numerous applications within the energy industry. The figures of merit of a three-phase AC-DC rectifier system are explained and the advantages of using medium or high frequency isolation are highlighted. Furthermore, the conventional state of the art and conventional three-phase AC-DC rectifiers are introduced and their limitations explained. Section 1 concludes with the research objective.

In Section 2, the three-phase push-pull based AC-DC rectifier is proposed. The section explains how the front-end of the proposed converter can be a retrofit replacement of bulky line-frequency transformers in conventional isolated 12-pulse systems. Only two active semiconductor devices are used to create a three-phase medium frequency AC link. A zig-zag multi-winding medium frequency transformer is proposed to achieve galvanic isolation and to improve power density. Furthermore, it is also explained how the topology can be extended for 18-pulse operation. After detailed mathematical analysis, the topology's circuit behavior is simulated using PSIM. The magnetic behavior of the transformer is analyzed using ANSYs Maxwell finite element analysis (FEA) simulation tools. The performance of the proposed topology is validated through experimental results on a 3.15 kW laboratory scaled-down prototype.

In Section 3, a full bridge based three-phase AC-DC rectifier system is proposed. This section explains how a three-phase high frequency AC link is created using an AC-AC converter in the front-end. A zig-zag high frequency ferrite core transformer is

employed for isolation and to improve power density. The secondary side of the zig-zag transformer is connected to a 12-pulse rectifier to achieve a DC output. A simple PI duty cycle control technique is used to regulate the output DC voltage. Through detailed mathematical analysis it is shown that varying the duty cycle does not affect the low order current harmonics. This system also has the advantage of being scalable to high voltage levels at the cost of component count. Different embodiments of the topology are also presented. Simulation results in PSIM and Maxwell are presented to verify functionality of the system. Experimental results on a 1 kW laboratory scaled-down prototype validate the proposed concept.

In Section 4, a PWM rectifier with high frequency (20 kHz) isolation is proposed. The converter is modulated using programmed PWM switching functions. This section shows that selected harmonics are eliminated from the utility input current. Solving non-linear equations yields the switching angles required to achieve output voltage control and elimination of low order harmonics. A 50 kW design example and detailed simulation results are presented to demonstrate the operation of the PWM rectifier. The main advantages of this topology include the absence of electrolytic capacitors, good input current quality, and high power density.

In Section 5, a matrix converter based three-phase rectifier system is proposed. The matrix converter takes a three-phase input voltage at line frequency and produces a quasi-square wave AC output at high frequency. The output of the matrix converter is interfaced to a single-phase high frequency ferrite core transformer through a series resonant tank. The secondary side of the transformer is connected to a PWM rectifier.

This section details the bidirectional power flow operation of the system and explains its soft switching characteristics. Detailed simulation results on a 30 kW design example are presented. Experimental results on a 500 W laboratory scaled-down prototype validate the operation of the series resonant tank and high frequency ferrite core transformer.

In Section 6, the analysis and design of medium and high frequency transformers is presented. The different characteristics of magnetic materials and their limitations are explained in detail. Finite element analysis (FEA) software such as Ansys Maxwell is used to assess the performance of the proposed medium and high frequency transformers. Using this FEA tool assists in making relevant conclusions about the transformers in terms of size, weight, and saturation effects.

The last section in this dissertation, Section 7, provides a summary of the obtained results for each of the proposed systems highlighting their advantages and disadvantages. Moreover, a list of possible areas of investigation is suggested for further work in three-phase AC-DC rectifier systems.

2. REDUCED ACTIVE SWITCH FRONT END MULTI-PULSE RECTIFIER WITH MEDIUM FREQUENCY TRANSFORMER ISOLATION*

This section presents a reduced switch count multi-pulse rectifier with medium frequency (MF) transformer isolation. The proposed topology consists of a three-phase push-pull based AC to DC rectifier with a MF AC link employing two active switches. A three-phase, five-limb, multi-winding MF transformer is employed for isolation. The secondary side of the transformer is connected in zig-zag configuration and is fed to two six-pulse diode rectifiers, achieving 12-pulse rectifier operation. The primary advantage of the proposed system is reduction in size/weight/volume compared to the conventional 60 Hz magnetic transformer isolation rectifier system. Operating the transformer at 600 Hz is shown to result in three times reduction in size. Furthermore, the proposed system employs only two active semiconductor switching devices operating under a simple pulse width modulation scheme. Also the zig-zag transformer connection helps to balance leakage inductance on the secondary side. Detailed analysis, simulation, and experimental results on a $208V_{l\text{-}l}$, 3.15 kW laboratory prototype are presented to validate the performance of the proposed approach.

---

* Part of this section is reprinted with permission from:

1. ©2016 IEEE. J. J. Sandoval, H. Krishnamoorthy, P. Enjeti, and S. Choi, "Reduced Active Switch Front End Multi-pulse Rectifier with Medium Frequency Transformer" in *IEEE Transactions on Power Electronics*, vol.PP.no.99, pp.1-1.
2. ©2015 IEEE. J. J. Sandoval, H. Krishnamoorthy, P. Enjeti, and S. Choi, "High power density adjustable speed drive topology with medium frequency transformer isolation," *2015 IEEE Energy Conversion Congress and Exposition (ECCE)*, Montreal, QC, 2015. pp. 6986-6992.
3. ©2016 IEEE. J. J. Sandoval, T. Kang, and P. Enjeti, "Reduced active switch AC to DC rectifier with high frequency isolation for electric vehicle chargers," *2016 IEEE Applied Power Electronics Conference and Exposition (APEC)*, Long Beach, CA, 2016. Pp. 3545-3552.

2.1 Introduction

Multi-pulse rectifier systems are used in a wide variety of applications in the industry [39, 40]. Both isolated and non-isolated transformer configured multi-pulse rectifier systems have been in use [25, 26, 41, 42]. The primary advantage of multi-pulse rectifier systems is high quality dc-output voltage with simultaneous elimination of low frequency harmonic currents at the input utility terminals. In particular, 12-pulse and 18-pulse rectifier systems result in input current THD less than 16%, thereby facilitating compliance with IEEE 519 harmonic current limits. Much of these systems employ low frequency (50/60 Hz) magnetics that contribute to size/weight/volume particularly in high power applications. The typical 12-pulse rectifier system with line frequency (50/60 Hz) isolation transformer configuration is shown in Figure 1-8. The star-delta transformer connection in Figure 1-8 creates a 30^{o} phase shift between the currents feeding the diode rectifiers. As a result, low order harmonics such as the 5^{th} and 7^{th} are eliminated from the line input current and a better THD is achieved. Nevertheless, such a system is large in size/weight with the bulky magnetics being the major limiting factor.

Reduction in size and weight is achieved with the half-power transformer based 12-pulse rectifier system as explained in [26]. In this approach, a line frequency transformer processing half the power is employed and thus size remains a concern. Furthermore, this system is not suitable in applications requiring to step down or step up the voltage level [26]. Auto-transformer based multi-pulse rectifier systems are detailed in [27, 28, 36, 43]. Reduction in size and weight is achieved due to reduced kVA rating of the auto-transformer configuration. Autotransformer rectifier configurations with

$0.18P_o$ and $0.38P_o$ ratings are reported in [27] and [36], respectively, compared to the $1.03P_o$ rating of the multi-winding transformer shown in Figure 1-8. However, these auto-transformer configurations do not have galvanic isolation and employ 60 Hz magnetics. Thus, the use of line frequency magnetics continues to have a negative impact on the size/weight of the rectifier system.

Modular three-phase power factor correction (PFC) AC to DC rectifier systems with high-frequency magnetics are detailed in [34, 35, 44, 45]. Despite the improvement in input current quality, these systems employ multiple power conversions and employ a high number of semiconductor devices. Furthermore, active PFC schemes require a significant sensing effort and are complicated to control. Also, electromagnetic interference (EMI) is a concern in these topologies due to their high switching frequency operation.

In contrast, the proposed topology shown in Figure 2-1 seeks to improve over the existing 12-pulse AC to DC rectifier systems (isolated and auto-connected) by reducing size/weight/volume and improving the performance. The advantages of the proposed system architecture are as follows.

1) The approach employs medium frequency (600Hz) magnetics that is shown to improve power density by reducing the size/weight of the system [46, 47].
2) The proposed approach employs only two active semiconductor devices. This contributes to system simplicity and reduced cost.
3) The 5^{th} and 7^{th} harmonics are eliminated in the input line current resulting in reduction in input current THD.

4) The system offers galvanic isolation between the input and output thereby minimizing the interference and contributing to safety.
5) The proposed approach is suitable for applications in ship board / subsea power systems, and offshore drilling rigs where power density, performance and simplicity in control are of paramount importance [48, 49].
6) The secondary side of the MF transformer can be configured to higher pulse operation (i.e., 18-pulse as shown in Figure 2-2, and 24-pulse) to further improve current quality. This, however, increases transformer design complexity.

These benefits make the topology suitable for operation up to 480V three-phase systems for powering loads up to 300 kW. The paper details the analysis and design of the proposed multi-pulse rectifier system along with a design example. Simulation and experimental results are discussed on a scale-down laboratory prototype.

2.2 Proposed Front-End Rectifier with Medium Frequency Transformer Isolation

The proposed system employing MF isolation with a multi-winding transformer is shown in Figure 2-1. The analysis and operation of the proposed topology is detailed in this sub-section.

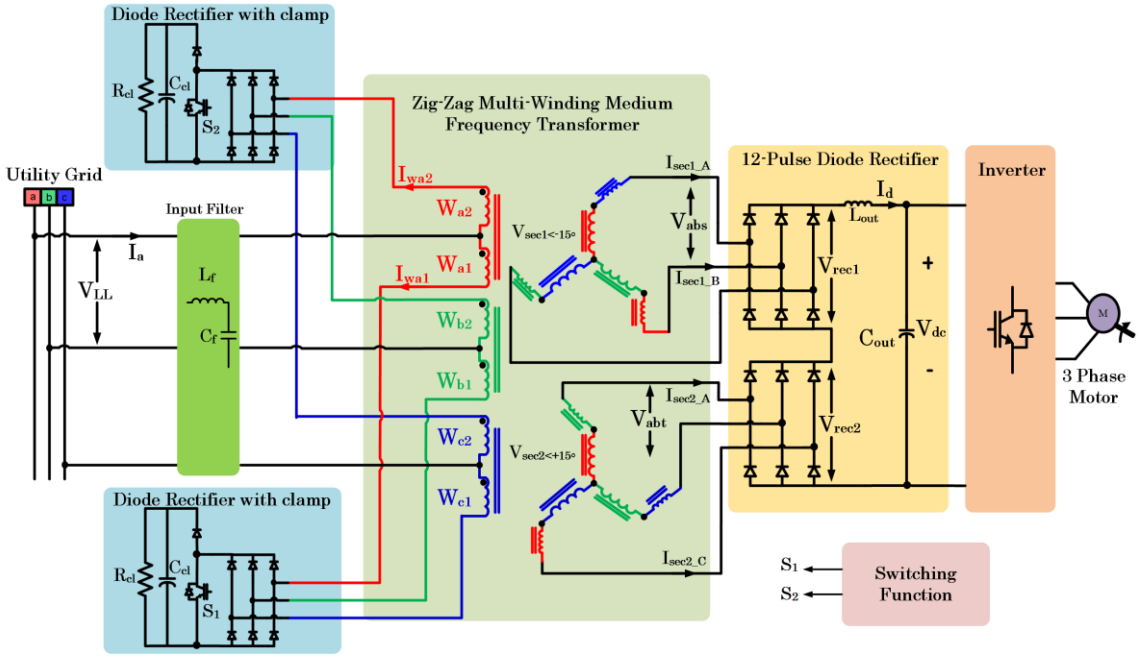

Figure 2-1: Proposed 12-pulse AC-DC rectifier system with medium frequency transformer isolation employing two active switches. An example adjustable speed drive system is shown at the output.

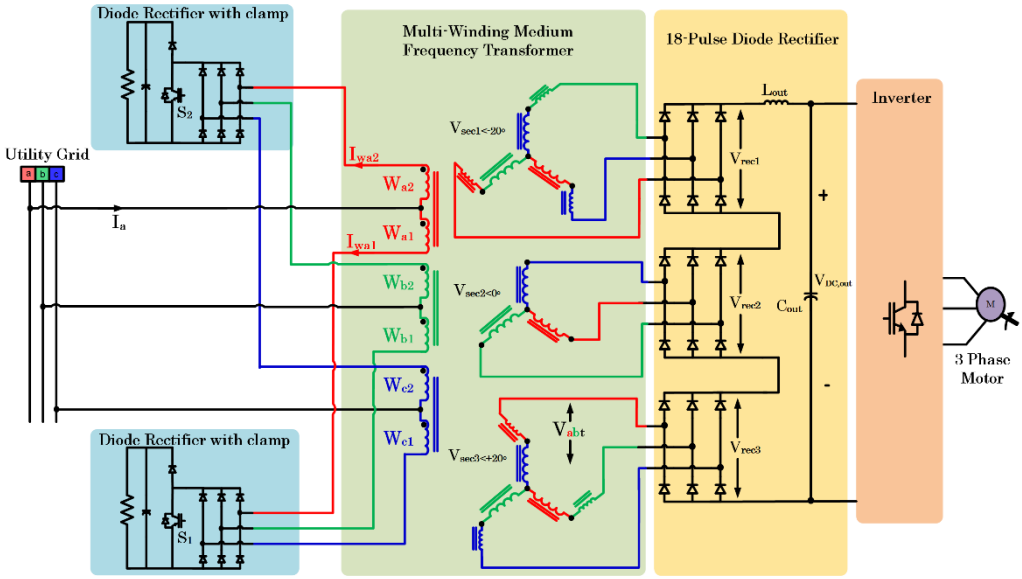

Figure 2-2: The topology in Figure 2-1 extended to 18-pulse configuration. This configuration requires three additional windings in the secondary side of the MF transformer.

2.2.1 Diode Rectifiers with Clamp Circuit

This part of the system is composed of two three-phase diode rectifiers, each connected to a high voltage active switch (S_1/S_2) and a clamp circuit, which consist of a capacitor and a bleeding resistor (Figure 2-1). The creation of the three-phase AC link across the transformer windings is achieved by switching S_1 and S_2 complementarily with 50% duty cycle as first described in [50] and as shown in Figure 2-3 (a), (b). The overall switching function for 50% duty cycle is shown in Figure 2-3 (c). The primary windings of the zig-zag transformer can be divided into two sets that are 180° phase shifted in magnetic coupling, namely windings (W_{a1}, W_{b1}, W_{c1}) and windings (W_{a2}, W_{b2}, W_{c2}). As shown in Figure 2-1, the center tap of each primary winding is connected to the utility grid. In addition, the switching terminals of windings (W_{a1}, W_{b1}, W_{c1}) are connected to a diode rectifier whose output is in turn connected to S_1. Similarly, the switching terminals of windings (W_{a2}, W_{b2}, W_{c2}) are connected to a diode rectifier whose output is in turn connected to S_2.

Figure 2-4 shows the behavior of the diode rectifier with clamp circuit and the primary side windings when S_1 is ON and S_2 is OFF. The switching terminals of windings (W_{a1}, W_{b1}, W_{c1}) are shorted through the diode rectifier while the switching terminals of windings (W_{a2}, W_{b2}, W_{c2}) are open. In essence, the switching terminals of windings (W_{a1}, W_{b1}, W_{c1}) are shorted to the utility's neutral point. Therefore, at this instant, the line-to-neutral voltages V_{an}, V_{bn}, and V_{cn} appear across windings W_{a1}, W_{b1}, and W_{c1} respectively. The voltages across windings (W_{a2}, W_{b2}, W_{c2}) have opposite polarity compared to the voltages across windings (W_{a1}, W_{b1}, W_{c1}) because they are

180° in magnetic coupling. Meanwhile, the induced voltages on the secondary side have the same polarity as the voltages across windings (W_{a1}, W_{b1}, W_{c1}).

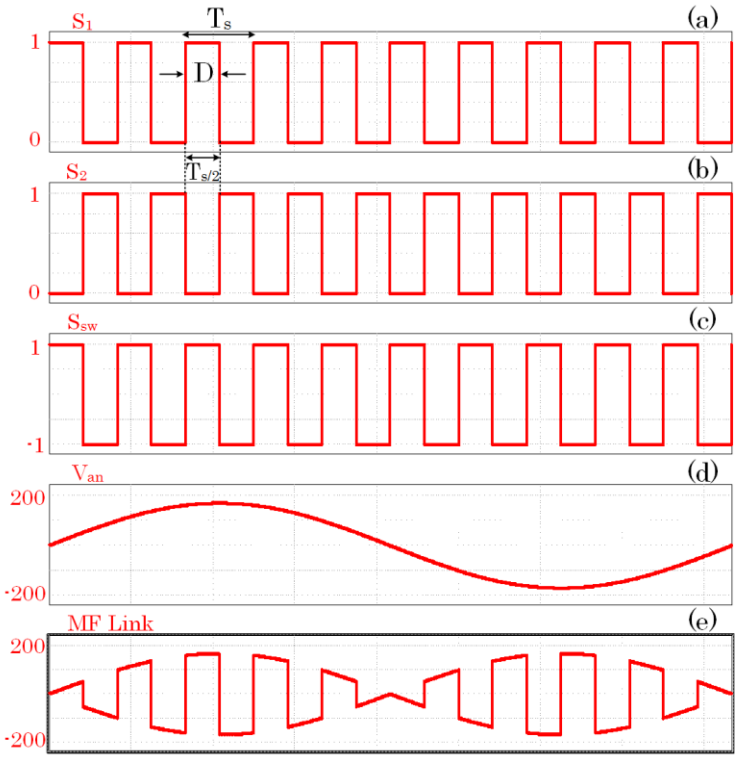

Figure 2-3: (a) Gating function for S_1 with D=0.5; (b) Gating function for S_2 with D=0.5; (c) Overall system switching function; (d) V_{an}, input line-to-neutral voltage; (e) Medium frequency AC link is the multiplication of S_{sw} and V_{an} created by switching S_1 and S_2 complementarily with 50% duty cycle.

When S_1 is gated OFF and S_2 is gated ON, the switching terminals of windings (W_{a1}, W_{b1}, W_{c1}) are open while the switching terminals of windings (W_{a2}, W_{b2}, W_{c2}) are shorted and are at the same potential as the utility's neutral point as shown in Figure 2-5. At this instant, the line-to-neutral voltages V_{an}, V_{bn}, and V_{cn} appear across windings W_{a2}, W_{b2}, and W_{c2} respectively. The induced voltages on the secondary side and the voltages across windings (W_{a1}, W_{b1}, W_{c1}) have opposite polarity compared to the utility grid line-

to-neutral voltages. The voltage polarity across each winding changes as S_1 and S_2 are switched. Therefore, by switching S_1 and S_2 at MF a three-phase MF AC link is created.

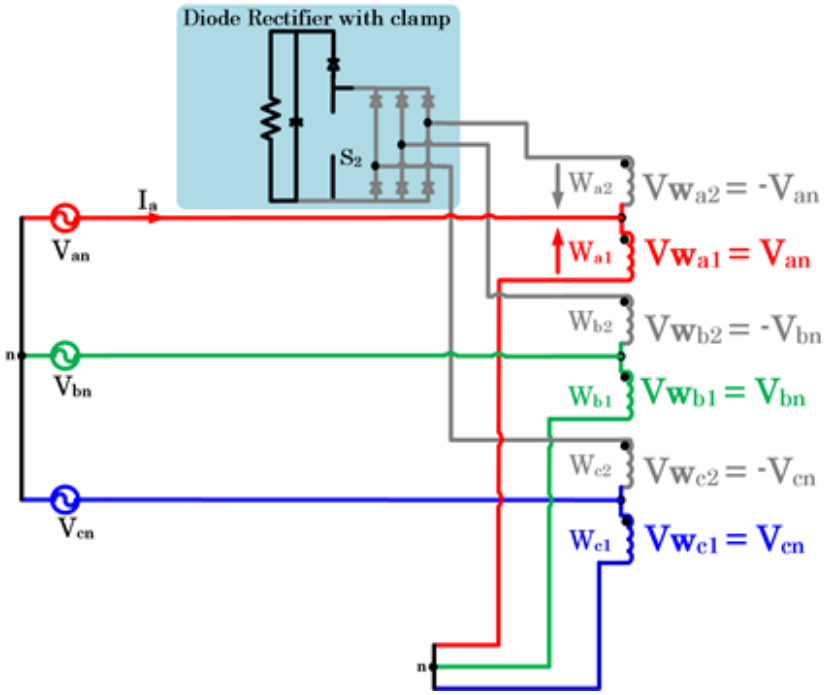

Figure 2-4: Operation when S_1 is gated ON and S_2 is gated OFF. The switching terminals of W_{a1}, W_{b1}, W_{c1} are neutrally connected while the switching terminals of W_{a2}, W_{b2}, W_{c2} are open.

The three-phase AC link is simply a multiplication of the line-to-neutral voltages with a square wave switching function. Figure 2-3(e) shows the mathematical AC voltage across winding W_{a1} when the system operates at 50% duty cycle. With a line-to-neutral voltage as in (2.1) and a square wave switching function described by (2.2), the resulting voltage across the transformer winding W_{a1} can be expressed as in (2.3). It is evident that the frequency of the square wave switching function determines the fundamental frequency of the AC link created across the two sets of windings. The

voltages across windings W_{b1} and W_{c1} have a similar expression as in (2.3) but are 120° and 240° phase shifted respectively. The expression at (2.3) is valid for 50% duty cycle operation.

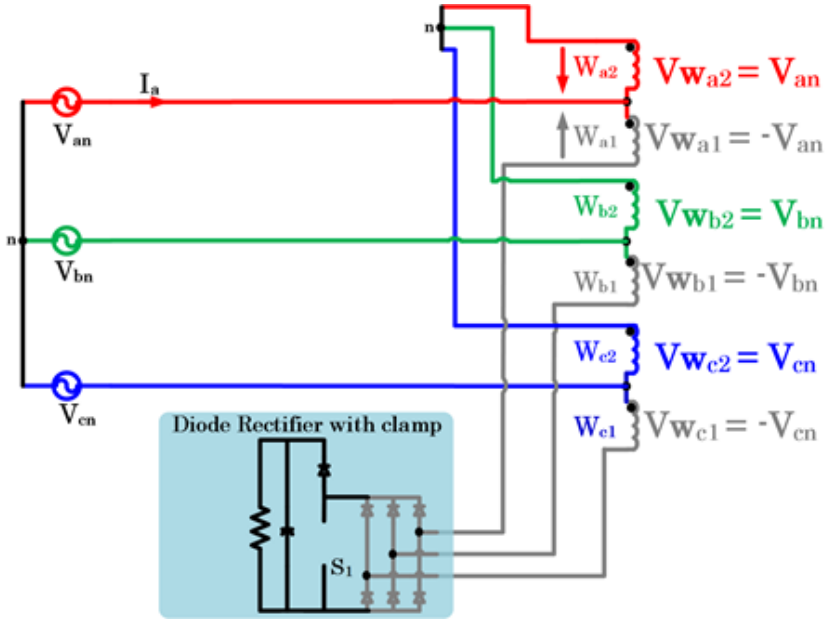

Figure 2-5: Operation when S_1 is gated OFF and S_2 is gated ON. The switching terminals of W_{a2}, W_{b2}, W_{c2} are neutrally connected while the switching terminals of W_{a1}, W_{b1}, W_{c1} are open.

$$V_{an} = \sqrt{\frac{2}{3}} V_{LL} \sin(\omega_s t) \tag{2.1}$$

$$S_{sw} = \frac{4}{\pi} \sum_{n=1,3,5,\ldots}^{\infty} \frac{1}{n} \sin(n\omega_{sqr} t) \tag{2.2}$$

$$V_{Wa1} = \sqrt{\frac{2}{3}} V_{LL} \sum_{n=1,3,5,7,..}^{\infty} \frac{2}{n\pi} \sin(\{n\omega_{sqr} \pm \omega_s\} \cdot t) \tag{2.3}$$

When the switching terminals of windings (W_{a1}, W_{b1}, W_{c1}) or (W_{a2}, W_{b2}, W_{c2}) are open, the clamp circuit provides a path for the energy stored in the leakage inductance of the windings. For example, when S_1 is OFF, the energy stored in the leakage inductance of windings (W_{a1}, W_{b1}, W_{c1}) is transferred to the capacitor which clamps to the highest line-to-line voltage. Furthermore, in order to avoid overlap (instances in which both S_1 and S_2 are ON) a dead time between S_1 and S_2 is necessary. During this dead time the clamp circuit also provides a path for the energy stored in the leakage inductance of the windings. The energy stored in the capacitor can be used to power a switch mode power supply (SMPS). This SMPS can power gate drive circuitry.

2.2.2 Medium Frequency Multi-Winding Transformer

The switching frequency of S_1 and S_2 determines the operating frequency of the transformer. The well-known trade-off between power density and efficiency must be considered when selecting the switching frequency. Operating at MF (600 Hz -1000 Hz) enables the transformer to be reduced in size and provides a good efficiency trade-off especially in high power applications [46]. Increasing the switching frequency to the kHz range increases transformer core loss and switching losses. Furthermore, operating in the kHz range increases the input EMI and introduces the need for additional EMI filtering at the input [36]. Thus, the transformer is designed to operate at 600 Hz.

Selection of the appropriate magnetic materials is also critical to achieve high power density. For high power MF applications, magnetic core materials such as ferrite, amorphous, and silicon steel should be considered [24]. Due to its high saturation flux density and relative low cost [51], a silicon steel core material was selected to build the

MF transformer for the scaled down laboratory prototype. The transformer can be built using three single-phase multi-winding transformers, or it can be a single three-phase multi-winding transformer. To achieve a more compact design, a single five-limb transformer is employed for isolation. The primary and secondary windings are wound around the interior three limbs of the transformer as depicted in Figure 2-6. The exterior limbs can carry any unbalanced flux in the transformer avoiding core saturation [52].

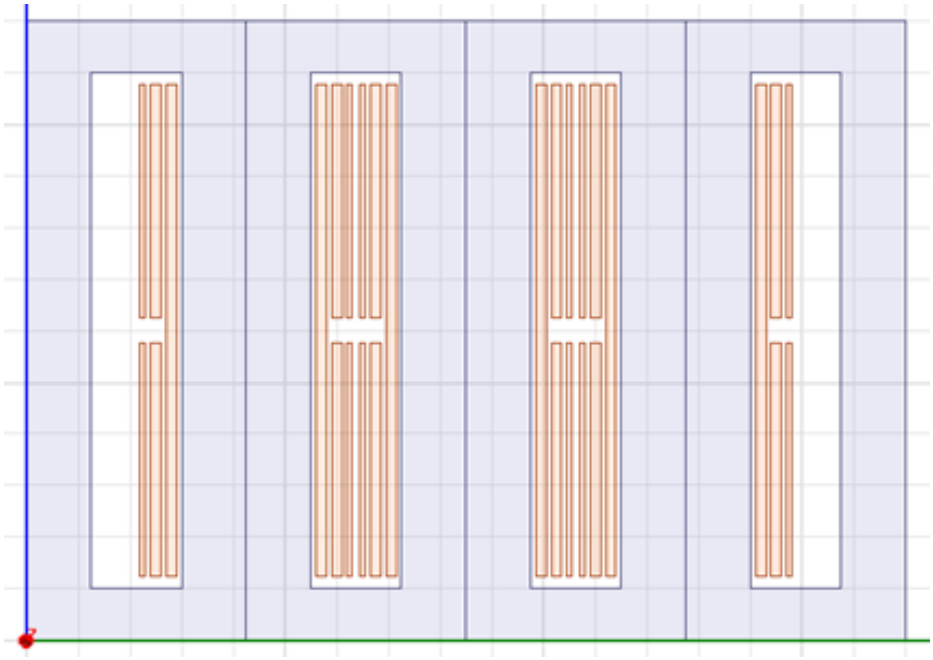

Figure 2-6: Multi-winding three-phase, five-limb transformer.

Generally, in 12-pulse applications a star-delta winding connection is used in the secondary side to generate a net 30^{o} phase difference. However, the leakage inductances of the terminals feeding the diode bridge rectifiers are not equal because the turns-ratio is different in the star-delta connected windings. This issue leads to unequal current

sharing between the diode bridges [27]. To mitigate this problem, the secondary side of the MF transformer in the proposed system is connected in zig-zag. With zig-zag arrangement the leakage inductances on the secondary side are balanced because the turns-ratio of the windings per phase is the same.

The MF transformer consists of two zig-zag connections on the secondary side, each creating a set of three-phase voltages that feed the output six-pulse rectifiers. The two sets of three-phase voltages have a net phase shift of 30° with respect to each other to achieve 12-pulse operation. One of the zig-zag connections creates a set of three-phase voltages with a +15° phase difference with respect to the primary side voltages. In a similar manner, the second zig-zag connection creates a set of three-phase voltages with a -15° phase difference with respect to the primary side voltages. A phasor diagram of the primary windings and the secondary windings is shown in Figure 2-7. The primary side in Figure 2-7 shows the line-to-line voltages forming an equilateral triangle with phasor V_{an} being the reference as expressed in (2.4). The phasor expressions for V_{bn}, V_{cn}, V_{ab}, V_{bc}, and V_{ca} are given by (2.5-2.9) respectively.

$$V_{an} = 1\angle 0° \quad (2.4) \qquad V_{bn} = 1\angle -120° \quad (2.5) \qquad V_{cn} = 1\angle +120° \quad (2.6)$$

$$V_{ab} = \sqrt{3}\angle 30° \quad (2.7) \qquad V_{bc} = \sqrt{3}\angle -90° \quad (2.8) \qquad V_{ca} = \sqrt{3}\angle 150° \quad (2.9)$$

In the secondary side of Figure 2-7, there are two zig-zag connections with the respective ±15° phase shift. In order to achieve the desired phase shift in the zig-zag connected windings, the turns-ratio of the windings must be set properly. The turns-ratio of the windings correspond to the magnitudes of the solid-phasors in Figure 2-7 and can

be obtained by performing phasor operations. For example, the phasor V_{as} has a -15° phase shift with respect to phasor V_{an} and is obtained by adding a positive portion of V_{an} and a negative portion of V_{cn} as expressed in (2.10). Similarly, (2.11) shows the relation to obtain phasor V_{at}. The magnitudes of V_{as}, V_{bs}, V_{cs}, are set so that the line-to-line voltages on the secondary side (i.e V_{abs}, V_{bcs}, V_{cas}) are equal in magnitude to primary side line-to-line voltages. Thus, the dashed-phasors V_{abs}, V_{bcs}, V_{cas} form an equilateral triangle whose vertices are shifted by -15° with respect to the triangle in the primary side. Similarly, the phasors V_{abt}, V_{bct}, V_{cat} form an equilateral triangle whose vertices are shifted by +15° with respect to the triangle in the primary side.

$$V_{as} = N_{s1}V_{an} - N_{s2}V_{cn} = N_{s1}\angle 0° - N_{s2}\angle +120° = 1\angle -15° \tag{2.10}$$

$$V_{at} = N_{s3}V_{an} - N_{s4}V_{bn} = N_{s3}\angle 0° - N_{s4}\angle -120° = 1\angle +15° \tag{2.11}$$

Each solid phasor in Figure 2-7 corresponds to a secondary side winding. Thus, the core will have four windings per phase. The turns-ratio of these windings can be found by solving (2.10) and (2.11). Breaking (2.10) and (2.11) into its real and imaginary components yields two systems of two equations and two unknowns and solving them gives the desired turns-ratio as expressed in (2.12). Figure 2-8 shows the interconnection between the secondary windings to achieve the zig-zag connection along with the turns-ratio.

$$\begin{aligned} N_{P1} : N_{P2} : N_{S1} : N_{S2} : N_{S3} : N_{S4} &= 1:1:\sqrt{\frac{2}{3}} : \frac{\sqrt{3}-1}{\sqrt{6}} : \sqrt{\frac{2}{3}} : \frac{\sqrt{3}-1}{\sqrt{6}} \\ &= 1:1:0.816:0.298:0.816:0.298 \end{aligned} \tag{2.12}$$

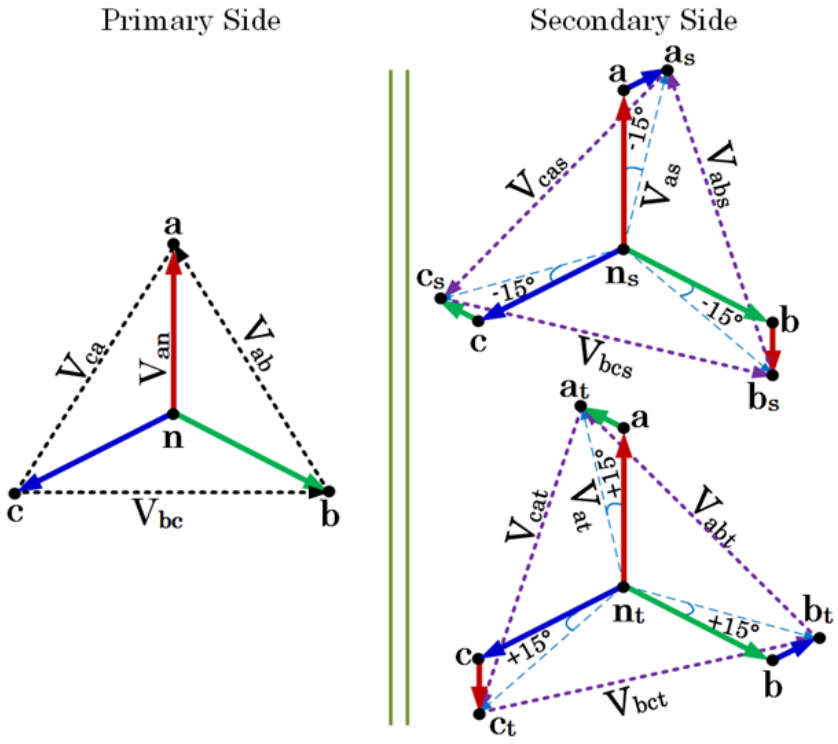

Figure 2-7: Phasor diagram to obtain two sets of three-phase voltages in the secondary side with a net 30° phase shift.

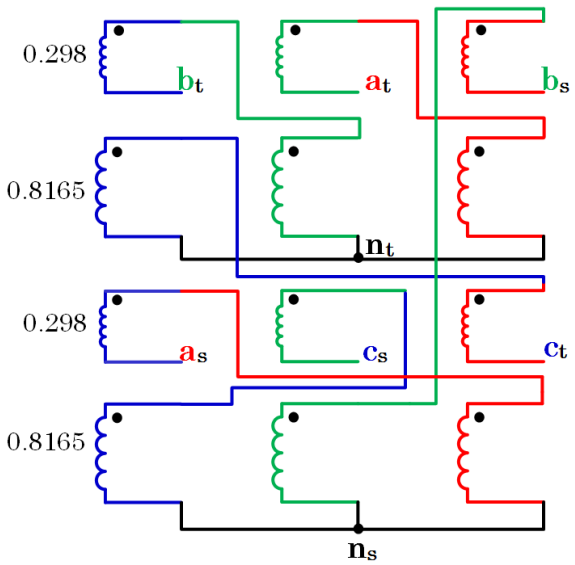

Figure 2-8: Zig-zag connection of secondary windings. Interior limbs of three-phase transformer, each limb has four secondary windings.

2.2.3 12-Pulse Diode Rectifier

Two sets of three-phase MF voltages with a net 30^o phase difference are created with the zig-zag arrangement. Each set is fed to a six-pulse diode rectifier achieving 12-pulse rectification. The operation of the bridge rectifiers is similar to the conventional line frequency 12-pulse configuration. The main difference is that the diodes should be able to switch at the operating switching frequency.

2.2.4 Output Voltage Analysis

The output voltage produced by the 12-pulse diode rectifier is the sum of voltages V_{rec1} and V_{rec2} and is described by (2.13), where V_{rec1} and V_{rec2} are the individual voltages produced by the individual six-pulse diode rectifiers.

$$V_{12-pulse}(\omega_s t) = V_{rec1}(\omega_s t) + V_{rec2}(\omega_s t) \tag{2.13}$$

The voltage V_{rec1} is given by (2.14). The voltages V_{ans}, V_{bns}, and V_{cns} represent the secondary side line-to-neutral voltages of the zig-zag windings creating a -15° phase shift. These secondary side voltages are expressed in equations (2.15-2.17) respectively assuming ideal conditions (i.e. no voltage drops in the semiconductor devices in the primary side). In these equations S_{sw} refers to the square wave switching function described by (2.2). The term S_d refers to the quasi-square wave switching function of six-pulse diode rectifiers and is given by (2.18).

$$V_{rec1}(\omega_s t) = V_{ans} \cdot S_{sw} + V_{bns} \cdot S_{sw} + V_{cns} \cdot S_{sw} \tag{2.14}$$

$$V_{ans} = \frac{\sqrt{2}V_{LL}}{\sqrt{3}} \sin\left(\omega_s t - \frac{\pi}{12}\right) \cdot S_{sw} \cdot S_d\left(\omega_s - \frac{\pi}{12}\right) \tag{2.15}$$

$$V_{bns} = \frac{\sqrt{2}V_{LL}}{\sqrt{3}} \sin\left(\omega_s t - \frac{\pi}{12} - \frac{2\pi}{3}\right) \cdot S_{sw} \cdot S_d\left(\omega_s - \frac{\pi}{12} - \frac{2\pi}{3}\right) \tag{2.16}$$

$$V_{cns} = \frac{\sqrt{2}V_{LL}}{\sqrt{3}} \sin\left(\omega_s t - \frac{\pi}{12} + \frac{2\pi}{3}\right) \cdot S_{sw} \cdot S_d\left(\omega_s - \frac{\pi}{12} + \frac{2\pi}{3}\right) \tag{2.17}$$

$$S_d(\omega_s t) = \sum_{n=1,3,5,7}^{\infty} \left(\frac{4}{n\pi} \cos\left(\frac{n\pi}{6}\right)\right) \cdot \sin(n\omega_s t) \tag{2.18}$$

Substituting equations (2.15-2.18) into equation (2.14) yields:

$$V_{rec1}(\omega_s t) = S_{sw} \cdot S_{sw} \cdot \frac{\sqrt{2}}{\sqrt{3}} V_{LL} \begin{bmatrix} \sin\left(\omega_s t - \frac{\pi}{12}\right) \cdot S_d\left(\omega_s - \frac{\pi}{12}\right) + \\ \sin\left(\omega_s t - \frac{\pi}{12} - \frac{2\pi}{3}\right) \cdot S_d\left(\omega_s - \frac{\pi}{12} - \frac{2\pi}{3}\right) + \\ \sin\left(\omega_s t - \frac{\pi}{12} + \frac{2\pi}{3}\right) \cdot S_d\left(\omega_s - \frac{\pi}{12} + \frac{2\pi}{3}\right) \end{bmatrix} \tag{2.19}$$

It is worth noting that for 50% duty cycle operation the term $S_{sw} \cdot S_{sw}$ yields a constant one. Simplifying the terms inside the brackets of (2.19) yield an output voltage V_{rec1} given by (2.20). From inspection, it is observed that V_{rec1} contains a DC term with some AC ripple riding on it.

$$V_{rec1}(\omega_s t) = \frac{3\sqrt{2} \cdot V_{LL}}{\pi} \left(1 + 0.057 \sin(6\omega_s t) + 0.014 \cos(12\omega_s t) + ...\right) \tag{2.20}$$

In a similar manner, the voltage V_{rec2} is given by (2.21). However, the voltages V_{ats}, V_{bts}, and V_{cts} represent the secondary side line-to-neutral voltages of the zig-zag windings creating a +15° phase shift. The +15° phase shift is evident from equations (2.22-2.24).

$$V_{rec2}(\omega_s t) = V_{ats} \cdot S_{sw} + V_{bts} \cdot S_{sw} + V_{cts} \cdot S_{sw} \tag{2.21}$$

$$V_{ats} = \frac{\sqrt{2}V_{LL}}{\sqrt{3}} sin\left(\omega_s t + \frac{\pi}{12}\right) \cdot S_{sw} \cdot S_d\left(\omega_s + \frac{\pi}{12}\right) \tag{2.22}$$

$$V_{bts} = \frac{\sqrt{2}V_{LL}}{\sqrt{3}} sin\left(\omega_s t + \frac{\pi}{12} - \frac{2\pi}{3}\right) \cdot S_{sw} \cdot S_d\left(\omega_s + \frac{\pi}{12} - \frac{2\pi}{3}\right) \tag{2.23}$$

$$V_{cts} = \frac{\sqrt{2}V_{LL}}{\sqrt{3}} sin\left(\omega_s t + \frac{\pi}{12} + \frac{2\pi}{3}\right) \cdot S_{sw} \cdot S_d\left(\omega_s + \frac{\pi}{12} + \frac{2\pi}{3}\right) \tag{2.24}$$

Substituting equations (2.22-2.24) into equation (2.21) yields the relation given by (2.25). Simplification of (2.25) and assuming 50% duty cycle yields an output voltage V_{rec2} given by (2.26). Substituting equations (2.20) and (2.26) into (2.13) gives the total output voltage produced by the 12-pulse diode rectifier and can be calculated by (2.27). It is observed that the total output voltage contains a DC component and an AC ripple whose frequency is twelve times the utility line frequency. This expression is the same as the conventional line-frequency 12-pulse configuration.

$$V_{rec2}(\omega_s t) = S_{sw} \cdot S_{sw} \cdot \frac{\sqrt{2}}{\sqrt{3}} V_{LL} \begin{bmatrix} \sin\left(\omega_s t + \frac{\pi}{12}\right) \cdot S_d\left(\omega_s + \frac{\pi}{12}\right) + \\ \sin\left(\omega_s t + \frac{\pi}{12} - \frac{2\pi}{3}\right) \cdot S_d\left(\omega_s + \frac{\pi}{12} - \frac{2\pi}{3}\right) + \\ \sin\left(\omega_s t + \frac{\pi}{12} + \frac{2\pi}{3}\right) \cdot S_d\left(\omega_s + \frac{\pi}{12} + \frac{2\pi}{3}\right) \end{bmatrix} \tag{2.25}$$

$$V_{rec2}(\omega_s t) = \frac{3\sqrt{2} \cdot V_{LL}}{\pi}\left(1 - 0.057\sin(6\omega_s t) + 0.014\cos(12\omega_s t) + ...\right) \tag{2.26}$$

$$V_{12-pulse}(\omega_s t) = V_{rec1}(\omega_s t) + V_{rec2}(\omega_s t) = \frac{6}{\pi}\sqrt{2}\cdot V_{LL} + \frac{12\sqrt{2}}{143\pi}\cdot V_{LL}\cos(12\omega_s t) + \ldots \quad (2.27)$$

2.2.5 Input Current Analysis

By virtue of the net 30 ^{o} phase shift given by the zig-zag arrangement in the secondary side, the 5th, 7th, 17th, 19th, etc. harmonics are eliminated in the utility line currents. Mathematical analysis is provided for the line current in phase "a" through Fourier series and under the assumption of negligible ripple in the output DC current I_d. Ideally the input current, I_a, divides equally through the center tap windings W_{a1} and W_{a2} and can be expressed as:

$$I_a = I_{wa1} + I_{wa2} \quad (2.28)$$

The turns-ratio of the center-tap windings, N_{P1} and N_{P2}, are the same. Thus, by VA balance:

$$N_{P1}(I_{wa1} + I_{wa2}) = N_{P1}\cdot I_a = N_{S1}\cdot I_{as1} + N_{S2}\cdot I_{as2} + N_{S3}\cdot I_{as3} + N_{S4}\cdot I_{as4} \quad (2.29)$$

where N_{S1}, N_{S2}, N_{s3}, N_{s4} are the turns ratio of the secondary windings associated with phase "a" and are determined by (2.10) and (2.11). Similarly, I_{as1}, I_{as2}, I_{as3}, and I_{as4} are the currents flowing through the secondary windings associated with phase "a"; these currents can be expressed in terms of the currents flowing through the output six-pulse diode rectifiers as follows:

$$I_{as1} = -I_{\sec 1\_B} \quad (2.30)$$

$$I_{as2} = I_{\sec 1\_A} \quad (2.31)$$

$$I_{as3} = -I_{\sec 2\_C} \quad (2.32)$$

$$I_{as4} = I_{\sec 2\_A} \tag{2.33}$$

Similarly, the currents flowing through the output six-pulse diode rectifiers can be expressed as:

$$I_{\sec 1\_A} = I_{diode}\left(\omega_s t - \frac{\pi}{12}\right) * S_{sw} \tag{2.34}$$

$$I_{\sec 1\_B} = I_{diode}\left(\omega_s t - \frac{\pi}{12} - \frac{2\pi}{3}\right) * S_{sw} \tag{2.35}$$

$$I_{\sec 2\_A} = I_{diode}\left(\omega_s t + \frac{\pi}{12}\right) * S_{sw} \tag{2.36}$$

$$I_{\sec 2\_C} = I_{diode}\left(\omega_s t + \frac{\pi}{12} + \frac{2\pi}{3}\right) * S_{sw} \tag{2.37}$$

The -15 ^{o} and +15 ^{o} phase shift is evident from (2.34) and (2.36) respectively. I_{diode} corresponds to the quasi-square wave nature of the current in six-pulse rectifiers and is expressed as:

$$I_{diode}(\omega_s t) = \sum_{n=1,3,5,7}^{\infty}\left(\frac{4I_d}{n\pi}\cos\left(\frac{n\pi}{6}\right)\right)\cdot\sin(n\omega_s t) \tag{2.38}$$

where I_d is the output current and is assumed to be purely DC. Thus, the input current I_a becomes:

$$I_a = \left[\begin{array}{l}\sqrt{\frac{2}{3}}\left\{I_{diode}\left(\omega t - \frac{\pi}{12}\right) + I_{diode}\left(\omega t + \frac{\pi}{12}\right)\right\} - \\ \frac{-1+\sqrt{3}}{\sqrt{6}}\left\{I_{diode}\left(\omega t - \frac{\pi}{12} - \frac{2\pi}{3}\right) + I_{diode}\left(\omega t + \frac{\pi}{12} + \frac{2\pi}{3}\right)\right\}\end{array}\right]\cdot S_{sw}^{\ 2} \tag{2.39}$$

The switching function, S_{sw}, is a square wave with duty cycle 0.5. Thus, squaring this function yields a constant one. After simplification, (2.39) becomes (2.40):

$$I_a = \frac{4\sqrt{3}\cdot I_d}{\pi}\left[\sin(\omega_s t) - \frac{1}{11}\sin(11\cdot\omega_s t) - \frac{1}{13}\sin(13\cdot\omega_s t) + \frac{1}{23}\sin(23\cdot\omega_s t) + \frac{1}{25}\sin(25\cdot\omega_s t) + \ldots\right]$$

From (2.40) it is observed that harmonics 5^{th}, 7^{th}, 17^{th}, and 19^{th} are eliminated as in conventional 12-pulse operation. This analysis demonstrates that the proposed front-end rectifier system with MF isolation can be a retrofit replacement of bulky line frequency transformers in conventional 12-pulse systems. The input current performance is maintained while improving power density with a reduced active switch count and simple modulation scheme. The theoretical THD value of the input current (16%) is the same as in the conventional 12-pulse rectifier. To improve the current performance, an input passive filter must be included as shown in Figure 2-1. Since the line input current in the proposed system has identical harmonic spectrum as the line current in the conventional 12-pulse rectifier, the requirements of the passive filter in terms of size remain the same.

2.2.5.1 Effect of Output Current Ripple in Utility Line Input Current

The assumption of having a purely dc output current I_d requires a large output inductor. In practice, the output current I_d has a DC component and an AC current ripple riding on it. Thus, the effect of this AC current ripple on the utility line input current is studied. The analysis is done for 50% duty cycle. The equations (2.28)-(2.29) remain

valid. The main difference in this analysis is that now the output DC current I_d is now expressed as in (2.41), where I_{dc} is the output DC component, I_x is the magnitude of the AC ripple (usually 2-5%) and k is an integer which determines the frequency of the ac ripple as a multiple of the line frequency ω_s. For a 12-pulse rectifier output, $k = 12$.

$$I_d = I_{dc} + I_x \sin(k\omega_s t) \tag{2.41}$$

The AC ripple on the inductor current is also present in the current flowing through the output 12-pulse diode rectifier. Therefore, equation (2.38) is rewritten as in (2.42). Equation (2.42) and (2.30)-(2.37) are then used in (2.29) to find an expression for the utility input current I_a. After simplification, I_a becomes (2.43).

$$I_{diode}(\omega_s t) = \sum_{n=1,3,5,7}^{\infty} \left(\frac{4(I_{dc} + I_x \sin(k\omega_s t))}{n\pi} \cos\left(\frac{n\pi}{6}\right) \right) \cdot \sin(n\omega_s t) \tag{2.42}$$

$$I_a = \frac{4\sqrt{3} \cdot (I_{dc} + I_x \sin(k\omega_s t))}{\pi} \left[\begin{array}{l} \sin(\omega_s t) - \frac{1}{11}\sin(11 \cdot \omega_s t) - \frac{1}{13}\sin(13 \cdot \omega_s t) \\ + \frac{1}{23}\sin(23 \cdot \omega_s t) + \frac{1}{25}\sin(25 \cdot \omega_s t) + \ldots \end{array} \right] \tag{2.43}$$

From (2.43), it can be observed that the ripple component is also present in the utility input current. This implies that the AC ripple affects the THD of the input current. For the 12-pulse rectifier case, the AC ripple increases the magnitude of the dominant harmonics (i.e. 11^{th}, 13^{th}, etc.) in the utility current but does not introduce lower order harmonics (i.e. 3^{rd}, 5^{th}, 7^{th}).

2.2.6 Passive Components

As stated in sub-section 2.2.4, the input filter requirements for the proposed topology are the same compared to the conventional line frequency 12-pulse rectifier.

The input filter must be designed to attenuate the 11^{th} and 13^{th} current harmonics. Therefore, the input filter must have a cutoff frequency of 500 Hz to accommodate a line frequency of 50/60 Hz.

The output filter design of the proposed topology is dictated by the load requirements. The output voltage of the 12-pulse diode rectifier in the proposed scheme is given by (2.27). This voltage has a DC component an AC voltage component. The AC voltage component appears across the output inductor L_{out} and creates an AC current component as calculated by (2.44). Since a DC current is desired at the output, the AC current component must flow through C_{out} creating a voltage ripple described by (2.45). A voltage ripple factor RF_V (typically 1-5%) can be defined as in (2.46). From these equations and from the DC component, the value for C_{out} is found and calculated by (2.47). Upon analyzing the current through the output inductor L_{out}, the minimum required inductance required for continuous conduction is given by (2.48). Typically, an output inductor value of 0.05 per unit gives a good performance in terms of input current THD.

$$I_{Lout,12} = \frac{0.0378 V_{LL}}{12\omega_s L_{out}} \tag{2.44}$$

$$V_{out,12} = \frac{I_{Lout,12}}{12\omega_s C_{out}} \tag{2.45}$$

$$RF_v = \frac{V_{out,12}}{V_{out}} = \frac{I_{Lout,12}}{12\omega_s C_{out} V_{out}} \tag{2.46}$$

$$C_{out} = \frac{9.72\times10^{-5}}{\omega_s^2 L_{out} RF_v} \tag{2.47}$$

$$L_{out,\min} = \frac{0.00324 V_{LL}}{\omega_s I_{d,avg}} \tag{2.48}$$

2.2.7 Modulation and Control Scheme

A major advantage of the proposed system is that no closed loop control is required because the topology intends to replicate the performance of a conventional line frequency transformer. Therefore, no sensing is required in the proposed scheme. Thus the topology would operate at fixed 50% duty cycle operation. Operation at 50% duty cycle provides the maximum MF AC link rms voltage.

If output voltage regulation is desired, the proposed system can operate with simple variable duty cycle operation. The duty cycle D can be varied theoretically from 0-50%. If the duty cycle is increased beyond 50%, short circuits occur across the transformer windings. The gating functions of S_1 and S_2 at variable duty cycle are shown in Figure 2-9(a), (b). It is evident that the gating functions are shifted by 180° with respect to each other. The resulting overall switching function is the subtraction of S_1 and S_2 and is shown in Figure 2-9(c). At duty cycles less than 50%, zero states are introduced in the MF AC link as depicted in Figure 2-9(e). These zero states would decrease the overall output DC voltage. Thus, by controlling the duty cycle the output voltage can be regulated.

Under variable duty cycle, the gating function S_1 is given by (2.49). The expression of the gating function S_2 is similar to (2.49) but is shifted by 180°. The overall system's switching function is given by (2.50). When the line-to-neutral input voltage described by (2.1) is multiplied to S_{sw}, the resulting voltage across winding W_{a1}

is given by (2.51). From (2.51), it can be noted that the rms voltage across the transformer windings depends on the duty cycle *D*.

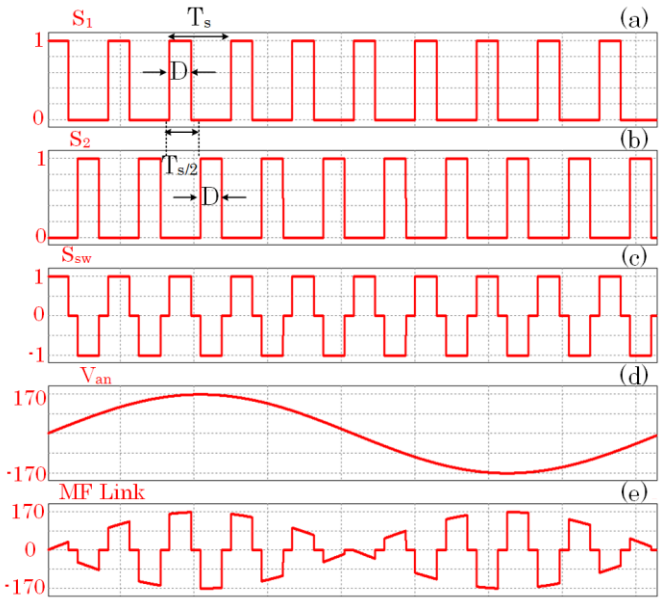

Figure 2-9: (a) Gating function for S_1 for variable duty cycle; (b) Gating function for S_2, it is 180° phase shifted compared to S_1; (c) S_{sw}, overall system switching function; (d) V_{an}, input line-to-neutral voltage; (e) MF AC Link is the multiplication of S_{sw} and V_{an}.

$$S_1 = D + \frac{2}{\pi}\sum_{n=1}^{\infty}\frac{1}{n}\sin(n\pi D)\cdot\sin(n\omega_{sqr}t) \tag{2.49}$$

$$S_{sw} = \frac{4}{\pi}\sum_{n=1,3,5,7,\ldots}^{\infty}\frac{1}{n}\sin(n\pi D)\cdot\sin(n\omega_{sqr}t) \tag{2.50}$$

$$V_{Wa1} = \sqrt{\frac{2}{3}}V_{LL}\sum_{n=1,3,5,7,..}^{\infty}\frac{2}{n\pi}\sin(n\pi D)\sin(\{n\omega_{sqr}\pm\omega_s\}\cdot t) \tag{2.51}$$

The output voltage is controlled using a simple proportional plus integral (PI) controller as shown in Figure 2-10. The output DC voltage must be sensed and compared to a reference voltage. The PI controller determines the duty cycle based on the error

signal. The switching controller then creates the appropriate gating signals for S_1 and S_2. A disadvantage of doing voltage regulation is that low order harmonics are introduced to the utility input current as *D* is varied. This occurs because the switching frequency (i.e. 600 Hz) is close to the 11th and 13th current harmonics. When *D* is not equal to 0.5, the term $S_{sw} \cdot S_{sw}$ does not equal unity. Instead, components at twice the switching frequency (i.e. 1200 Hz) are created and interact with the 11th and 13th current harmonics producing lower order current harmonics such as the 7th. Thus, this topology is not well suited for applications requiring voltage regulation. This problem, however, can be solved by switching at HF.

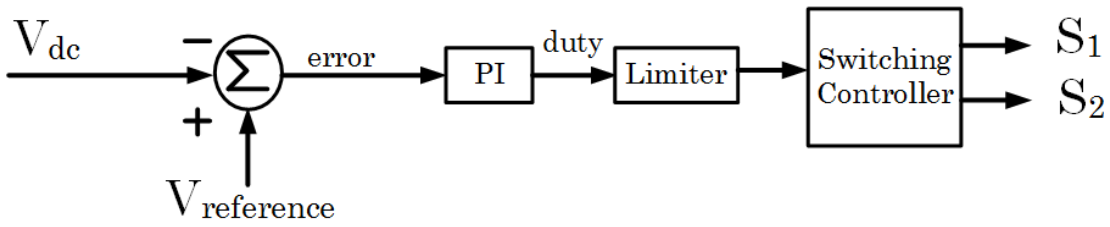

Figure 2-10: Simple control strategy to regulate the output DC voltage.

2.2.8 Design Example

A 208 V_{LL}, 10 kW design example is considered to demonstrate the operation of the proposed front-end rectifier system in Figure 2-1. The output DC voltage is calculated is the DC component of equation (2.27) and thus becomes:

$$V_{dc} = \frac{6}{\pi}\sqrt{2} \cdot V_{LL} = 561\,V. \tag{2.52}$$

For a 10 kW load, the output current I_d becomes:

$$I_d = \frac{P_o}{\mathrm{V}_{dc}} = 17.8\,\mathrm{A}. \tag{2.53}$$

The volt-ampere (VA) rating of the multi-winding MF transformer can be calculated using the rms voltage and rms current of each winding under the assumption that the output current I_d has negligible ripple. Ideally, the rms value of the currents flowing through the secondary windings is:

$$I_{as} = \sqrt{\frac{2}{3}} \cdot I_d = 14.5\,\mathrm{A}. \tag{2.54}$$

Similarly, the rms value of the current following through the primary windings is:

$$I_{wa1} = 1.11 \cdot I_d = 19.76\,\mathrm{A}. \tag{2.55}$$

The rms value of the voltage across the primary windings is:

$$V_{wa1} = \frac{\mathrm{V}_{LL}}{\sqrt{3}} = 0.577 \cdot \mathrm{V}_{LL} = 0.214 \cdot \mathrm{V}_{dc} = 120\,\mathrm{V}. \tag{2.56}$$

The rms voltage across the windings with turns-ratio N_{s1} is:

$$V_{s1} = \sqrt{\frac{2}{3}} \cdot \frac{\mathrm{V}_{LL}}{\sqrt{3}} = 0.47 \cdot \mathrm{V}_{LL} = 0.175 \cdot \mathrm{V}_{dc} = 98.2\,\mathrm{V}. \tag{2.57}$$

Similarly, the rms voltage across the windings with turns-ratio N_{s2} is:

$$V_{s2} = \frac{\sqrt{3}-1}{\sqrt{6}} \cdot \frac{\mathrm{V}_{LL}}{\sqrt{3}} = 0.17 \cdot \mathrm{V}_{LL} = 0.064 \cdot \mathrm{V}_{dc} = 35.9\,\mathrm{V}. \tag{2.58}$$

Then the sum total of the volt-ampere product of the MF transformer is:

$$VA_{tot} = 6 \cdot I_{wa1} \cdot \mathrm{V}_{wa1} + 6 \cdot I_{as}(V_{s1} + V_{s2}) = 6.96\mathrm{V}_{LL} I_d = 2.58\mathrm{V}_{dc} I_d = 28.5\,\mathrm{kVA}. \tag{2.59}$$

Thus, the required equivalent VA rating of the MF transformer is:

$$VA_{eq} = \frac{1}{2} VA_{tot} = 1.29 \mathrm{V}_{dc} I_d = 1.29 P_o = 12.9 \,\mathrm{kVA}. \tag{2.60}$$

Although the VA rating of the proposed transformer configuration is slightly higher than the conventional 12-pulse isolation transformer ($1.03P_o$), the proposed transformer configuration does not carry the line frequency component. Instead, the transformer operates at MF enabling a size reduction.

The ratings of the semiconductor devices employed in the proposed scheme are listed in Table 2-1. The voltage ratings are normalized with respect to the line-to-line voltage V_{LL}, while the current ratings are normalized with respect to the output current I_d. The peak voltage of the active semiconductor devices S_1/S_2 is 2.83 p.u. Thus, switching devices rated for 600V are required. This rating places a limitation in terms of input voltage. For example, if the utility grid is $690V_{l\text{-}l}$, the active switching devices must have a rating of approximately 2kV. Such a device could be expensive. Thus, it is recommended to operate this topology with input voltages up to $480V_{l\text{-}l}$. To calculate the peak current rating of the high voltage switches a power factor of 0.985 is used. This power factor value is expected because the input current has 12-pulse performance.

Table 2-1: Component rating for semiconductor devices

Component	Parameter	Expression	P.U. Value	Design Value (10 kW)
Active switch (S_1/S_2)	peak voltage	$2\sqrt{2}\mathrm{V_{LL}}$	2.83	588 V
	peak current	$\frac{4\sqrt{3}}{\pi \cdot \mathrm{pf}} I_d$	2.24	40 A
	rms current	$1.5 I_d$	1.5	26.7 A
Diode clamp circuit	peak voltage	$2\sqrt{2}\mathrm{V_{LL}}$	2.83	588 V
	peak current	$\frac{4\sqrt{3}}{\pi \cdot \mathrm{pf}} I_d$	2.24	40 A
	rms current	$0.8 I_d$	0.8	14 A
12-Pulse Diode Rectifier	peak voltage	$\sqrt{2}\mathrm{V_{LL}}$	1.414	294 V
	peak current	I_d	1	17.8 A
	rms current	$I_d \sqrt{\frac{2}{\pi}\left(\frac{\pi}{12}+\frac{1}{4}\right)}$	0.57	10.1 A

Figure 2-1 depicts the diode clamp circuit with a clamping capacitor C_{cl} and a lossy resistor R_{cl}. This clamping circuit is necessary to provide a path for the energy stored in the leakage inductance of the transformer. The capacitor clamps to the peak voltage of the active semiconductor device. In this design example, it is desired to maintain the associated power losses of the resistor to $0.003P_o$. The value of C_{cl} is then calculated as follows:

$$C_{cl} = \frac{2 \cdot 0.003 P_o}{V_{cl}{}^2 f_{sqr}} = 0.3\mu\mathrm{F} \tag{2.61}$$

Since R_{cl} is in parallel to the clamping capacitor, R_{cl} is calculated as:

$$R_{cl} = \frac{V_{cl}^{\ 2}}{0.003 P_o} = 11.5\, k\Omega \tag{2.62}$$

2.3 Simulation Results

The proposed topology in Figure 2-1 was simulated to verify its functionality. The electrical performance of the topology was simulated in PSIM while the magnetic behavior of the MF zig-zag transformer was simulated using Ansys Maxwell Finite Element Analysis (FEA) software.

2.3.1 Simulations in PSIM

The parameters in Table 2-2 were used for simulation in PSIM. The simulations were performed without an input LC filter to compare with a conventional 12-pulse rectifier. Adding a passive filter with L_f = 1.7 mH (0.13 p.u) and C_f = 140 μF results in a line current with THD <5 % and a system power factor >0.98. The three-phase multi-winding MF transformer used in PSIM is close to an ideal transformer model.

Table 2-2: Specifications and operating conditions for the system in Figure 2-1.

Grid voltage (line-to-line rms)	208 V
Grid frequency	50 Hz
Rectifier output voltage	560 V_{dc}
Rated power	10 kW
Switching frequency (f_{sqr})	600 Hz
Clamping capacitor (C_{cl})	10 μF
Clamping resistor (R_{cl})	5 kΩ
Output Inductor (L_{out})	2 mH
Output Capacitor (C_{out})	200 μF

As stated in subsection 2.2.1, a three-phase MF AC link is created across the transformer windings by switching S_1 and S_2 complementarily. The three-phase MF AC link can be observed in Figure 2-11(a); it is evident that the voltages across the windings (W_{a1}, W_{b1}, W_{c1}) are displaced by 120° from each other. The voltages across the windings (W_{a2}, W_{b1}, W_{c2}) are also a set of three-phase voltages with 120° phase shift; but they are opposite in polarity with respect to the voltages across the first set of windings. Figure 2-11(b) shows the line-to-line voltages (V_{abs}, V_{abt}) which feed the 12-pulse diode rectifier. The voltages are 30° phase shifted, with respect to each other, as in conventional 12-pulse operation. The input currents of the diode rectifiers I_{sec1_A} and I_{sec2_A} in Figure 2-11(c) also demonstrate the 30° phase shift.

The fast Fourier transform (FFT) of the voltage across winding W_{a1} confirms MF operation as shown in Figure 2-12. The fundamental voltage frequency occurs at 600±50 Hz; this enables the use of MF transformers thereby reducing the weight/size of the system [47]. The output DC voltage and the individual rectified voltages V_{rec1} and V_{rec2} are depicted in Figure 2-13. The 30° phase shift is also noticeable in the individual rectified voltages ensuring 12-pulse operation. The current through the primary winding W_{a1} is shown in Figure 2-14(a) and the voltage across the active device S_1 is given in Figure 2-14(b). When S_1 is ON, there is current flowing through the primary winding and the voltage drop across the device is ideally zero. When S_1 is OFF, the current through the primary winding is zero as expected and the peak voltage across the device is 588V as calculated in the design example.

Fig. 2-15(a) shows the input current for phase "a"; 12-pulse operation can be observed in the input current. The simulated THD is 16%. The FFT of the line current is shown in Figure 2-15(b); the dominant harmonics are 11^{th} and 13^{th} as in conventional 12-pulse configuration. This is in agreement with the input current analysis and demonstrates that the proposed topology can be a retrofit replacement of the bulky line frequency multi-winding transformer in conventional 12-pulse systems.

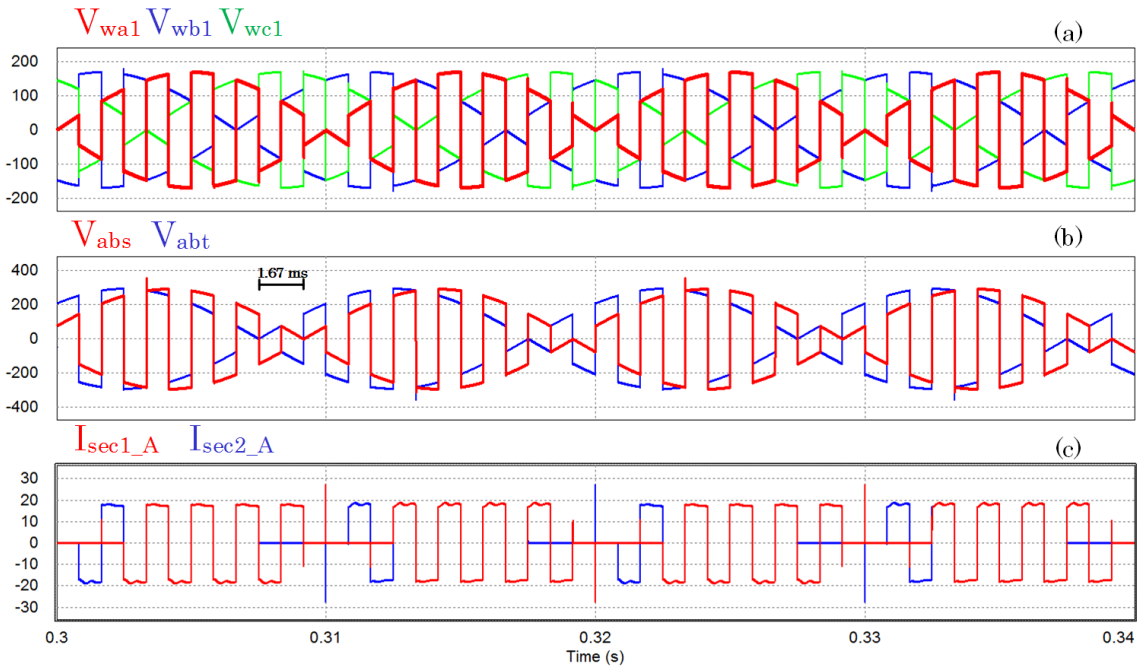

Figure 2-11: (a) Transformer winding voltage due to 50% duty cycle operation of S_1 and S_2 at 600Hz. Note the voltages across windings W_{a1}, W_{b1}, W_{c1} are displaced by 120°; (b) Line-to-line voltages V_{abs} and V_{abt} are 30° phase shifted. (c) Rectifier input currents on the secondary side of the transformer.

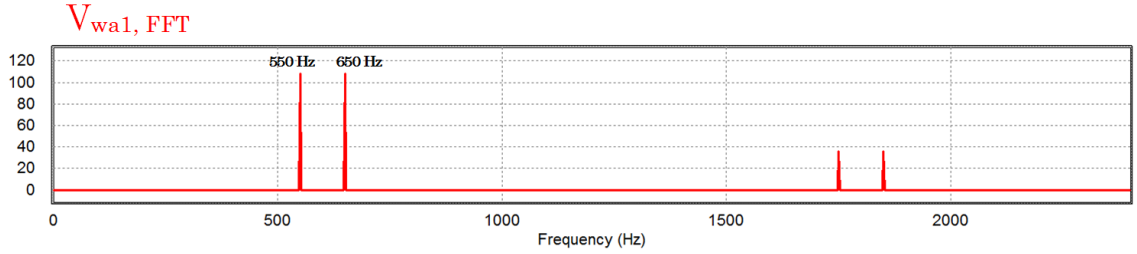

Figure 2-12: FFT of the voltage across transformer winding W_{a1}. Fundamental frequency of operation is 600±50 Hz enabling the use of MF transformers. Other components appear at $3f_{sqr} \pm 50$ Hz.

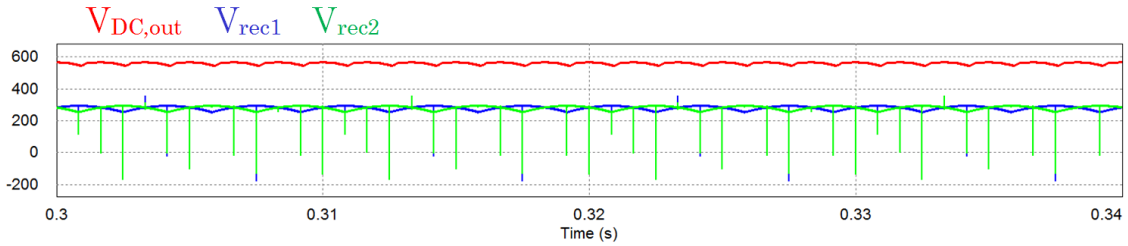

Figure 2-13: DC output voltage at 560V. Individual rectified voltages have 30° phase shift as in conventional 12-pulse operation.

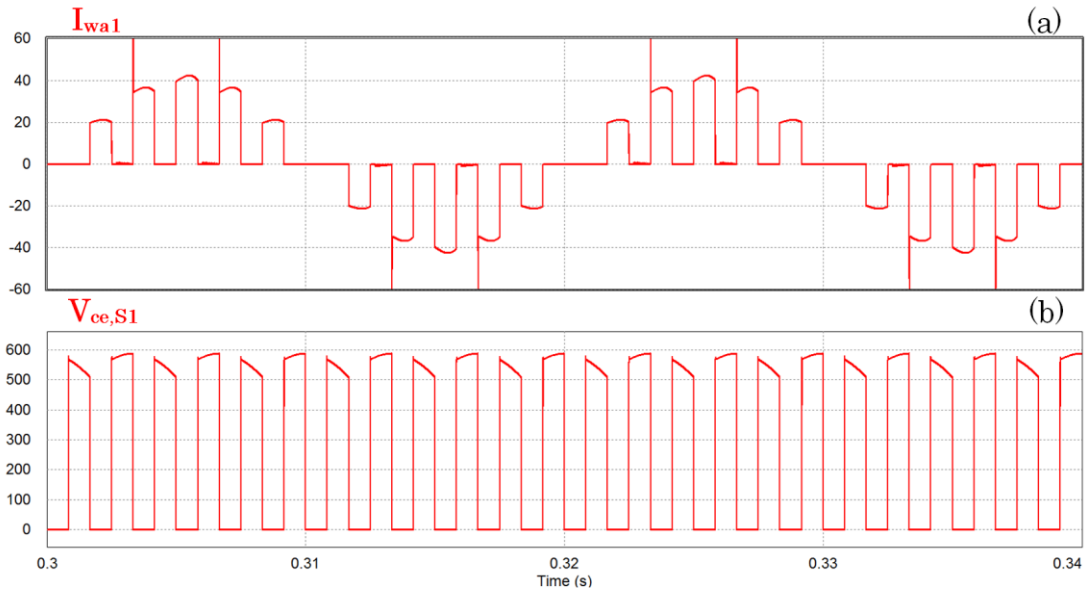

Figure 2-14: (a) I_{wa1} is the current through one of the center-tap primary windings. Simulated rms current is 20A as expected. (b) Voltage across the active device S_1. When the device is in the OFF state the peak voltage is 588V.

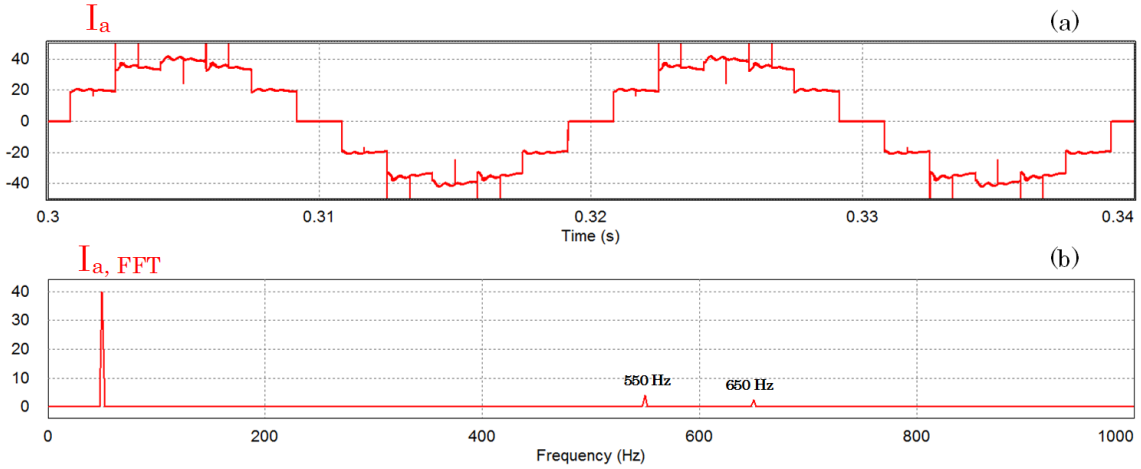

Figure 2-15: (a) Input line current for phase "a"; 12-pulse operation is evident. (b) FFT of the input current verifies 12-pulse operation. Note: the dominant harmonics are 11th and 13th (550 Hz and 650 Hz). Simulated THD of the current is 16%.

2.3.2 Simulations in Ansys Maxwell FEA Software

In addition to the simulations in PSIM, the magnetic behavior of the proposed MF transformer was simulated using Ansys Maxwell finite element analysis (FEA) software. The primary windings of the modelled transformer were excited using the voltage expression derived in (2.3). The material of the core was selected to be M19 silicon steel which has a saturation flux density of 1.4 T at MF. A plot of the magnetic field density for a 2D simulation of the proposed transformer is given in Figure 2-16. From the simulation, it is shown that the flux density is higher in the interior three-limbs of the transformer as expected. The core of the transformer is shown to operate at 0.8 T which is below the saturation region. In Figure 2-17, the corresponding magnetic flux lines plot is presented. The flux lines also concentrate along the interior three-limbs of the transformer. Using the M19 core loss data at 600 Hz, the FEA software is used to

simulate the core losses of the MF transformer. The simulated core losses shown in Figure 2-18 are compared with the actual losses to evaluate the efficiency of the proposed topology as discussed in the next section.

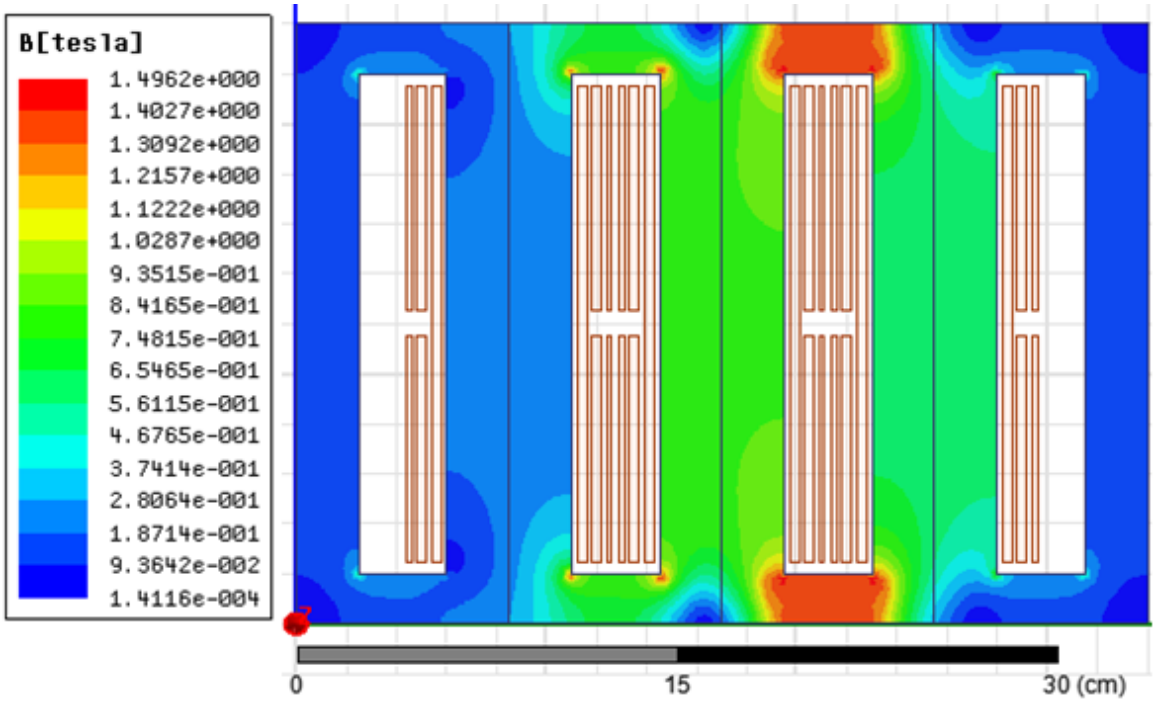

Figure 2-16: Magnetic field density plot of the proposed 5-limb, three-phase transformer when excited with a MF AC link. The 2D dimensions of the transformer are (34 cm X 24 cm). The model has a depth of 5cm.

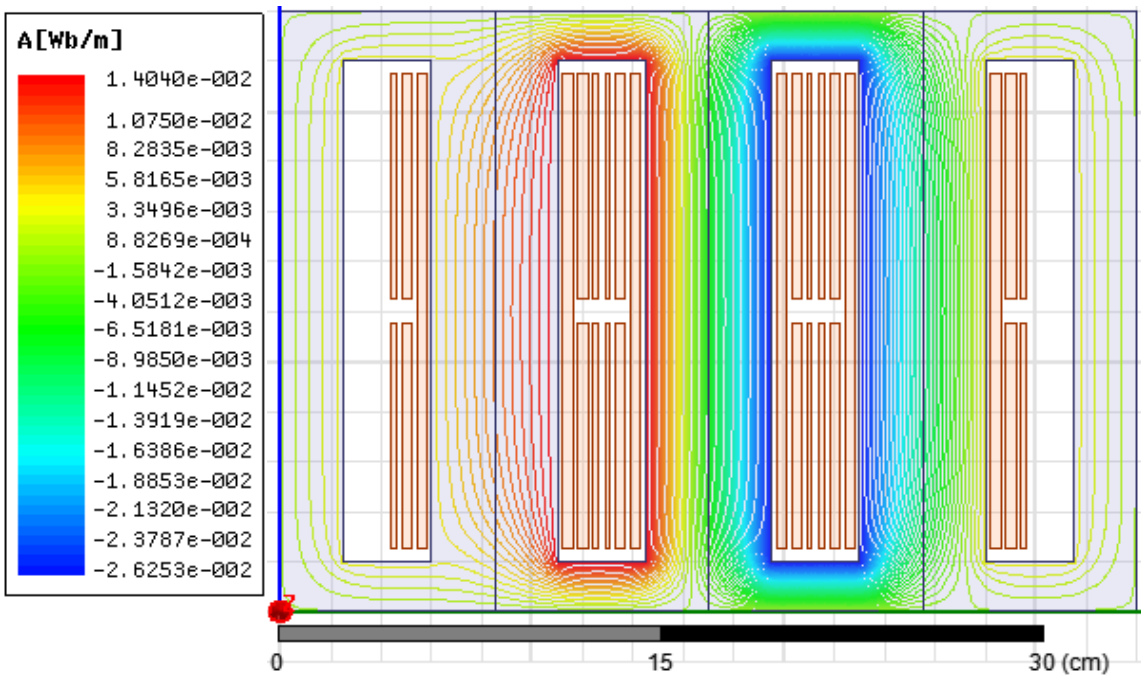

Figure 2-17: Magnetic flux lines of the proposed 5-limb, three-phase transformer when excited with a MF AC link. The flux lines concentrate in the interior three limbs of the transformer.

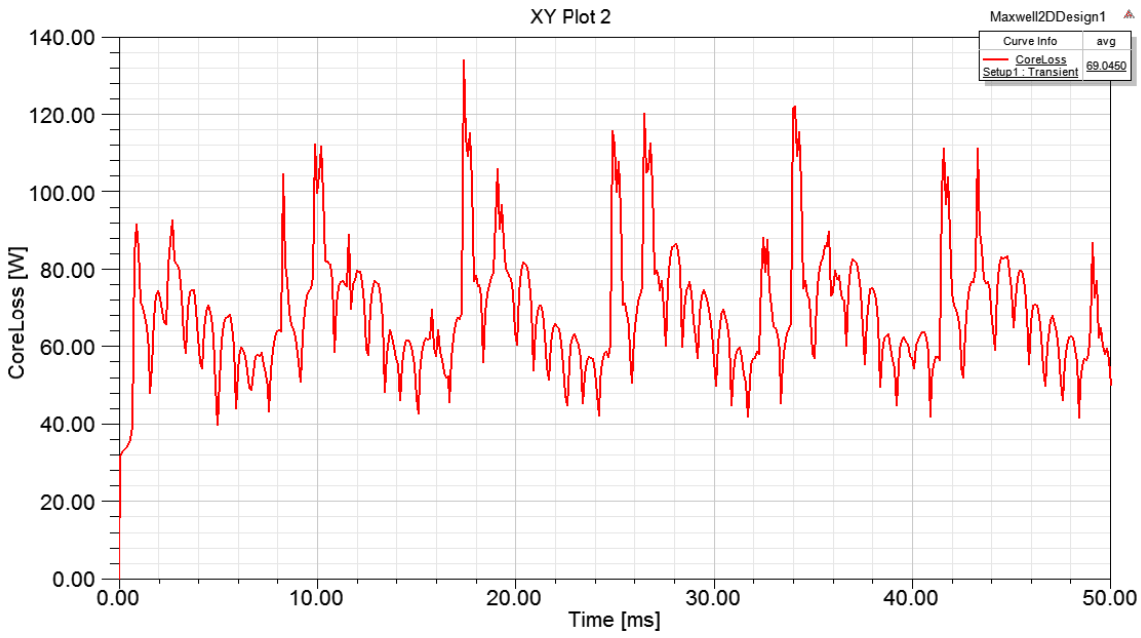

Figure 2-18: Simulated core losses using FEA software. The average core loss is 69 W.

2.4 Efficiency Analysis of Multi-Pulse AC-DC Conversion Stage

The efficiency of the proposed reduced active switch multi-pulse rectifier can be calculated by analyzing switching and conduction losses, and transformer core and winding losses. The switching losses and conduction losses of the two high voltage active switches (S_1/S_2) can be approximated by looking at the switching/conducting characteristics of commercially available high voltage IGBTs. The switching loss of the IGBTs and diodes is calculated using the turn-on and turn-off energy pulses of the device as in (2.63).

$$P_{sw\_loss} = (E_{on} + E_{off}) \cdot f_{sw} \tag{2.63}$$

The IGBT in [53] is selected for this computation. The conduction losses for this device can be computed by analyzing conduction forward voltage drop and by observing the average current through the device in simulation. The conduction losses of the two three-phase diode rectifiers with clamp circuit are calculated using the characteristics of the device in [54] and the average current through the diodes. The switching losses for these diodes are essentially zero as stated in [54]. The losses for the 12-pulse diode rectifier in the secondary side are obtained in similar manner but using the characteristics of the device in [55]. Table 2-3 shows the commercial semiconductor devices used for the power loss analysis.

Table 2-3: Semiconductor devices used for power loss analysis

System Component	Part Number	Manufacturer
S1/S2	IRG4PH50SPbF	Infineon
Diode clamp circuit	C4D40120D	Cree
12-pulse diode rectifier	C3D20060D	Cree

From calculation, it is determined that the switching and conduction losses of the active switches (S_1/S_2) account for 18% of the total losses. Similarly, the diode clamp circuit accounts for 42% of the system's losses while the 12-pulse diode rectifier on the secondary side accounts for 15% of the losses.

An estimate of the transformer core losses was obtained using FEA analysis. The FEA simulation yields an average core loss of 69 W when the transformer primary windings are excited with a three-phase MF AC link. The FEA simulation results were experimentally verified through an open circuit test of the MF transformer. Through experiments, a core loss of 80 W was obtained. The difference between the simulated and tested core losses occurs because the FEA model cannot account for all physical effects in a core with laminations [56]. The total transformer losses account for 25% of the system's losses. Using finer grades of steel or amorphous materials would decrease the transformer losses but the increase in cost must be considered [46]. The breakdown of the system losses is shown in Figure 2-19. Overall, the efficiency of the proposed system is calculated to be 96.5%.

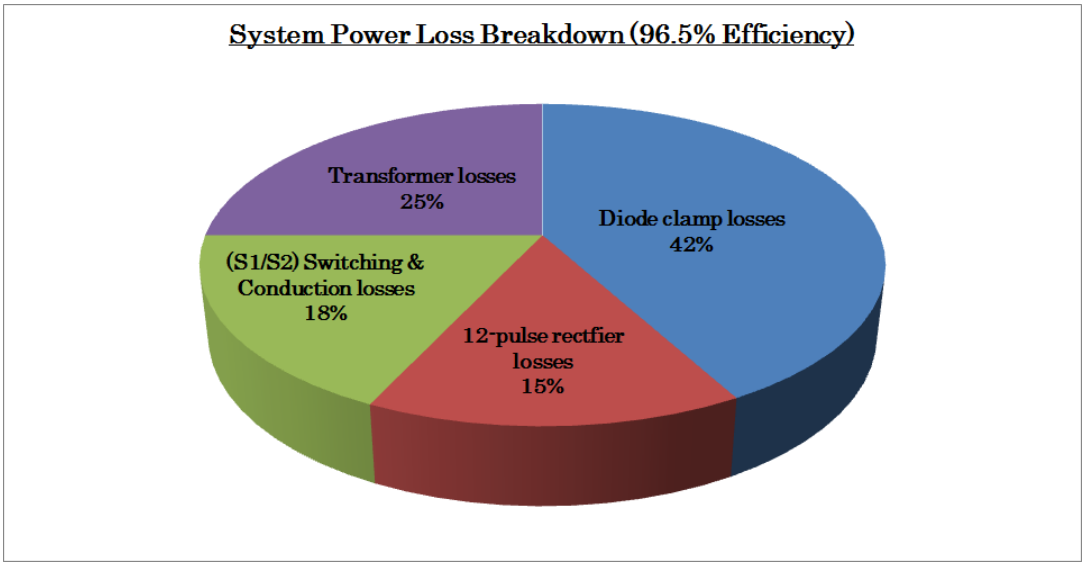

Figure 2-19: System power loss breakdown for a 10 kW design example. The efficiency of the system is 96.5%.

2.5 Comparative Evaluation of the Proposed Multi-pulse Rectifier

In this section, the proposed multi-pulse front-end rectifier is compared with other existing schemes. The multi-pulse schemes considered for evaluation include the conventional 12-pulse rectifier, the half power 12-pulse rectifier, and two active techniques. The results of the comparison are shown in Table 2-4. The proposed scheme uses only two active switches reducing the gate drive circuitry allowing for a compact system but the active switches must be rated for $2.83V_{LL}$. Due to the low number of active switches and simple modulation scheme, the proposed scheme has a low realization complexity compared to the three-phase modular PFC scheme. Similar to the active 12-pulse scheme, the sensing effort and modulation complexity of the proposed scheme is low which is attractive in industrial settings.

Among the five compared topologies, only in the proposed topology the phase-shifting transformer ($1.29P_o$) operates at MF with galvanic isolation. Operating at MF enables the power density (W/L) of the proposed phase-shifting transformer to be the highest among the topologies employing phase-shifting transformers. Power density is defined in (1.3). For power density calculation, the power rating and physical size of the transformers/matching inductors reported in [36] were used. The proposed zig-zag MF isolation transformer rated at 7 kW has a 1700 W/L power density, which is nearly 3.4 times larger than the power density of the conventional line frequency 12-pulse transformer. Compared to the half power 12-pulse scheme described in [26], the power density of the proposed transformer configuration is nearly seven times larger. Similarly, compared to the active 12-pulse scheme in [36] the power density of the proposed transformer configuration is about 4.8 times larger. This advantage in power density makes the proposed topology very attractive in applications where size is a constraint and isolation is required.

In addition, the volume of the proposed MF transformer is compared to the volume of a line frequency transformer through Ansys Maxwell FEA modeling. Two three-phase transformers, one operating at line frequency and the other at MF frequency, were modeled for the same output load (7 kW) input voltage (208 $V_{l\text{-}l}$), and efficiency (~98%) requirements. Also, the same M19 silicon steel core material was considered for comparison. Considering the B-H curves of the M19 material at different operating frequencies, a peak flux density of 1.6 T with 105 primary turns was used for the line frequency transformer design while a peak flux density of 0.8T with 68 primary turns

was used for the MF transformer design. A comparison of the size between the three-phase line-frequency transformer and the three-phase MF transformer is shown in Figure 2-20. For the same output load, input voltage, and transformer efficiency requirements the line frequency transformer has a volume of 13.8 L (51 cm x 36 cm x 7.5 cm) while the MF transformer has a volume of 4 L (34 cm x 24 cm x 5 cm). Thus, the volume of the MF three-phase transformer is 30% of the volume of the line frequency transformer.

Table 2-4: Comparative evaluation of proposed rectifier with other schemes

Topologies		Conventional 12-Pulse	Half Power 12-Pulse	Active 12-Pulse [36]	Three single-phase PFC	Proposed
Configuration		ac-dc	ac-dc	ac-dc-dc	ac-dc-dc-dc	ac-ac-dc
No. of active switches	front-end	------	------	------	3	2
	dc-dc	------	------	4	12	------
	Total	------	------	4	15	2
Galvanic Isolation		Yes	No	No	Yes	Yes
Sensing effort & modulation complexity		None	Low	Low	High	Low
Phase-Shifting Transformer VA rating (operation frequency)		$1.03P_o$ (line frequency)	$0.5P_o$ (line frequency)	$0.38P_o$ (line frequency)	------	$1.29P_o$ (medium frequency)
Power Density of Phase-Shifting transformer (Output Watts/Liter)		507	252*	352*	------	1700

*The volume for these topologies was obtained using the physical size of the phase-shifting transformer and the size of the matching inductors reported in [36].

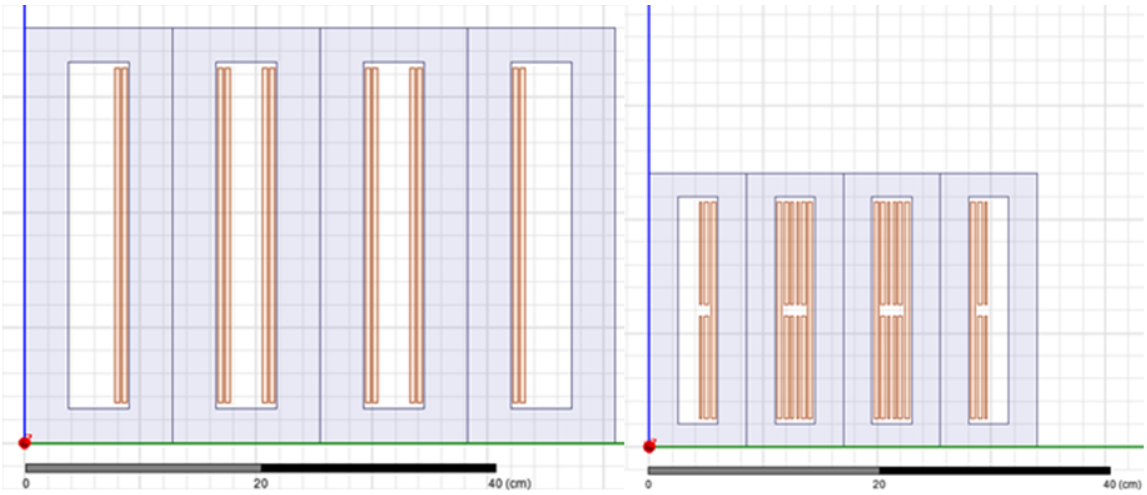

Figure 2-20: Size comparison of three-phase transformers. Line frequency transformer (left) has a volume of 13.8 L while the medium frequency transformer (right) has a volume of 4.1 L.

2.6 Experimental Results

In order to validate the proposed topology a scaled-down laboratory prototype rated at 3.15 kW is built and tested. The input three-phase line-to-line voltage is $208V_{rms}$ with fundamental frequency of 50 Hz. A small input passive filter with L_f=100 µH was used. The switching frequency of the active devices, namely S_1 and S_2, is set to 600 Hz. The clamp circuit is composed of a film capacitor C_{cl}=10 µF and R_{cl}=10 kΩ. The gate drive signals for the active devices are generated using a Texas Instruments microcontroller. Within the microcontroller, a dead time of 2µs is assigned to the gating signals of S_1 and S_2 to avoid overlap operation. The zig-zag MF transformer is designed to operate at the desired switching frequency and is built using silicon steel material. Figure 2-21 shows an image of the zig-zag transformer.

The experimental results are shown to be similar to simulation results. Figure 2-22 shows the three-phase MF AC link across windings W_{a1}, W_{b1}, and W_{c1}. It is evident that the set of 3 phase voltages are displaced by 120° (6.67 ms) from each other.

Operation at MF is confirmed from Figure 2-23. The FFT of the voltage V_{wa1} shows fundamental components at 550 Hz and 650 Hz enabling the transformer to operate at MF. From Figure 2-24, 12-pulse operation is observed; the secondary side voltages V_{abs} and V_{abt} show a net 30° phase shift (1.67 ms) with respect to each other. This figure also shows a smooth DC output voltage as in 12-pulse operation. Similarly, the 30° phase shift is evident from the currents feeding the 12-pulse diode rectifiers in the secondary side as shown in Figure 2-25. To further validate the operation of the proposed topology, the experimental waveform of the current through one of the primary windings, I_{wa1} and the collector-emitter voltage across active switch S_1 is given in Figure 2-26. It can be noticed that when the device is turned ON current flows through the primary winding W_{a1} and when the switch is OFF the current drops to zero as expected. From the amplitude of the collector-emitter voltage it can also be noted that the active switches S_1 and S_2 must be rated for at least twice the peak of the line-line input voltage.

The line input current I_a is shown in Figure 2-27 along with its FFT. The frequency spectrum shows that the 5^{th}, 7^{th}, 17^{th}, 19^{th} harmonics have been eliminated confirming 12-pulse operation. The measured THD of the current is 17% but can be improved with an input passive filter with L_f = 0.13 p.u. The measured 11^{th} and 13^{th} harmonic of the input current are about 10% and 7% respectively from the fundamental. From Figure 2-28, high displacement power factor is shown between the line-to-neutral voltage V_{an} and the line input current. Furthermore, Figure 2-28 shows that the effect of the switching frequency on the utility voltage is minimal.

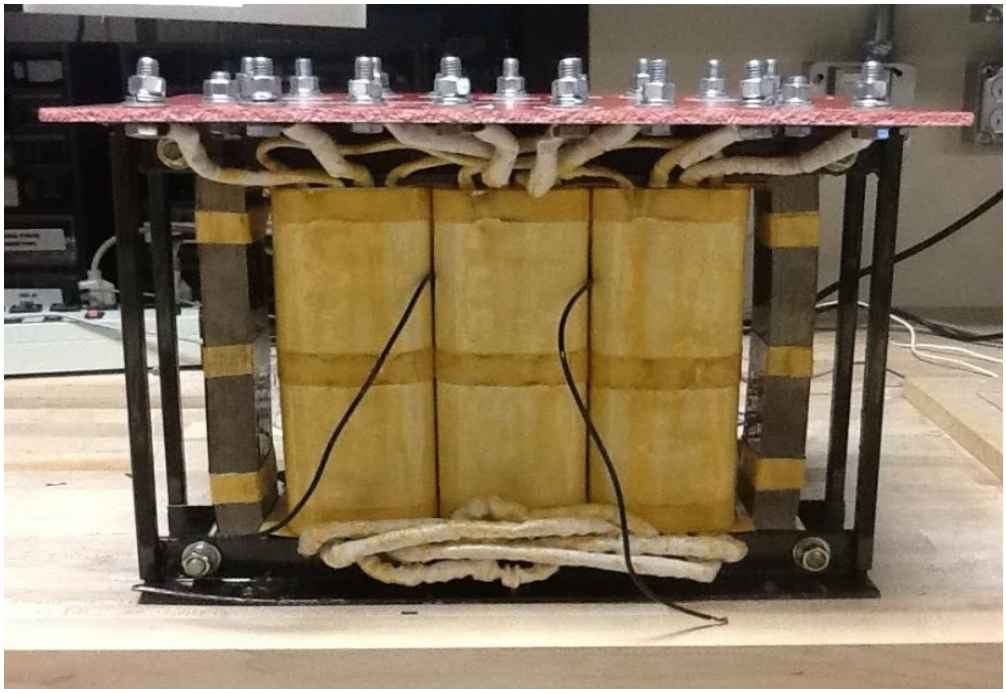

Figure 2-21: Silicon steel core MF three-phase transformer used for experiments. (Dimensions: 32 cm x 24 cm x 5 cm)

Figure 2-22: Experimental results. Ch.1: Voltage across winding W_{a1}; Ch.2: Voltage across winding W_{b1}; Ch.3: Voltage across winding W_{c1}. Note: voltages are displaced by 120°.

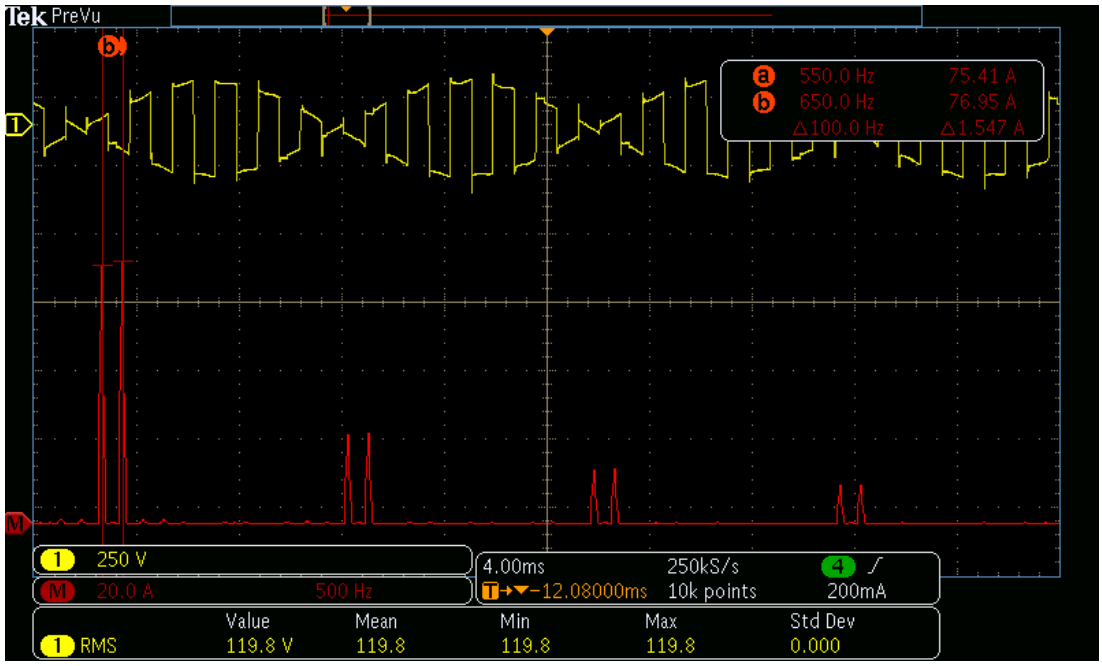

Figure 2-23: Experimental results. Ch. 1: Primary side voltage V_{wa1}; Ch. M: FFT of V_{wa1} shows fundamental components at 550 Hz and 650 Hz enabling MF operation.

Figure 2-24: Experimental results. Ch.1: Line-to-line voltage on the secondary side V_{abs}; Ch.2: Line-to-line voltage on the secondary side V_{abt}; Ch.3: DC output voltage. Note: V_{abs} and V_{abt} are displaced by 30° from each other to achieve 12-pulse rectification.

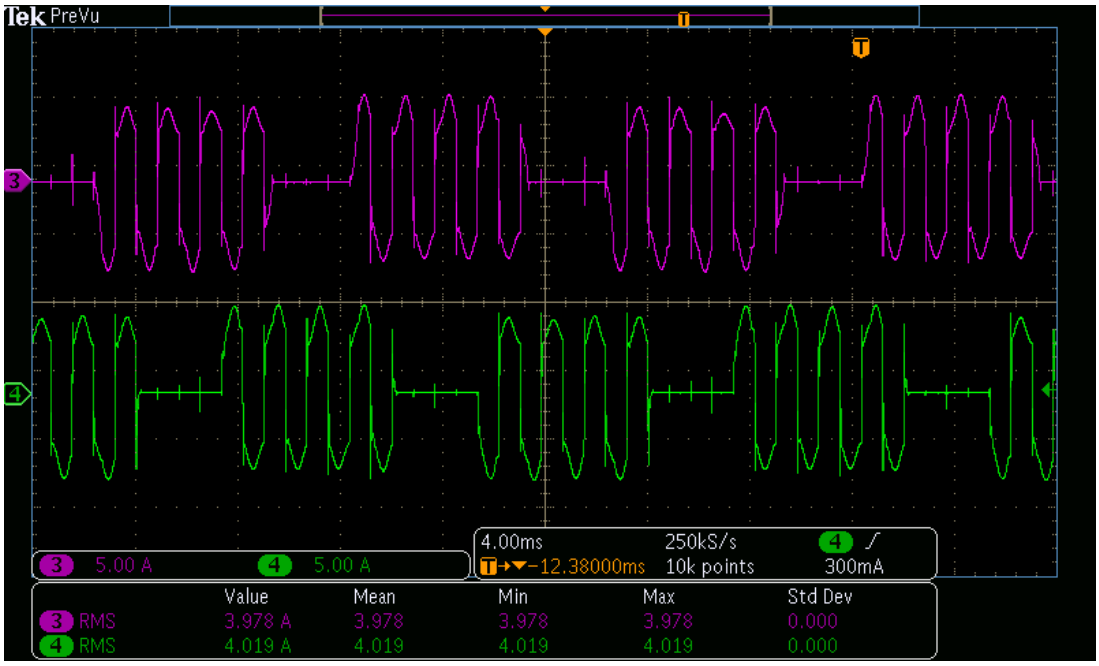

Figure 2-25: Experimental results. (Ch.3) Secondary side current I_{sec1_A}; (Ch.4) Secondary side current I_{sec2_A}. Note the 30° phase shift between the currents.

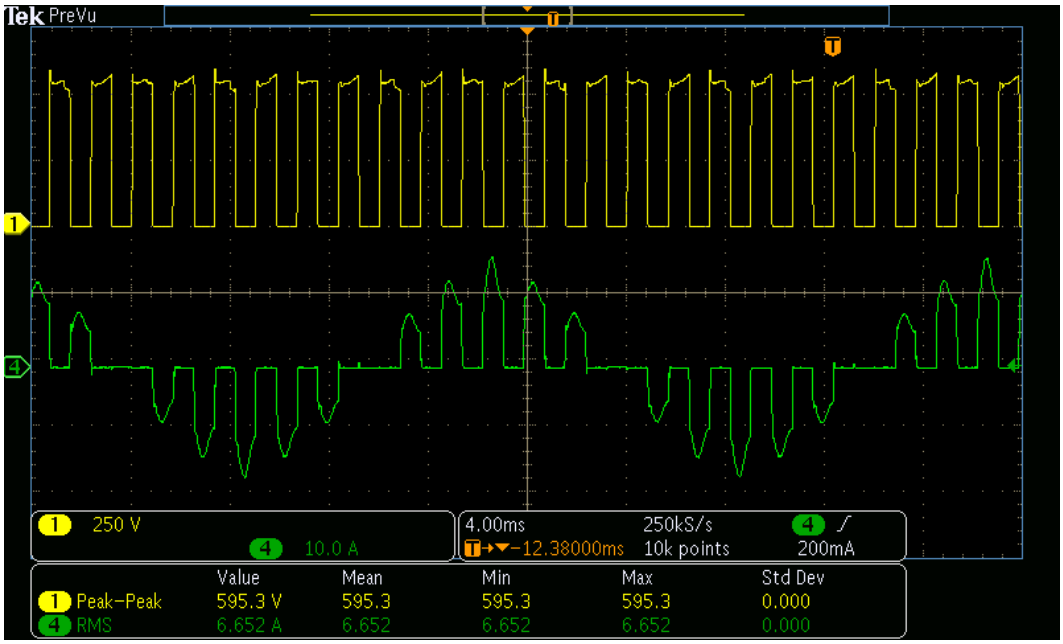

Figure 2-26: Experimental results. (Ch.1) Collector-emitter voltage across active switch S_1; (Ch.4) Current I_{wa1} through primary winding W_{a1}.

Figure 2-27: Experimental results. Ch.4: Line input current I_a; Ch. M: FFT of I_a shows dominant harmonics to be 11th (550 Hz) and 13th (650 Hz) as in 12-pulse operation. The 5th, 7th, 17th, and 19th harmonics are eliminated. The measured THD is 17%.

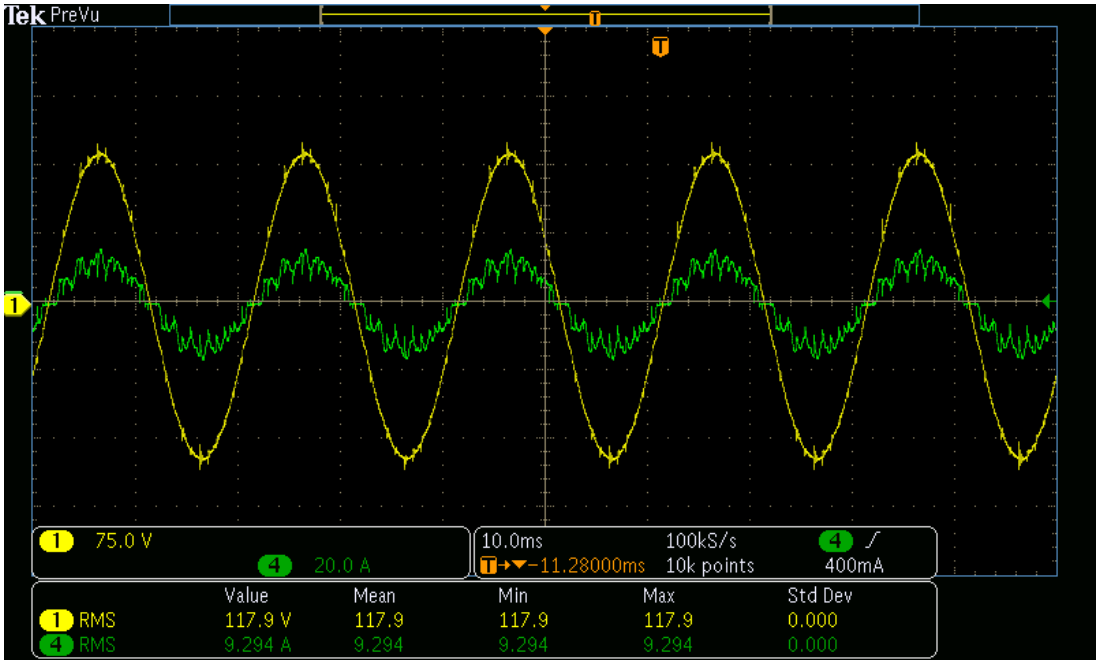

Figure 2-28: Experimental results. Ch.1: Utility line-to-neutral voltage V_{an}; Ch.4: Line input current I_a.

2.7 Conclusion

This section proposes a reduced switch multi-pulse rectifier with MF transformer isolation employing two active semiconductor devices. It has been shown that operating at MF of 600 Hz, the transformer size is 1/3 of the equivalent 60 Hz design. A 10 kW design example has been shown to achieve 96.5% efficiency. Simulation and experimental results on a laboratory prototype demonstrate the 12-pulse operation with high input current quality. Overall, the advantages of the system include high power density, reduced active switch count, and simple pulse width modulation scheme.

3. HIGH DENSITY THREE-PHASE AC-DC RECTIFIER WITH HIGH FREQUENCY TRANSFORMER ISOLATION

This section presents a simplified three-phase ac to dc rectifier system employing high frequency (20 kHz) transformer isolation for high power applications. In the proposed scheme, the three-phase utility grid (50/60 Hz) voltage is modulated via indirect AC-AC converters. The output of the AC-AC converters is connected to the primary windings of a three-phase multi-winding high frequency (HF) ferrite core transformer which provides galvanic isolation and desired output voltage range. The transformer's windings on the secondary side are connected in zig-zag fashion to realize a 12-pulse rectifier to achieve a high quality dc output voltage with simultaneous harmonic free input current at unity input power factor. The DC output voltage of the rectifier is adjustable via a simple duty cycle control. Major advantages of the proposed approach include: high power density; high input current quality; and simple modulation and control scheme to regulate the output DC voltage. The operation of the topology is explained through detailed analysis and simulation. Different embodiments of the topology are elucidated. Results from a 1 kW downscale laboratory prototype are also presented.

3.1 Introduction

The previous section introduced a push-pull based three-phase AC-DC rectifier with medium frequency transformer isolation. By switching the active semiconductor devices of the push-pull rectifier at 600 Hz, the transformer volume is reduced by 70%

compared to its line frequency transformer counterpart. Despite the great benefits provided by this topology, one of the limitations of switching at 600 Hz is that low order harmonics are introduced in the input current when the output voltage is regulated. Therefore, the push-pull based rectifier is suitable for applications where DC output voltage regulation is not needed such as the front-ends of adjustable speed drive systems. Another concern is that the two active semiconductor devices in the push-pull based rectifier must be rated for twice the line-to-line voltage and thus experience high voltage stress. Moreover, the transformer's power density can be improved even further by switching at higher frequencies.

To address the drawbacks of the push-pull based three-phase rectifier and the drawbacks of conventional three-phase rectifier, this section introduces a full-bridge based three-phase rectifier with HF (20 kHz) transformer isolation. The advantages of the proposed full-bridge based three-phase AC-DC rectifier are as follows.

1.) The approach uses high frequency (20 kHz) magnetics that is shown to improve power density [46] [57].
2.) The 5^{th} and 7^{th} harmonics are eliminated in the input line current over a wide range of output voltage control thereby resulting in reduction in input current THD.
3.) No electrolytic capacitors are used in the primary side of the system.
4.) Simplicity in modulation and control scheme. Output voltage is controlled by varying the duty cycle of the pulse width modulated signal.

5.) The system offers galvanic isolation between the input and output thereby minimizing the interference and contributing to safety.

6.) The secondary side of the HF ferrite core transformer can be configured to higher pulse operation (i.e., 18-pulse and 24-pulse) to further improve input current quality.

7.) The proposed system is a modular approach. The modules can be configured to create different topology embodiments.

8.) Improved switch utilization ratio and transformer utilization compared to the push-pull based rectifier in section 2.

These benefits make the proposed full-bridge based three-phase rectifier suitable for applications such as electric vehicle charging, telecomm rectifiers, data centers, and adjustable speed drives. This section details the analysis and design of the proposed system along with a design example. Simulation and experimental results are discussed on a scaled-down laboratory prototype.

3.2 Proposed Three-Phase AC-DC Multi-Pulse Rectifier with HF Isolation

The proposed three-phase AC-DC rectifier with HF transformer isolation is shown in Figure 3-1. The analysis of the topology is divided into the following stages: 1) unidirectional AC-AC converter; 2) HF ferrite core transformer; 3) 12-pulse diode rectifier; 4) input current analysis, 5) passive filtering; and 6) control scheme.

3.2.1 Unidirectional AC-AC Converter

As shown in Figure 3-1, the proposed system employs three AC-AC converters, one connected to each phase. Each AC-AC converter is composed of a single-phase bridge rectifier, a small film capacitor, and a full-bridge inverter built with silicon IGBT devices. A total of 12 passive diodes and 12 active semiconductor devices are needed to implement the AC-AC converters. The inputs for each AC-AC converter are the utility line-to-neutral voltages. In systems where the neutral wire is absent, the AC-AC converter inputs can be the line-to-line utility voltages.

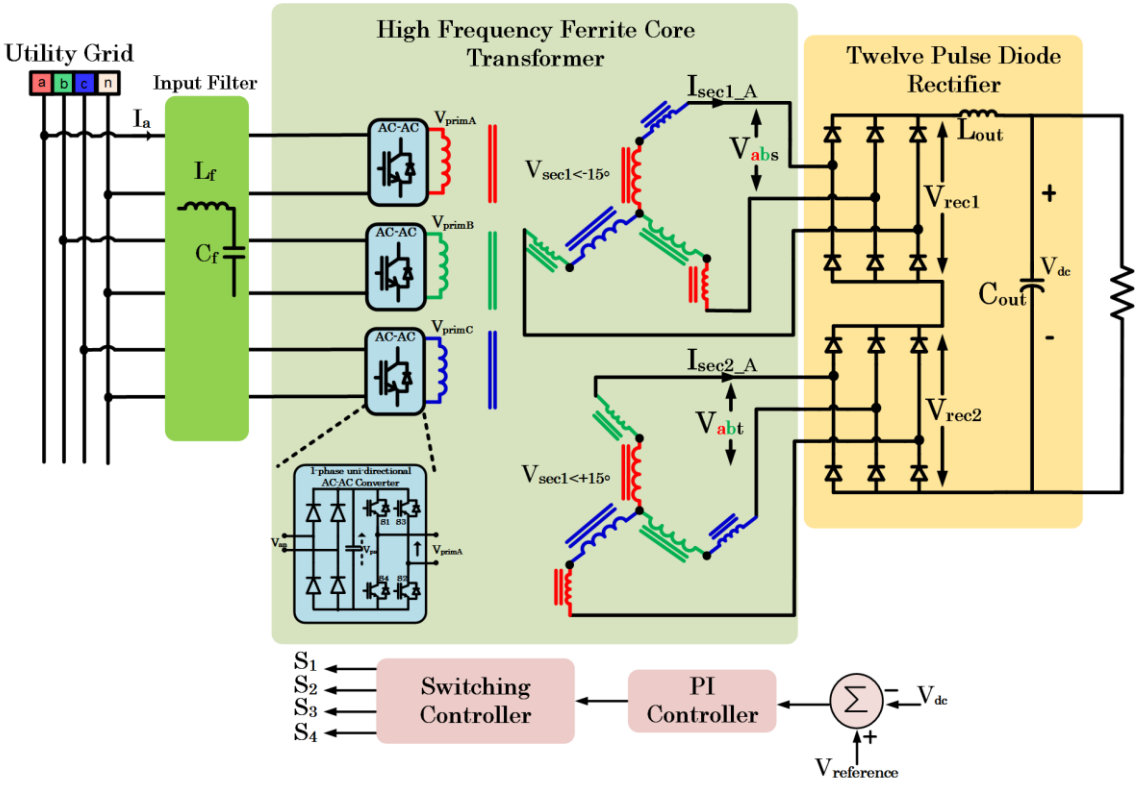

Figure 3-1: Proposed three-phase AC-DC Rectifier with high frequency transformer isolation.

The primary functions of the AC-AC converters are to modulate the amplitude of the utility line voltage for output voltage regulation and to provide the transformer a three-phase HF (20 kHz) AC link. Since the inputs to the AC-AC converters are the utility line-to-neutral voltages (Fig.3-2(a)), each single-phase rectifier operates at line frequency with a switching function as shown in Fig. 3-2(b). Thus, the diodes switch at line frequency with negligible switching loss and produce a pulsating DC voltage across the film capacitor as shown in Figure 3-2(c). Since the inputs to each AC-AC converter are phase shifted by 120°, as in balanced three-phase operation, the pulsating voltages across the film capacitors will also be displaced by 120°. For a utility voltage described by (3.1), and a single-phase diode rectifier switching function described by (3.2), the resulting pulsating voltage is expressed as in (3.3). In equations (3.1-3.3) ω_s is the utility line frequency.

$$V_{an} = \sqrt{\frac{2}{3}} V_{LL} \sin(\omega_s t) \tag{3.1}$$

$$S_d = \frac{4}{\pi} \sum_{n=1,3,5,..}^{\infty} \frac{1}{n} \sin(\omega_s t) \tag{3.2}$$

$$V_{pa} = V_{an} \cdot S_d = \sqrt{\frac{2}{3}} V_{LL} \left(\frac{2}{\pi} - \frac{4}{\pi} \sum_{n=2,4,6,..}^{\infty} \frac{\cos(n\omega_s t)}{n^2 - 1} \right) \tag{3.3}$$

The modulation of the full-bridge inverters in the AC-AC converters is synchronized in such a way that the overall switching function for the three AC-AC

converters is the same pure square wave with fundamental frequency of 20 kHz. The switching function for the full-bridge inverter connected to V_{an} is given in Figure 3-2(d), while the overall switching function for the three AC-AC converters is shown in Figure 3-2(e). Under this modulation scheme, the utility voltages are essentially being multiplied with the overall HF switching function (S_{sw}) and thus a HF AC link is created at the output of each AC-AC converter as portrayed in Figure 3-2(f). Since the utility voltages are displaced by 120° and the three AC-AC converters have the same overall switching function (S_{sw}), the voltages across the transformer windings add to zero allowing the magnetic flux to be balanced. The blocking voltage of the semiconductor devices in the AC-AC converters must be rated for the peak of the utility-line to-neutral voltages.

The overall switching function S_{sw} is given by (3.4) and the resulting voltage across the transformer winding connected to the AC-AC converter associated with phase "a" is given by (3.5). In (3.5), D refers to the duty cycle of the square wave switching function and ω_{sqr} corresponds to the frequency of the switching function which is set to 20 kHz. The voltages across the transformer windings connected to the AC-AC converters associated with phase "b" and "c" have the same expression except for a 120° phase shift. By inspecting (3.5) it is noted that the fundamental frequency of the voltage across the transformer depend primarily on ω_{sqr}. It is also evident that the three-phase HF AC link voltages across the transformer windings are a function of the duty cycle D implying that the output DC voltage can be regulated by adjusting the duty cycle of the AC-AC converters. At 50% duty cycle operation, the voltage across the transformer

windings appears as in Figure 3-2(f). Also the maximum DC output voltage is obtained at 50% duty cycle. For duty cycles above 50% short circuit across the pulsating DC voltage occurs and should be avoided. For duty cycles below 50%, zero states are introduced in the HF AC link voltages and the output DC voltage is decreased. Thus the modulation is simple and robust.

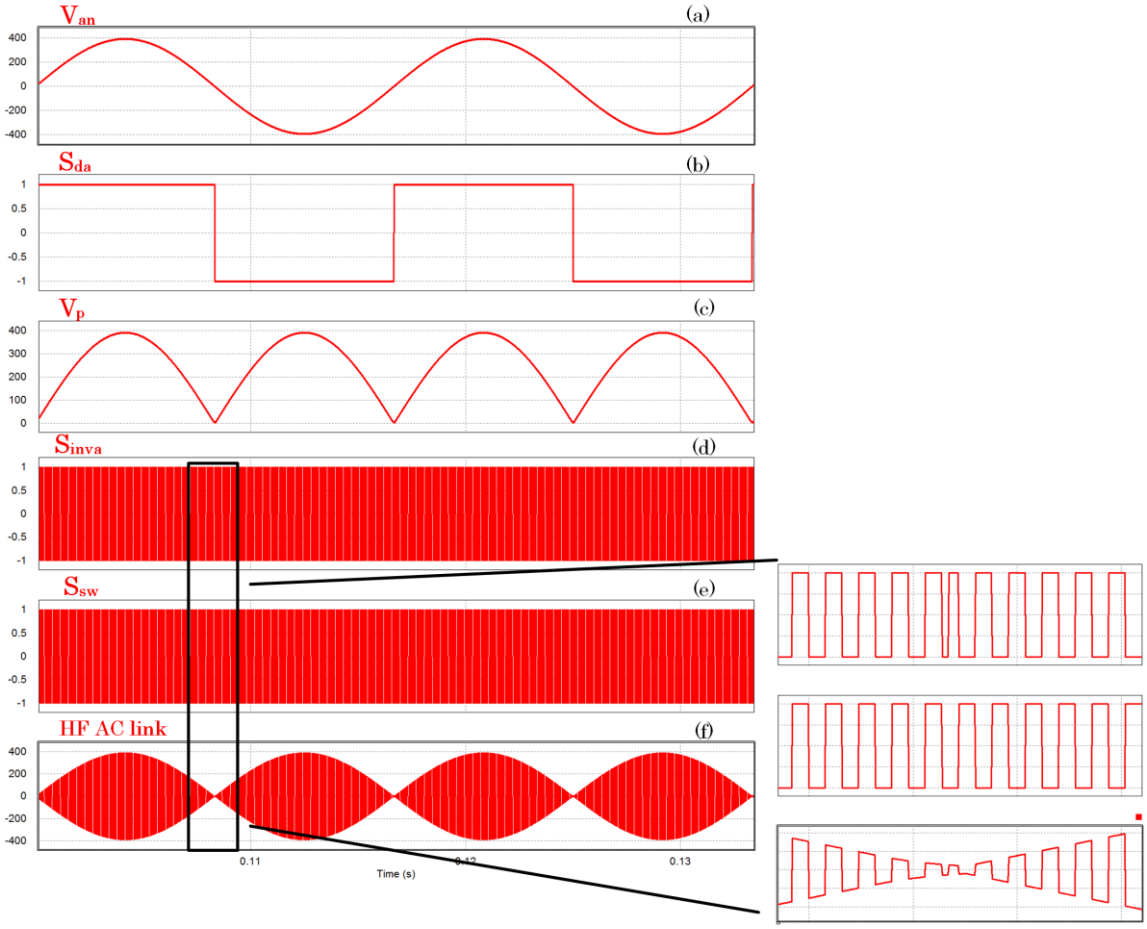

Figure 3-2: (a) Line-to-neutral utility voltage; (b) Single-phase diode rectifier switch function; (c) Pulsating DC voltage; (d) Full-bridge inverter switching function; (e) Overall ac-ac converter switching function; (f) HF AC link

$$S_{sw} = S_d \cdot S_{inv} = \frac{4}{\pi} \sum_{n=1,3,5,7,\ldots}^{\infty} \frac{1}{n} \sin(n\pi D) \cdot \sin(n\omega_{sqr} t) \tag{3.4}$$

$$V_{pri,A} = V_{an} \cdot S_d \cdot S_{inv} = V_{an} \cdot S_{sw} = \frac{\sqrt{2}}{\sqrt{3}} V_{LL} \sum_{n=1,3,5,7,..}^{\infty} \frac{2}{n\pi} \sin(n\pi D) \sin(\{n\omega_{sqr} \pm \omega_s\} \cdot t) \tag{3.5}$$

Although the modulation scheme is simple, the utility line-to-neutral voltages must be sensed in order to determine their zero crossing point. From the zero crossing point information, the switching function S_{da} for each single-phase rectifier in the AC-AC converters can be determined. After obtaining the respective switching functions S_{da}, S_{db}, S_{dc}, the switching functions of each full-bridge inverter, namely S_{inva}, S_{invb}, S_{invc} can be synchronized to achieve an overall switching function S_{sw} that is the same for the three AC-AC converters.

3.2.2 HF Ferrite Core Transformer

The HF ferrite core transformer plays a crucial role in the power density of the proposed topology. The switching frequency of the full-bridge AC-AC converters determines the frequency of operation of the transformer. The selection of the switching frequency must take into account the tradeoff between power density and efficiency. Albeit increasing the frequency of operation reduces the size of the transformer it also increases the power loss in the core and the switching devices. The efficiency of the system is studied in subsection 3.2.9. It is shown that operating at 20 kHz yields a reasonably high efficiency (>94%) and reduces the transformer size by a significant amount. Also switching at 20 kHz avoids the human audible noise region and thus the

switching action of the proposed system does not disrupt the human ear during operation.

Selection of the appropriate magnetic core is also essential to achieve high power density and high system efficiency. For high power MF applications, magnetic core materials such as ferrite, amorphous, and silicon steel should be considered [24]. At the desired frequency operation (i.e. 20 kHz) silicon steel cores exhibit significant core losses. Therefore a silicon steel core is not suitable for this application. Amorphous and ferrite materials exhibit high resistivity in a wide frequency range and are suitable for 20 kHz operation [58]. Due to its lower cost, a ferrite core material (3C94) is selected for the transformer core.

The transformer built is a three-phase, five-limb transformer. The transformer is built using ferrite blocks to form a core structure as shown in Figure 3-3. The primary and secondary windings are wound around the interior three limbs of the transformer. The outer limbs carry any unbalanced flux avoiding core saturation [52]. The transformer consists of three primary windings, one per phase, and a total of 12 secondary windings, four secondary windings per phase. As shown in Figure 3-1, the secondary side of the transformer feeds a 12-pulse rectifier. For proper 12-pulse operation, the two sets of three-phase voltages feeding the 12-pulse rectifier must have a net 30° phase shift with respect to each other. To create this phase shift, the secondary windings of the HF transformer are connected in zig-zag. This is the same secondary side connection employed for the MF transformer in section 2. Therefore, the phasor diagram in Figure 2-7 and the winding connections in Figure 2-8 also apply to the

secondary windings of the HF transformer. The turns-ratio of the secondary windings of the HF transformer is determined in the same manner as in the MF transformer. The only difference is that in the HF transformer a $1/\sqrt{3}$ factor is applied to the turns-ratio of the secondary windings. The turns-ratio is given by (3.6).

$$\begin{aligned} N_{P1} : N_{S1} : N_{S2} : N_{S3} : N_{S4} &= 1 : \frac{\sqrt{2}}{3} : \frac{\sqrt{3}-1}{3\sqrt{2}} : \frac{\sqrt{2}}{3} : \frac{\sqrt{3}-1}{3\sqrt{2}} \\ &= 1 : 0.471 : 0.173 : 0.471 : 0.173 \end{aligned} \tag{3.6}$$

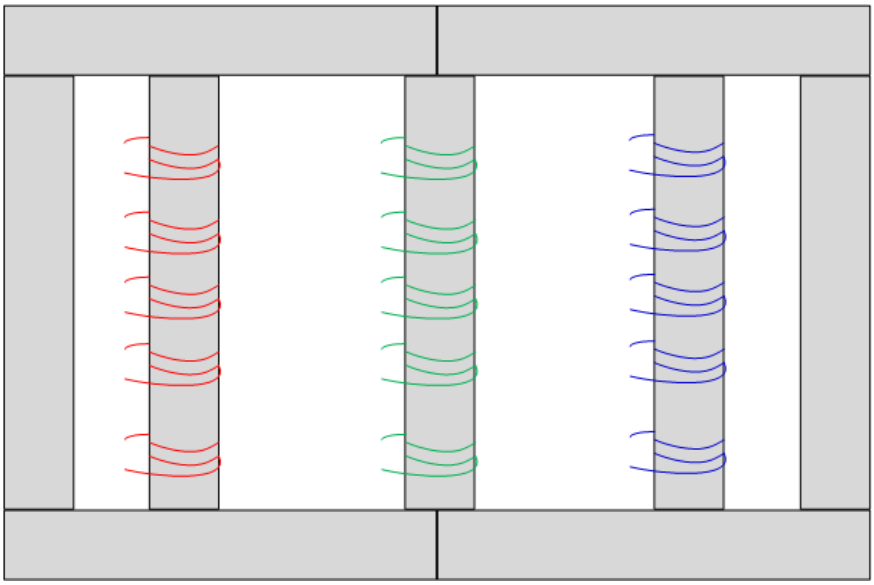

Figure 3-3: High frequency ferrite core transformer. Primary and secondary windings are in the interior three limbs of the transformer.

3.2.3 12-Pulse Diode Rectifier

Two sets of three-phase voltages (V_{abs}, V_{bcs}, V_{cas}) and (V_{abt}, V_{bct}, V_{cat}) are fed to the 12-pulse diode rectifier. These sets of voltages have a fundamental frequency close to 20 kHz and are 30° phase shifted with respect to each other. This phase shift enables a

high quality 12-pulse DC output voltage and elimination of low order current harmonics on the utility side. The operation of the 12-pulse diode rectifier is similar to the conventional line frequency multi-pulse systems. The main difference is that the 12-pulse diodes must switch at 20 kHz. Therefore, fast switching frequency diodes must be used in this topology. Diodes with fast reverse recovery times are needed.

3.2.4 Output Voltage Analysis

The output voltage analysis of the HF proposed system proceeds in a very similar manner to the output voltage analysis of the MF system in Section 2. Equations (2.13-2.27) remain valid at HF operation. But since the HF transformer has a $1/\sqrt{3}$ factor in the turns-ratio, this factor must be applied to equations (2.13-2.27). Considering this factor and carrying the same analysis, the output voltage of the 12-pulse diode rectifier is expressed as:

$$V_{12-pulse}(\omega_s t) = V_{rec1}(\omega_s t) + V_{rec2}(\omega_s t) = \frac{6}{\pi}\sqrt{\frac{2}{3}} \cdot V_{LL} + \frac{12}{143\pi}\sqrt{\frac{2}{3}} \cdot V_{LL} \cos(12\omega_s t) + \ldots \qquad (3.7)$$

3.2.5 Input Current Analysis

The utility input current is shown to have a 12-pulse behavior at unity power factor. Through mathematical analysis it is demonstrated that the utility input current's dominant harmonics are the 11^{th} and 13^{th}. Lower order harmonics such as the 5^{th} and 7^{th} are eliminated by virtue of the 30° phase shift in the zig-zag transformer connections. To perform the analysis, the output current I_d is assumed to be ideally DC and ripple free. Analysis is done for phase "a".

The utility input current is given by (3.8), where S_{sw} refers to the AC-AC converter overall switching function given in (3.4) and $I_{prim,A}$ is the current flowing through the primary winding.

$$I_a = S_{sw} * I_{prim,A} \tag{3.8}$$

By VA balance a relationship between the primary side and secondary side currents is obtained. In equation (3.9), N_p refers to the number of turns in the primary windings and N_{s1}, N_{s2}, N_{s3}, N_{s4} refers to the number of turns in the secondary windings associated with phase "a". The turns-ratio relation in (3.6) is used in (3.9). Similarly, I_{as1}, I_{as2}, I_{as3}, and I_{as4} are the currents flowing through the secondary windings associated with phase "a"; these currents can be expressed in terms of the currents flowing through the output six-pulse diode rectifiers as follows:

$$N_p \cdot I_{prim,A} = N_{s1} \cdot I_{as1} + N_{s2} \cdot I_{as2} + N_{s3} \cdot I_{as3} + N_{s4} \cdot I_{as4} \tag{3.9}$$

$$I_{as1} = I_{d1a} \tag{3.10}$$

$$I_{as2} = -I_{d1b} \tag{3.11}$$

$$I_{as3} = I_{d2a} \tag{3.12}$$

$$I_{as4} = -I_{d2c} \tag{3.13}$$

Using (3.10-3.13) into (3.9) results in (3.14):

$$I_{prim,A} = N_{s1} \cdot (I_{d1a} + I_{d2a}) - N_{s2}(I_{d1b} + I_{d2c}) \tag{3.14}$$

The currents flowing through the output diode rectifiers (i.e. I_{d1a}, I_{d2a}, I_{d1b}, I_{d2c}) have a quasi-square wave nature as determined by (3.15) but also have the overall switching function S_{sw} operating on them. These currents are given by (3.16-3.19) respectively.

$$S_d(\omega_s t) = \sum_{n=1,3,5,7}^{\infty} \left(\frac{4I_d}{n\pi} \cos\left(\frac{n\pi}{6} \right) \right) \cdot \sin(n\omega_s t) \tag{3.15}$$

$$I_{d1a} = S_d\left(\omega_s t - \frac{\pi}{12} \right) * S_{sw} \tag{3.16}$$

$$I_{d1b} = S_d\left(\omega_s t - \frac{\pi}{12} - \frac{2\pi}{3} \right) * S_{sw} \tag{3.17}$$

$$I_{d2a} = S_d\left(\omega_s t + \frac{\pi}{12} \right) * S_{sw} \tag{3.18}$$

$$I_{d2c} = S_d\left(\omega_s t + \frac{\pi}{12} + \frac{2\pi}{3} \right) * S_{sw} \tag{3.19}$$

The -15 ^{o} and +15 ^{o} phase shift is evident from (3.16) and (3.18) respectively. Substituting equations (3.16-3.19) into (3.14) yields:

$$I_{prim,A} = S_{sw} * \left\{ \begin{array}{l} N_{s1}\left[S_d\left(\omega t - \frac{\pi}{12} \right) + S_d\left(\omega t + \frac{\pi}{12} \right) \right] - \\ N_{s2}\left[S_d\left(\omega t - \frac{\pi}{12} - \frac{2\pi}{3} \right) + S_d\left(\omega t + \frac{\pi}{12} + \frac{2\pi}{3} \right) \right] \end{array} \right\} \tag{3.20}$$

Then from (3.8), the utility input current I_a is given by:

$$I_a = S_{sw} * S_{sw}\left\{\begin{array}{l} N_{s1}\left[S_d\left(\omega t - \frac{\pi}{12}\right) + S_d\left(\omega t + \frac{\pi}{12}\right)\right] - \\ N_{s2}\left[S_d\left(\omega t - \frac{\pi}{12} - \frac{2\pi}{3}\right) + S_d\left(\omega t + \frac{\pi}{12} + \frac{2\pi}{3}\right)\right] \end{array}\right\} \tag{3.21}$$

Simplification of the terms inside the bracket of equation (3.21) yield:

$$I_a = \frac{4\sqrt{3}\cdot I_d}{\pi}\left[\begin{array}{l} \sin(\omega_s t) - \frac{1}{11}\sin(11\cdot\omega_s t) - \frac{1}{13}\sin(13\cdot\omega_s t) \\ + \frac{1}{23}\sin(23\cdot\omega_s t) + \frac{1}{25}\sin(25\cdot\omega_s t) + \ldots \end{array}\right]\cdot S_{sw}\cdot S_{sw} \tag{3.22}$$

For $D = 0.5$,

$$S_{sw}\cdot S_{sw} = \left[\frac{4}{\pi}\sum_{n=1,3,5,7,\ldots}^{\infty}\frac{1}{n}\left|\sin(n\pi D)\right|\cdot\sin(n\omega_{sqr}t)\right]^2 = 1$$

Therefore, equation (3.22) becomes:

$$I_a = \frac{4\sqrt{3}\cdot I_d}{\pi}\left[\begin{array}{l} \sin(\omega_s t) - \frac{1}{11}\sin(11\cdot\omega_s t) - \frac{1}{13}\sin(13\cdot\omega_s t) \\ + \frac{1}{23}\sin(23\cdot\omega_s t) + \frac{1}{25}\sin(25\cdot\omega_s t) + \ldots \end{array}\right] \tag{3.23}$$

From equation (3.23) it is evident that the utility input current has a 12-pulse behavior. The 5th, 7th, 17th, 19th, etc. harmonics are eliminated. This analysis demonstrates that the proposed topology has a very good input current quality which facilitates compliance with IEEE-519 harmonic standards [10]. The topology has the same performance in terms of input current quality compared to the push-pull topology

proposed in Section 2 while improving power density due to HF operation. For $D \neq 0.5$, the term $S_{sw} \cdot S_{sw}$ on (3.22) produces frequency components at DC, $2f_{sqr}$, $4f_{sqr}$, $6f_{sqr}$, $8f_{sqr}$, $10f_{sqr}$, etc. These frequency components interact with the fundamental frequency and with the low order current harmonics of the utility current (i.e. f_s, $11f_s$, $13f_s$, $23f_s$, $25f_s$). Since the intended switching frequency is f_{sqr} = 20 kHz, the harmonics being produced by varying the duty cycle occur at very high frequencies and the lower order harmonics remain intact. This means that regulating the output voltage by duty cycle control does not affect the input current quality. The theoretical THD of the utility input current is 16%. This is the same value for the conventional line frequency 12-pulse rectifier.

3.2.6 Passive Components

As proven in the previous sub-section, the harmonic spectrum of the utility input current is identical to the spectra of the conventional 12-pulse isolation transformer scheme. Thus, the input filter must be designed to attenuate the 11^{th} and 13^{th} harmonic. A cut-off frequency of 500 Hz is desired for the input filter. The design of the output filter is the same compared to the push-pull based rectifier in Section 2. The output capacitor and minimum inductance for continuous conduction mode are given by (2.47) and (2.48) respectively.

3.2.7 Control Scheme by Varying Duty Cycle D

One of the advantages of the proposed system is the simplicity of its modulation and control scheme. From equation (3.5) it is clear that the output DC voltage can be regulated by duty cycle control. It was also determined in sub-section 3.2.4 that varying the duty cycle does not affect the utility input current. The output voltage is controlled

by a simple proportional-integral (PI) controller. As observed in Figure 3-6, the error signal feeding the controller is the difference between the sensed output DC voltage and the desired reference voltage. The output of the PI controller then feeds the switching controller. Essentially, the PI controller dictates the required duty cycle of operation to obtain the desired reference voltage. Within the switching controller, the gating signals for the full-bridge inverters are determined.

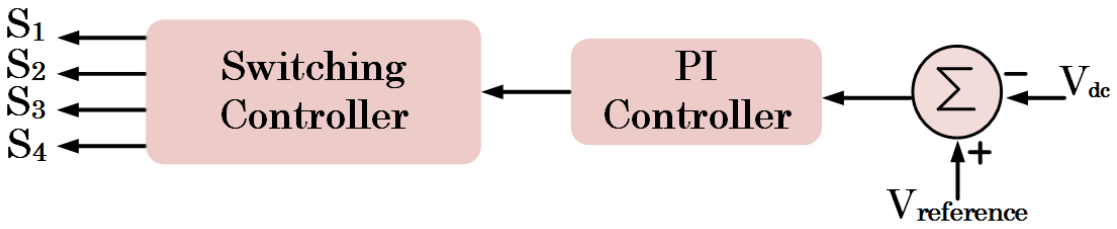

Figure 3-4: Closed loop control to regulate the output DC voltage of the proposed system.

3.2.8 Design Example

A $480V_{l\text{-}l}$, 50kW, $500V_{dc}$ design example is considered to demonstrate the functionality of the proposed system shown in Figure 3-1. The output DC voltage of the proposed system is dictated by the DC component of (3.7) and is calculated as:

$$V_{dc} = \frac{6}{\pi}\sqrt{\frac{2}{3}} \cdot V_{LL} = 749\ \text{V}. \tag{3.24}$$

Since the actual desired output voltage is $500V_{dc,}$ the turns-ratio of the secondary windings must be adjusted by a factor k_t which is calculated as:

$$k_t = \frac{500\,\mathrm{V}}{\frac{6}{\pi}\sqrt{\frac{2}{3}} \cdot \mathrm{V}_{LL}} = 0.67 \tag{3.25}$$

For 50kW operation, the output current I_d is:

$$I_d = \frac{P_o}{\mathrm{V}_{dc}} = 100\,\mathrm{A}. \tag{3.26}$$

The volt-ampere (VA) rating of the HF ferrite core transformer can be calculated using the rms voltage and rms current of each winding under the assumption that the output current I_d has negligible ripple. The voltage and current expressions for the primary and secondary windings of the HF ferrite core transformer are listed in Table 3-1. The expressions in this table are valid when the input source to the AC-AC converters is the utility line-to-neutral voltages. In the table, the equivalent VA rating is calculated to be $1.07P_o$. This rating is lower than the VA rating of the medium frequency transformer in Section 2 (i.e. $1.29P_o$) and slightly higher than the VA rating of the conventional 12-pulse isolation transformer (i.e. $1.03P_o$). However, the transformer proposed in this section operates at HF allowing for further improvement in power density. More details about the transformer design are given in Section 5.

The voltage and current ratings of the semiconductor devices are listed in Table 3-2. The voltage ratings are normalized using the utility line-line voltage V_{LL}, while the current ratings are normalized using the output current I_d. From Table 3-2 it is observed that the diodes and IGBTs in the AC-AC converter must have a voltage rating of 0.816 p.u. This is a much better rating compared to the 2.83 p.u rating of the semiconductor devices in the push-pull based rectifier of Section 2. This 0.816 p.u rating facilitates the

interface of the proposed topology with utility line voltages in the 690V-2.3 kV range. The 12-pulse diode rectifier voltage and current ratings are the same compared to the 12-pulse diode rectifier of the topology in Section 2. A power factor *pf* of 0.985 is assumed to calculate the per unit values of the peak and rms current ratings of the AC-AC converter.

Table 3-1: HF ferrite core transformer VA rating for HF 12-pulse rectifier

HF Ferrite Core Transformer VA rating		
Primary Side Winding	Voltage expression (rms)	$\frac{V_{LL}}{\sqrt{3}} = 0.577 V_{LL} = 0.37 V_{dc}$
	Current expression (rms)	$0.9 \cdot I_d$
Secondary Side Windings with turns-ratio *Ns1*	Voltage expression (rms)	$\frac{\sqrt{2}}{3} \cdot \frac{V_{LL}}{\sqrt{3}} = 0.272 V_{LL} = 0.1746 V_{dc}$
	Current expression (rms)	$\sqrt{\frac{2}{3}} \cdot I_d = 0.816 I_d$
Secondary Side Windings with turns-ratio *Ns2*	Voltage expression (rms)	$\frac{\sqrt{3}-1}{3\sqrt{2}} \frac{V_{LL}}{\sqrt{3}} = 0.0996 V_{LL} = 0.064 V_{dc}$
	Current expression (rms)	$\sqrt{\frac{2}{3}} \cdot I_d = 0.816 I_d$
VA rating calculation		
$VA_{tot} = 3 \cdot \frac{V_{LL}}{\sqrt{3}} \cdot 0.88 I_d + 6\sqrt{\frac{2}{3}} I_d \left(\frac{\sqrt{3}-1}{3\sqrt{2}} \frac{V_{LL}}{\sqrt{3}} + \frac{\sqrt{2}}{3} \frac{V_{LL}}{\sqrt{3}} \right) = 3.3447 V_{LL} I_d = 2.1456 V_{dc} I_d$		
$VA_{eq} = \frac{1}{2} VA_{tot} = 1.07 V_{dc} I_d = 1.07 P_o$		

Table 3-2: Voltage and current ratings of semiconductor devices

Component	Parameter	Expression	P.U. Value	Design Value (50 kW)
AC-AC converter (single-phase rectifier diodes)	peak voltage	$\sqrt{\frac{2}{3}}\mathrm{V_{LL}}$	0.816	392 V
	peak current	$k_t \frac{4}{\pi \cdot \mathrm{pf}} I_d$	$1.3k_t$	87 A
	rms current	$k_t \frac{2}{\pi \cdot \mathrm{pf}} I_d$	$0.65k_t$	43 A
AC-AC converter (full-bridge inverter IGBTs)	peak voltage	$\sqrt{\frac{2}{3}}\mathrm{V_{LL}}$	0.816	392 V
	peak current	$k_t \frac{4}{\pi \cdot \mathrm{pf}} I_d$	$1.3k_t$	87 A
	rms current	$k_t \frac{2}{\pi \cdot \mathrm{pf}} I_d$	$0.65k_t$	43 A
12-Pulse Diode Rectifier	peak voltage	$k_t\sqrt{\frac{2}{3}}\mathrm{V_{LL}}$	$0.816k_t$	263 V
	peak current	I_d	1	100 A
	rms current	$I_d\sqrt{\frac{2}{\pi}\left(\frac{\pi}{12}+\frac{1}{4}\right)}$	0.57	57 A

3.2.9 Simulation Results

The proposed system in Figure 3-1 is simulated to demonstrate its operation. The electrical operation is verified using PSIM, while the performance of the HF transformer in terms of flux density and core losses is simulated using Ansys Maxwell.

3.2.9.1 Simulations in PSIM

Table 3-3 lists the parameters used in simulation. The transformer used for simulation was close to ideal conditions. The turns-ratio was set as given by (3.6).

Table 3-3: Operating conditions used for simulation in PSIM

Grid voltage (line-to-line rms)	480V
Grid frequency	60 Hz
Output dc voltage	500 V_{dc}
Rated power	50 kW
Switching frequency (f_{sqr})	20 kHz
Input inductor (L_f)	25 μH (0.002 p.u)
Output Inductor (L_{out})	500 μH (0.042 p.u)
Output Capacitor (C_{out})	2.2 mF

Figure 3-5 shows the relevant voltage waveforms of the system. Figure 3-5(a) shows the pulsating voltages at twice the line frequency across the film capacitors in the AC-AC converters. The three-phase HF AC output of the AC-AC converter is shown in Figure 3-5(b); these three-phase HC AC link are fed to the transformer primary windings. The secondary side line-to-line voltages V_{abs} and V_{abt} are shown in Figure 3-5(c), these voltages exhibit the 30° phase shift required for 12-pulse operation. The high quality DC output voltage at 500V is shown in Figure 3-5(d). The frequency spectrum of voltage V_{primA} is given in Figure 3-6 demonstrating that the transformer is operating at HF, thereby increasing power density. The HF nature of the transformer is also evident from the currents on the primary windings. Figure 3-7(a) shows the current I_{primA}. The 12-pulse operation of the system is confirmed from the currents I_{d1a} and I_{d2a} which feed the 12-pulse rectifier; these currents have a 30° phase shift as expected.

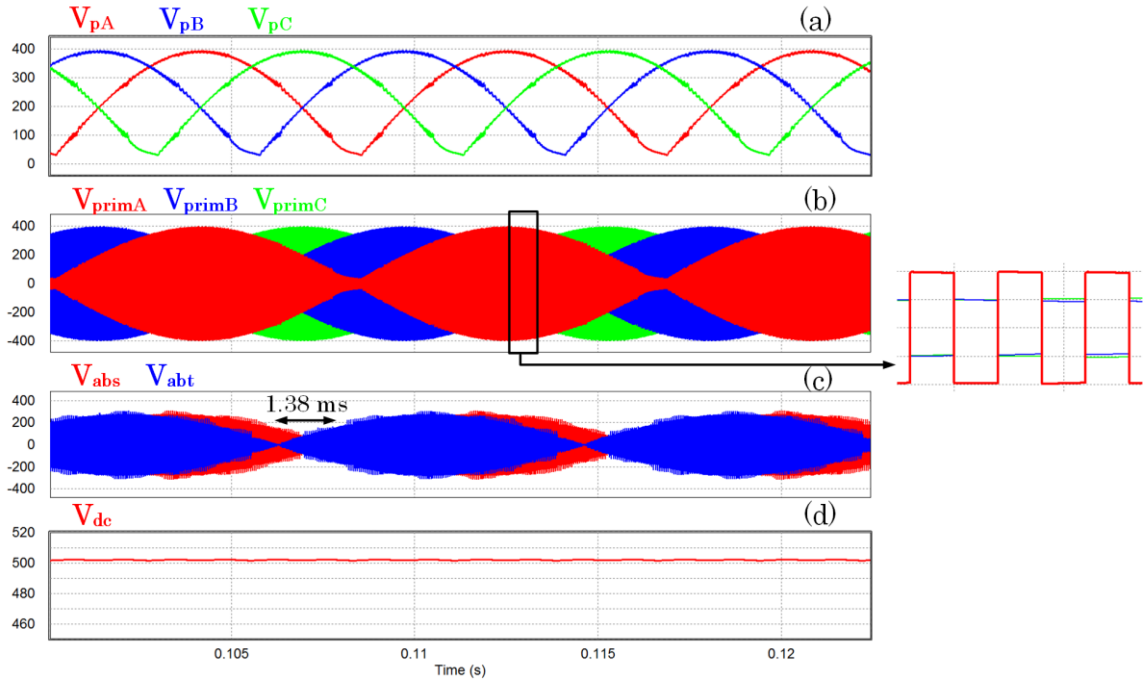

Figure 3-5: (a) Pulsating voltages across the film capacitors in AC-AC converters; (b) Three-phase HF AC link across transformer windings; (c) Secondary side line-to-line voltages are displaced by 30°; (d) High quality DC output voltage at 500V.

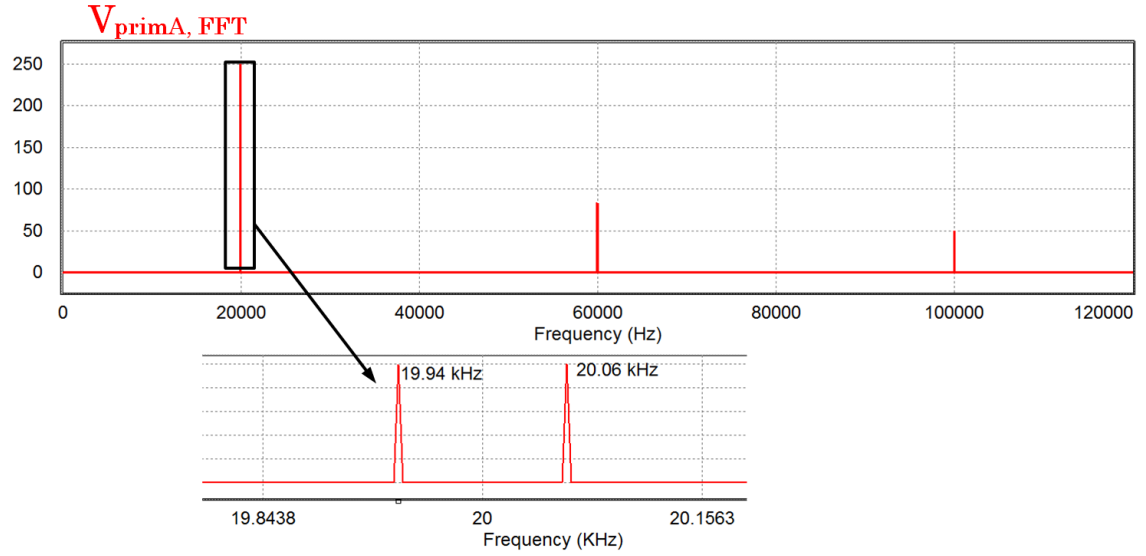

Figure 3-6: FFT of voltage across transformer winding. Fundamental component occurs at HF allowing the transformer size to be decreased.

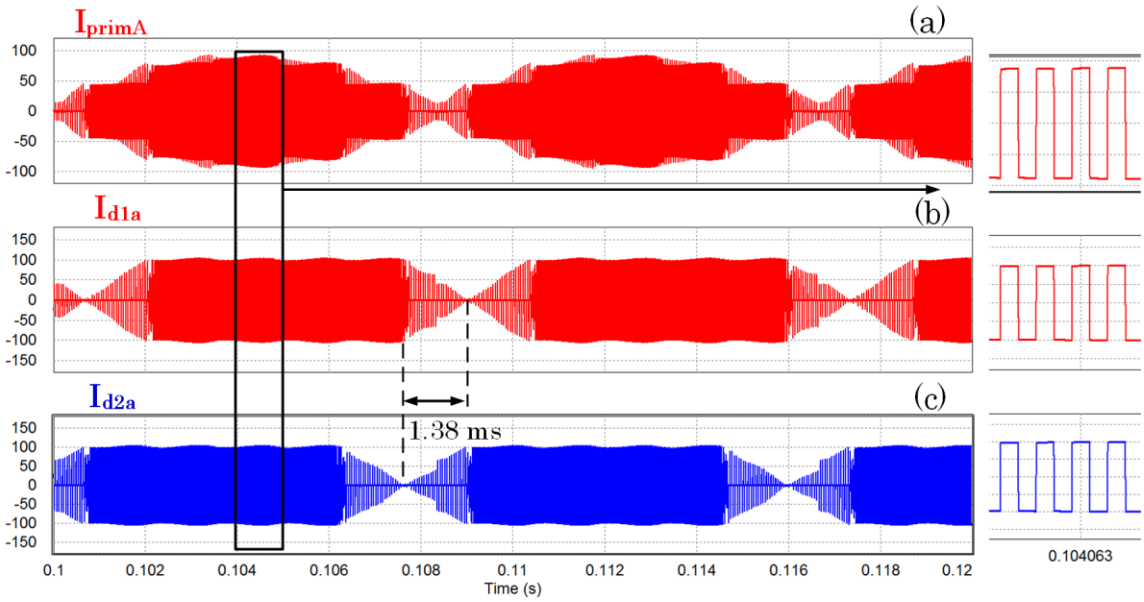

Figure 3-7: (a) Current on primary side winding, high frequency nature is evident; (b) I_{d1a}, current feeding one of the six-pulse diode rectifiers in the output; (c) I_{d2a}, current feeding second six-pulse diode rectifier in the output. I_{d1a} and I_{d2a} are shifted by 30°.

The functionality of the system is further confirmed by Figure 3-8. The utility line input current for phase "a" is shown in Figure 3-8(a). The 12-pulse nature of the current is evident. Furthermore, the harmonic spectrum of the input current, given in Figure 3-8(b), shows that the dominant harmonics are the 11^{th} and 13^{th} as in conventional 12-pulse operation. This simulation result is in accordance with the input current analysis provided in sub-section 3.2.5. The simulated THD of the line current is 12%; this is lower than the theoretical value due to the small input filter used in the simulation.

The closed loop control of the system is verified by introducing a step change in the output DC voltage. A step of $500V_{dc}$ to $400V_{dc}$ is applied at t=0.25 sec. It is expected for the duty cycle to decrease since the relationship between duty cycle and output

voltage is linear. The step change simulation results are shown in Figure 3-9. It is evident that 12-pulse behavior of the utility line current is maintained for variable duty cycle operation. The harmonic content on the utility line current remains the same. Figure 3-10 shows a plot of the input current THD as the duty cycle is varied from 10-50%. As observed from the plot, the THD is pretty much constant. The reported THD values are less than 16% because a small filter was used in the simulations.

Similarly, the output voltage relation with the duty cycle is plotted and shown in Figure 3-11. The plot shows that the relationship is linear. As the duty cycle decreases, zero states are introduced in the three-phase HF AC link which in turn decreases the rectified DC voltage on the output. The rated voltage occurs at $D = 0.5$ as expected.

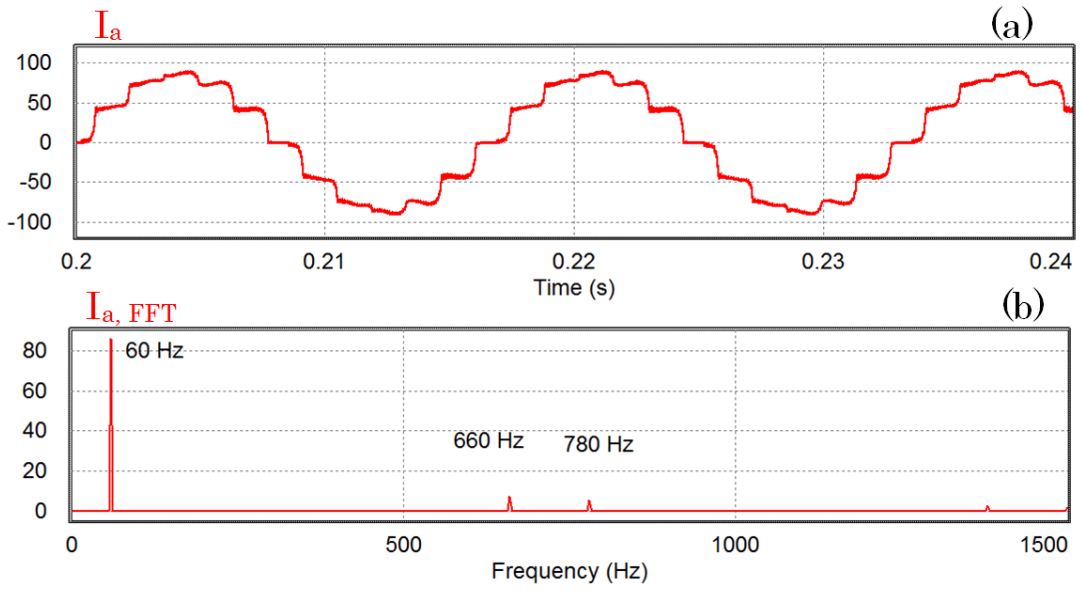

Figure 3-8: (a) Utility line input current for phase "a"; 12-pulse behavior is evident. Simulated THD is 12%. (b) FFT of line current confirms 12-pulse operation, dominant harmonics are the 11th and 13th.

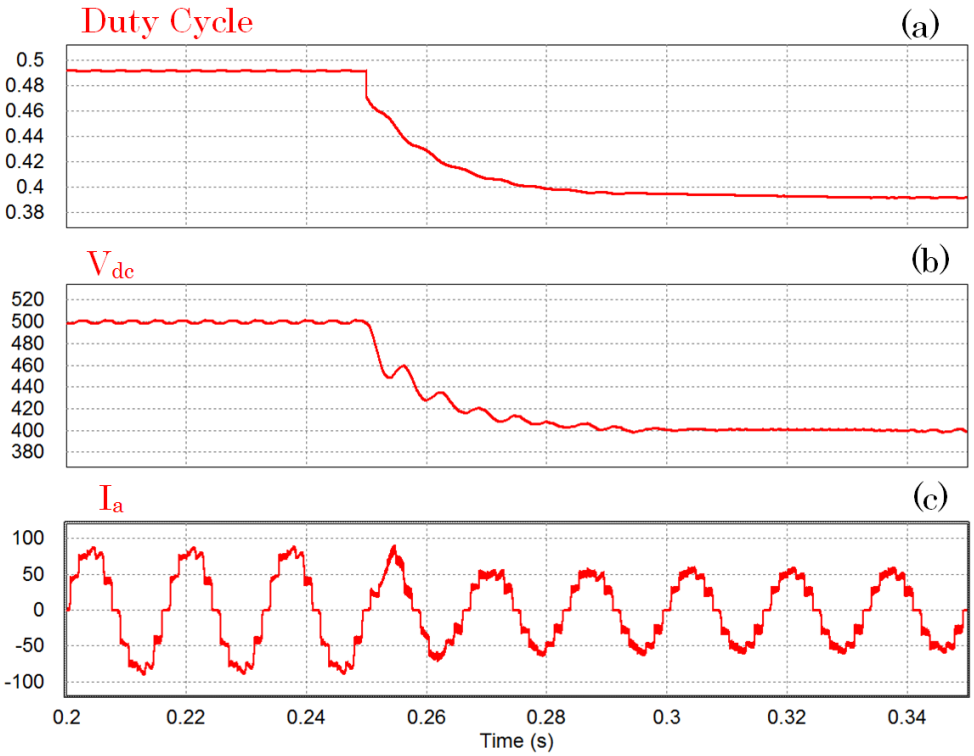

Figure 3-9: (a) Duty cycle drops due to step change in the output DC voltage; (b) Step change in output DC voltage; (c) Utility line input current for phase 'a', 12-pulse behavior is maintained for variable duty cycle.

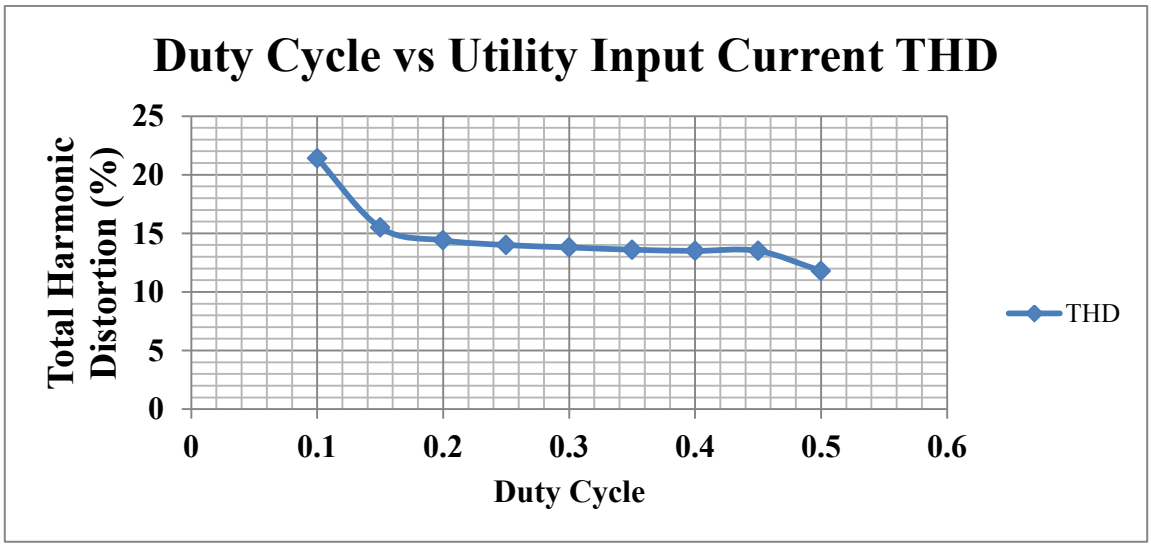

Figure 3-10: Duty cycle vs. utility input current THD.

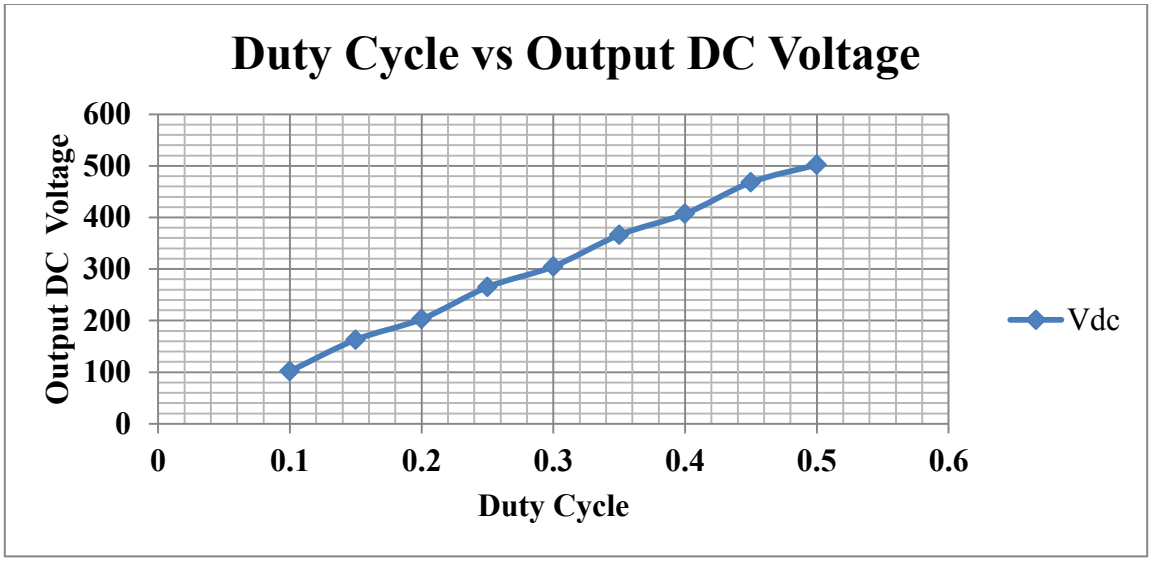

Figure 3-11: Duty cycle vs. output DC voltage. A linear relationship is evident.

3.2.9.2 Simulations in Ansys Maxwell FEA Software

The magnetic characteristics of the HF transformer are studied using Ansys Maxwell FEA software. The primary windings of the modelled transformer were excited using the voltage expression derived in (3.5). The voltage excitation is $120V_{rms}$. This is done to match the excitation given during experimental results. The material of the core was selected to be Ferroxcube 3C94 which has a saturation flux density of 0.42 T at HF. A plot of the magnetic field density for a 2D simulation of the proposed transformer is given in Figure 3-12. From the simulation, it is shown that the flux density is higher in the interior three-limbs of the transformer as expected. The core of the transformer is shown to operate at 0.34 T which is below the saturation region. In Figure 3-13, the corresponding magnetic flux lines plot is presented. The flux lines also concentrate along the interior three-limbs of the transformer. Using the 3C94 core loss data at HF, the FEA software is used to simulate the core losses of the MF transformer. The simulated core

losses shown in Figure 3-14 and are used to evaluate the efficiency of the proposed topology as discussed in the next section.

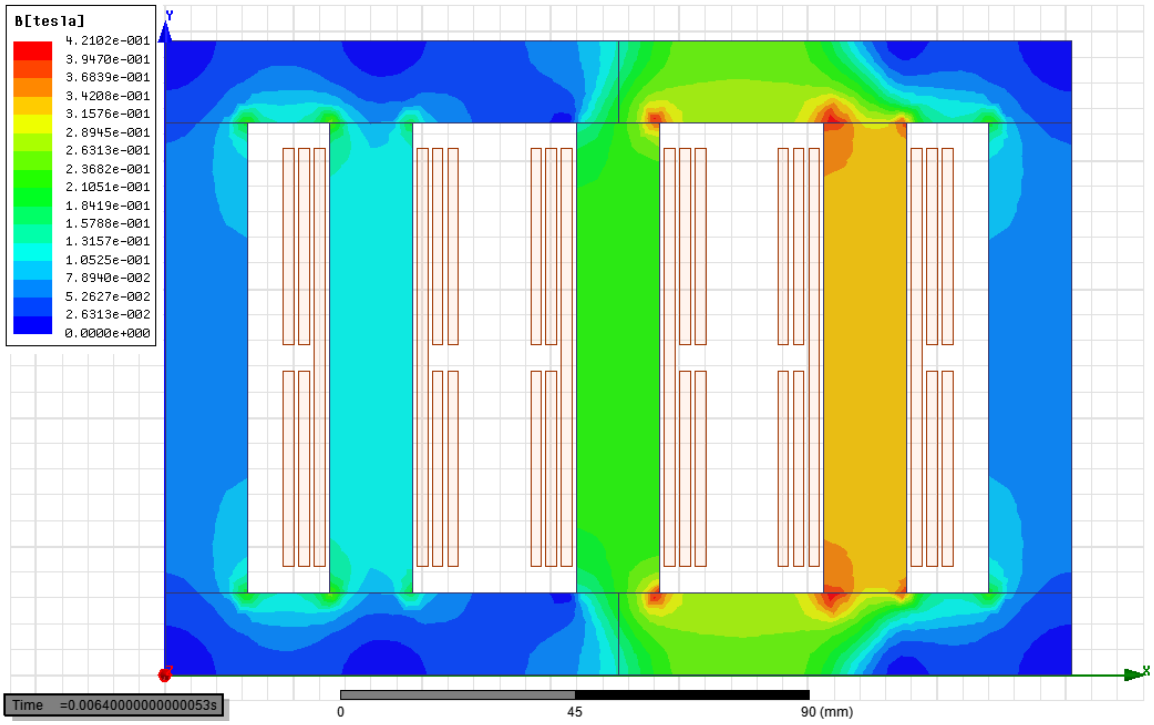

Figure 3-12: Magnetic field density plot of the proposed transformer for HF three-phase excitation. The dimensions of the transformer are 17.6 cm x 12.32 cm x 3 cm (0.65 L)

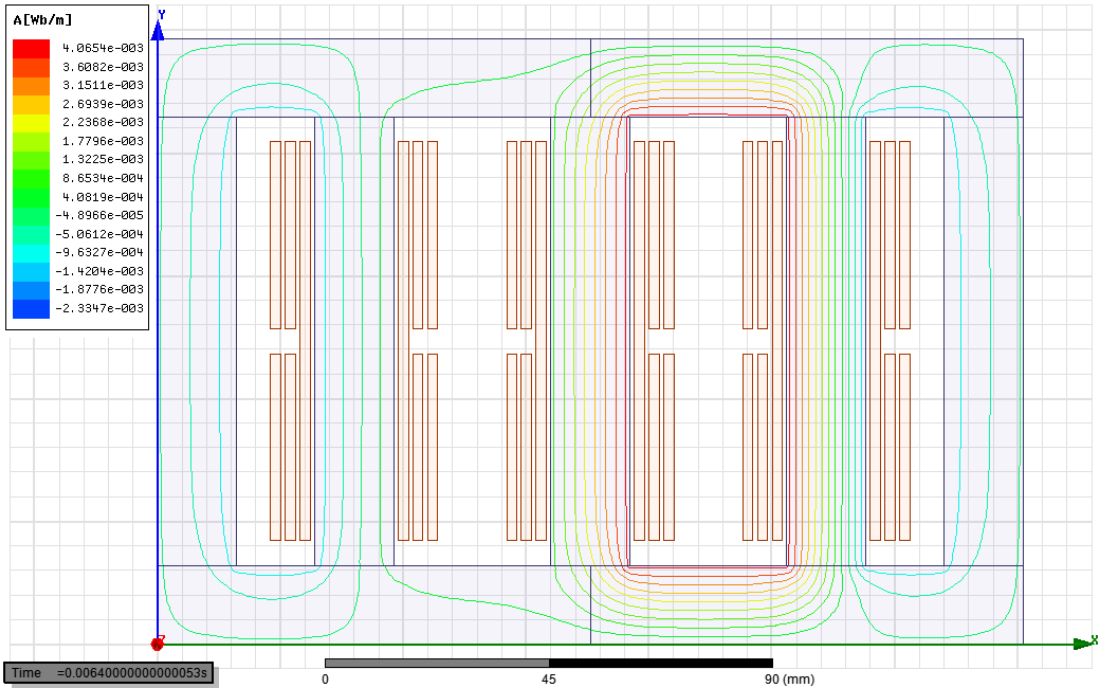

Figure 3-13: Magnetic flux lines for three-phase HF excitation.

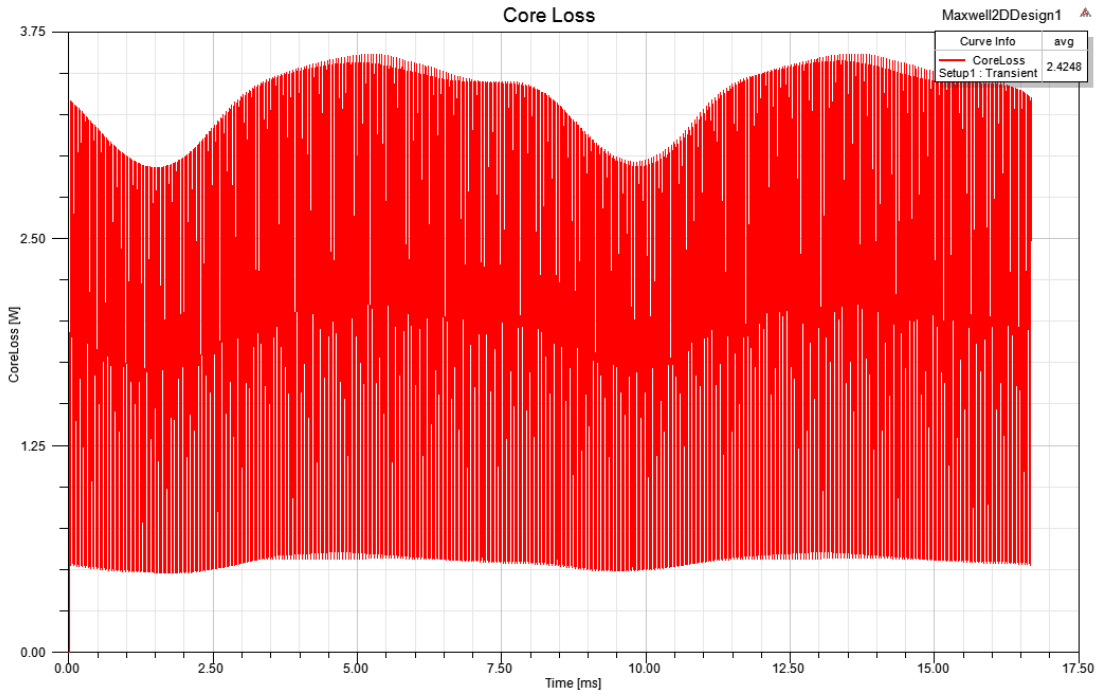

Figure 3-14: Simulated core losses of HF transformer for three-phase HF excitation.

3.2.10 Efficiency Analysis

The efficiency of the proposed system in Figure 3-1 is analyzed using the thermal models in the software simulation package PLECS. With the thermal model in PLECS the switching and conduction losses of the semiconductor devices are calculated. In order to calculate the losses, the software requires data from datasheets of commercial semiconductor devices. Thus, commercially available semiconductor devices must be selected to gather the appropriate data. Table 3-4 lists the components selected to calculate the efficiency of the 50 kW design example described in subsection 3.2.8. The relevant data required in the software to calculate the switching losses are the switching energy loss versus collector current curves. Both the turn on and turn off energy loss curves are required. The conduction losses for the IGBT are calculated from its output characteristics curves (i.e. collector current vs. collector-emitter voltage). Similarly, the conduction losses of the diodes in the system are calculated using the forward current versus forward drop voltage curve. The switching losses for the selected diodes are essentially zero due to their fast reverse recovery time.

Figure 3-15 shows a breakdown of the switching and conduction losses of the semiconductor devices used. The conduction losses of the semiconductor devices are considerable as noted from the figure and amount to 2.5 kW. In fact the conduction losses account for 76% of the system's total losses as shown in Figure 3-16. The switching losses in turn account for 25% of the losses while the transformer accounts for only 1% of the losses. The calculated efficiency for this 50 kW design example is 94%. This can be improved by selecting better semiconductor devices such as GaN or SiC.

Table 3-4: Semiconductors used for power loss analysis using PLECS thermal models.

AC-AC converter IGBT	IXXH50N60C3D1
AC-AC converter diodes	VUE 75-06NO7
Output 12-pulse rectifier	VUE 75-06NO7

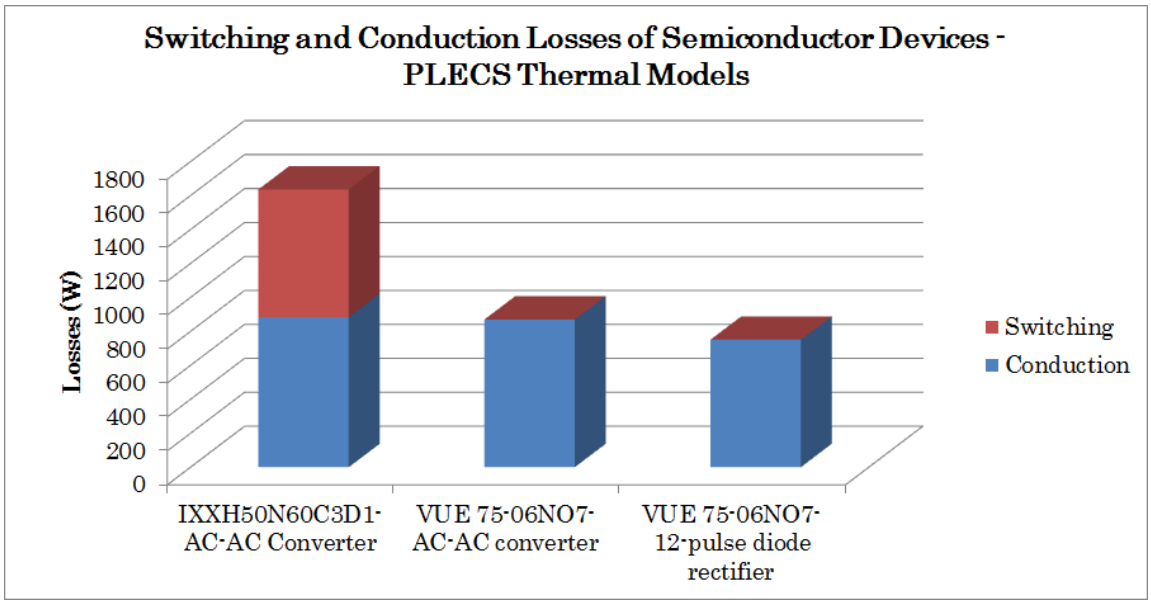

Figure 3-15: Switching and conduction losses for 50 kW design example.

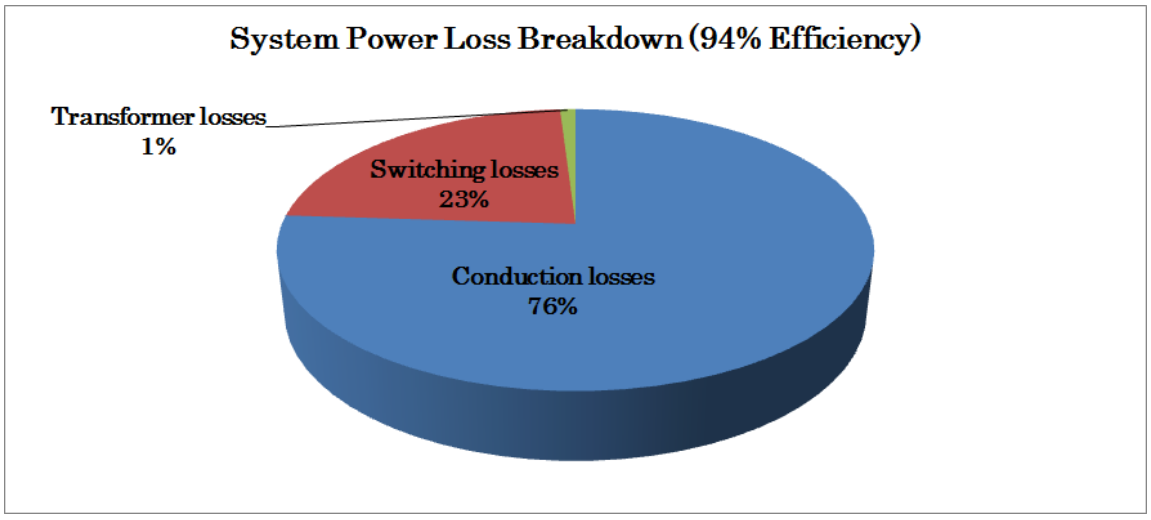

Figure 3-16: System power loss breakdown for 50 kW design example.

3.2.11 Comparative Evaluation

The proposed scheme in Figure 3-1 is compared with other three-phase AC-DC rectifier systems. The systems considered for comparison include the conventional 12-pulse rectifier, the active 12-pulse rectifier [36], the modular three-phase PFC scheme, and the push-pull based rectifier proposed in Section 2. The results of the comparison evaluation are listed in Table 3-5. The proposed scheme in this section utilizes a total of 12 active switching devices in the front-end to create a three-phase HF AC link. This number of active devices is a disadvantage when compared to the number of active devices in the push-pull based topology proposed in Section 2. However, the p.u voltage rating of the active devices in the push-pull based topology is a concern. In fact the voltage rating of the semiconductor devices is better for the proposed scheme in this section. Similar to the active 12-pulse topology and the push-pull based topology, the sensing effort and modulation complexity is low.

The proposed scheme has an advantage over the modular three-phase PFC scheme in terms of the number of electrolytic capacitors used in the front-end. The proposed scheme does not require energy storage and thus electrolytic capacitors are not needed which benefits the reliability and density of the system. Among the compared topologies employing phase-shifting transformers, only in the proposed scheme the transformer operates at HF. The proposed HF transformer rated at 10 kW has a power density of 15,380 W/L. This is nine times the power density of the MF transformer proposed in Section 2. This makes the proposed scheme very attractive for applications where size and weight are of paramount importance.

Table 3-5: Comparison of proposed system with other three-phase AC-DC rectifier systems.

Topologies		Conventional 12-Pulse	Active 12-Pulse [36]	Three single-phase PFC	Push-Pull based, Section 2	Full-bridge based, Section 3
Configuration		ac-dc	ac-dc-dc	ac-dc-dc-dc	ac-ac-dc	ac-ac-dc
No. of active switches	front-end	------	------	3	2	12
	dc-dc	------	4	12	------	
	Total	------	4	15	2	12
Galvanic Isolation		Yes	No	Yes	Yes	Yes
Sensing effort & modulation complexity		None	Low	High	Low	Low
No. of DC link capacitors (front-end)		None	None	3	None	None
Phase-Shifting Transformer VA rating (operation frequency)		$1.03P_o$ (line frequency)	$0.38P_o$ (line frequency)	------	$1.29P_o$ (medium frequency)	$1.07P_o$ (high frequency)
Power Density of Phase-Shifting transformer (Output Watts/Liter)		507	352*	------	1700	15,380

3.2.12 Experimental Results

A scaled-down laboratory prototype rated at 1 kW is built and tested to validate the operation of the proposed system in Figure 3-1. Table 3-6 lists the hardware components used in the experiment. The utility line-to-line voltage is set to 208Vrms with a 60 Hz frequency. A small input passive filter with L_f=100 μH was used. Three voltage sensors are used to detect the zero crossing of the line-to-neutral voltages. These signals are fed to the ADC module of the microcontroller to synchronize the gating functions of the full-bridge inverters. The gating signals are generated using a Texas

Instruments microcontroller. The switching frequency of the gating signals is set to 20 kHz. The transformer core is built using ferrite 3C94 material.

Table 3-6: Hardware components used for laboratory scaled-down prototype

AC-AC converter	Semikron SK13GD063
Gate Driver	Semikron SKHI 61 (R)
Voltage sensors	TI AMC1100
Microcontroller	TMS320F28335
Transformer core material	3C94
Output six-pulse rectifier	IXYS VUE 75-06NO7

The obtained experimental results are similar to the simulation results. The pulsating voltages across the film capacitors in the AC-AC capacitors are shown in Figure 3-17. The pulsating voltages are full-wave rectified as expected. The three-phase HF AC link across the transformer primary windings is shown in Figure 3-18. It is evident that the voltages are shifted by 120°. Figure 3-19 presents a zoom out of Figure 3-18. The HF operation of the transformer is verified from Figure 3-20 which shows the frequency spectrum of the voltage across the transformer winding. The fundamental components appear at 20 kHz ±60 Hz enabling the transformer to operate at HF. The transformer's winding primary current along with the winding voltage is shown in Figure 3-21 further demonstrating HF operation. Figure 3-22 shows the secondary side line-to-line voltages V_{abs} and V_{abt}. These voltages are shifted by 30° as expected.

Similarly, the currents I_{d1a} and I_{d2a} are shifted by 30° from each other as shown in Figure 3-23. The utility line input current for phase "a" along with its frequency spectrum is shown in Figure 3-24. The 12-pulse nature of the current is evident. The

dominant harmonics are the 11th and 13th as expected. The frequency spectrum shows that the 5th, 7th, 17th, 19th harmonics have been eliminated confirming 12-pulse operation. Unity power factor operation is evident from Figure 3-25 which shows the utility line-to-neutral voltage V_{an} and the utility line input current I_a. This figure also shows that the switching nature of the AC-AC converters does not affect the utility voltages and thus EMI is not a concern. These experimental results validate the functionality of the proposed system proving its attractiveness for EV charging applications, data centers, telecomm rectifiers, etc.

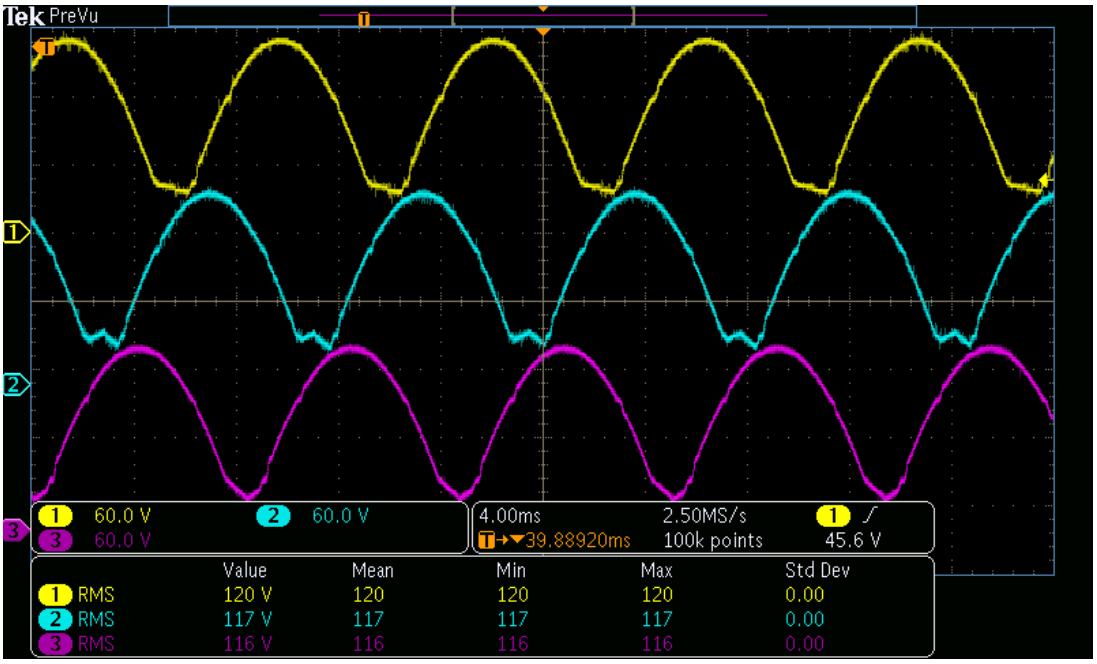

Figure 3-17: Experimental Results. (Ch.1): Pulsating voltages V_{pa}; (Ch.2) Pulsating voltages V_{pb}; (Ch. 3) Pulsating voltages V_{pc}. These voltages are across the film capacitors in the AC-AC converters.

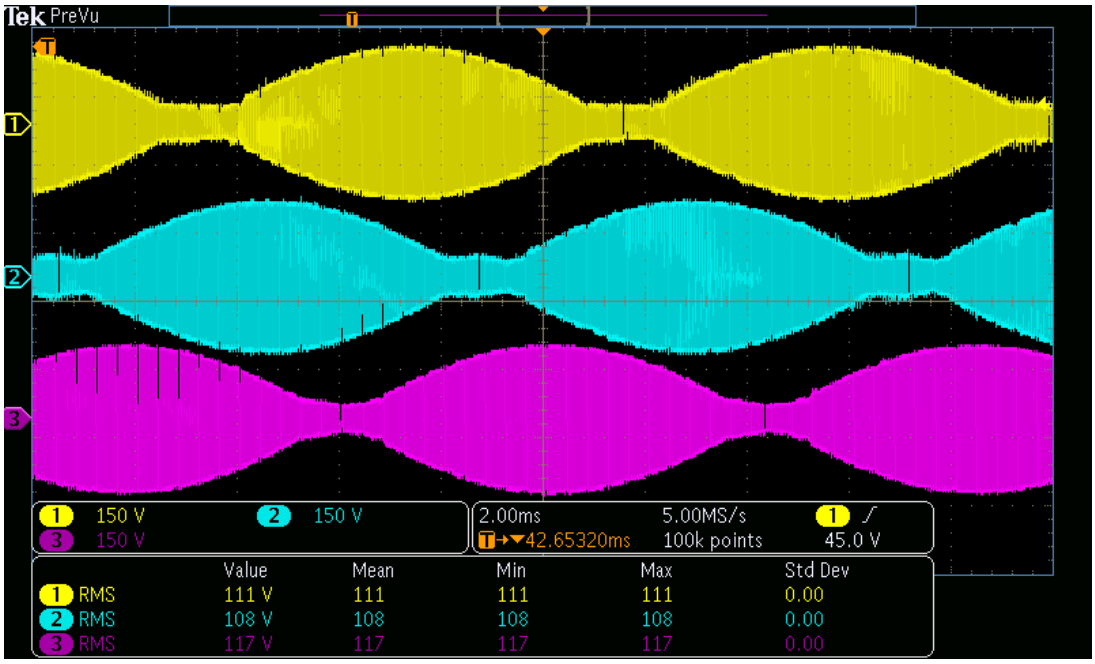

Figure 3-18: Experimental results. (Ch.1): Voltage across transformer primary winding V_{primA}; (Ch.2): Voltage across transformer primary winding V_{primB}; (Ch.3): Voltage across transformer primary winding V_{primC}. This is the three-phase HF AC link created by the AC-AC converters.

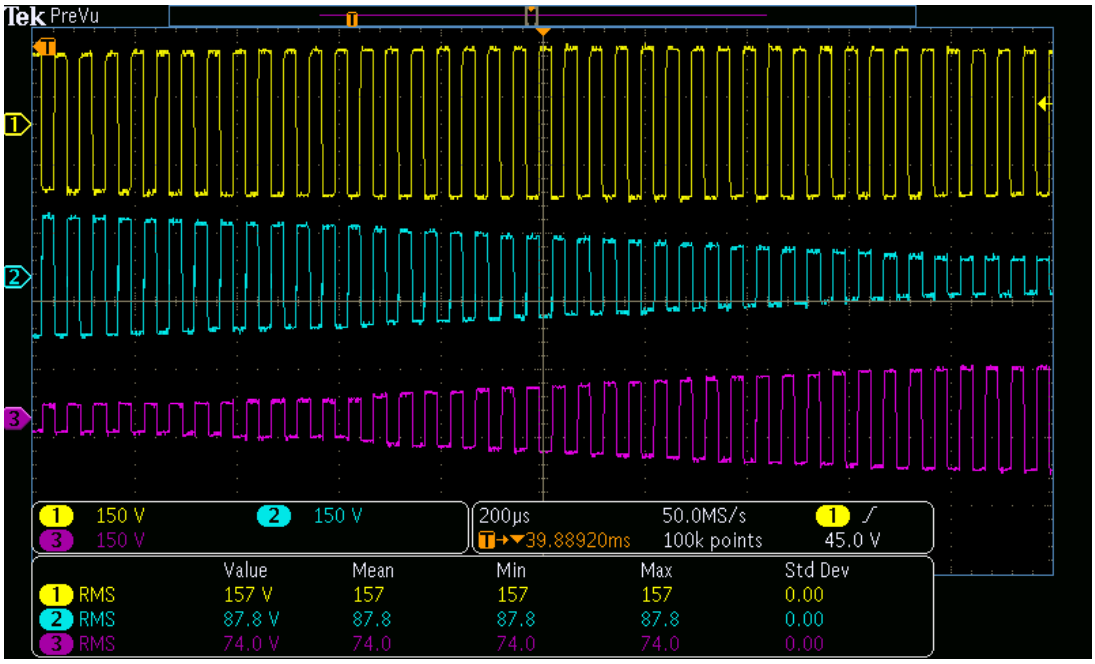

Figure 3-19: Experimental results. Zoom out of three-phase HF AC link in Figure 3-15. The HF nature of the voltages is evident.

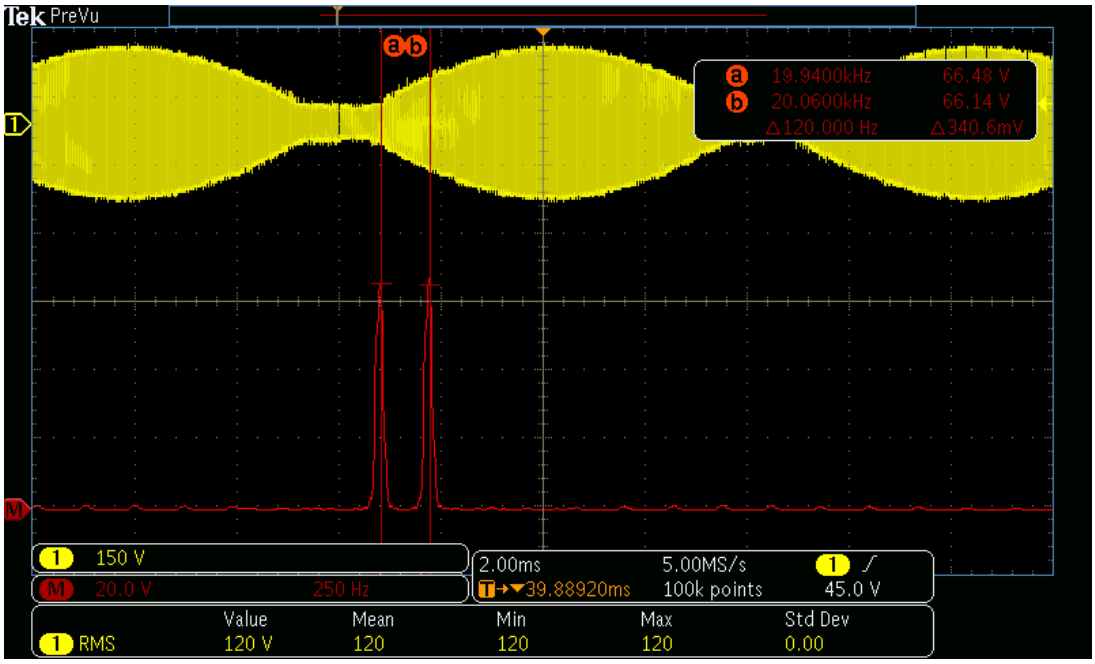

Figure 3-20: Experimental results. (Ch.1): Voltage across transformer primary winding V_{primA}; (Ch. Math): Frequency spectrum of transformer voltage V_{primA}. The fundamental components appear at 20 kHz ± 60 Hz. Other frequency components appear at $3f_{sqr} \pm f_s$, $5f_{sqr} \pm f_s$, etc.

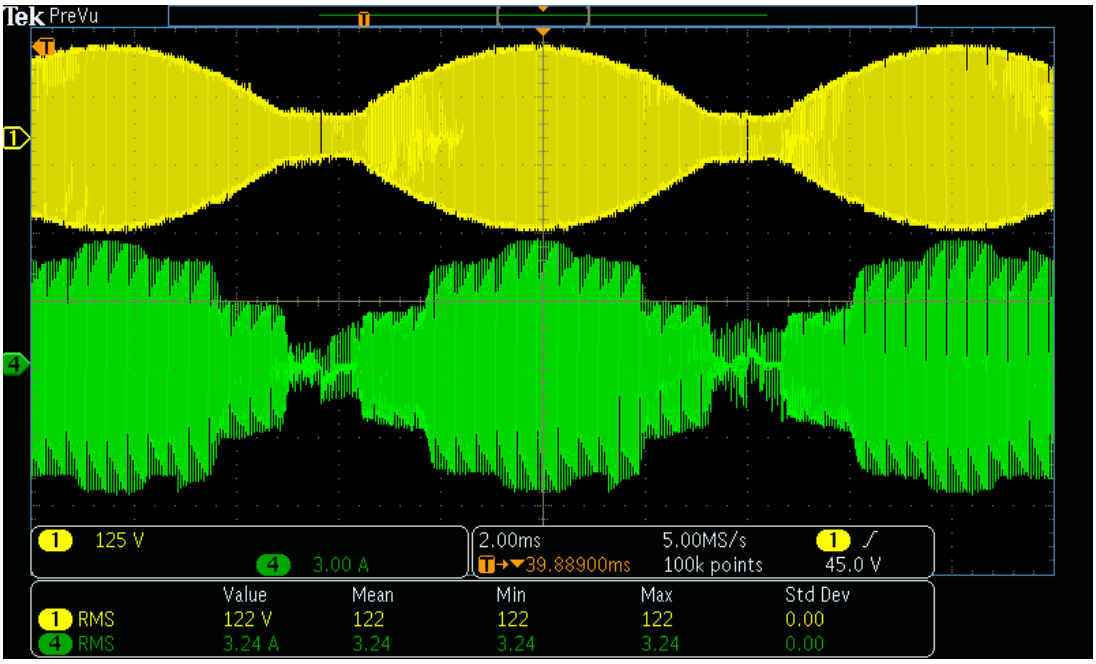

Figure 3-21: Experimental results. (Ch.1): Voltage across transformer primary winding V_{primA}; (Ch.3): Current through primary winding. HF operation is evident.

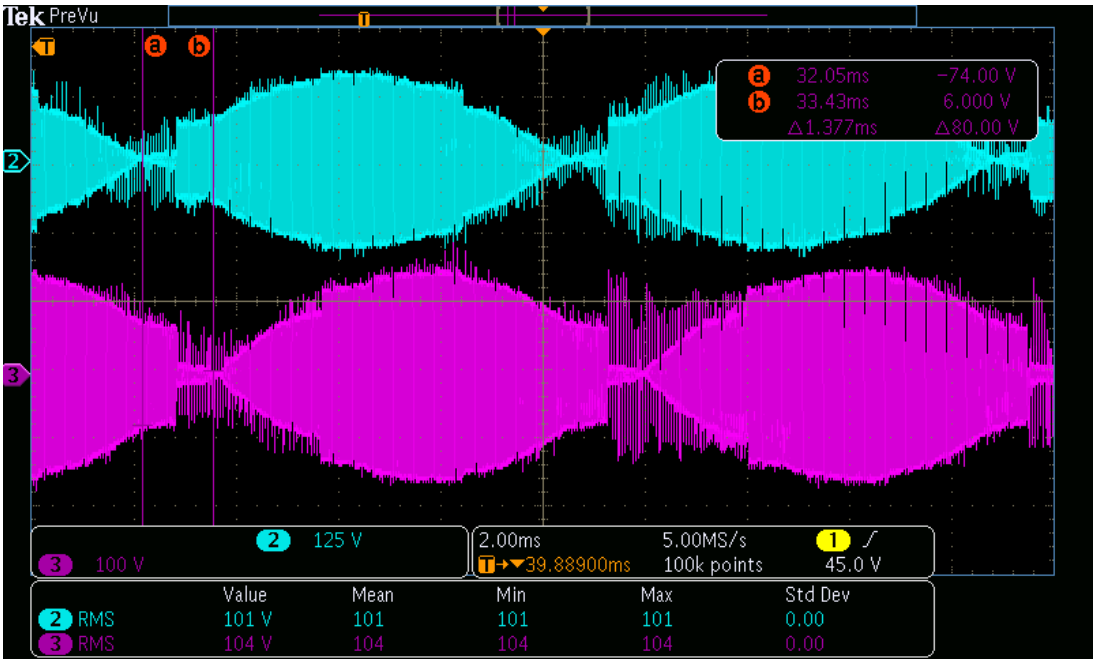

Figure 3-22: Experimental results. (Ch.2): Secondary side line-to-line voltage V_{abs}; (Ch.3): Secondary side line-to-line voltage V_{abt}. The voltages are displaced by 30° for 12-pulse operation.

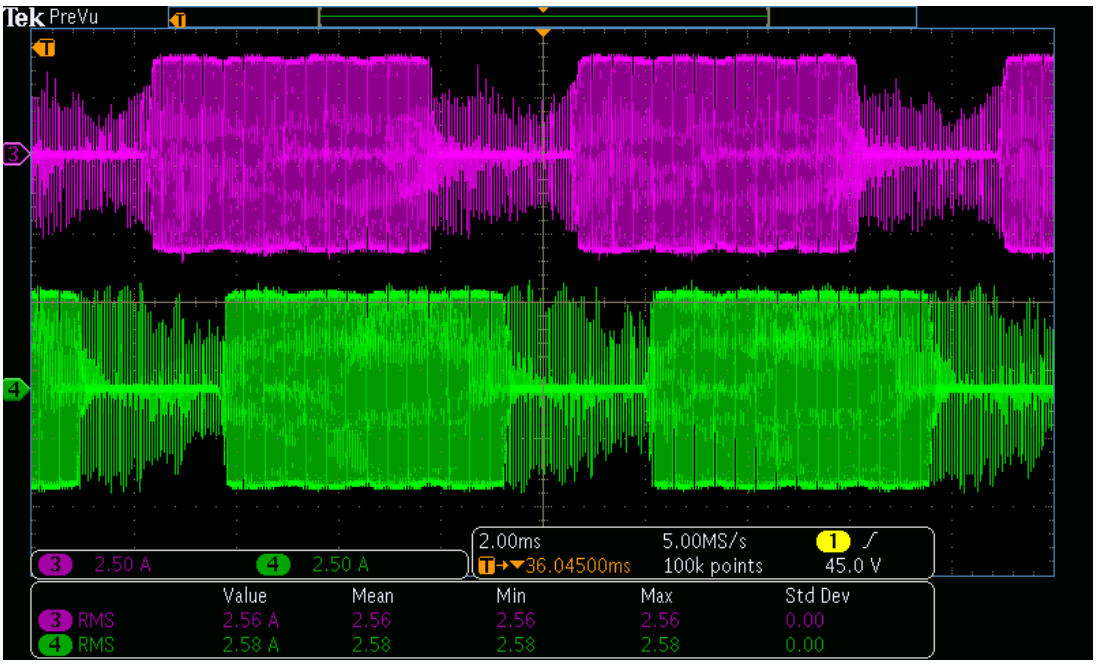

Figure 3-23: Experimental results. (Ch.3): Six-pulse diode rectifier input current I_{d1a}; (Ch.4): Six-pulse diode rectifier input current I_{d2a}. These currents are also displaced by 30°.

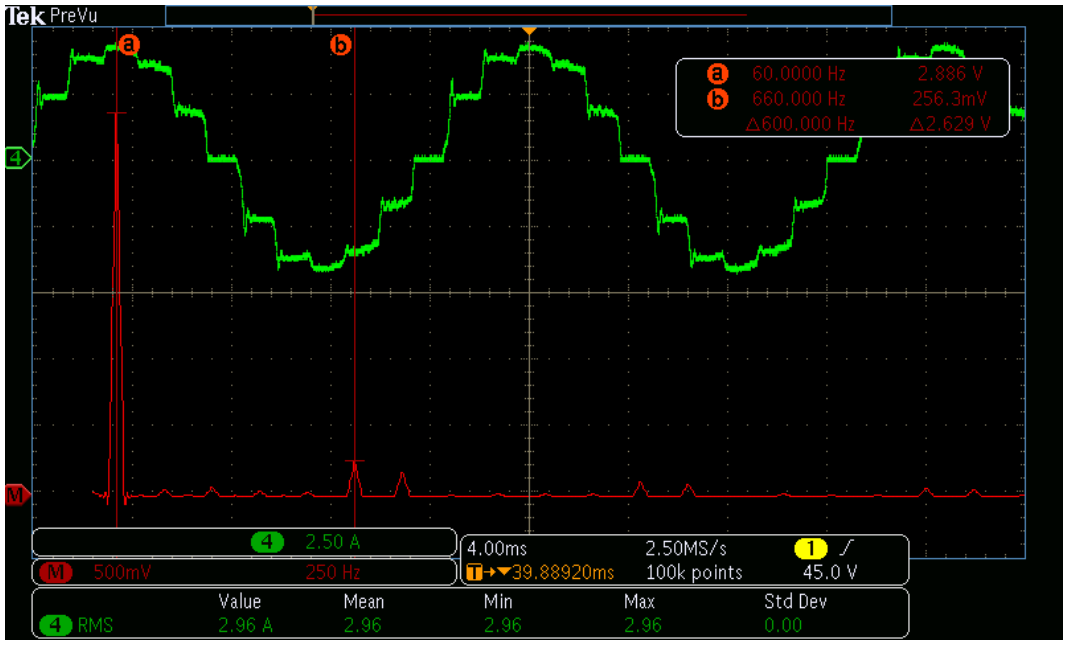

Figure 3-24: Experimental results. (Ch.4): Utility line input current I_a. The 12-pulse nature of the current is evident; (Ch. Math): Frequency spectrum of the line input current I_a. The fundamental component appears at 60 Hz and the dominant harmonic appears at 660 Hz as expected. Lower order harmonics such as the 5^{th} and 7^{th} are eliminated.

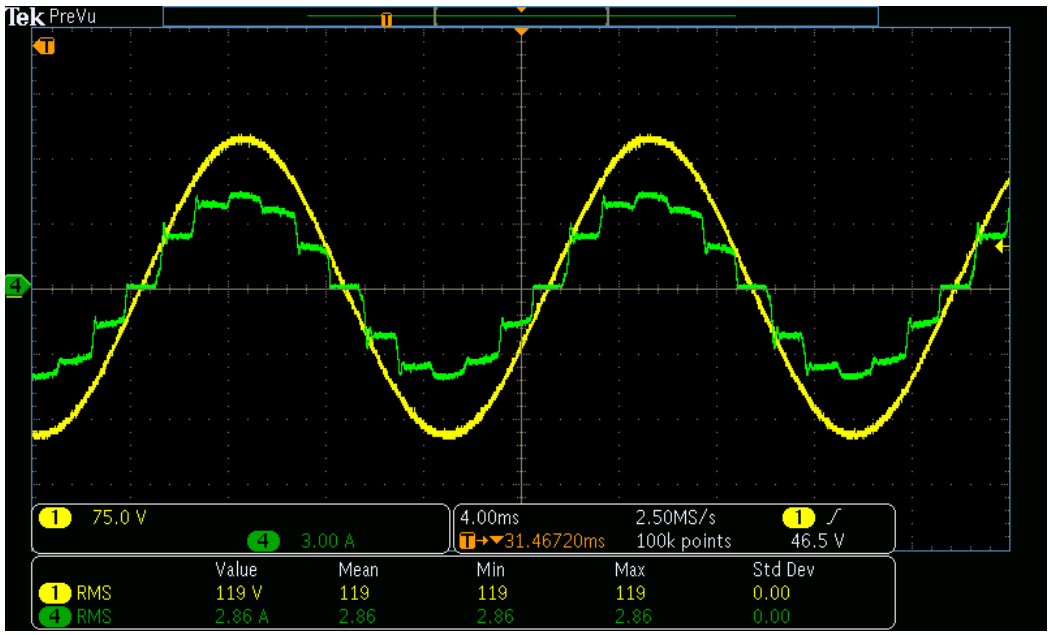

Figure 3-25: Experimental results. (Ch.1): Utility line-to-neutral input voltage V_{an}; (Ch.4): utility line input current I_a. High power factor operation is observed. Also, the effect of the switching frequency on V_{an} is minimal.

3.3 Different Embodiments of the Proposed Multi-Pulse System

One of the attractive features of the proposed 12-pulse system is its versatility. The proposed system has the ability to be adapted for multiple embodiments. Each embodiment has the AC-AC converter as the fundamental building block. Such embodiments include the following: 1) higher-pulse operation, 2) open-delta configuration of AC-AC converters, and 3) medium voltage (MV) series connected AC-AC converters.

3.3.1 Higher-Pulse Operation

The secondary side of the proposed system in Figure 3-1 can be configured for higher pulse operation (i.e. 18-pulse, 24-pulse, etc.). Figure 3-26 shows an 18-pulse embodiment of the proposed system. The advantage of this 18-pulse configuration is that the utility input current is almost sinusoidal in nature because the 5^{th}, 7^{th}, 11^{th}, 13^{th}, etc. harmonics are eliminated from the input current. This elimination of harmonics reduces the input filter size. Another advantage is that the output DC voltage has better quality which reduces the output filter size. The AC-AC converters and its modulation/control scheme remain the same compared to the 12-pulse configuration. The main difference lies in the transformer design. The transformer core structure is the same as the one shown in Figure 3-3 but required three additional secondary wye-connected windings to create 18-pulse operation. Thus a total of 15 secondary windings are required (five per phase). Also an additional six-pulse diode rectifier is required. Furthermore, the turns-ratio of the zig-zag connected windings are set such that there is a ±20° degree phase difference with respect to the primary windings.

To obtain the desired phase difference for 18-pulse operation, the turns-ratio of the zig-zag connected windings must be set as in (3.27). The zig-zag turns-ratio is found by solving (3.28) and (3.29). This ratio yields line-to-line voltages, on the secondary side, with the appropriate phase-shift and with magnitude equal to the primary side line-to-line voltages (neglecting conduction losses). Figure 3-27 shows a phasor diagram of the primary and secondary windings for the 18-pulse embodiment. The secondary side of the diagram shows to zig-zag connections and one wye-connection. One of the zig-zag connections creates line-to-line voltages that are displaced by -20° with respect to the primary side line-to-line voltages. Similarly, the second zig-zag connection creates line-to-line voltages that are displaced by +20° with respect to the primary side line-to-line voltages. The zig-zag winding connections are the same as in Figure 2-8 but with the different turns-ratio. The wye-connected secondary windings are in phase with the primary side line-to-line voltages. To achieve the same line-to-line voltages, the secondary wye-connection must have a 1:1 turn-ratio.

$$N_{P1} : N_{S1} : N_{S2} : N_{S3} : N_{S4} = 1 : 0.7422 : 0.395 : 0.7422 : 0.395 \tag{3.27}$$

$$V_{as} = N_{s1} V_{an} - N_{s2} V_{cn} = N_{s1} \angle 0° - N_{s2} \angle +120° = 1 \angle -20° \tag{3.28}$$

$$V_{at} = N_{s3} V_{an} - N_{s4} V_{bn} = N_{s3} \angle 0° - N_{s4} \angle -120° = 1 \angle +20° \tag{3.29}$$

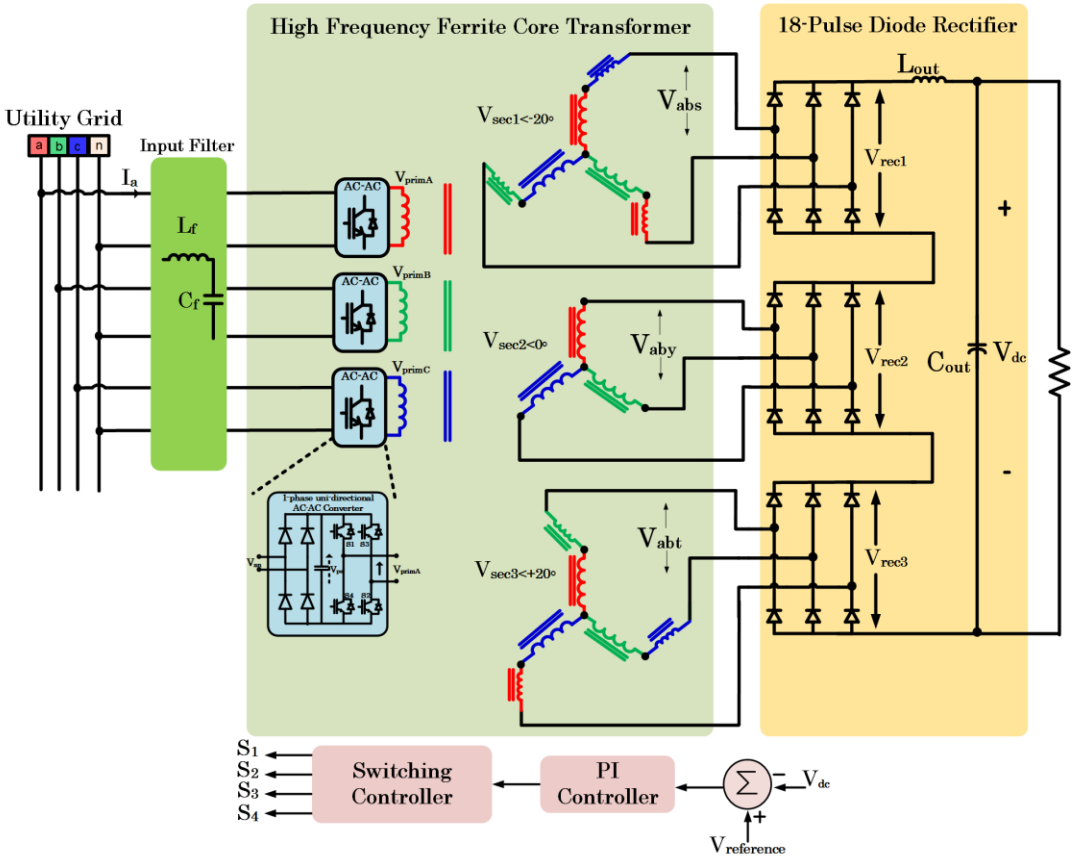

Figure 3-26: Proposed 18-pulse embodiment. High quality input current and DC output voltage.

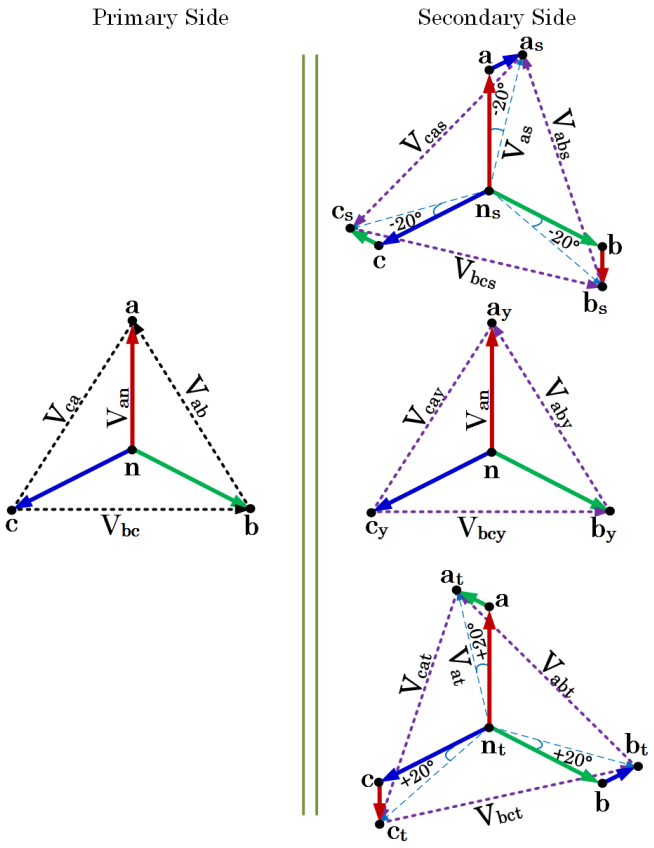

Figure 3-27: Phasor diagram of HF transformer for 18-pulse embodiment.

3.3.1.1 Design Example and Simulation Results

A 480$V_{l\text{-}l}$, 50kW, 500V_{dc} design example is simulated in PSIM for this 18-pulse embodiment. The output DC component produced by the 18-pulse rectifier is given by (3.30), where k_t is a factor included in turns-ratio and must be set to 0.25 for 500V_{dc} operation. For a 50 kW load, the output current I_d is equivalent to 100 A.

$$V_{dc} = k_t \frac{9}{\pi}\sqrt{2} \cdot V_{LL} = 500\ \text{V}. \tag{3.30}$$

Table 3-7 lists the voltage and current expressions for the 18-pulse HF transformer windings. The VA rating of the 18-pulse HF transformer is calculated to be

$1.07P_o$. Therefore, in terms of VA rating the 18-pulse HF transformer is equivalent to the 12-pulse HF transformer.

Table 3-7: HF 18-pulse transformer VA rating

Primary Side Winding	Voltage expression (rms)	$\frac{V_{LL}}{\sqrt{3}} = 0.577V_{LL} = 0.143V_{dc}$
	Current expression (rms)	$2.36 \cdot I_d$
Secondary Side Windings with turns-ratio *Ns1*	Voltage expression (rms)	$0.742 \cdot \frac{V_{LL}}{\sqrt{3}} = 0.428V_{LL} = 0.106 \cdot V_{dc}$
	Current expression (rms)	$\sqrt{\frac{2}{3}} \cdot I_d = 0.816I_d$
Secondary Side Windings with turns-ratio *Ns2*	Voltage expression (rms)	$0.395 \cdot \frac{V_{LL}}{\sqrt{3}} = 0.228V_{LL} = 0.056 \cdot V_{dc}$
	Current expression (rms)	$\sqrt{\frac{2}{3}} \cdot I_d = 0.816I_d$
Secondary Wye-Connected Windings	Voltage expression (rms)	$\frac{V_{LL}}{\sqrt{3}} = 0.577V_{LL} = 0.143V_{dc}$
	Current expression (rms)	$\sqrt{\frac{2}{3}} \cdot I_d = 0.816I_d$
VA rating calculation		
$VA_{tot} = 3\frac{V_{LL}}{\sqrt{3}} \cdot 2.36I_d + 2\sqrt{2}(0.742 + 0.395)V_{LL}I_d + \sqrt{2}V_{LL}I_d = 8.68V_{LL}I_d = 2.14V_{dc}I_d$		
$VA_{eq} = \frac{1}{2}VA_{tot} = 1.07V_{dc}I_d = 1.07P_o$		

The relevant simulation waveforms are presented. Figure 3-28 shows the secondary side line-to-line voltages which feed the 18-pulse rectifier. As shown in the figure, the voltage V_{abs} lags the voltage V_{aby} by 20 degrees. Similarly, V_{abt} leads the V_{aby}

by 20 degrees. These phase shifts between the voltages enable 18-pulse operation. The HF nature of the voltage is also appreciated from the figure. Since the modulation scheme remains the same compared to the proposed 12-pulse topology, the frequency spectrum of these voltages is equivalent to that shown in Figure 3-6. Thus, the transformer operates at HF enabling size reduction.

The operation of the 18-pulse embodiment is confirmed by the utility input currents shown in Figure 3-29(a). The 18-pulse behavior and balanced operation of the input currents is evident. In the simulation, a small input filter L_f with 20μH is used. The simulated THD of the input currents is 8%. The frequency spectrum of I_a is given in Figure 3-29(b). The spectrum shows the fundamental component and the 17^{th} and 19^{th} harmonics. This harmonic content is in accordance with equation (1.5).

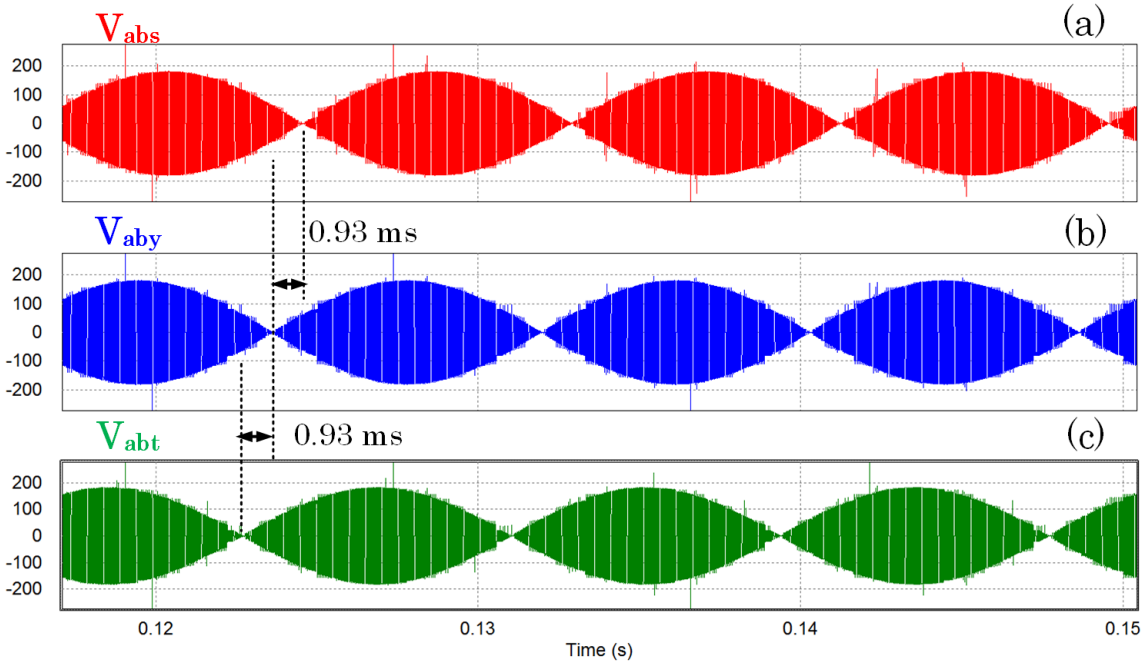

Figure 3-28: Secondary side line-to-line voltages feeding the 18-pulse diode rectifier.

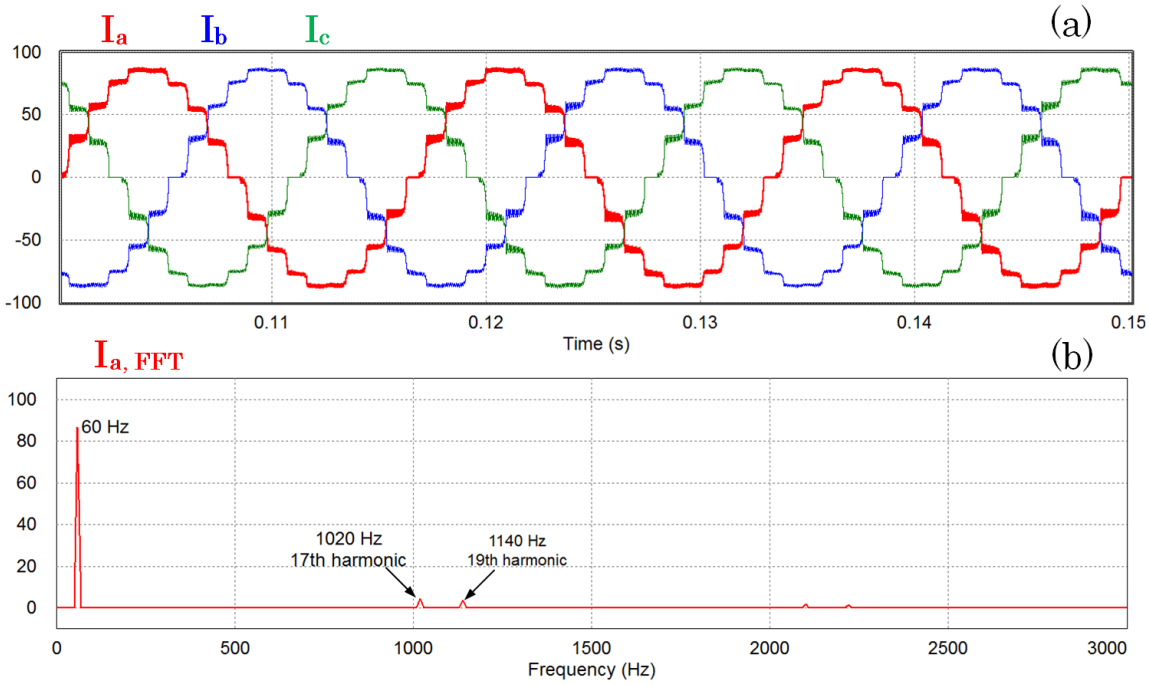

Figure 3-29: (a) Utility line input currents (61.5 A_{rms}) showing 18-pulse behavior, simulated THD is 8%; (b) Frequency spectrum of line input current I_a.

3.3.2 Open-Delta Configuration of AC-AC Converters

In the proposed system of Figure 3-1, 12 diodes and 12 active switching devices are needed to implement the AC-AC converters. It is possible to reduce the number of semiconductor devices by an open-delta embodiment of the AC-AC converters as shown in Figure 3-30. In this open-delta embodiment only two AC-AC converters are required reducing the number of semiconductor devices to 16 instead of 24. The fundamental difference lies in the transformer design. Only two vectors, V_{ab} and V_{bc}, are magnetically available to generate a net 30° phase difference between the secondary side line-to-line voltages. Figure 3-30 details the winding connections on the secondary side which create two sets of three-phase voltages with a net 30° phase difference. These voltages are then

fed to a 12-pulse rectifier for DC conversion. Another difference is the voltage rating of the semiconductor devices in the AC-AC converters. Since the input to the AC-AC converters are the line-to-line voltages, the peak voltage across the diodes and IGBTs is 1.414 p.u.

In the open-delta embodiment, the HF transformer must be built using two single-phase transformers. Each single-phase transformer has one primary winding and six secondary windings. The phasor diagram representation of the open-delta connection is shown in Figure 3-31. The primary side phasor representation shows that only the phasors V_{ab} and V_{bc} are available. With these two phasors, the secondary side is configured to generate two sets of three-phase line-to-line voltages equal in magnitude to the primary side line-to-line voltages. One set has a -15° phase difference with respect to the primary voltages, while the second has a +15° phase difference. This creates a 30° phase difference between the two sets of three-phase voltages as required for 12-pulse operation. By virtue of this phase shift, the utility input current has 12-pulse performance (i.e. 5^{th}, 7^{th}, 17^{th}, 19^{th} harmonics are eliminated). In order to achieve the ±15° phase shift and desired voltage magnitude the turns-ratio of the windings in each single-phase transformer must be set as in (3.31). This ratio is found by solving (3.32).

$$N_{P1} : N_{S1} : N_{S2} : N_{S3} : N_{S4} : N_{S5} : N_{S6} = 1 : 0.15 : 0.15 : 0.97 : 0.97 : 0.15 : 0.15 \tag{3.31}$$

$$N_{s3}V_{ab} + N_{s1}V_{bc} + N_{s1}V_{ab} + N_{s1}V_{bc} = N_{s3}\angle 30° + N_{s1}\left(2\angle -90° + 1\angle 30°\right) = 1\angle -15° \tag{3.32}$$

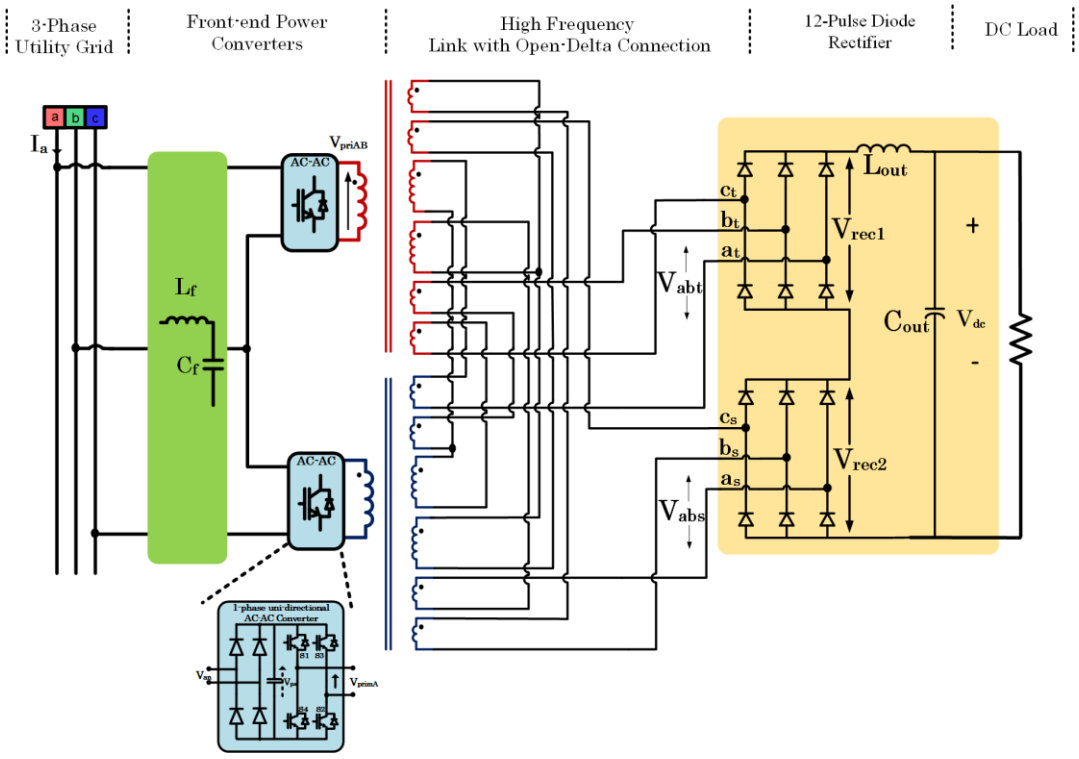

Figure 3-30: Proposed system –Open-delta embodiment enables a reduction in the number of semiconductors needed; only two AC-AC converters required.

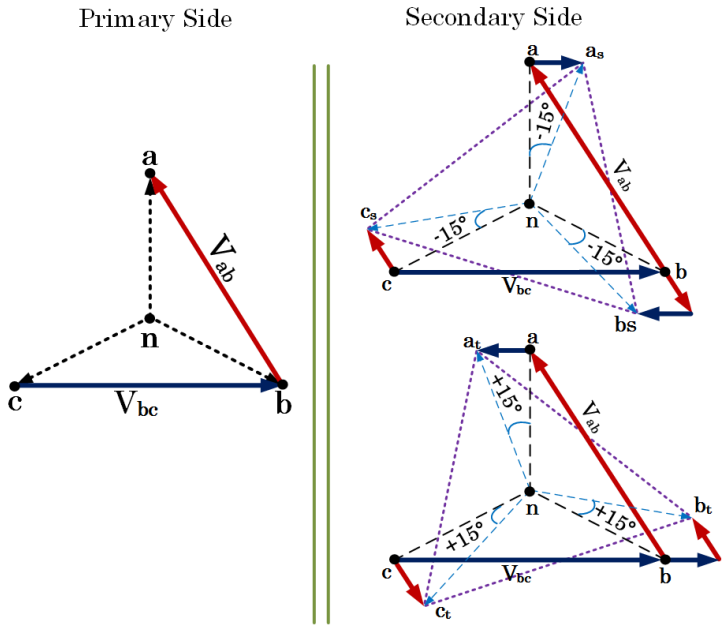

Figure 3-31: Open-delta phasor diagram

3.3.2.1 Design Example and Simulation Results

For comparison purposes the same $480V_{l\text{-}l}$, 50 kW design example is simulated in PSIM. The output DC component produced by the open-delta 12-pulse diode rectifier is given by (3.33), where k_t is set to 0.39 for $500V_{dc}$ operation. The output current I_d is 100A.

$$V_{dc} = k_t \frac{6}{\pi} \sqrt{2} \cdot V_{LL} = 500\ \text{V}. \tag{3.33}$$

Table 3-8 lists the voltage and current expressions of the open-delta HF transformer windings. For the primary winding current expression a power factor of 0.985 is assumed since 12-pulse behavior is expected. The open-delta transformer VA rating is calculated to be $1.35P_o$. The operation of the open-delta 12-pulse system is confirmed by simulation. Figure 3-32 shows the primary side voltage V_{priAB} and the secondary side line-to-line voltages V_{abs} and V_{abt}. As expected, the voltage V_{abs} lags V_{primAB} by 15° while V_{abt} leads V_{primAB} by 15°. Thus V_{abs} and V_{abt} have a net 30° phase shift (i.e. 1.38 ms) with respect to each other ensuring 12-pulse operation. The HF content of the voltages is evident. Indeed, the frequency content of these voltages is the same as in Figure 3-6.

The utility line input currents are shown in Figure 3-33(a). The currents are balanced and have 12-pulse performance as expected. The frequency spectrum of utility line current I_a is given in Figure 3-33(b), currents I_b and I_c have an identical frequency content. It is shown that the fundamental current component appears at the line frequency and the dominant harmonics appear at 660 Hz and 780 Hz (i.e. 11^{th} and 13^{th}

harmonic respectively). The simulated current THD is 14%. These results validate the operation of the open-delta 12 pulse topology with HF isolation.

Table 3-8: Open-delta HF transformer VA rating

Primary Side Winding	Voltage expression (rms)	$V_{LL} = 0.37V_{dc}$
	Current expression (rms)	$\frac{2\sqrt{6}}{\pi \cdot pf} \cdot I_d = 1.58I_d$
Secondary Side Windings with turns-ratio *Ns1*	Voltage expression (rms)	$0.15 \cdot V_{LL} = 0.055 \cdot V_{dc}$
	Current expression (rms)	$\sqrt{\frac{2}{3}} \cdot I_d = 0.816I_d$
Secondary Side Windings with turns-ratio *Ns3*	Voltage expression (rms)	$0.966 \cdot V_{LL} = 0.357 \cdot V_{dc}$
	Current expression (rms)	$\sqrt{\frac{2}{3}} \cdot I_d = 0.816I_d$
VA rating calculation		
$VA_{tot} = V_{LL} \cdot 1.58I_d + 2 \cdot 0.966V_{LL} \cdot 0.816I_d + 4 \cdot 0.15V_{LL} \cdot 0.816I_d = 3.646V_{LL}I_d$		
$VA_{eq} = \frac{1}{2}VA_{tot} = 1.35V_{dc}I_d = 1.35P_o$		

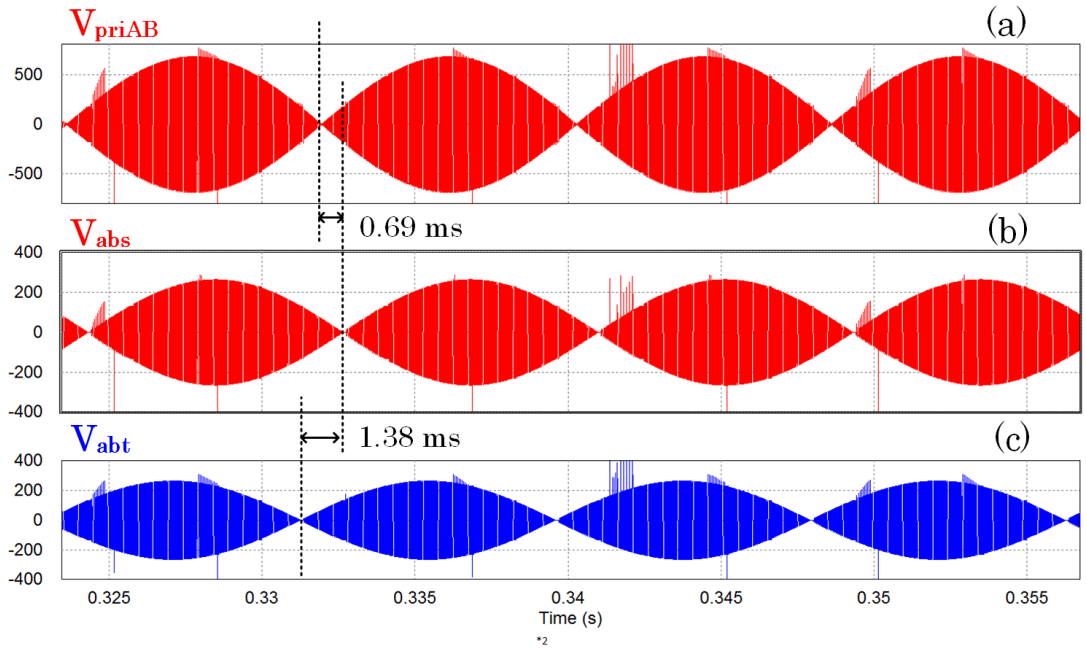

Figure 3-32: (a) Voltage across the transformer primary winding ; (b) Secondary side line-to-line voltage V_{abs}, (c) Secondary side line-to-line voltage V_{abt}. Note the 30° phase shift between V_{abs} and V_{abt} for 12-pulse operation.

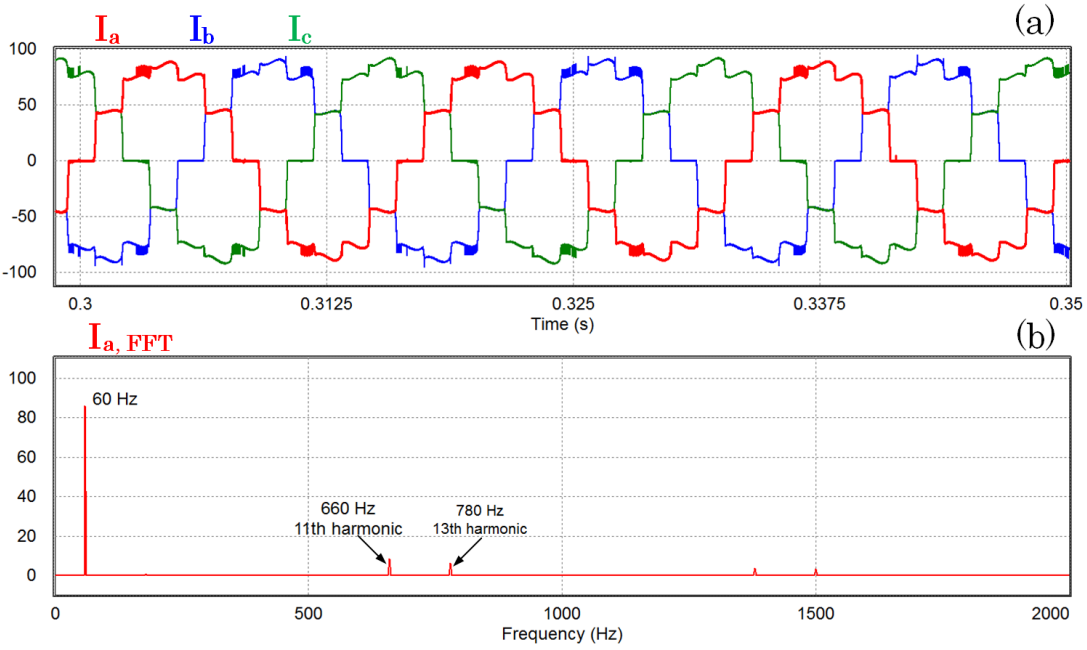

Figure 3-33: (a) Utility line input currents with 12-pulse performance; (b) FFT of line input current I_a. Harmonic content confirms 12-pulse operation.

3.3.3 Medium Voltage Series-Connected AC-AC Converters

A typical application for multi-pulse systems is adjustable speed drives (ASDs). In medium voltage (MV) ASD applications, the input AC voltage may range from 2.3 kV to 6.9 kV. In MV voltage application, the blocking voltage of the semiconductor devices is a concern. To address this concern, the proposed system can be configured as shown in Figure 3-34. The AC-AC converter is built using cells connected in series to relax the blocking voltage requirement of the semiconductor devices. Each cell is composed of the same unidirectional AC-AC converter studied in sub-section 3.2.1. The optimum number of cells connected in series depends on the utility MV amplitude and on cost analysis. In Figure 3-34, the secondary side of the HF transformer is configured for multi-pulse operation (i.e. 18-pulse, 24-pulse). The secondary side windings are interfaced to a three-phase motor through multiple power cells which consist of six-pulse rectifiers and multi-level NPC inverters.

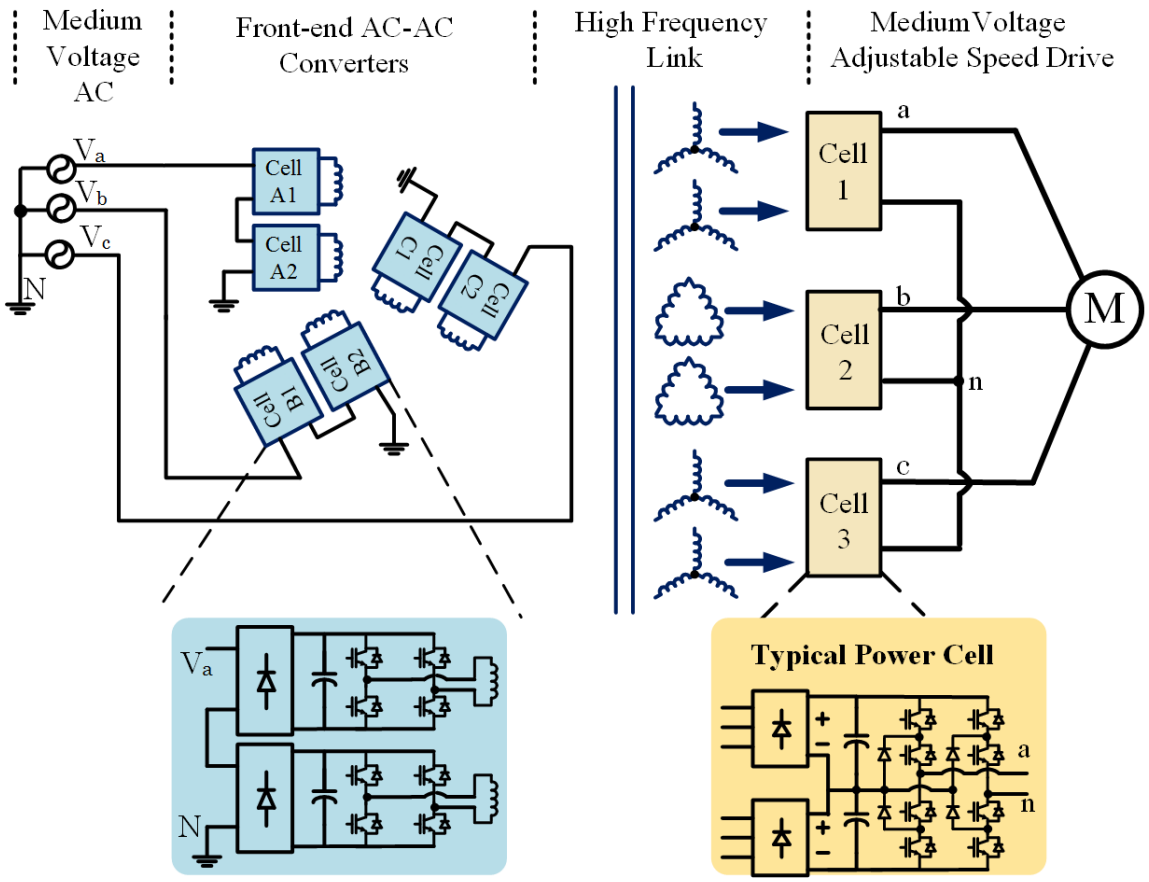

Figure 3-34: Proposed system – medium voltage embodiment with series connected AC-AC converters for ASD applications.

3.4 Comparison of the Proposed System and Its Embodiments

The proposed HF 12-pulse system in Figure 3-1 is compared with the 18-pulse embodiment along with the open delta 12-pulse embodiment. The criteria used for comparison includes the transformer VA rating, input current THD, number of semiconductor devices and their peak voltage rating. Table 3-9 lists the results of the comparison.

In terms of transformer VA rating, the transformer of Figure 3-1 is equivalent to the 18-pulse HF transformer. However, the winding losses in the 18-pulse transformer

are expected to be higher due to the additional wye-connected windings. In comparison, the open-delta transformer VA rating is $1.35P_o$. This is a 26% increase in VA rating compared to the 12-pulse and 18-pulse HF transformer. The main benefit of the open-delta embodiment is that it employs the least number of semiconductor devices among the compared systems. However, the reduction in the number of AC-AC converter modules comes at the cost of an increase in transformer VA rating. If an application is limited by cost, then this open-delta embodiment is an attractive alternative because the number of modules, gate drivers, and sensors is reduced. If however the design is limited by size and weight, the proposed system in Figure 3-1 is more suitable.

In terms of input current performance, the 12-pulse systems have a theoretical THD of 16%. Meanwhile, the 18-pulse HF rectifier has an input current that is nearly sinusoidal at unity power factor. The input current has a THD of 9%, this is a 4% improvement compared to the 12-pulse scheme. Therefore, this system facilitates compliance with current harmonic standards. The improved input current performance however comes at the cost of increased transformer complexity and an additional six-pulse rectifier on the secondary side.

Table 3-9: Comparison of embodiments

Parameter	12-Pulse HF Rectifier (Figure 3-1)	Open-Delta 12-Pulse HF Rectifier (Figure 3-30)	18-Pulse HF Rectifier (Figure 3-26)
Transformer Configuration	five-limb, three-phase transformer	Two single-phase transformers	five-limb, three-phase transformer
No. of windings	3-primary, 12-secondary	1-primary, 6-secondary (per transformer)	3-primary, 15-secondary
Transformer VA rating	$1.07P_o$	$1.35P_o$	$1.07P_o$
No. of semiconductor devices	24-diodes 12-active semiconductor devices	20-diodes 8-active semiconductor devices	30-diodes 12-active semiconductor devices
Peak voltage rating for semiconductor devices.	$0.816V_{LL}$	V_{LL}	$0.816V_{LL}$
Input Current THD	16%	16%	9%

3.5 Conclusion

A three-phase AC-DC rectifier with HF (20 kHz) transformer isolation is presented in this section. Extended analysis and simulation results demonstrate the feasibility of the proposed approach. The proposed scheme is versatile and different embodiments of the system were presented. A 50 kW design example is shown to have 94% efficiency. Operating the transformer at 20 kHz yields a power density of 15,380 W/L for a 10 kW three-phase transformer. The main advantages include high power density, high input current quality over a wide output voltage range and a simple pulse width modulation and control scheme.

4. THREE-PHASE AC-DC PWM RECTIFIER WITH HIGH FREQUENCY ISOLATION AND IMPROVED INPUT CURRENT QUALITY

This section presents a three-phase AC-DC PWM rectifier system with high frequency isolation (HF) and improved input current quality. The rectifier system interfaces the utility grid to AC-AC converters which produce a HF output. The outputs of the AC-AC converters are connected to the primary windings of a three-phase HF transformer. The secondary windings of the HF transformer are delta-connected and interfaced to a three-phase diode rectifier to produce an output DC voltage. The AC-AC converters are modulated using selective harmonic elimination techniques; it is shown that with a programmed PWM switching function lower order harmonics (i.e. 5^{th}, 7^{th}, 11^{th}, 13^{th}, etc.) are eliminated from the utility input current. The main advantages of this topology include the absence of electrolytic capacitors, good input current quality, and high power density. Detailed analysis and simulation results are presented to demonstrate the operation of the proposed rectifier system.

4.1 Introduction

The most simple three-phase AC-DC rectifier is shown in Figure 1-7. Each diode conducts for 120° of the line frequency cycle. The switching functions of the diodes are determined by the utility line-to-line voltages as shown in Figure 4-1. The switching function S_1 corresponds to diode pair D_1-D_4, S_2 corresponds to diode pair D_3-D_6, and S_3 corresponds to diode pair D_5-D_2. When S_1 is positive D_1 conducts and when S_1 is negative D_4 conducts. The same logic applies to the other two legs of the rectifier. The

output voltage of the rectifier is given by (4.1), where V_{an}, V_{bn}, V_{cn} are the utility line-to-neutral voltages.

$$V_{out} = S_1 V_{an} + S_2 V_{bn} + S_3 V_{cn} \tag{4.1}$$

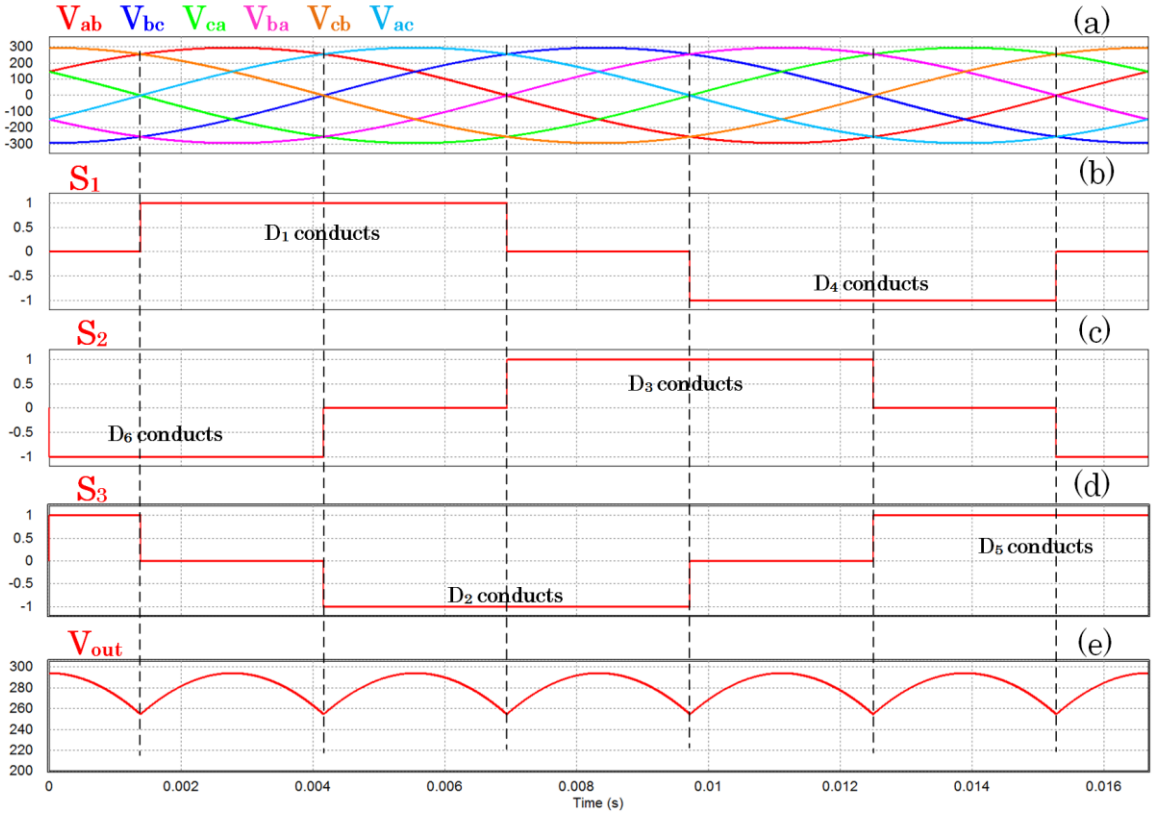

Figure 4-1: Operation of three-phase rectifier in Figure 1-7. (a) Line-to-line input voltages (b) Switching function for leg 1 of the rectifier; (c) Switching function for leg 2 of the rectifier; (d) Switching function for leg 3 of the rectifier; (e) Output voltage of three-phase rectifier given by (4.1).

In ideal conditions, the utility input currents I_a, I_b, and I_c are identical in shape to S_1, S_2, and S_3 respectively. This is an important realization because it means that the utility input current can be shaped solely by switching functions and has led to the development of the six-switch PWM rectifier [38]. Essentially, the diodes are replaced

by active semiconductor devices and S_1, S_2, and S_3 are generated using carrier based sine PWM. By using sine PWM, S_1, S_2 and S_3 are free from low order harmonics and since they are identical in shape to the input currents a very low THD is achieved.

The proposed PWM rectifier, shown in Figure 4-2, uses the same switching function concept to improve the utility input current. It is shown that modulating the AC-AC converters with a programmed PWM switching function results in the elimination of pre-selected utility input current harmonics. The main advantages of this system are as follows:

1.) Improved utility input current due to the use of selective harmonic elimination modulation techniques.
2.) The approach uses HF magnetics which improves power density and provides isolation between input and output.
3.) The AC-AC converter modules do not use electrolytic capacitors.
4.) Output voltage control with high voltage gain due to over-modulation index amplitude $m_a = 1.15$.
5.) Reduced number of transformer windings and output diode rectifiers compared to the previous proposed systems in Sections 2 and 3.

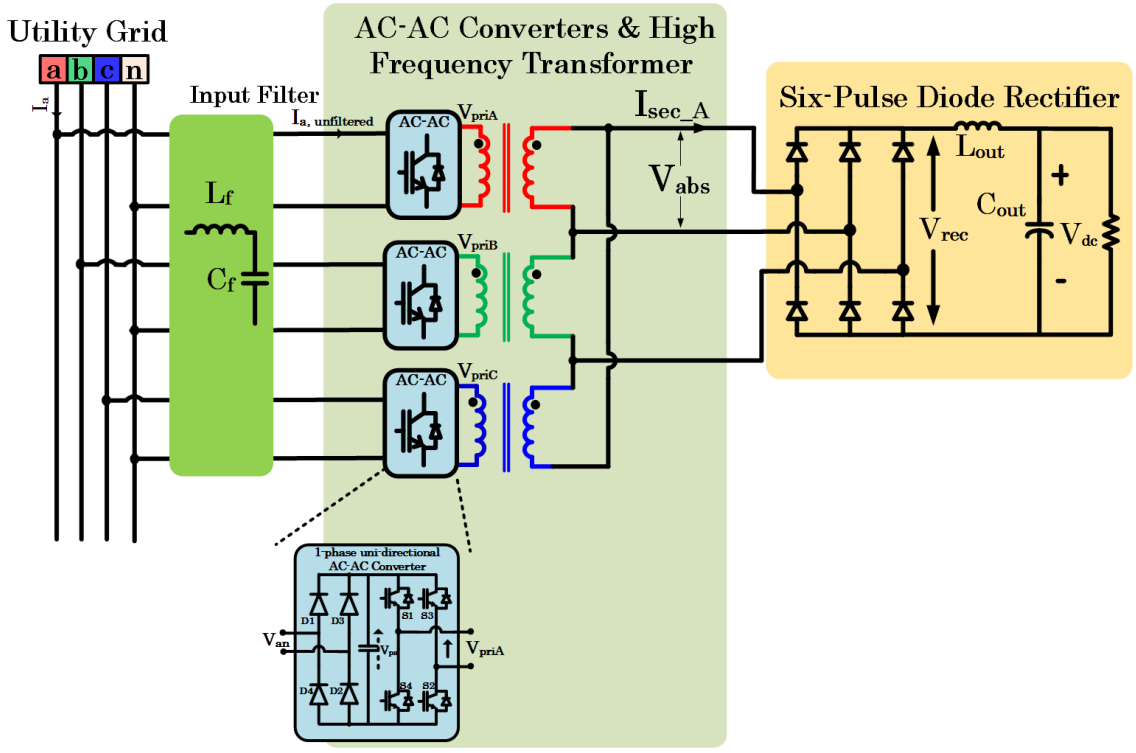

Figure 4-2: Proposed PWM rectifier with selective harmonic elimination modulation scheme.

4.2 Proposed Three-Phase PWM Rectifier with HF Isolation

The analysis and operation of the proposed three-phase PWM Rectifier is detailed in this sub-section.

4.2.1 Unidirectional AC-AC Converter with Programmed PWM

In terms of semiconductor device hardware, the primary side of the proposed PWM rectifier system is essentially the same as the primary side of the proposed three-phase AC-DC 12-pulse rectifier in sub-section 3.2. It uses the same number of AC-AC modules and therefore the same number of semiconductor devices. Similarly, the outputs of the AC-AC converters are connected to the primary windings of a three-phase HF transformer. The fundamental difference in this PWM rectifier is that the AC-AC

converters are modulated using selective harmonic elimination techniques. The benefits of programmed PWM techniques over conventional carrier-based sine PWM schemes are outlined in [59],[60], [61].

With the programmed PWM technique low order harmonics are eliminated from the switching functions of the AC-AC converters. With the line-to-neutral waveform optimization method, one can eliminate selected non-tripplen odd harmonics up to the preferred first significant harmonic [59]. All tripplen harmonics are eliminated by virtue of the 120° phase shift in three-phase operation. As explained in [59], the Fourier coefficients of the switching functions are given by (4.1) and (4.2). The Fourier coefficients b_n are equal to zero due to quarter wave symmetry of the switching functions. In (4.1), N refers to the number of switching angles (α_1 to α_N) that must be obtained for a desired switching function. The solutions for these angles are obtained by solving equations that are nonlinear and transcendental in nature [59]. Equation (4.3) shows the nonlinear equations that must be solved to eliminate low order harmonics such as the 5th, 7th, etc. In (4.3), N-1 harmonics are set to zero and a value is assigned to Fourier coefficient a_1 for output voltage control. The solutions to (4.3) must satisfy the criteria given by (4.5)

$$a_n = \frac{4}{n\pi}\left[-1-2\sum_{k=1}^{N}(-1)^k \cos(n\alpha_k)\right] \tag{4.1}$$

$$b_n = 0 \tag{4.2}$$

$$\begin{bmatrix} 2\cos\alpha_1 & -2\cos\alpha_2 & 2(-1)^{N+1}\cos\alpha_N \\ 2\cos 5\alpha_1 & -2\cos 5\alpha_2 & 2(-1)^{N+1}\cos 5\alpha_N \\ \vdots & \vdots & \vdots \\ 2\cos(x_1)\alpha_1 & -2\cos(x_1)\alpha_2 & 2(-1)^{N+1}\cos(x_1)\alpha_N \end{bmatrix} = \begin{bmatrix} \frac{\pi \cdot a_1}{4}+1 \\ 1 \\ . \\ 1 \end{bmatrix} \tag{4.3}$$

$$x_1 = 3N-2 \text{ for odd } N \tag{4.4}$$

$$\alpha_1 < \alpha_2 < \alpha_3 < ...\alpha_N < \frac{\pi}{2} \tag{4.5}$$

Therefore, the first step to obtain the switching functions for the AC-AC converters is to select the harmonics to be eliminated from the switching function (which will also be eliminated from the utility input current). After this determination is done, a set of equations similar to (4.3) must be solved. Once the equations are solved, a bipolar switching function is constructed from the switching angles. This switching function will be associated with phase "a". Bipolar switching functions associated with phase "b" and "c" are obtained by shifting the obtained angles by -120° and +120° respectively. Figure 4-3 shows an example of bipolar switching functions (S_a, S_b, S_c) used eliminate the 5th, 7th, and 11th harmonic and to set the Fourier coefficient a_1 to 1. The FFT of these switching functions are shown in Figure 4-4 confirming the elimination of the selected harmonics and the amplitude of the fundamental component. These functions however do not represent the desired utility input current waveforms. A set of unipolar switching functions (S_1, S_2, S_3) are obtained as follows:

$$S_1 = S_a - S_b \tag{4.6}$$

$$S_2 = S_b - S_c \tag{4.7}$$

$$S_3 = S_c - S_a \tag{4.8}$$

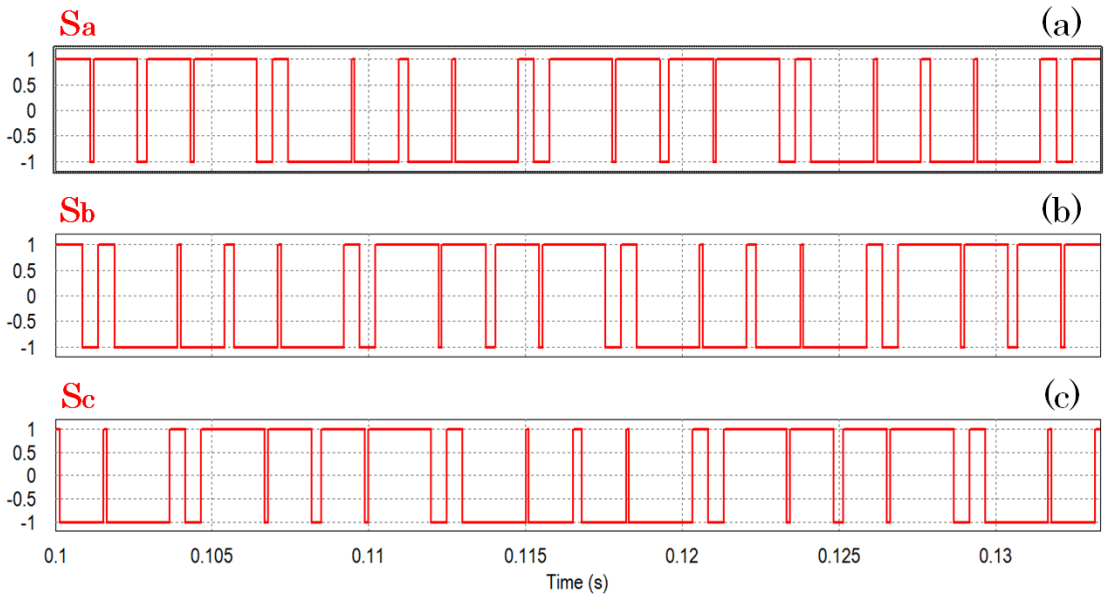

Figure 4-3: Bipolar functions built using the solved switching angles.

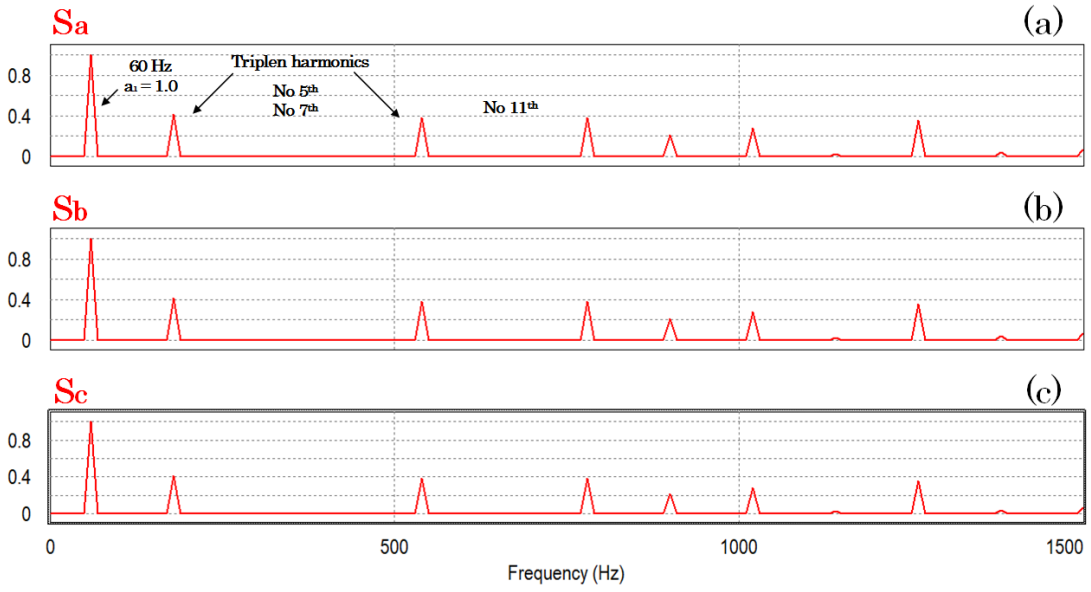

Figure 4-4: Frequency spectrum of the bipolar switching functions. The selected harmonics are eliminated (i.e. 5th, 7th, and 11th). Triplen harmonics are present.

These unipolar switching functions are shown in Figure 4-5 and have the desired harmonic content and correspond to the desired utility input current waveforms. Thus, the addition of these three switching functions adds to zero for balanced operation. The frequency spectrum of these functions is shown in Figure 4-6. It is shown that the tripplen harmonics are eliminated due to the subtraction of the bipolar switching functions. To obtain a HF link, these unipolar switching functions are multiplied with a HF square wave. The product of these functions (seen in (4.9-4.11)) yields the gating functions for the semiconductor devices in the AC-AC converters. For example, when F_a is positive the switching devices S_1 and S_2 conduct, and when F_a is negative the switching devices S_3 and S_4 conduct. Similarly, F_b and F_c determine the conduction state of the AC-AC converters connected to phase "b" and "c" respectively. When determining the gating signals, the switching function introduced by the single-phase diode rectifier in the AC-AC converters must also be taken into account.

$$F_a = S_1 \cdot S_{sw} \tag{4.9}$$

$$F_b = S_2 \cdot S_{sw} \tag{4.10}$$

$$F_c = S_3 \cdot S_{sw} \tag{4.11}$$

By switching in this manner, a three-phase HF AC link is produced at the output of the AC-AC converters with simultaneous elimination of the selected input current harmonics.

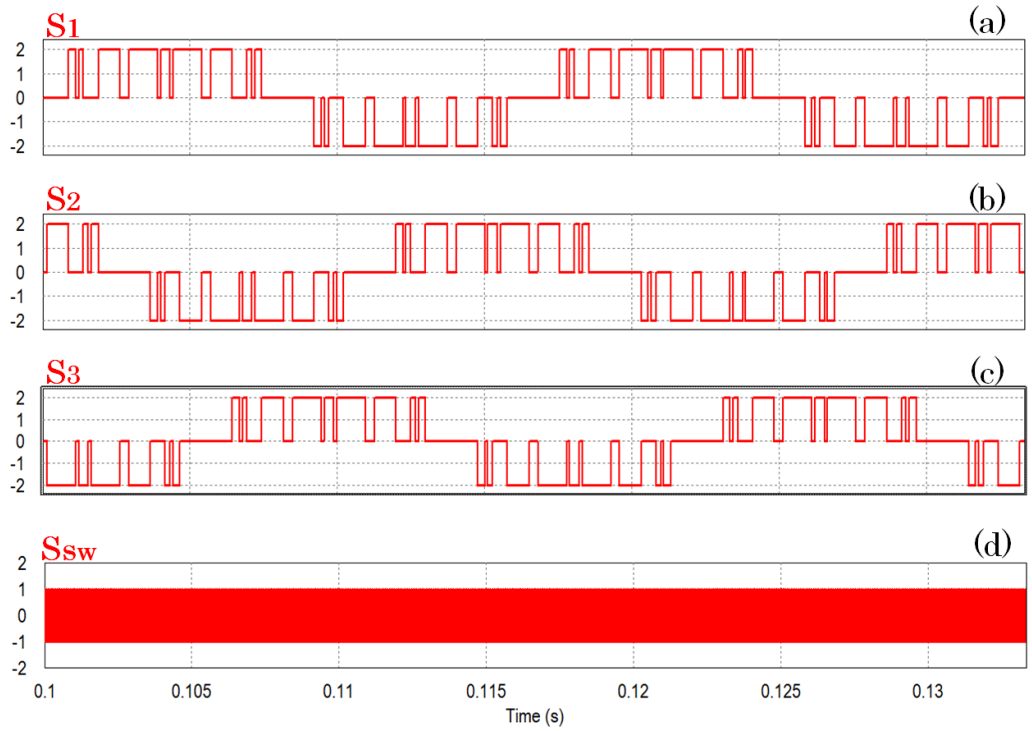

Figure 4-5: (a)-(c) Unipolar switching functions obtained by subtraction of the bipolar switching functions; (d) HF square wave switching function.

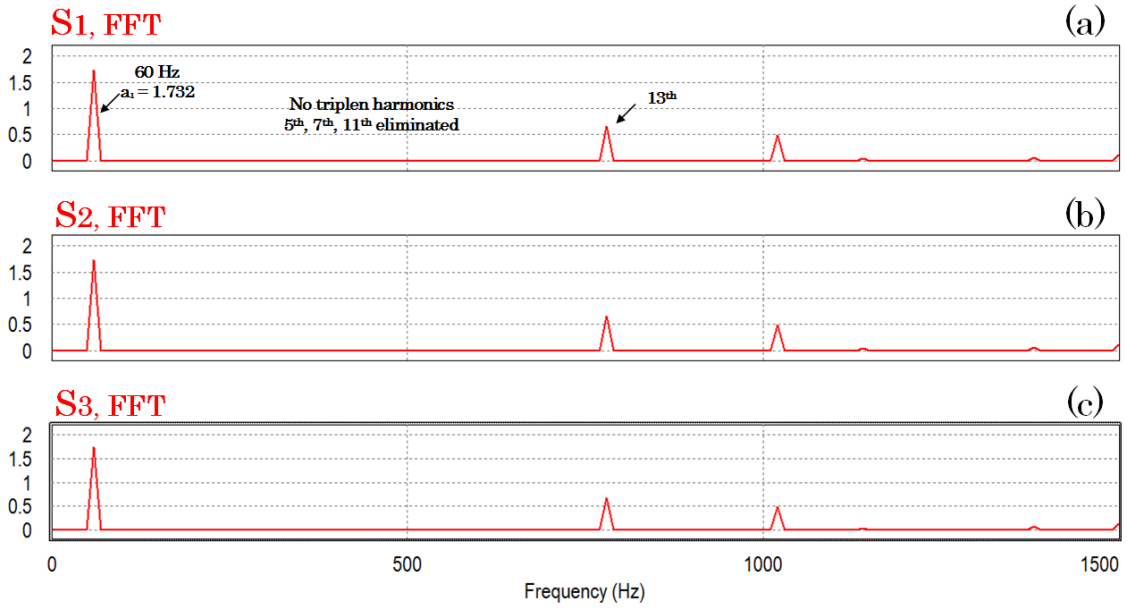

Figure 4-6: FFT of unipolar switching functions. The selected harmonics are eliminated. Tripplen harmonics cancel due to 120° phase shift.

4.2.2 Three-Phase HF Transformer

The output of the AC-AC converters is interfaced to a three-phase HF transformer. The HF transformer is envisioned to be a five-limb transformer similar in structure to the transformer shown in Figure 3-3, albeit different core dimensions. The transformer has three primary windings and three secondary windings with a 1:1 turns-ratio. Therefore, the transformer is simple in terms of number of windings and connections. The secondary windings are delta-connected to ensure that the voltages across the transformer windings add to zero. With the programmed PWM modulation scheme described previously, there are instances in which the gating signal F_a is equal to zero. At this instant the switching devices in the AC-AC converter remain open and the voltage V_{priA} is determined by the voltages V_{priB} and V_{primC}.

4.2.3 Six-Pulse Diode Rectifier and Output Voltage Analysis

The transformer secondary side is interfaced to a six-pulse diode rectifier as shown in Figure 4-1. The diodes are passive and conduct based on the amplitude of the secondary side line-to-line voltages. The diodes must be able to switch at the operating frequency (i.e. 20 kHz) and must have a fast recovery time to avoid switching losses.

The rectified output voltage of the six-pulse diode rectifier is given by (4.12). This is the same expression as the output voltage produced by the simple diode rectifier in (4.1), except that S_1, S_2, S_3 refer now to the unipolar programmed PWM switching functions. This result is expected because the utility input currents of the PWM rectifiers have the same harmonic content as S_1, S_2, and S_3.

$$V_{rec} = S_1 V_{an} + S_2 V_{bn} + S_3 V_{cn} \tag{4.12}$$

When the utility line-to-neutral voltages are multiplied with the unipolar switching functions a DC component is produced. The DC component of the voltage V_{rec} is given by (4.13). Note that this relation considers a 1:1 ratio of the transformer windings. It is observed that the output DC component is proportional to the fundamental component a_1. Therefore, the output voltage is controlled by changing the amplitude of this component, albeit different switching angles must be obtained for a different a_1.

$$V_{rec,avg} = \frac{3}{4} \cdot a_1 \cdot \sqrt{2} \cdot V_{LL} \tag{4.13}$$

4.2.4 Passive Components

The passive components in the proposed PWM rectifier include the input and output filter. Numerous studies have been done on input filter design [62], [63], [64]. Due to simplicity a second order L_fC_f input filter design is commonly used in three-phase AC-DC rectifier systems [62]. The per-phase equivalent circuit is shown in Figure 4-7(a). The converter is modelled as a source of current harmonics. The first significant harmonic of the current source I_h will be the next odd non-tripplen harmonic not eliminated by the switching function. For example, if the 5th, 7th, and 11th harmonics were eliminated by the switching functions, the first significant harmonic of I_h would be the 13th harmonic. The circuit in Figure 4-7(a) can be represented as in Figure 4-7(b) for the harmonic frequencies. Ideally, the fundamental component I_{1h} should be zero. In practice, the fundamental component I_{1h} should be much smaller compared to I_h.

From Figure 4-7(b) it is evident that the amplitude of the fundamental component I_{1h} can be obtained by current division as given by (4.14). It is also evident that the

magnitude of Z_L must be much higher than the magnitude of Z_c at the desired first significant harmonic frequency. In this manner, the first significant harmonic will flow through the filter capacitor and a small amount will be present in the utility input current. Another important relation for the input filter design is the cut-off frequency as given by (4.15). The cut-off frequency must be less than the frequency of the first significant harmonic.

$$\frac{I_{1h}}{I_h} = \frac{Z_C}{Z_c + Z_L} = \frac{1}{1 + s^2 L_f C_f} \tag{4.14}$$

$$f_{cut-off} = \frac{1}{2\pi\sqrt{L_f C_f}} \tag{4.15}$$

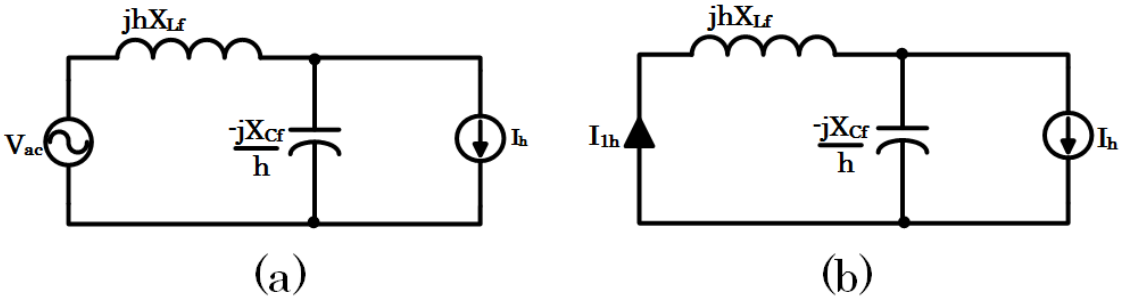

Figure 4-7: (a) Per-phase equivalent circuit with second order input filter. (b) Representation of per-phase equivalent circuit for current harmonics.

4.2.5 Design Example (Elimination of 5th, 7th, 11th, and 13th Harmonics)

To demonstrate the functionality of the proposed PWM rectifier a design example rated at 480 $V_{l\text{-}l}$, 500V_{dc}, 50 kW is considered. The harmonics eliminated from the input current are selected to be the 5th, 7th, 11th, and 13th. The amplitude of the

fundamental component a_1 is varied from 0.5 to 1.15 for output voltage control. Different angle solutions are obtained for each a_1 and are listed in Table 4-1. The calculated output DC component for each a_1 is also given in the table. For this particular example N=5 (i.e. four harmonics eliminated and an additional angle for voltage control). Therefore the number of equations set to zero is equivalent to:

$$N-1=4 \tag{4.14}$$

Similarly, x_1 is given by:

$$x_1=3N-2=13 \tag{4.15}$$

The equations solved for a_1=1.15 are given by (4.16). These equations are solved in MATLAB using the *fsolve* function. Using this function gives angle solutions in a fast manner. An initial guess of the angles must be given to the function in order to perform the calculations. The initial guess must satisfy relation (4.5).

$$\begin{bmatrix} 2\cos\alpha_1-2\cos\alpha_2+2\cos\alpha_3-2\cos\alpha_4+2\cos\alpha_5=1+\dfrac{1.15\pi}{4} \\ 2\cos 5\alpha_1-2\cos 5\alpha_2+2\cos 5\alpha_3-2\cos 5\alpha_4+2\cos 5\alpha_5=0 \\ 2\cos 7\alpha_1-2\cos 7\alpha_2+2\cos 7\alpha_3-2\cos 7\alpha_4+2\cos 7\alpha_5=0 \\ 2\cos 11\alpha_1-2\cos 11\alpha_2+2\cos 11\alpha_3-2\cos 11\alpha_4+2\cos 11\alpha_5=0 \\ 2\cos 13\alpha_1-2\cos 13\alpha_2+2\cos 13\alpha_3-2\cos 13\alpha_4+2\cos 13\alpha_5=0 \end{bmatrix} \tag{4.16}$$

Table 4-1: Switching angle solutions for varying modulation index.

a_1	Switching angles	$V_{rec,\,avg}$ (V)
1.15	α_1=7.89°, α_2=22.54°, α_3=25.64°, α_4=76.93°, α_5=77.91°	585
1.0	α_1=7.05°, α_2=24.39°, α_3=29.83°, α_4=69.83°, α_5=73.25°	509
0.9	α_1=6.40°, α_2=24.40°, α_3=31.28°, α_4=68.45°, α_5=73.56°	458
0.8	α_1=5.73°, α_2=24.15°, α_3=32.49°, α_4=67.33°, α_5=74.12°	407
0.7	α_1=5.05°, α_2=23.76°, α_3=33.57°, α_4=66.31°, α_5=74.77°	356
0.6	α_1=4.36°, α_2=23.29°, α_3=34.58°, α_4=65.35°, α_5=75.48°	305
0.5	α_1=3.65°, α_2=22.78°, α_3=35.54°, α_4=64.42°, α_5=76.21°	255

For a_1 = 1.15, the DC component of the rectified voltage is 585V. Thus, for 500V operation the turns-ratio of the transformer must be adjusted by a factor k_t given by:

$$k_t = \frac{500\ \text{V}}{585\ \text{V}} = 0.855 \tag{4.16}$$

The ratings of the semiconductor devices are listed in Table 4-2. The voltage ratings are normalized using the line-to-line voltage V_{LL} while the current ratings are normalized using the output current I_d. A power factor, *pf*, of 0.97 is assumed. For 50kW operation, the output current I_d is:

$$I_d = \frac{P_o}{V_{dc}} = 100\ \text{A}. \tag{4.17}$$

Table 4-2: Semiconductor device ratings for the proposed PWM rectifier.

Component	Parameter	Expression	P.U. Value	Design Value (50 kW)
AC-AC converter (single-phase rectifier diodes)	peak voltage	$\sqrt{\frac{2}{3}}\mathrm{V_{LL}}$	0.816	392 V
	peak current	$k_t I_d$	$1 \cdot k_t$	85 A
	rms current	$k_t \frac{a_1\sqrt{6}}{4\sqrt{2}\cdot pf} I_d$	$k_t \frac{a_1\sqrt{6}}{4\sqrt{2}\cdot pf} I_d$	43.6 A
AC-AC converter (full-bridge inverter IGBTs)	peak voltage	$\sqrt{2}\cdot k_t \cdot \mathrm{V_{LL}}$	$1.414k_t$	580 V
	peak current	$k_t I_d$	$1 \cdot k_t$	85 A
	rms current	$k_t \frac{a_1\sqrt{6}}{4\sqrt{2}\cdot pf} I_d$	$k_t \frac{a_1\sqrt{6}}{4\sqrt{2}\cdot pf} I_d$	43.6 A
6-Pulse Diode Rectifier	peak voltage	$\sqrt{2}\cdot k_t \cdot \mathrm{V_{LL}}$	$1.414k_t$	580 V
	peak current	I_d	1	100 A
	rms current	$I_d\sqrt{\frac{2}{\pi}\left(\frac{\pi}{12}+\frac{1}{4}\right)}$	0.57	57 A

The VA rating of the three-phase HF transformer is listed in Table 4-3. The voltage and current expressions are given for a_1=1.15. The expressions vary slightly for different modulation indices but the transformer VA rating is the same. From calculation, the transformer VA rating is $1.77P_o$. The turns-ratio of the transformer is assumed to be 1:1.

Table 4-3: HF ferrite core transformer VA rating for PWM rectifier.

HF Ferrite Core Transformer VA rating		
Primary Side Winding	Voltage expression (rms)	$0.9V_{LL} = 0.74V_{dc}$
	Current expression (rms)	$0.8 \cdot I_d$
Secondary Side Windings	Voltage expression (rms)	$0.9V_{LL} = 0.74V_{dc}$
	Current expression (rms)	$0.8I_d$
VA rating calculation		
$VA_{tot} = 3 \cdot (0.9V_{LL} \cdot 0.8I_d) \cdot 2 = 4.32V_{LL}I_d = 3.54V_{dc}I_d$ $VA_{eq} = \frac{1}{2}VA_{tot} = 1.77V_{dc}I_d = 1.77P_o$		

4.3 Simulation Results

The design example in sub-section 4.2.5 was simulated in PSIM. The design parameters are listed in Table 4-4. The obtained simulation results are in accordance with the analysis and calculations.

Table 4-4: Operating conditions for simulation in PSIM

Grid line-to-line voltage (rms)	480 V
Grid frequency	60 Hz
Output Power	50 kW
Output dc voltage	500 V_{dc}
Switching frequency (f_{sqr})	20 kHz
Fundamental component a_1	1.15
Transformer turns-ratio 1:k_t	1 : 0.85
Input filter inductor (L_f)	750 µH (0.06 p.u)
Input filter capacitor (C_f)	150 µF
Output Inductor (L_{out})	5 mH (0.41 p.u)
Output Capacitor (C_{out})	2.2 mF

Figure 4-8 shows the unipolar switching functions obtained by using the switching angles in Table 4-1 for a_1= 1.15. As expected, these unipolar switching functions add to zero. Figure 4-9 shows the corresponding frequency spectrum of the unipolar switching functions. The fundamental component amplitude is √3*1.15 due to line-to-line operation. Also the 5^{th}, 7^{th}, 11^{th}, and 13^{th} harmonic are eliminated from the switching function and the first dominant harmonic is the 17^{th} as expected.

These switching functions are multiplied with a HF (20 kHz) square wave to determine the gating signals for the AC-AC converter. The three-phase HF AC link across the transformer windings is shown in Figure 4-10. The HF nature of the AC link is evident. The voltages have two envelopes, one is the line-to-neutral voltage and the other is the line-to-line voltage associated with the other two windings as explained in sub-section 4.2.2. The FFT of voltage V_{priA} is given in Figure 4-11, the fundamental voltage components appear near 20 kHz which means that the transformer operates at HF resulting in core volume reduction. The output DC voltage is shown in Figure 4-12, as expected the output voltage is of high quality at $506V_{dc}$. This means that the turns-ratio of the transformer must be slightly adjusted to get $500V_{dc}$ but it is a trivial matter. Figure 4-13 portrays the current through diode D_1 in the AC-AC converter connected to phase "a". The simulated peak value is 85A and the simulated rms current is 44A as calculated in the design example.

The functionality of the proposed PWM rectifier is further confirmed by the unfiltered utility line currents as shown in Figure 4-14. This figure shows that the unfiltered currents have the same shape as the unipolar switching functions in Figure 4-

8. Therefore, it is expected for the unfiltered utility line currents to have an equivalent frequency spectrum as the unipolar switching functions. Indeed, the FFT of the unfiltered line currents in Figure 4-15 shows that the 5^{th}, 7^{th}, 11^{th}, and 13^{th} harmonics are eliminated. The first significant harmonics appear at 1020 Hz and 1140 Hz. The magnitudes of these harmonics are 21% and 30% from the fundamental respectively. Therefore, the role of the input filter is to reduce the amplitude of these harmonics in the utility line currents. Figure 4-16(a) shows the filtered utility line input current I_a along with the utility line-to-neutral voltage; high power factor operation is observed. The effectiveness of the filter is evident from Figure 4-16(b) which shows the FFT of I_a. After the filter, the magnitudes of the 17^{th} and 19^{th} harmonics are greatly reduced. The magnitudes of the 17^{th} and 19^{th} harmonic are reduced to 5% and 5.8% of the fundamental respectively. The simulated THD of I_a is 8.4%.

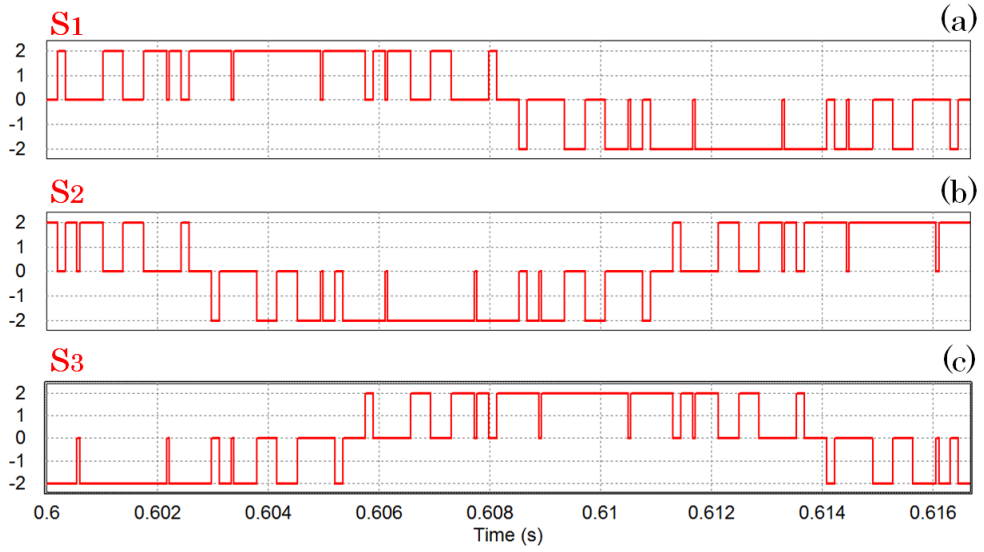

Figure 4-8: (a)-(c) Unipolar switching functions used to eliminate 5^{th}, 7^{th}, 11^{th}, and 13^{th} harmonic and to set a_1=1.15. Angles are α_1=7.89°, α_2=22.54°, α_3=25.64°, α_4=76.93°, α_5=77.91°.

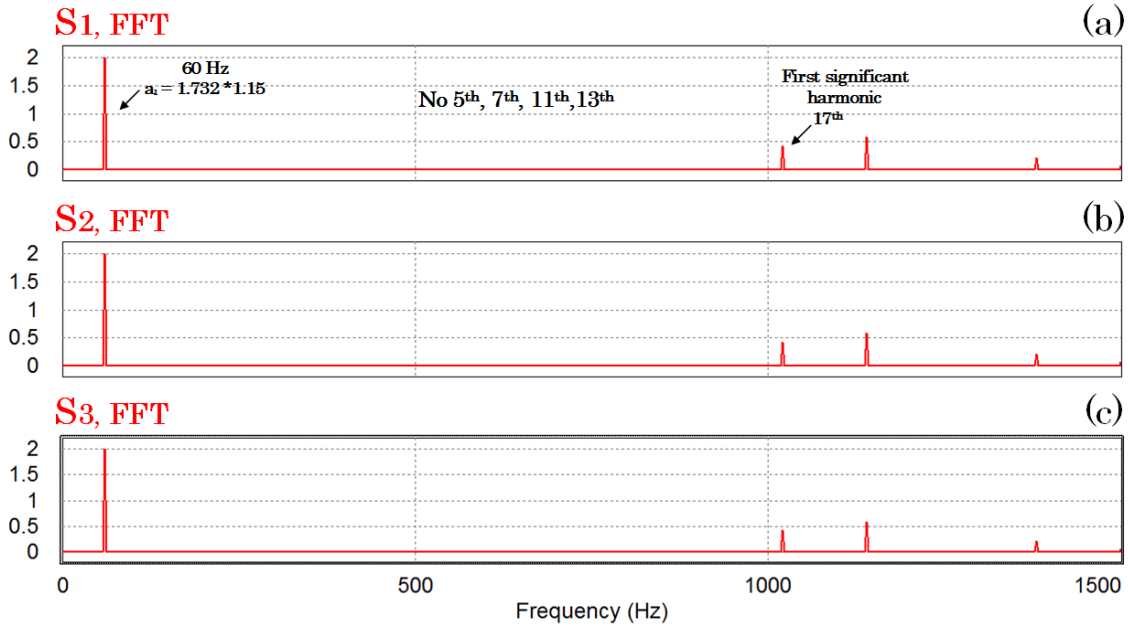

Figure 4-9: (a)-(c) FFT of unipolar switching functions confirm the desired performance. Harmonics 5^{th}, 7^{th}, 11^{th}, and 13^{th} are eliminated.

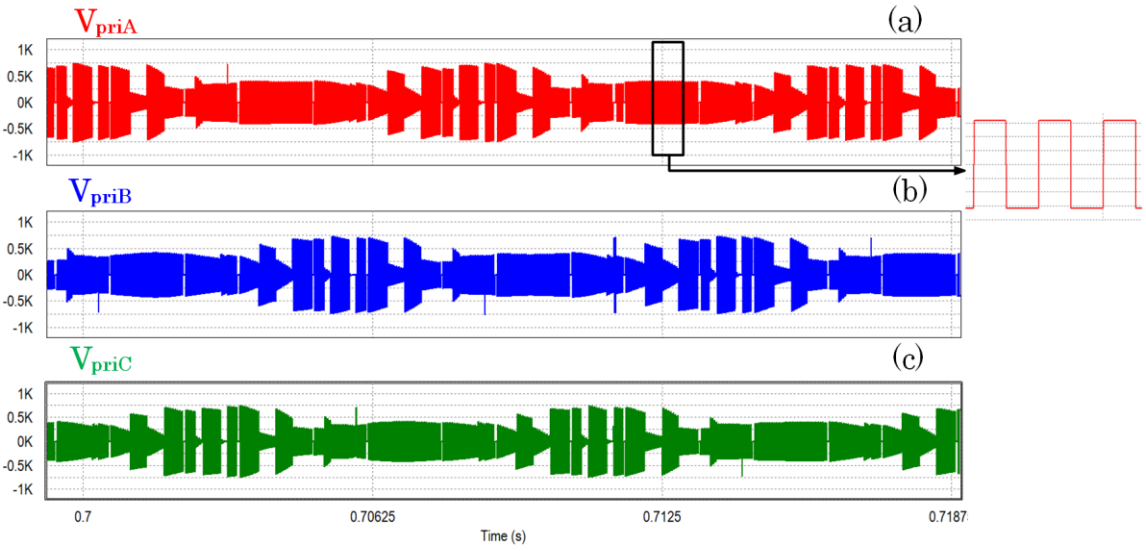

Figure 4-10: (a)-(c) High frequency three-phase AC-link; AC-AC converter output voltages.

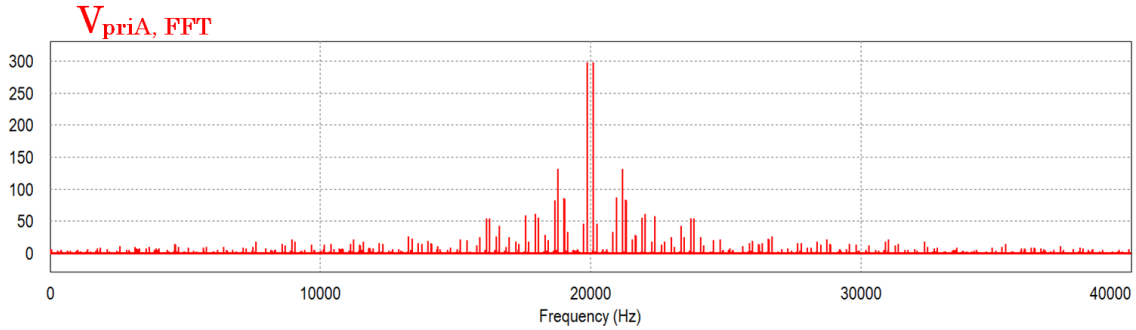

Figure 4-11: FFT of voltage V_{priA}. The fundamental voltage components appear at 20 kHz.

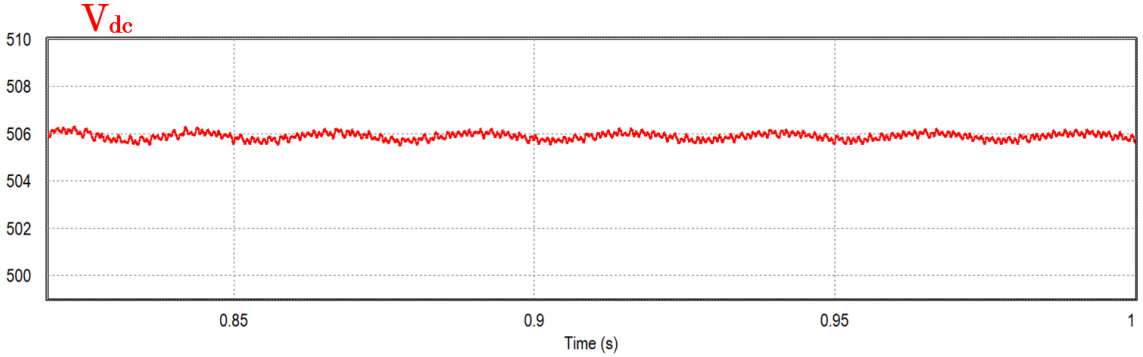

Figure 4-12: High quality DC output voltage at 506V.

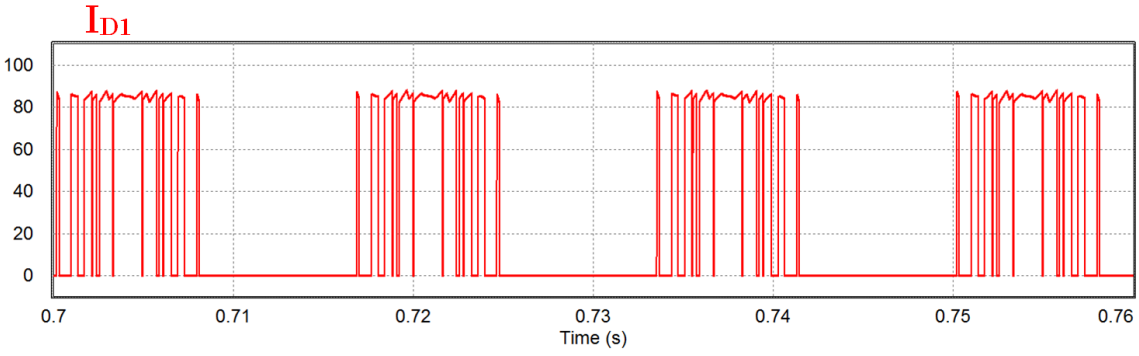

Figure 4-13: AC-AC converter single-phase diode rectifier current. Peak value is 85 A and rms value is 44 A confirming design calculations.

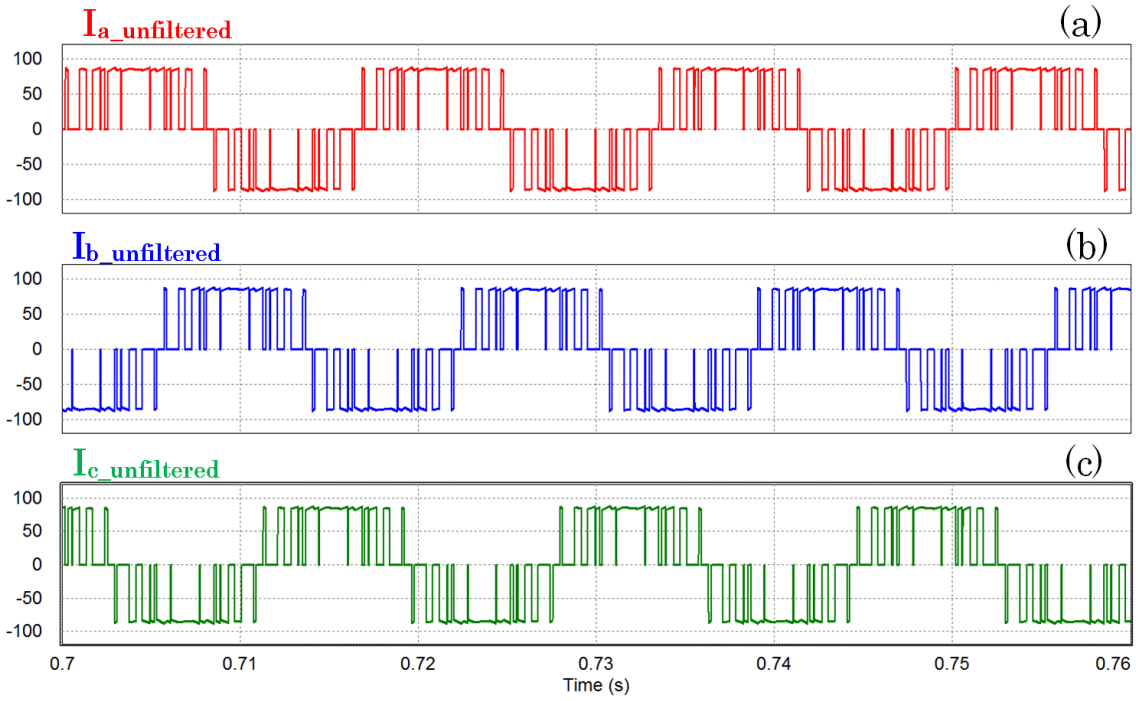

Figure 4-14: (a)-(c) Unfiltered line input currents. These currents are equivalent in shape to the unipolar switching functions in Figure 4-7.

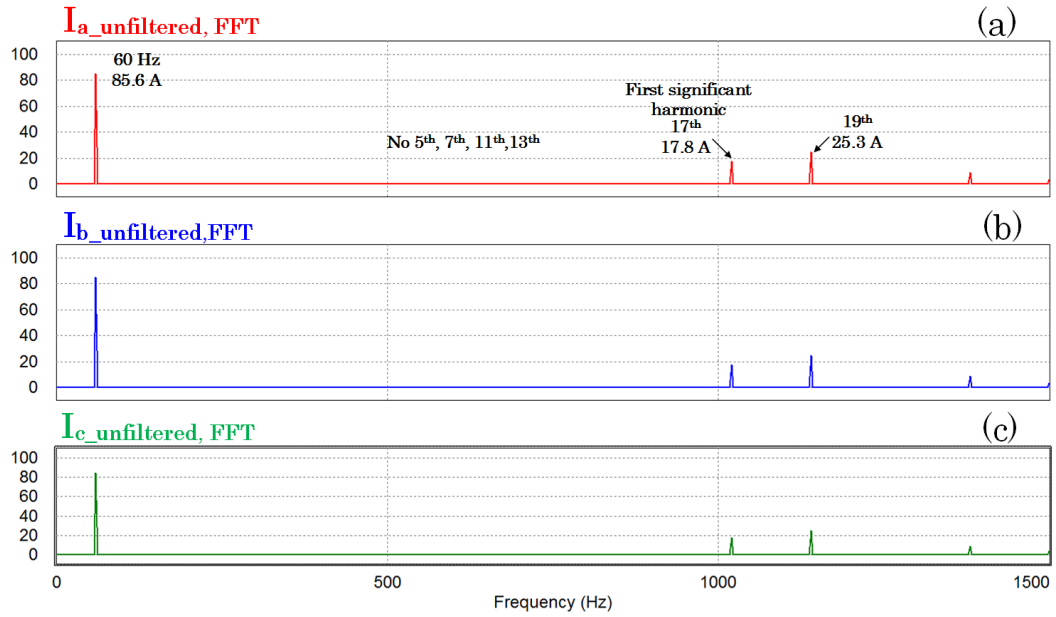

Figure 4-15: FFT of unfiltered input currents. The harmonic content matches the desired performance. The 5^{th}, 7^{th}, 11^{th}, and 13^{th} harmonics are eliminated.

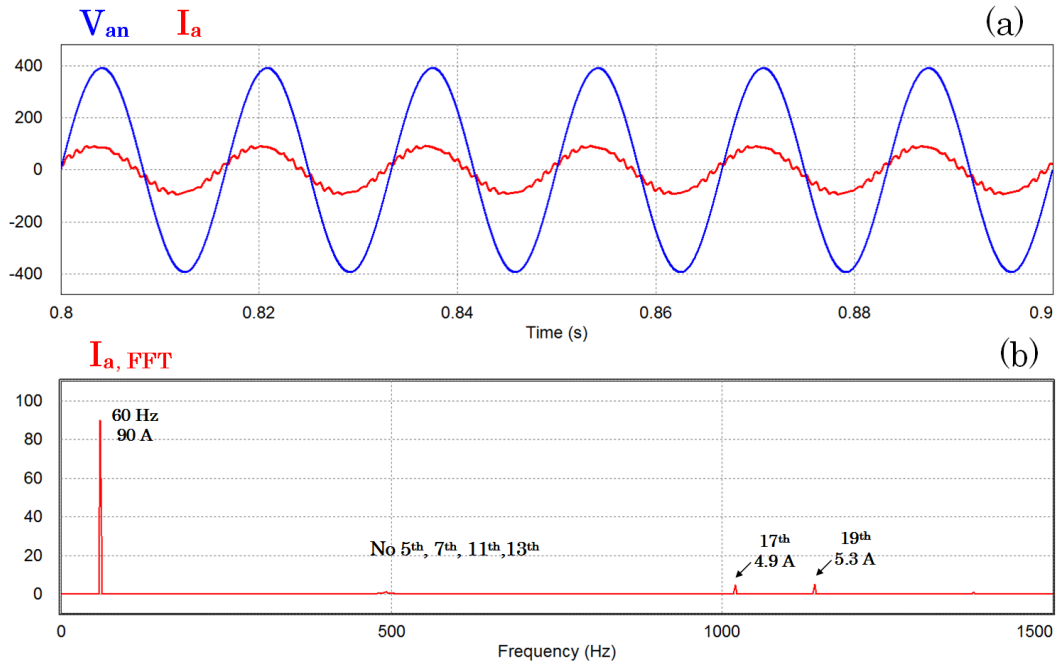

Figure 4-16: (a) Utility line-to-neutral voltage V_{an} and line input current I_a after filter. Simulated power factor is 0.97 and simulated current THD is 8.4%. (b) FFT of line current I_a. Note the absence of the eliminated harmonics. The amplitude of the first two significant harmonics is reduced due to filter operation.

Using the obtained angles in Table 4-1, the PWM rectifier was simulated for different modulation indices. The modulation index a_1 was varied from 0.5 to 1.15. Figure 4-17 shows the relationship between the output DC component and the modulation index. It is shown that the relation is linear. This also shows that the output voltage can be regulated but different switching angles must be obtained. The obtained values are in accordance with the calculated values. Note that the k_t was set to one.

Figure 4-18 shows the second order distortion factor (DF_2) as a function of a_1. The DF_2 represents the harmonic attenuation of a second order L_f-C_f filter. The DF_2 is defined as [59]:

$$DF_2 = \frac{100}{I_1}\sqrt{\sum_{n=5}^{\infty}\left[\frac{I_n}{n^2}\right]^2} \tag{4.18}$$

A low DF_2 is desired. As a1 decreases, the DF_2 increases because the amplitude of the fundamental is decreasing relative to the harmonics amplitude. The best DF_2 is therefore obtained at a_1=1.15 where the fundamental amplitude is maximum.

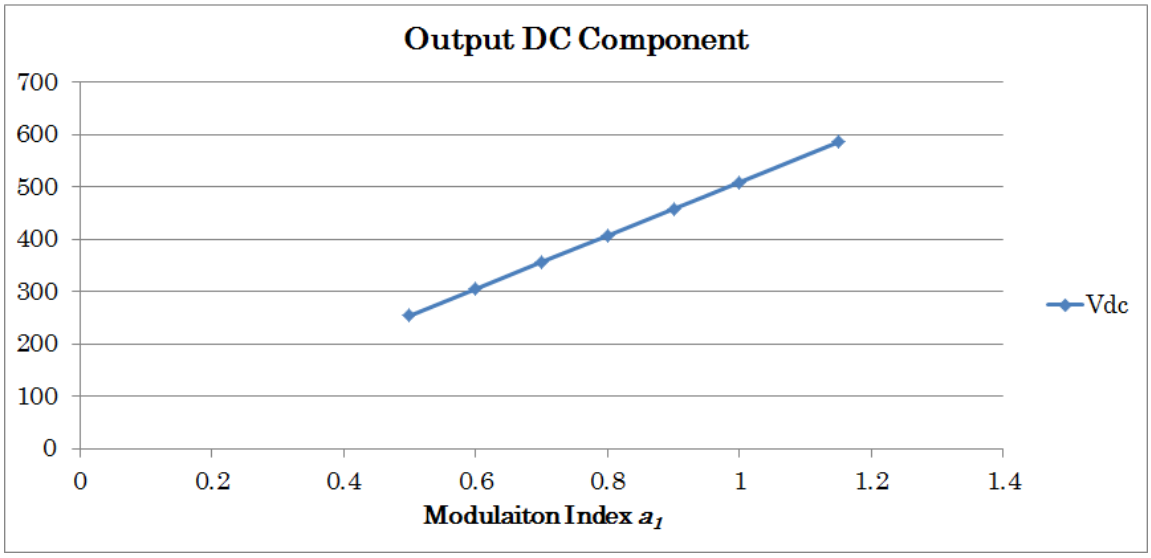

Figure 4-17: Output DC component vs. modulation index a_1.

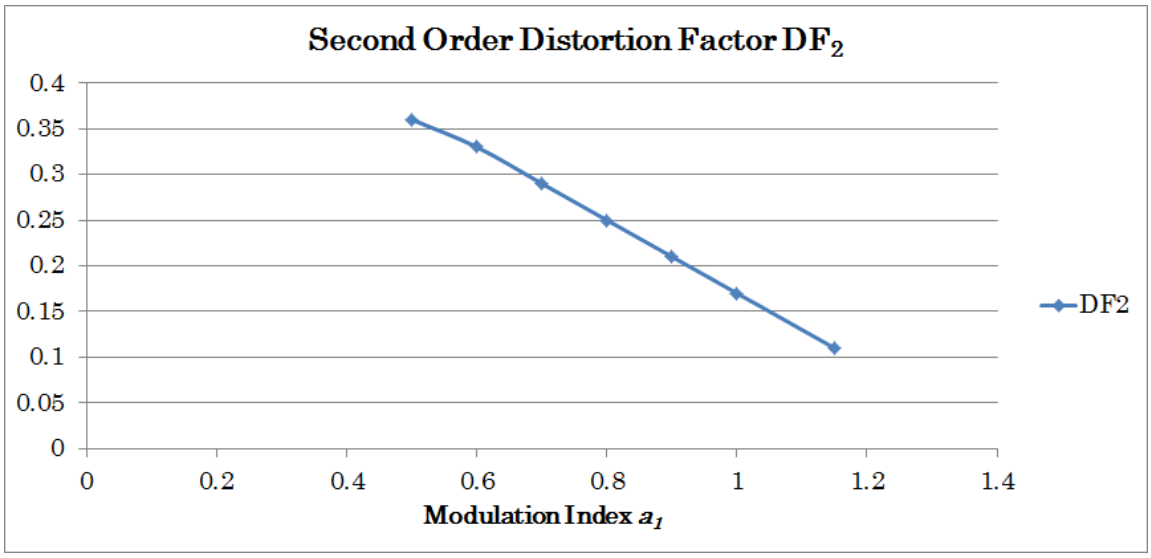

Figure 4-18: Distortion factor DF2 vs. modulation index a_1.

4.4 Efficiency Analysis

The efficiency of the proposed PWM rectifier is analyzed using PLECS thermal models, similar to the efficiency analysis of the proposed system in Section 3. In fact the same semiconductor devices listed in Table 3-4 were used to perform the efficiency analysis of the proposed PWM rectifier for 50 kW operation. The relevant curves used in the thermal models are given in Appendix A. The parameters listed in Table 4-3 were also used in the PLECS simulation.

The recorded switching and conduction losses of the semiconductor devices are shown in Figure 4-19. The majority of the losses come from the active devices in the AC-AC converter. Within the active devices of the AC-AC converters, the conduction losses amount to 1 kW, while the conduction losses amount to 850 W. The conduction losses of the single-phase diode rectifiers within the AC-AC converters are equal to 610

W. The output six-pulse rectifier has conduction losses of 387 W. The switching loss of the diodes is negligible due to their fast recovery time.

Figure 4-20 shows the power loss breakdown for the PWM rectifier. The conduction losses account for 70% of the system's overall losses. Meanwhile, the switching losses account for 29% of the total losses. The transformer losses are assumed to be 1% because of the efficiency of ferrite materials at 20 kHz. The transformer designed in Section 6 supports this assumption. Based on these results, the efficiency of the PWM rectifier at 50 kW operation is 94%. This is the same efficiency obtained for the proposed three-phase HF 12-pulse rectifier in Section 3.

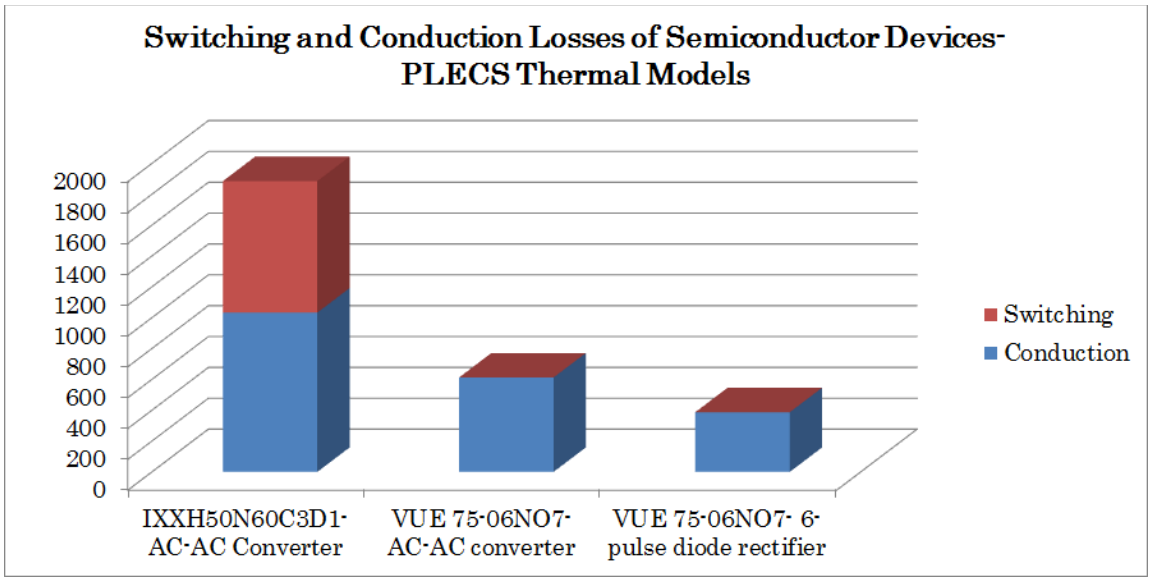

Figure 4-19: Switching and conduction losses for 50 kW design example of PWM rectifier.

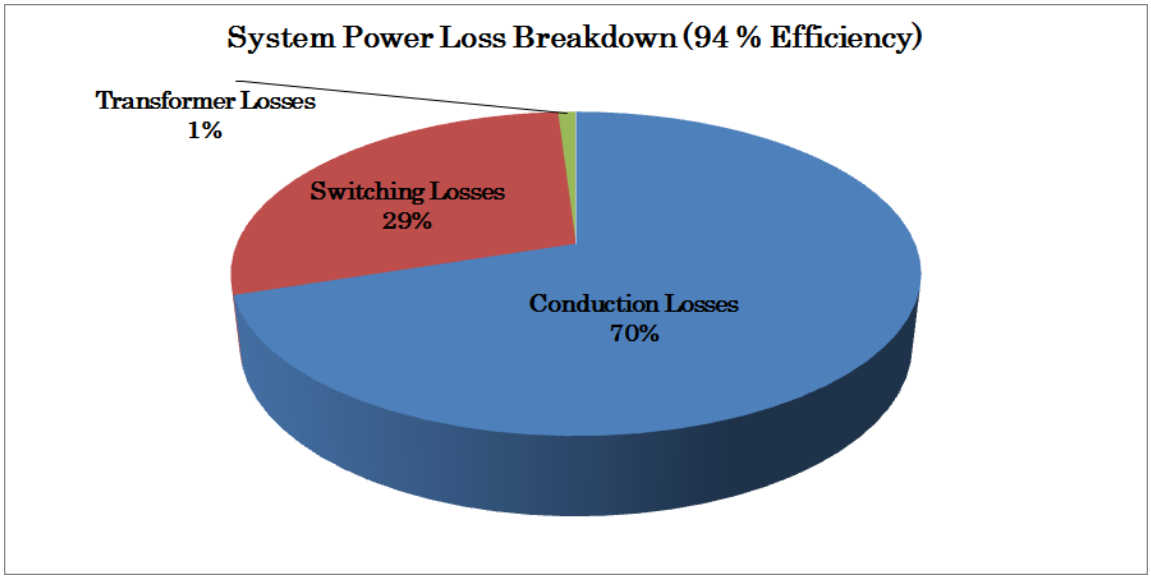

Figure 4-20: 50 kW design example power loss breakdown, 94% efficiency is achieved.

4.5 Conclusion

This section presented a three-phase AC-DC PWM rectifier with HF isolation. Using a selective harmonic elimination modulation scheme, the utility input current low order harmonics are eliminated. The analysis of the proposed rectifier was studied in detail. A design example rated at 50 kW demonstrates the elimination of the 5^{th}, 7^{th}, 11^{th}, and 13^{th} harmonic from the utility line input current. Detailed simulation results demonstrate the functionality of the system. The main advantages of this PWM rectifier include improved utility current THD, high power density, and output voltage control with over-modulation.

5. BIDIRECTIONAL MATRIX CONVERTER BASED THREE-PHASE AC-DC RECTIFIER FOR ELECTRIC VEHICLE DC FAST CHARGING†

A series resonant matrix converter (MC) based topology for high power electric vehicle (EV) battery charging is presented in this section. The system performs DC fast charging and is capable of bidirectional power flow, for *V2G* (vehicle-to-grid) applications. The proposed topology can be divided into three sections: (i) a front-end 3x1 matrix converter, (ii) L_rC_r series resonant tank and high frequency (HF) transformer, and (iii) a single-phase PWM rectifier. The MC takes a three-phase line frequency voltage and produces a high frequency (14.94 kHz) AC output. The resonant tank frequency is set to 13.7 kHz and helps to achieve zero voltage switching (ZVS) turn ON and low turn OFF switching losses. The secondary of the transformer is then interfaced to the EV battery bank through a PWM rectifier.

The advantages of such a system include high efficiency due to soft switching operation, low VA transformer ratings due to resonant operation, and high power density due to the absence of electrolytic capacitors. A design example rated 30 kW, which charges a 500 V battery system, is presented. Analysis and simulation results demonstrate the performance of the proposed bidirectional topology. Preliminary experimental results are provided for a scaled down prototype operating at 500 W using a 15 kHz ferrite transformer.

---

†Part of this section is reprinted with permission from:

1. © 2015 IEEE. Part of this section is reprinted, with permission, from Sandoval, J.J; Essakiappan, S.; Enjeti, P.N,. "A Bidirectional Series Resonant Matrix Converter Topology for Electric Vehicle DC Fast Charging," *2015 IEEE Applied Power Electronics Conference and Exposition (APEC)*, March 2015.

5.1 Introduction

The proposed three-phase AC-DC rectifier systems introduced in the previous Sections are unidirectional in nature. In these topologies, power flows only from the utility grid to the load. There are however some applications that require bidirectional power flow capability. In bidirectional systems power flows in both directions (i.e. from source to load and from load to source). Recently, there has been a growing interest to develop electric vehicle chargers with bidirectional capability. Indeed, the motivation to become more independent of fossil fuels, and provide cleaner personal transportation alternatives has led to increased production of plug-in electric (PEV) and electric vehicles (EV). With initiatives such as the *EV Everywhere Grand Challenge*, it is expected that PEVs and EVs will play a significant role in the personal transportation sector [65]. To achieve greater market penetration of these technologies, improvements have to be made in batteries, electric drivetrain systems and charging infrastructure.

It is well known that the acceptance of EVs by consumers is deeply affected by charging times [66], [67], [68]. The ability to fully charge the batteries in long-range EVs, within a reasonably short period of time is crucial to accelerate mass adoption. This opens up a wide window of research opportunities in battery fast-charging power electronic topologies. Such topologies must be highly efficient, highly reliable, and cost-effective, in addition to having very high input power quality.

V2G (Vehicle-to-Grid), or bidirectional power flow capability, is another facet of the burgeoning EV charging infrastructure. The motivations for *V2G* and its benefits have been comprehensively identified before, [69, 70], including: improved and reliable

utility supply, better load following, revenue potential for the vehicle owner, and renewables capacity firming. Employing DC fast charging topologies for *V2G* applications has been increasingly of interest to researchers. As of date of this publication, technology validation of *V2G* using DC fast chargers has been performed [71], [72]. In addition, pilot programs using multiple *V2G* – DC fast chargers are in progress [73]. As *V2G* – DC fast chargers become mainstream, the development of high-efficiency, highly compact bidirectional systems becomes crucial.

DC fast charging topologies have been previously proposed in [74], [75] which use simple topologies or easy-to-use control systems. Various high power density solutions which achieve high power factor operation are presented in [5]. However, they often use electrolytic capacitors on the DC link potentially decreasing the reliability of the system [76], and they lack bidirectional power flow capability. In [77], a matrix converter based topology is proposed eliminating the need for an electrolytic capacitor while achieving power quality and bidirectional power flow. Nonetheless, this topology uses 12 semiconductor devices operated in hard switching mode, which leads to a decrease in the system efficiency due to switching losses.

The proposed MC based battery charging topology seeks to overcome the limitations of existing solutions by employing soft switching techniques and being able to perform *V2G* power transfer. The proposed architecture has many advantages:

- Bidirectional high power flow between utility grid and battery bank for *V2G*.

- Soft switching of MC semiconductor switches greatly reduces turn on and turn off losses, increasing system efficiency, even though the topology still uses 12 semiconductor devices in the front-end converter.
- The use of an L_rC_r resonant tank leaves the transformer to process only selected frequencies, thereby decreasing its VA rating requirement.
- Direct AC-AC conversion via MC eliminates the need for electrolytic capacitors and potentially increases reliability and power density of the system.
- The use of high frequency (HF) transformer also increases power density, while providing galvanic isolation.

5.2 Proposed Matrix Converter Topology for DC Fast Charging

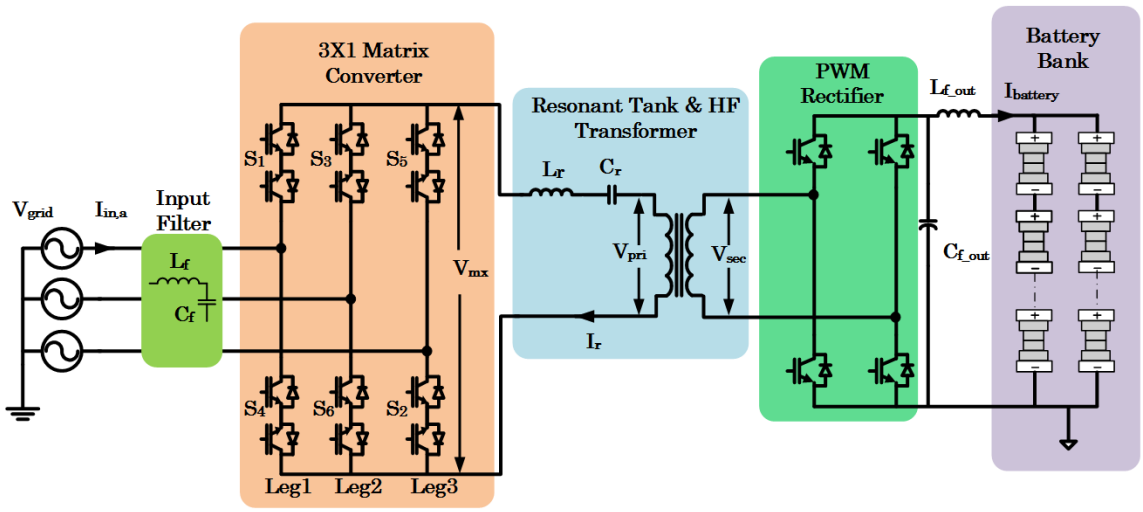

Figure 5-1: Proposed series resonant MC topology for EV battery charging. MC semiconductor switches are turned ON at zero voltage and turned OFF at low currents. This topology is capable of bidirectional power flow between the grid and battery bank.

The proposed topology for EV battery charging uses a high frequency transformer for power processing as shown in Figure 5-1. The design of this topology can be divided into the following sub-sections: 3x1 matrix converter, L_rC_r resonant tank and HF transformer, and a single-phase PWM rectifier.

5.2.1 3x1 Matrix Converter Modulation Scheme

The three-phase utility grid is interfaced to the MC via an L_fC_f filter. The MC consists of six bidirectional switches (S_1-S_6) as shown in Figure 5-1. The converter takes a line frequency three-phase sinusoidal input voltage and delivers a high frequency quasi-square wave output. S_1-S_6 are capable of operating in all four quadrants of the V-I plane by virtue of their construction.

Different modulation techniques for the 3x1 MC have been studied in [77], [78], [79], [80]. The modulation technique proposed for this topology has been described as follows. A unipolar SPWM switching function, S_{AB}, is obtained from two bipolar SPWM signals, PWM_A and PWM_B ($S_{AB} = PWM_A - PWM_B$). The resulting S_{AB}, seen in (5.1), is then multiplied by a square wave switching function $S_{inv,}$ seen in (5.2), to produce the resultant switching function of leg one of the MC, as illustrated in Figure 5-2. This resultant switching function F_1 of the bidirectional switch S_1 is the product of unipolar SPWM and a square wave with high frequency f_{sq}, as seen in (5.3).

$$S_{AB} = m_a \cdot \begin{bmatrix} 0.866\sin(2\pi f_{grid} t) + 0.275\sin(2\pi \{m_f \pm 2\} f_{grid} t) \\ +0.01548\sin(2\pi \{m_f \pm 4\} f_{grid} t) \\ +0.157\sin(2\pi \{2m_f \pm 1\} f_{grid} t) + ... \end{bmatrix} \tag{5.1}$$

$$S_{inv} = \sum_{n=1,3,5,\ldots}^{\infty} \frac{4}{\pi} V_{sq} \sin(2n\pi f_{sq} t) \tag{5.2}$$

$$F_1 = S_{AB} \cdot S_{inv} \tag{5.3}$$

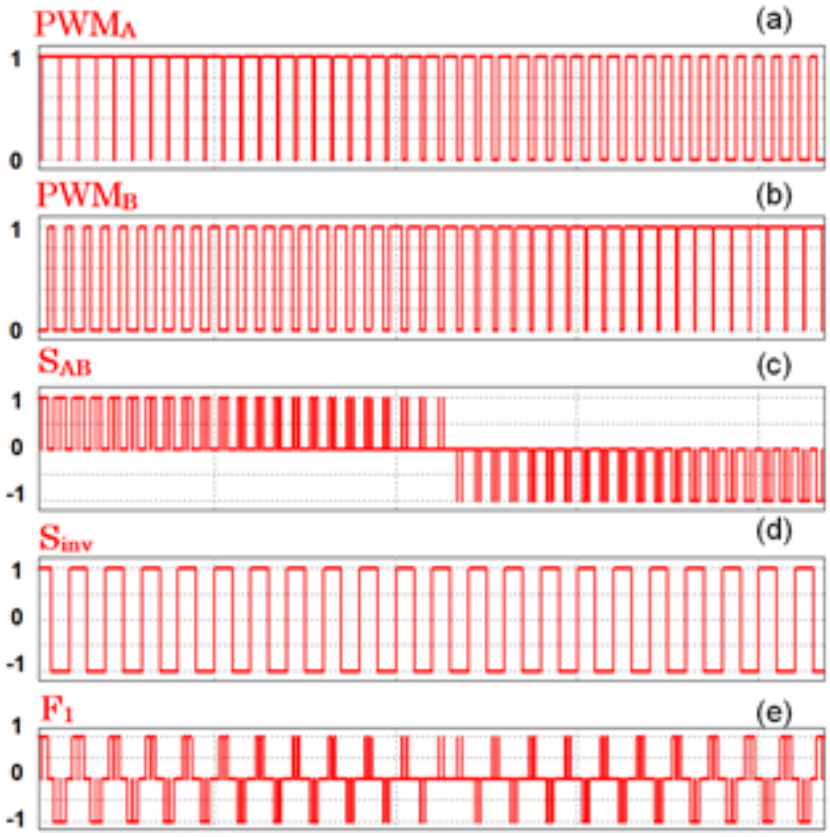

Figure 5-2: (a) PWM_A obtained by comparing a high frequency (14.94 kHz) carrier wave with a line frequency sinusoidal modulating function. (b) PWM_B obtained as in (a) but modulating function has a 120° phase shift. (c) Switching function S_{AB} is the subtraction PWM_A-PWM_B. (d) S_{inv} is a high frequency square wave switching function. This frequency determines the output frequency of the MC (e) Overall switching function is the product of S_{AB} and S_{inv}.

Unipolar switching functions S_{BC} and S_{CA} are shifted 120° and 240° (of the line frequency) respectively compared to S_{AB}. Switching functions F_2 and F_3 are the products

of S_{BC} and S_{CA} with S_{inv} respectively (seen in (5.4) and (5.5)). From switching functions F_1-F_3, the gating signals for the devices S_1-S_6 are obtained. When F_1 is positive S_1 is turned ON, and when F_1 is negative S_4 is turned ON. Similarly F_2 and F_3 determine the gating signals for the devices in the second and third half-bridges in the matrix converter respectively. There are instances where F_1, F_2 and F_3 are all zero simultaneously. During these zero states one of the three half-bridges is shorted to provide a freewheeling path for the transformer current. Hence the output of the MC is described by (5.6), where V_{an}, V_{bn} and V_{cn} are the utility line-to-neutral voltages. The fundamental component of the voltage produced by the MC is given by (5.7).

$$F_2 = S_{BC} \cdot S_{inv} \tag{5.4}$$

$$F_3 = S_{CA} \cdot S_{inv} \tag{5.5}$$

$$V_{mx} = F_1 \cdot V_{an} + F_2 \cdot V_{bn} + F_3 \cdot V_{cn} \tag{5.6}$$

$$V_{mx,1} = \frac{3}{2}\sqrt{\frac{2}{3}}0.866 \cdot \frac{4}{\pi} m_a \cdot V_{LL} \tag{5.7}$$

Using this modulation method, only two of the six bidirectional devices conduct at any given time. In fact, the operation of the MC can be divided in six intervals as shown in Figure 5-3. Each interval is determined by the magnitudes of the utility grid line-to-line voltages. For example, interval one occurs when the most positive line-to-line voltage is V_{ab}. Similarly, interval two occurs when the most positive line-to-line

voltage is V_{ac} and so on. Within each interval, the MC behaves as two alternating full bridge converters. For instance, in interval one the current commutates between (leg 1 & leg 2) of the MC and also between (leg 1 & leg 3) of the MC as shown in Figure 5-4. Thus, in this interval, the possible voltages produced by the MC are V_{ab}, V_{ba}, V_{ca}, V_{ac}, and 0 for the freewheeling state. Since these voltages are being modulated with a HF square wave, the output of the MC has a quasi-square wave nature.

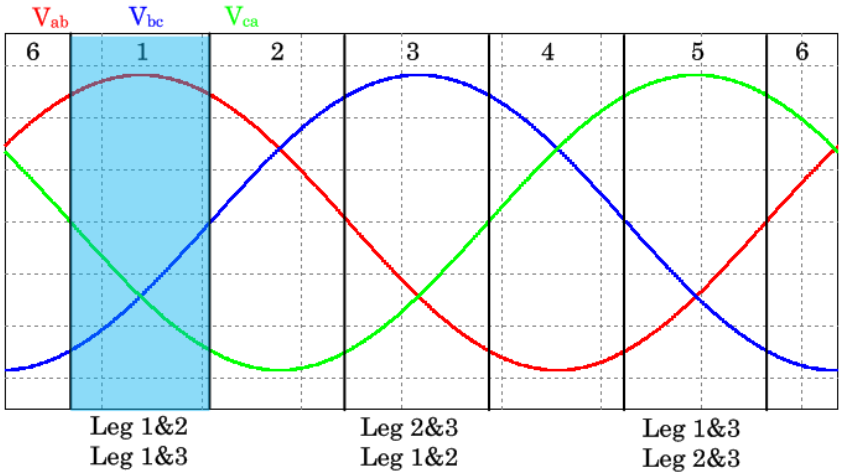

Figure 5-3: Operating intervals of MC. Every 60°, the MC behaves as two alternating full bridge converters.

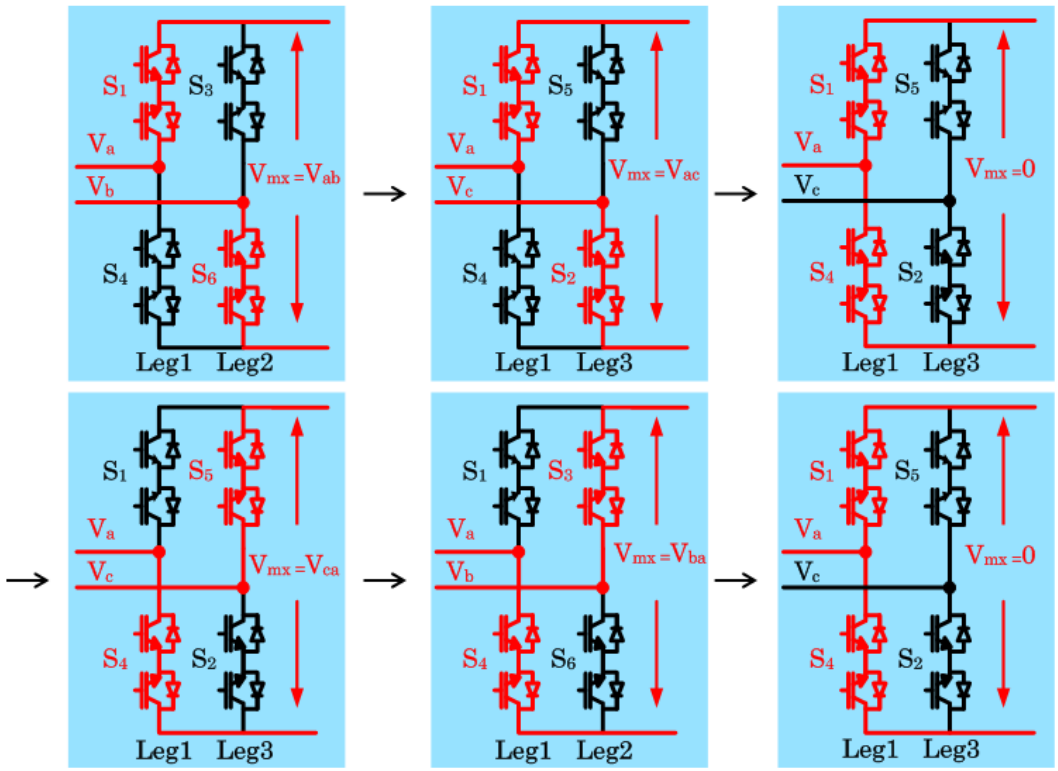

Figure 5-4: Operation of MC in interval 1. The current commutates between two full bridge converters. Leg 1 and leg 2 form one full bridge converter while leg 1 and leg 3 form a second one. This sequence repeats within interval 1 at the switching frequency of the MC.

5.2.2 Resonant Tank and High Frequency Transformer

An L_rC_r resonant tank is connected across the output of the MC in series with the HF transformer primary. The resonant tank frequency is set to 13.7 kHz and helps to achieve ZVS turn ON conditions and low turn OFF switching losses. The resonant capacitor C_r also serves to block any DC voltage preventing core saturation. The square wave frequency, f_{sq}, used for modulation of the MC is set above the resonant frequency of the L_rC_r tank which is given by (5.8).

$$f_r = \frac{1}{2\pi\sqrt{L_rC_r}} \tag{5.8}$$

Since the output of the MC is a quasi-square wave with frequency close to resonance, the current through the filter tank, I_r, has a sinusoidal nature with frequency f_{sq}. The magnetizing inductance of the transformer does not play a role in the resonance of the tank but it has an effect on the voltage across the primary. The fundamental component of the voltage across the primary is given by (5.9), where where R_{eq} is effective impedance referred to the primary side. X_{Lm}, X_{Cr}, X_{Lr} are the reactances of the magnetizing inductance, resonant tank capacitor, and resonant tank inductor respectively.

$$V_{pri,1} = \frac{X_{Lm} \cdot R_{eq} \cdot V_{mx,1}}{\sqrt{(R_{eq}[X_{Lr} + X_{Lm} - X_{Cr}])^2 + (X_{Lm}(X_{Lr} - X_{Cr}))^2}} \tag{5.9}$$

The dependency of voltage gain of the series resonant tank on operational frequency is shown in Figure 5-5. The normalized frequency f_n is the ratio of the operating square wave frequency f_{sq} to the resonant frequency f_r. As anticipated, the voltage gain is unity at resonant frequency, since the resonant tank impedance is at a minimum at this frequency and the resistance component is dominant. It can also be observed that operating above resonance, the voltage gain is less than unity.

An HF transformer was designed for a 500 W scaled-down prototype. Due to its low cost and moderate power loss [23], a ferrite magnetic core material is selected. To avoid saturation, the operational magnetic flux density of the selected core is limited to 0.25 T and the magnetic flux intensity to 60 Am^{-1}. At this operating point, the magnetic permeability of the core is 0.004 Hm^{-1}. The characteristics of the ferrite core chosen for this application are given in Table 5-1.

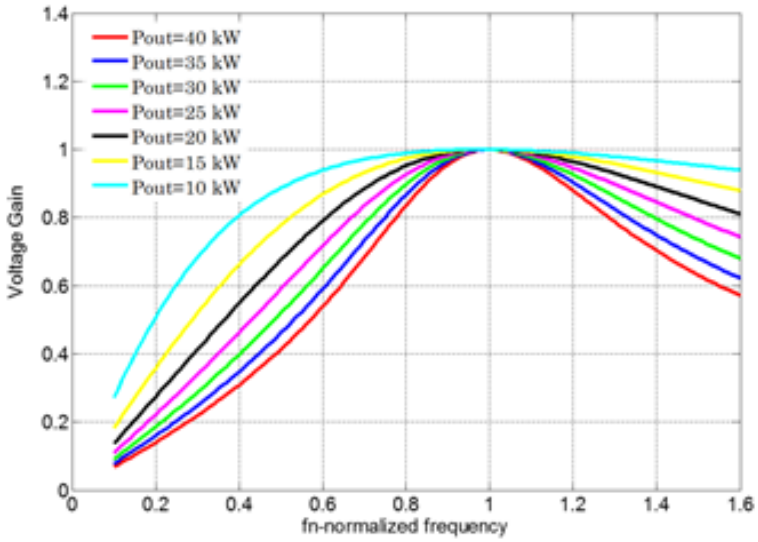

Figure 5-5: Voltage gain-frequency curves of series resonant tank. Operating above resonance yields a gain < 1. Furthermore, operating above the resonant frequency enables ZVS turn ON and low turn losses.

Table 5-1: Ferrite core characteristics

Core type	3C85
Maximum flux density, B_{max}	0.4 T at 25 °C
Effective cross sectional area, A_e	0.000625 m^2
Effective magnetic path length, l_e	0.42 m
Power loss, P_v	150 W m^{-3} at 15 kHz
Density	4800 kg m^{-3}

In order to determine the number of turns in the primary side (N_{pri}), the relationship shown in (5.10) is used. The number of turns in the primary is set to 30 which achieves 281V on the primary side. The expected magnetizing inductance is determined by (5.11). The magnetizing inductance of the designed transformer was calculated to be 6.7 mH. The worst case magnetizing current (i_m) for an applied voltage

of 300 V is 0.5 A. The magnetic field intensity is found by (5.12). The value at this operating point is calculated to be 32 A m^{-1} which is below the 60 A m^{-1} saturation limit.

$$V_{pri} = 4 \cdot B \cdot A_e \cdot N_{prim} \cdot f \tag{5.10}$$

$$L_m = \frac{\mu \cdot N^2 A_e}{l_e} \tag{5.11}$$

$$H = \frac{N \cdot i_m}{l_e} \tag{5.12}$$

The transformer turns ratio is a factor of the required output voltage. The prototype is designed for a 450 V output. Since the primary side can reach 281 V, the turns ratio (n_1:n_2) must be at least 1:1.6. In order to account for conduction losses, the transformer turns ratio is set to 1:1.7. Performing a transformer short circuit test, the leakage inductance $L_{leakage}$ was measured to be 4 μH. Similarly, an open circuit test yielded a magnetizing inductance L_m of 4.6 mH. The resonant tank and transformer frequency characteristics are experimentally obtained using a frequency response analyzer and the results are produced. The Bode gain and phase plots are shown in Figure 5-6 and the impedance characteristics are in Figure 5-7. It can be verified that the gain reaches unity at the resonant frequency. Likewise, the resonant tank and transformer impedance is at its minimum when the frequency reaches resonance. The inductance used for the resonant tank L_r is 23 μH and the capacitance C_r is 4.3 μF.

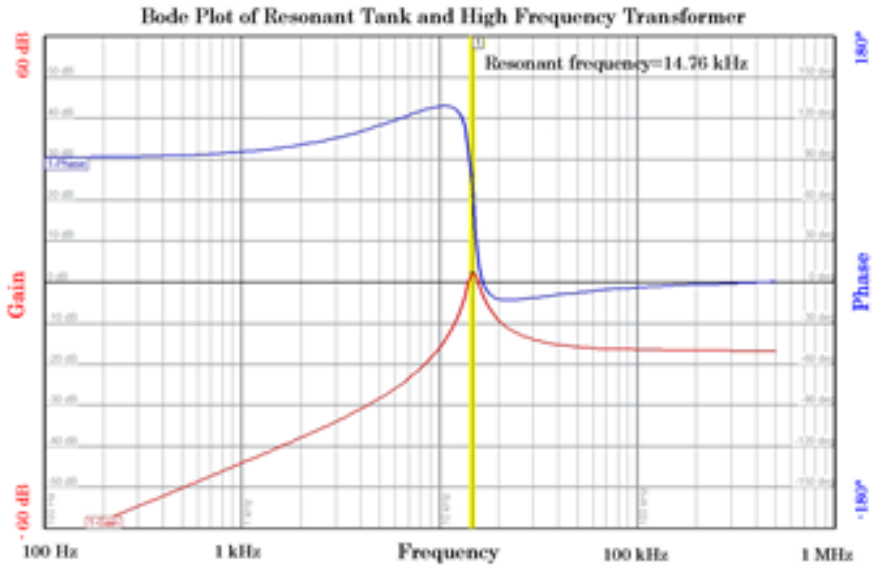

Figure 5-6: Frequency response of resonant tank and high frequency transformer showing a notch-filter type performance. The gain reaches unity (0 dB) at the resonant frequency as expected and other frequencies are attenuated. The phase approaches zero as the frequency gets close to resonance. (L_r=23 µH, C_r=4.3 µF, $L_{leakage}$=4 µH, L_m=4.6mH).

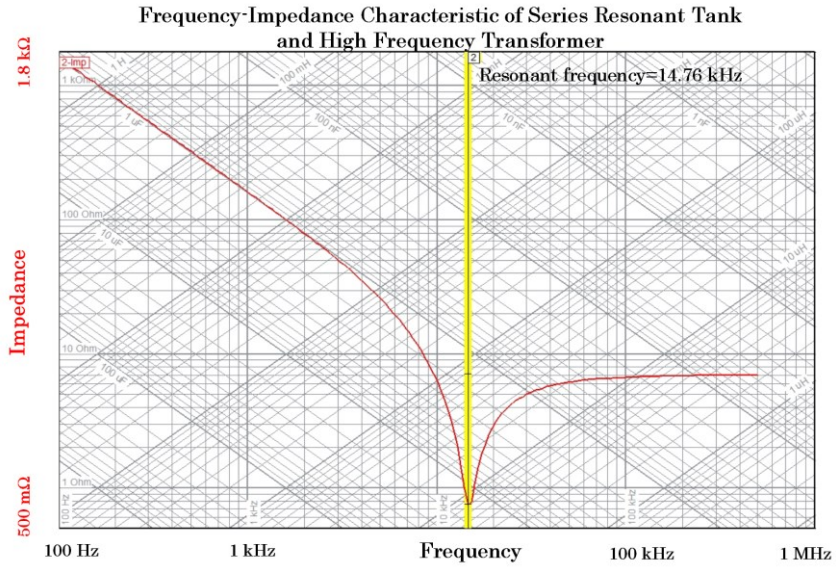

Figure 5-7: Impedance characteristic of resonant tank and high frequency transformer. As expected, the impedance reaches its minimum value at the resonant frequency.

5.2.3 Single-Phase PWM Rectifier

The L_rC_r resonant tank is interfaced to a single-phase PWM rectifier via the HF transformer. The single-phase PWM rectifier is operated in close loop to regulate the battery current, $I_{battery}$. The rectifier is operated with square wave PWM at the same frequency as f_{sq}. The power transfer is determined by the phase angle difference between the secondary winding voltage and the voltage imposed by the rectifier, akin to a dual active bridge operation. The current flowing through the secondary of the transformer is a high frequency sinusoid; for grid to vehicle (*G2V*) operation when the current is positive the antiparallel diodes of S_{1_rect} and S_{2_rect} conduct, when the current is negative the antiparallel diodes of S_{3_rect} and S_{4_rect} conduct. For *V2G* operation, the corresponding IGBTs perform current conduction.

5.3 Design Example and Simulation Results

A 30 kW fast-charging design example for a 500 V battery is considered, to demonstrate the operation of the proposed bidirectional series resonant MC in Figure 5-1. The parameters in Table 5-2 were used for analysis and simulation.

Simulations of the proposed topology in Figure 5-1 are performed for two modes of operation: *(A) G2V* (Grid-to-vehicle mode, charging), in which power flows from the utility grid to the vehicle's battery bank, *(B) V2G* (Vehicle-to-grid mode, discharging), in which power flows from the battery bank to the utility grid. *G2V* mode is operated at a maximum power of 30 kW and *V2G* mode processes a maximum of 15 kW. The

analysis is performed both in steady state and in transient between the two operating modes.

Table 5-2: Specifications and operating conditions user for series resonant MC design example

Grid voltage (line-to-line rms)	480 V
Battery open circuit voltage (OCV)	500 V_{dc}
Rated power	30 kW
Square wave switching frequency (f_{sq})	14.94 kHz
Resonant tank frequency (f_r)	13.7 kHz
Resonant Inductor (L_r)	240 μH
Resonant Capacitor (C_r)	0.56 μF

5.3.1 Grid-to-Vehicle (G2V) Mode of Operation

In this mode of operation, the utility grid supplies power to the EV battery bank. The battery voltage and battery current in simulation are shown in Figure 5-8. It can be observed that the battery current has very low ripple, with an AC rms value less than 1 A. Figure 5-9(a) shows the line-to-neutral voltages and Figure 5-9(b) shows the input line currents; the line-to-neutral voltages and the line currents are in phase achieving high displacement power factor. In addition, the THD of the input currents is less than 3%, which makes the system power factor very close to unity.

The output voltage of the 3x1 MC and the resonant tank current, I_r, are shown in Figure 5-10(a). The quasi-square wave nature of the voltage can be appreciated. It can also be observed that the current lags the voltage, as one would expect from the inductive nature of the tank at above-resonance operation. The sinusoidal nature of the

current I_r can be observed. The frequency spectrum of the matrix converter voltage and the resonant tank current, seen in Figure 5-10(b), show the fundamental component at 14.94 kHz as expected. Furthermore, the HF transformer only processes the selected frequency (14.94 kHz) which contributes to a reduction of its VA rating.

Soft switching operation of the topology can be appreciated from Figure 5-11, which shows the current through one of the four-quadrant switching devices and the voltage across that device. From the figures, it is evident that the antiparallel diode of a switch conducts before the switch. This means that the switch is turning ON at zero voltage. Similarly, the device turns OFF at zero voltage. Similar ZVS operation may be observed in all other switching devices.

A step response of the battery current, $I_{battery}$, is obtained to verify the robustness of the control strategy. The battery current reference is changed from 60 A to 30 A in a rapid manner, which is not expected in real world EV charging system. However this helps to verify the controller performance. The battery voltage and battery current during this transient are shown in Figure 5-12. The battery voltage shown here is the terminal voltage of the battery, which includes voltage drops across the battery equivalent resistance, hence it displays a step change when the charging current is changed. It may also be seen that the phase angle between the transformer secondary voltage and the input terminal voltage of the PWM rectifier is changed by the controller in response to the step change in the battery current reference. Figure 5-13 shows the line input currents during the step response, decreasing in amplitude in a smooth manner. Figure 5-13 also

shows the simulated power factor which remains at unity and only displays a very short reduction during the transient.

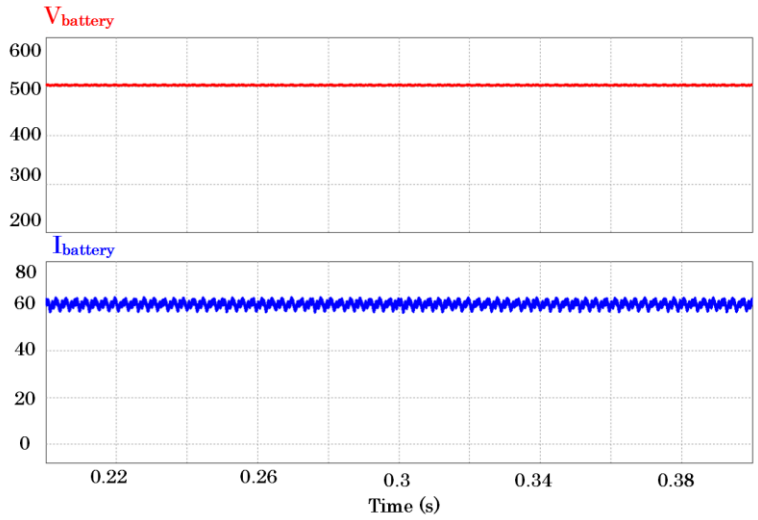

Figure 5-8: Battery current (60 A) and voltage (500 V) shown in charging (*G2V*) mode. The output power is 30 kW. The battery current has negligible ripple with an AC rms < 1 A.

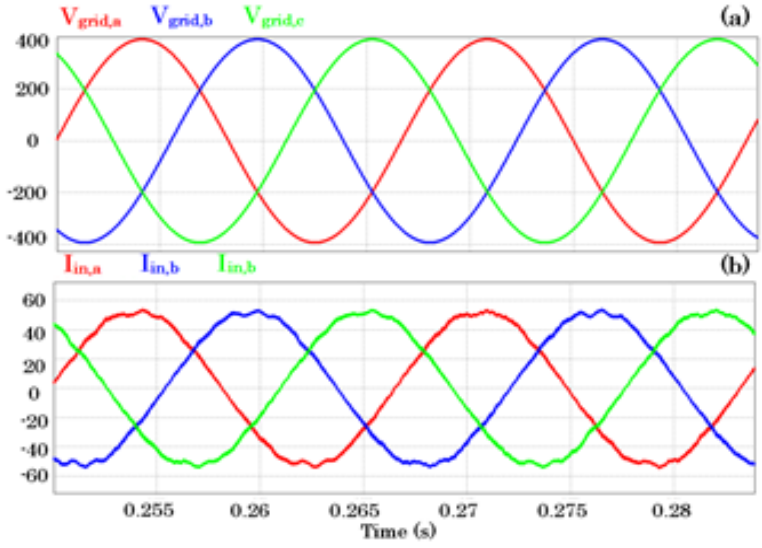

Figure 5-9: (a) Line-to-neutral input voltages. (b) Line input currents (rms 36 A). It can be observed that the line currents are in phase with the line-to-neutral voltages. Simulated power factor is 0.99 and simulated THD of the currents is less than 3%.

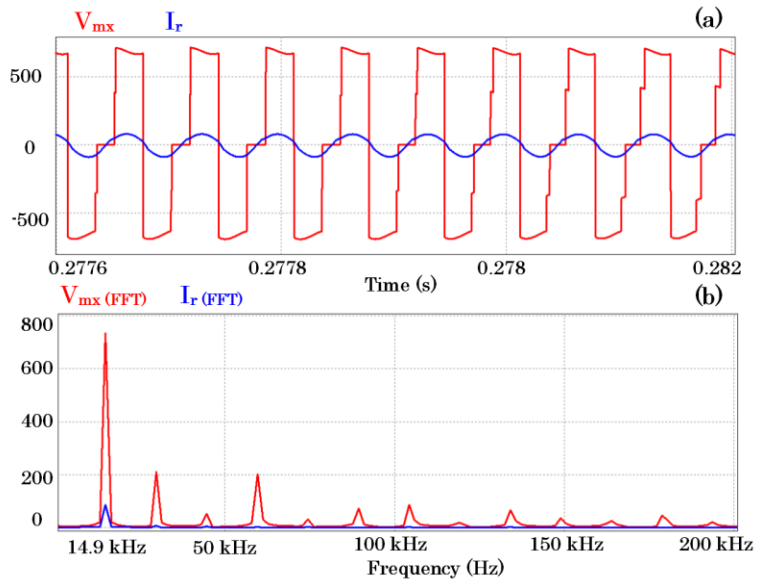

Figure 5-10: (a) Output voltage of matrix converter and resonant tank current. The square wave nature of V_{mx} can be observed. (b) The FFT of V_{mx} and I_r show the high frequency operation of the transformer. The transformer responds only to the resonant frequency. The L_rC_r tank blocks all other components since it presents higher impedance to all other frequencies.

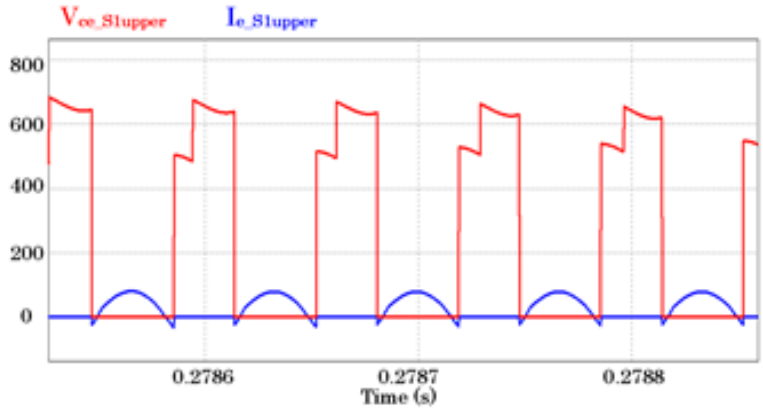

Figure 5-11: Soft switching operation of the semiconductor S_{1_upper}. The device turns ON and OFF at zero voltage. Other semiconductor devices operate in similar manner. The device V_{CE} voltage reaches the amplitude of the line-line voltage. Note the absence of ringing in V_{CE} due to soft-switching.

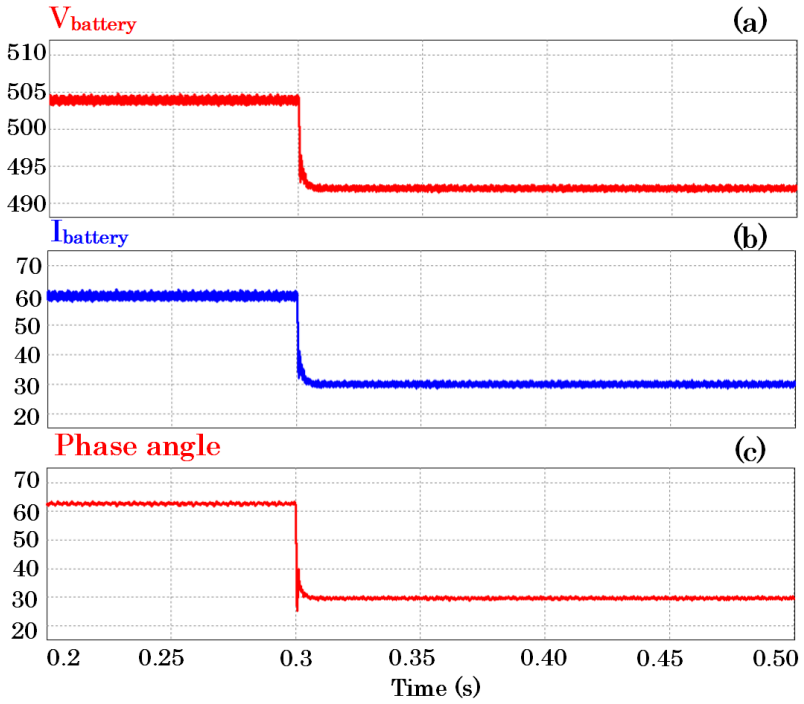

Figure 5-12: (a) Battery terminal voltage, (b) Battery charging current, and (c) Phase angle between secondary voltage and rectifier input terminal voltage. The phase angle is changed in response to the current reference change.

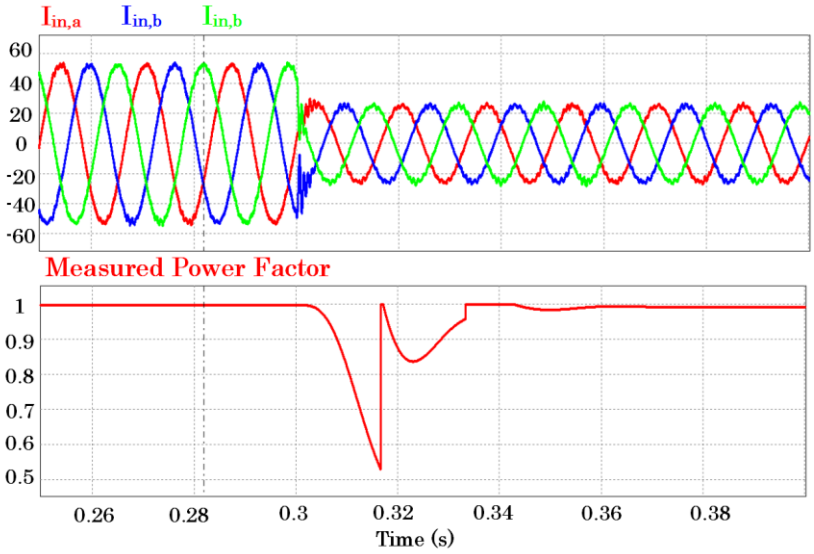

Figure 5-13: Three-phase line input currents and measured input power factor during transient. The input current quality remains very high (less than 3% THD) and the power factor only displays a short reduction during transient.

5.3.2 Vehicle-to-Grid (V2G) Mode of Operation

During this mode, the EV battery bank is supplying power to the utility grid. Figure 5-14 shows the battery voltage and current during discharging operation, with the battery current being negative, as one would expect. As in the charging mode, the battery current has a very low AC rms value – less than 1 A. Figure 5-15 shows the grid line-to-neutral voltages and the input line currents. It can be noted that the currents have a phase shift of 180° with respect to the line-to-neutral voltages, which demonstrates *V2G* operation. In this mode of operation, the line currents THD are also less than 5%.

In this mode of operation, the semiconductor devices of the MC also operate under soft switching conditions. Figure 5-16(a) shows the V_{CE} voltage across the upper switch S_1 and the current I_e flowing through the device. Similarly, Figure 5-16(b) shows the voltage across S_{1_rect} of the PWM rectifier. The figure shows that the device turns ON and OFF under ZVS conditions.

The step response of the system as it rapidly enters discharging mode from charging mode is shown in Figure 5-17. The battery terminals display a predictable voltage drop as it enters discharging mode. The measured power factor of the system, which was unity in *G2V* mode becomes negative unity in *V2G* which means the input line currents are out-of-phase with the line-to-neutral voltages.

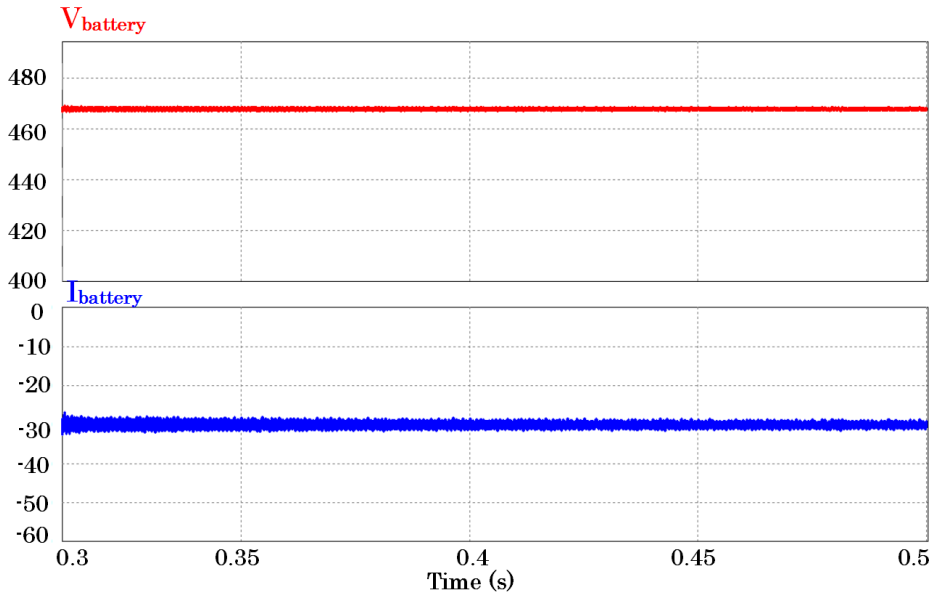

Figure 5-14: Battery voltage and battery current during *V2G* mode. As expected, the battery voltage drops during discharging mode and the current is negative.

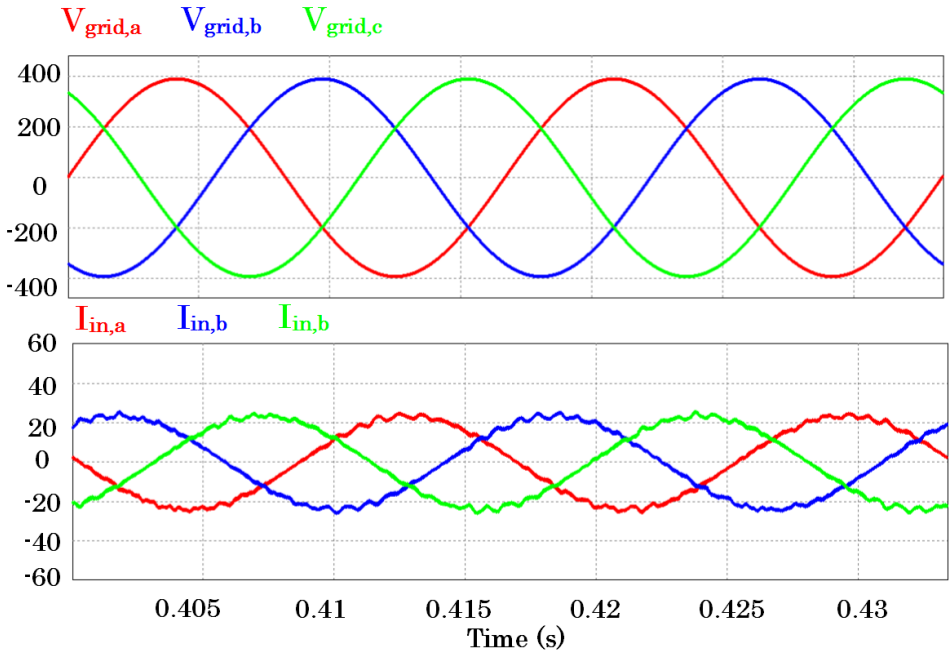

Figure 5-15: Line-to-neutral input voltages and line input currents. The currents are 180° phase shifted with respect to the voltages implying power flow to the grid. The line currents waveforms are of high quality, with THD less than 5%.

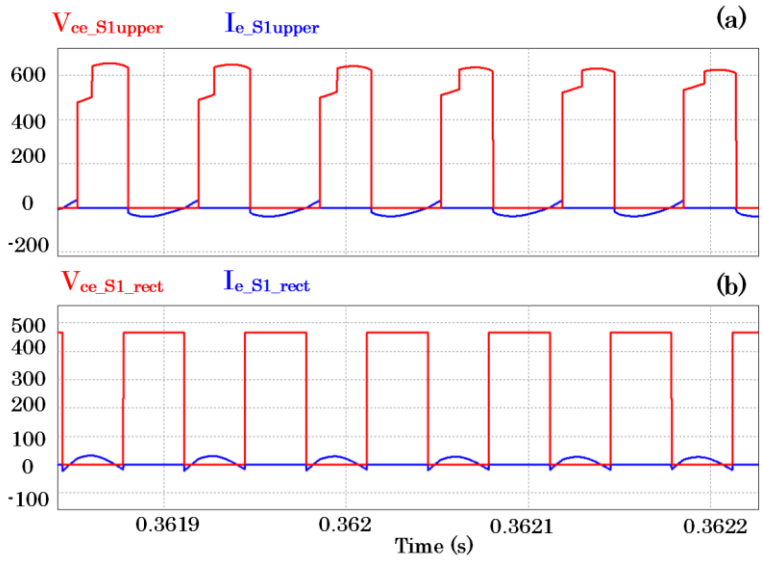

Figure 5-16: (a) MC device voltage and current and (b) PWM rectifier device voltage and current. The devices turn ON and OFF at zero voltage. The rest of the devices in the PWM rectifier exhibit similar operational performance.

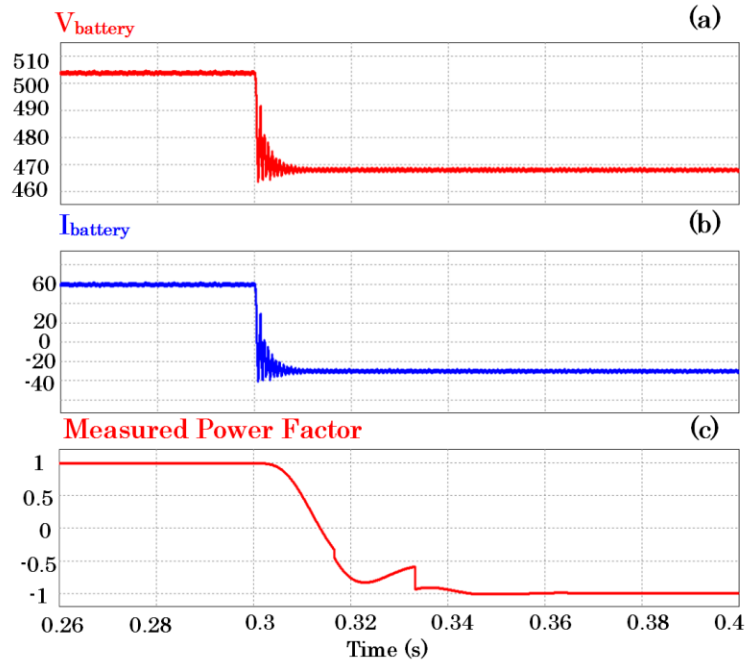

Figure 5-17: (a) Battery terminal voltage, (b) Battery current, (c) Measured power factor, as the system moves from *G2V* to *V2G*. The measured power factor changes from positive to negative unity during this transient.

5.4 Experimental Results

A scaled-down prototype of the L_rC_r resonant tank and a HF transformer, rated at 500 W, was built and tested in the laboratory. The resonant inductor was designed using an amorphous "Metglas®" core which provides low loss and high saturation flux density. The resonant inductor was designed to be 23 μH, so that along with the HF transformer leakage inductance of 4.15 μH it produces an overall inductance of 27.15 μH. The resonant capacitor value was calculated to be 4.2 μF. The resonant frequency of this set up was 14.9 kHz. The front-end converter for the resonant tank – transformer is a full bridge inverter. The secondary side of the HF transformer was connected to a silicon carbide diode rectifier. The diode rectifier has essentially zero reverse recovery losses. The gate drive signals for the front-end converter were generated using a Texas Instruments TMS320F28335 microcontroller.

Figure 5-18 shows the resonant tank current, the voltage across the secondary winding, the voltage (V_{CE}) across one of the semiconductor devices, and the current (I_e) through that device. The sinusoidal nature of the resonant tank current can be appreciated from the figure. Figure 5-19 presents a detailed version of Figure 5-18 illustrating soft switching operation in the front-end full bridge inverter. It can be observed that the device turns ON under ZVS conditions and encounters a small switching loss during turn OFF. The switching and conduction losses in the semiconductor device can be observed in the the multiplication of V_{CE} and I_e waveforms of the device. Figure 5-20 shows that at the switching instances the power loss is

minimal and conductions losses are as expected. Overall, this device is seen to have a loss of 2.2 W.

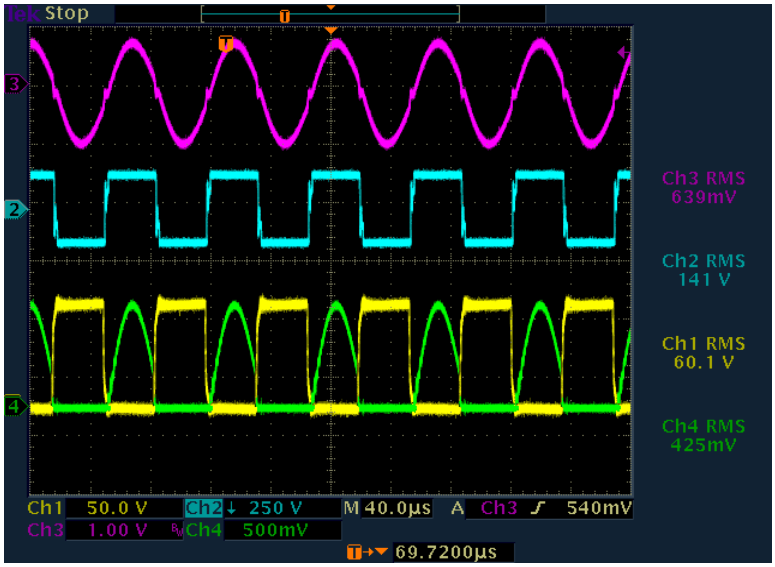

Figure 5-18: Resonant tank current I_r (Ch3: 1 div = 10 A), HF transformer secondary voltage (Ch2: 1 div = 250 V), device voltage V_{CE} (Ch1: 1 div = 50 V) and device current I_e (Ch4: 1 div = 5 A).

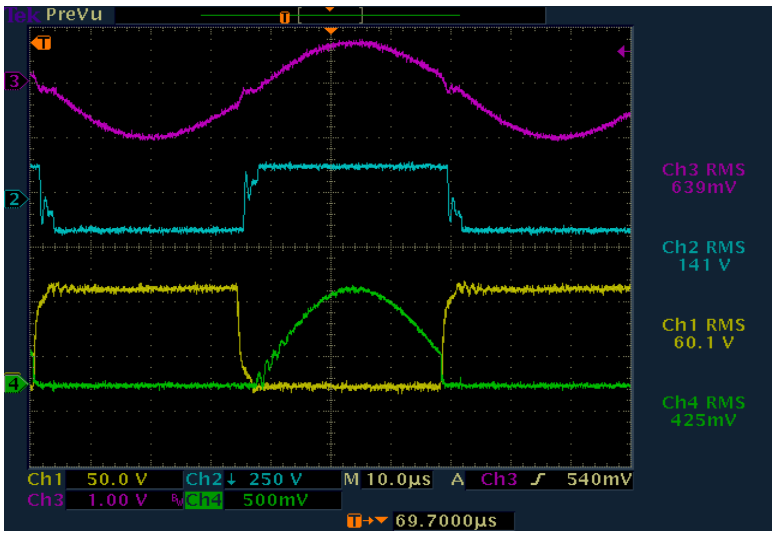

Figure 5-19: Detailed version of Figure 5-18 to appreciate the soft switching operation. The device current I_e (Ch.4: 1 div = 5 A) turns ON at zero voltage and the turn OFF current is low.

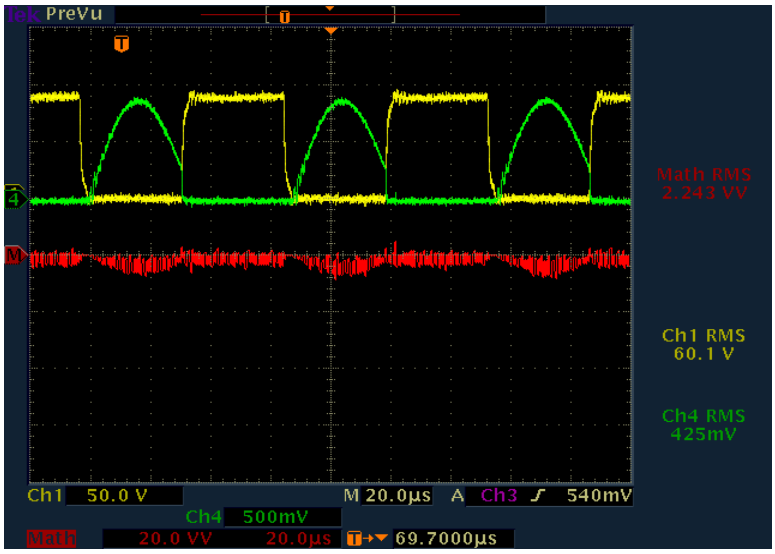

Figure 5-20: Multiplication of device voltage V_{CE} (Ch1: 1 div = 50 V) and device current I_e (Ch4: 1 div = 5 A) results in the power loss of the semiconductor device and can be observed in channel M. At switching instances the power loss is near-zero due to soft-switching. Conduction losses occur as anticipated.

5.5 Conclusion

A bidirectional series resonant MC topology for electric vehicle DC fast charging was introduced. The proposed topology has many advantages over existing fast charging architectures such as bidirectional power flow capability, ZVS turn ON and low turn OFF losses which increase efficiency, and high power factor operation. The operation of the proposed topology was described along with extensive analysis of the resonant tank. A design example of a 30 kW/500 V MC EV battery charger was presented and simulation results illustrate the operation of the proposed architecture in both *G2V* and *V2G* modes. Preliminary experimental results on a 500 W scaled down high frequency transformer and L_rC_r resonant tank were provided. It was demonstrated that the semiconductor devices operated under soft switching conditions enabling high system efficiency. The front-end 3x1 MC with soft switching capabilities is currently under development.

6. DESIGN OF TRANSFORMERS OPERATING AT MEDIUM OR HIGH FREQUENCY

The three-phase AC-DC rectifier systems presented in this dissertation employ transformers for galvanic isolation. As stated Section 1, these transformers have an impact in the power density and efficiency of the overall system. Thus, a comprehensive analysis and design of the transformers is critical to achieve three-phase AC-DC rectifier systems with good performance. In this section, design procedures for transformers operating at medium frequency (400 Hz – 2 kHz) are explained. Similarly, this section explains design considerations for transformers operating at high frequency (> 5 kHz) in high power applications. Using these procedures different transformer designs are compared in terms of volume and efficiency. Finally, the designed transformers are modelled in Ansys Maxwell FEA software. This FEA tool validates the performance of the transformers and assists in making relevant conclusions about the size and losses of the transformers.

6.1 Introduction

As mentioned in the Section 1, when a transformer operates at line frequency (50/60 Hz) it tends to be bulky and negatively impacts the power density of a power electronics converter. The size of a transformer can be decreased by increasing its frequency of operation [81]. The extent to which the size of the transformer can be reduced is limited by efficiency requirements. Indeed, increasing the frequency of operation increases the transformer's core losses and switching losses of the

semiconductor devices. Therefore, an appropriate design procedure is needed to achieve high power density without compromising the overall system's efficiency.

6.1.1 Magnetic Materials Characteristics

The material selected for the core of the transformer also plays an essential role in the design of the transformer. The core materials used for high power applications include silicon-steel, ferrite, amorphous materials and nanocrystalline materials [24, 58, 82]. The magnetic properties of several magnetic materials are given in Table 6-1 [83]. From Table 6-1 it can be observed that silicon steel materials have the highest saturation flux density. The B-H curve for silicon steel M19 material is given in Figure 6-1. A saturation flux density of 1.6 T occurs at a magnetic field intensity of 1500 A/m. In the other hand, silicon steel materials exhibit the highest core loss density among the listed materials. This material is suitable for operation in the frequency range of 50 Hz – 2 kHz. Above this frequency range, the transformer's efficiency deteriorates.

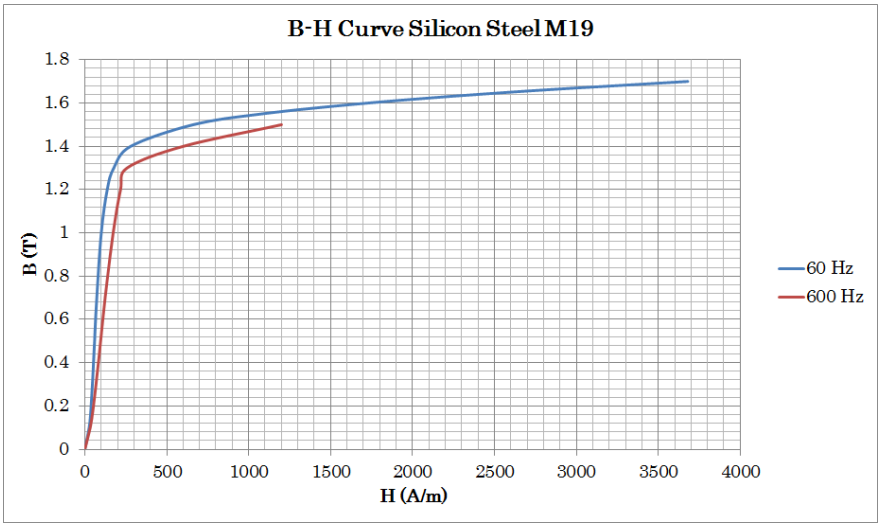

Figure 6-1: B-H curve for silicon steel M19 at 60 Hz and 600 Hz

Table 6-1: Magnetic properties of materials used in power electronics [83].

Material	Flux Density B_s (T)	Curie Temperature (°C)	Relative permeability $\mu_{r,1kHz}$ (X 10^3)	Core loss P_{cv} (kW/m^3)
3% Silicon Steel	1.9	750	2.7	8400
6.5 % Silicon Steel	1.3	700	1.2	5800
Mn-Zn high permeability ferrite	0.44	>150	5.3	1200
Mn-Zn low core loss ferrite	0.49	>200	2.4	680
Fe based amorphous	1.56	415	5.0	2200
Co-based high permeability amorphous metal	0.55	180	115	280
Nanocrystalline FINEMET® FT-3M	1.23	570	70	300
Nanocrystalline FINEMET® FT-3L	1.23	570	50	250

Amorphous and nanocrystalline materials exhibit high saturation flux density relative to ferrite materials. The B-H curve for Amorphous Metglass 2605SA1 material is shown in Figure 6-2 [84]. The high permeability of this material is evident from the B-H curve; a high magnetic field intensity of 1.4 T is achieved at a relatively low magnetic field intensity of 30 A/m. Nanocrystalline materials such as FINEMET FT-3L exhibit even higher values of permeability. These high relative permeability values help reduce the size of the core when designing a transformer. Furthermore, the low core loss density of amorphous and nanocrystalline materials makes them suitable for high power operation at high switching frequencies [85]. However, the main limitation of these materials is their cost. The B-H curve of ferrite material 3C94 is shown in Figure 6-3 [86]. A saturation flux density of 0.4 T occurs at a magnetic field intensity of 100 A/m.

Even though ferrite materials exhibit the lowest saturation flux density among the listed materials, ferrites still find wide application in power electronics because they have high resistivity limiting losses in a wide frequency range [58].

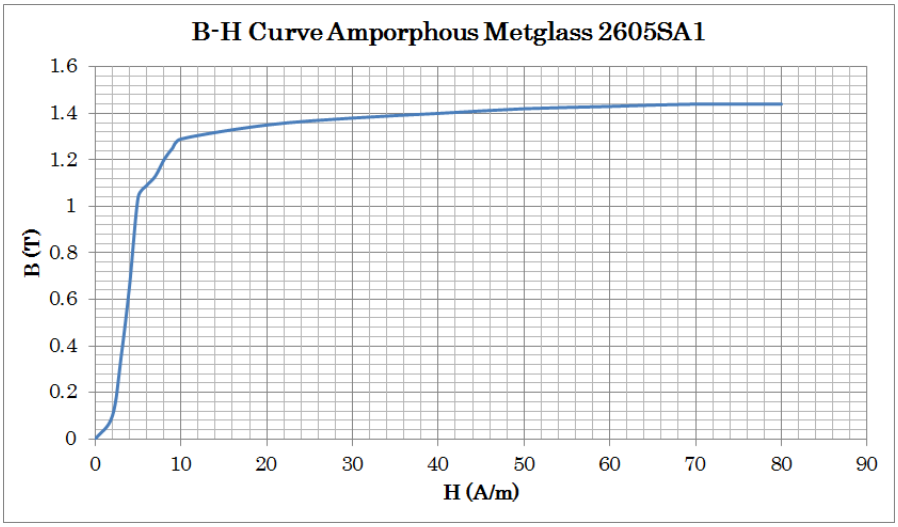

Figure 6-2: B-H curve for amorphous Metglass 2605SA1 material [84].

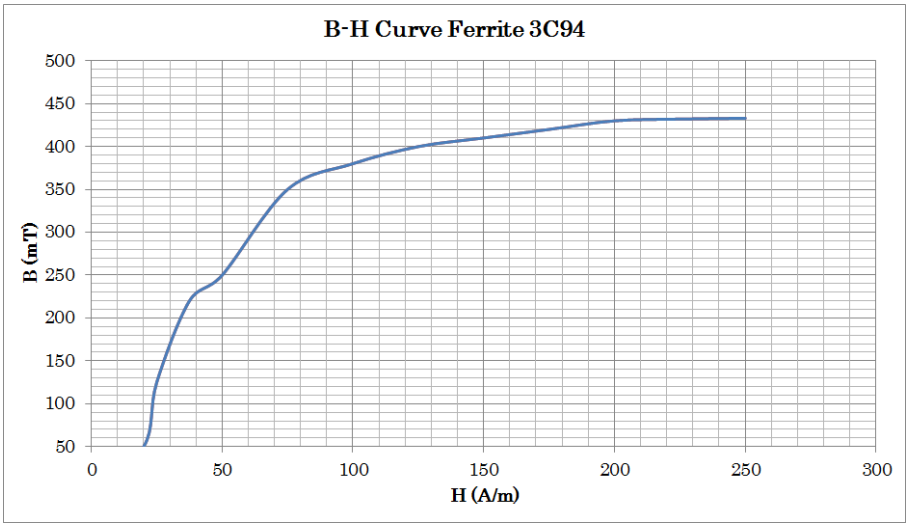

Figure 6-3: B-H curve for ferrite 3C94 material [86].

Figure 6-4 shows a comparison of power loss curves for different materials [87]. The figure plots the volumetric power loss density against flux density for core materials operating at 20 kHz [87]. The lowest amount of volumetric power loss density is exhibited by Vitroperm 500F which is a nanocrystalline core. Contrastingly, the highest amount of volumetric power loss density is obtained when using Mix-26 and XFlux 60 which are powder iron and silicon steel cores respectively.

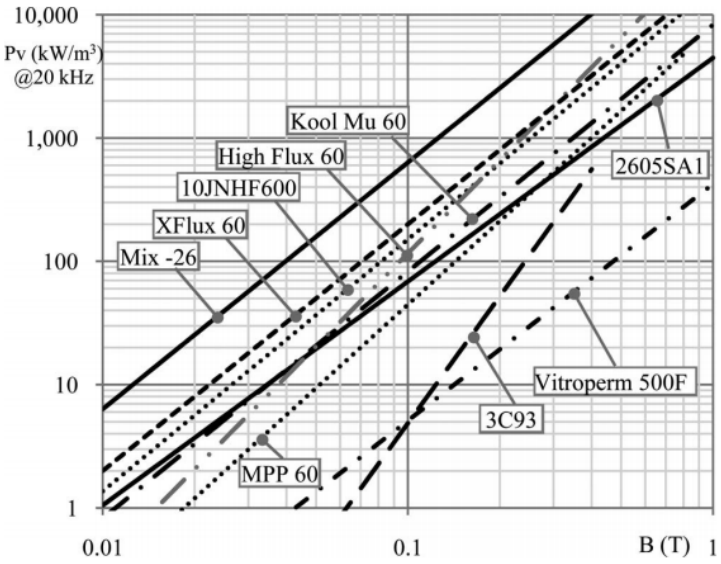

Figure 6-4: Volumetric power loss density versus flux density for various materials [87]. ©2011 IEEE

6.2 Design Procedure for Transformer Design

The transformers employed for isolation are designed using the area product method described in [82]. The design methodology is explained in this sub-section. A flowchart describing the area product method is shown in Figure 6-5. Following this flowchart, the steps to design a medium or high frequency transformer are as follows:

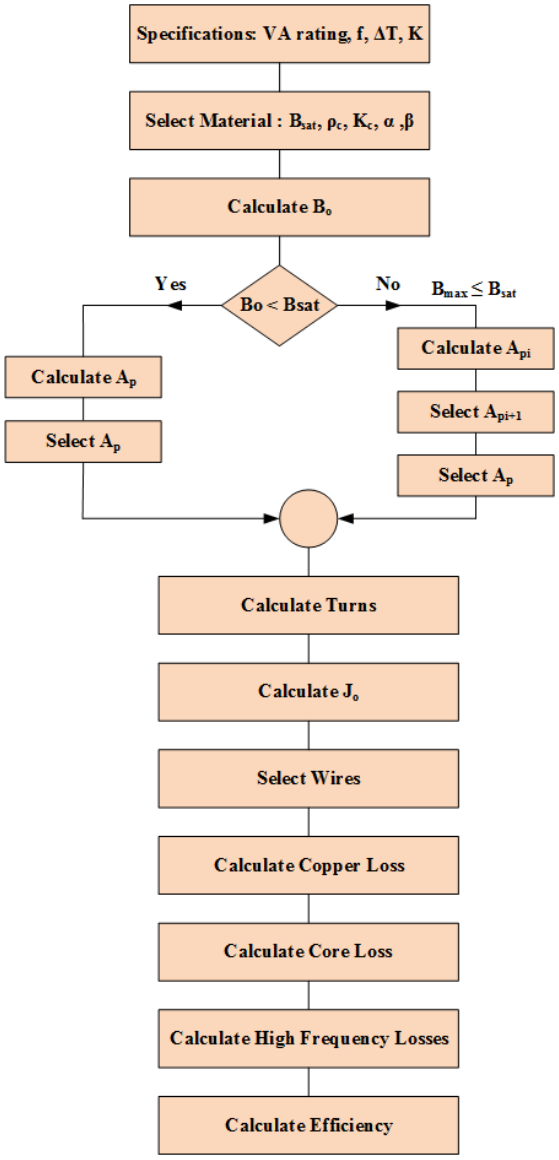

Figure 6-5: Transformer design flowchart [82]

1. The design starts by analyzing the specifications and operating conditions. The specifications and operating conditions include the transformer's volt-ampere (VA) rating, output power, frequency of operation, the ambient temperature and the permitted temperature rise, and the load output power. The VA rating of the transformer is defined in (6.1) where *n* is the total number of windings (primary and

secondary) in the transformer, and V_{rms} and I_{rms} are the voltage and current through each winding.

$$VA_{tot} = \sum_{i=1,2,..}^{n} (V_{rms,i} \cdot I_{rms,i}) \tag{6.1}$$

2. Based on the specifications a core material can be selected. When operating in the medium frequency range, core materials such as silicon steel and amorphous provide a good trade-off in terms of size, losses, and cost. By choosing the material, a B-H curve of operation is obtained and the saturation flux density B_{sat} is determined. The material constants α and β are also obtained in this step.

3. Once the core material is selected the optimal flux density B_o is calculated using (6.2). This optimal flux density occurs when the core losses are equal to the winding losses [82]. The obtained B_o must be compared to B_{sat} as given by the material's B-H curve.

$$B_o = \frac{\left[h_c k_a \Delta T\right]^{\frac{2}{3}}}{2^{\frac{2}{3}} \left[\rho_w k_w k_u\right]^{\frac{1}{12}} \left[k_c K_c f^{\alpha}\right]^{\frac{7}{12}}} \left[\frac{K_v f k_f k_u}{VA_{tot}}\right]^{\frac{1}{6}} \tag{6.2}$$

4. If B_o is less than B_{sat} the design is not limited by saturation and the area product A_p is calculated using (6.3) [82]. However, if B_o is greater than B_{sat} the design is limited by saturation and the operating flux density B_s must be chosen to be below B_{sat} (e.g. $0.85B_{sat}$). At this new operating point the winding losses and the copper losses will

not be equal and therefore the area product equation must be adjusted and calculated using (6.4), (6.5), (6.6), (6.7), (6.8). The calculation for A_p in this condition is an iterative process and the initial value A_{p1} is given by (6.4). One iteration is enough to find the new area product as described in [82].

For $B_o < B_{sat}$

$$A_p = \left[\frac{\sqrt{2} \cdot VA_{tot}}{K_v f B_o k_f K_t \sqrt{k_u \Delta T}} \right]^{\frac{8}{7}} \tag{6.3}$$

For $B_o > B_{sat}$

$$A_{p1} = \left[\frac{\sqrt{2} \cdot VA_{tot}}{K_v f B_s k_f K_t \sqrt{k_u \Delta T}} \right]^{\frac{8}{7}} \tag{6.4}$$

$$a_0 = \frac{k_c K_c f^{\alpha} B_s^{\beta}}{\rho_w k_w k_u} \tag{6.5}$$

$$a_1 = \frac{h_c k_a \Delta T}{\rho_w k_w k_u} \tag{6.6}$$

$$a_2 = \frac{VA_{tot}}{K_v f B_s k_f k_u} \tag{6.7}$$

$$A_{p_{i+1}} = A_{p_i} - \frac{a_0 A_{p_i}^2 - a_1 A_{p_i}^{\frac{7}{4}} + a_2}{2a_0 A_{p_i} - \frac{7}{4} a_1 A_{p_i}^{\frac{3}{4}}} \tag{6.8}$$

With the resulting area product a specific core is selected. Usually, the area product A_p is a parameter listed by core's manufacturers. This parameter is also identified as

the product of the window area W_a and the core cross-sectional area A_c [24]. The selected core's area product should be equal or higher compared to the calculated value. From the core selected the following parameters are obtained: A_c, W_a, A_p, mean length of a turn (MLT), and the volume of the core.

5. The number of turns in the primary side is calculated using (6.9), where V_{pri} is one of the design specifications and refers to the maximum rms voltage applied to the primary windings. The turns for the windings on the secondary side are obtained using the well-known relation in (6.10).

$$N_p = \frac{V_{pri}}{K_v B A_c f} \tag{6.9}$$

$$\frac{N_s}{N_p} = \frac{V_{\text{sec}}}{V_{pri}} \tag{6.10}$$

6. The current density J_o is calculated using (6.11). With this value and with the currents through the primary (I_{pri}) and secondary windings (I_{sec}), the cross-sectional area A_w of the winding conductors can be determined using (6.12). Note that the cross-sectional area of for the primary and secondary side winding conductors will be different if the currents are not the same.

$$J_o = \sqrt{\frac{h_c k_a \sqrt{A_p \Delta T - V_c K_c f^{\alpha} B_s^{\beta}}}{\rho_w V_w k_u}} \tag{6.11}$$

$$A_w = \frac{I_{pri}}{J_o} \tag{6.12}$$

7. From A_w the wire diameter can be obtained assuming a circular conductor. A wire with a similar diameter must be selected. From the wire specifications the DC resistance (R_{dc}) is obtained in order to calculate the winding resistance. The resistance of each winding (R_w) is calculated using (6.13).

$$R_w = MLT \cdot N \cdot R_{dc}(1 + \alpha_{20}(T_{\max} - 20)) \tag{6.13}$$

8. Once the winding resistance has been calculated for every transformer winding, the copper losses are calculated using (6.14).

$$P_{copper} = \sum_{i=1,2,..}^{n} (I_{rms,i}^2 \cdot R_{w,i}) \tag{6.14}$$

9. The core losses are calculated using Steinmetz's equation (6.15)

$$P_{core} = V_c K_c f^{\alpha} B_s^{\beta} \tag{6.15}$$

10. In medium or high frequency operation phenomena such as the skin depth might increase the copper and core losses and must be accounted for in order to determine

the transformer's efficiency. The skin depth of a conductor is calculated using (6.16). Additional losses in the windings occur when the radii of the selected conductors is larger than the skin depth. In essence, the resistance of the windings is increased. The resistance under this high frequency effect can be approximated using (6.17) [82], where r_o refers to the radius of the selected wires and σ is the conductivity of the wire. This AC resistance is then used to evaluate the copper loss. Note that if the skin depth is larger than the radii of the conductors selected, this step is skipped.

$$\delta = \frac{1}{\sqrt{\pi \cdot f \cdot \mu \cdot \sigma}} \qquad (6.16)$$

$$R_{ac} = R_{dc}\left[1 + \frac{(r_o/\delta)^4}{48 + 0.8(r_o/\delta)^4}\right] \qquad (6.17)$$

11. The last step is to calculate the transformer's efficiency using (6.18).

$$\eta_{tr} = \frac{P_o}{P_o + P_{copper} + P_{core}} \qquad (6.18)$$

6.3 Transformer Design Examples

The three-phase AC-DC rectifier system introduced in Section 2 employs a transformer operating at 600 Hz. Meanwhile, the three-phase 12-pulse AC-DC rectifier system introduced in Section 3 employs a transformer operating at 20 kHz. This sub-section details the design of these two transformers and compares their performance to a line frequency (50/60 Hz) transformer design.

6.3.1 Medium Frequency Transformer Design

The operating conditions for the design of the medium frequency transformer are listed in Table 6-2. From the output load power requirement, the transformer VA rating is calculated. When employed with the push-pull based AC-DC rectifier system in Section 2, the transformer's total VA rating is $2.58P_o$.

Table 6-2: Design specifications for medium frequency transformer

Parameter	Value
Output Power (P_o)	7 kW
Output Voltage (V_{dc})	560 V_{dc}
Input Voltage ($V_{l\text{-}l}$)	208 V_{rms}
Transformer Operating frequency (f)	600 Hz
Temperature rise (ΔT)	100 °C
Ambient temperature (T_a)	40 °C

Taking into account these conditions, silicon steel M19 material is chosen for the transformer's core. The associated materials constants and properties associated with grain oriented silicon steel material are given in Table 6-3.

Table 6-3: Silicon steel material constants and properties

Parameter	Value
Core loss constant α	1.7
Core loss constant β	1.9
Material parameter K_c	3.388
Saturation flux density B_{sat}	1.6 T

Using these parameters, the optimum flux density B_o is calculated to be 0.57 T. Thus, the design is not limited by saturation. Using (6.3), the area product A_p is calculated to be 1460 cm^4. A core satisfying this requirement must be chosen. The

characteristics of the core chosen for this design are listed in Table 4. Other winding specifications are also listed in this table. Using these specifications, the number of turns in the primary side is approximately 55 turns (55T). For the proposed zig-zag transformer, the secondary side has four secondary windings per phase. Based on the turns-ratio, the secondary side windings have 17T, 45T, 17T, 45T. Using (6.11), the current density for the selected core is 0.414 x10^6 A/m^2.Wires for the primary windings and secondary windings are selected based on the calculated bare wire diameter. The winding selected for the primary side windings has a 66mΩ resistance. The windings on the secondary side with 17T have an 8mΩ resistance while the secondary side windings with 45T have a 38mΩ resistance. The total copper losses are calculated to be 67 W using (6.13) and (6.14). The core losses are calculated to be 164 W. This results in a transformer efficiency of approximately 97%. The skin depth in this application is 2.7 mm which is greater than the radii of the selected wire for both the primary and secondary side. Thus no additional losses occur by operating at medium frequency.

Table 6-4: Core and windings characteristics for 600 Hz transformer

Parameter	Value
Core cross-sectional area (A_c)	25 cm^2
Window Area (W_a)	70 cm^2
Area product (A_p)	1750 cm^4
Mean length per turn (MLT)	28.3 cm
Core volume (V_e)	2680 cm^3
Core stacking factor (k_f)	0.95
Window utilization factor (k_u)	0.4
Conductor resistivity at 20 °C (ρ_{20})	1.72 μΩ-cm
Copper temperature coefficient at 20 °C (α_{20})	0.00393

6.3.2 High Frequency Transformer Design

The design specifications for the HF transformer are listed in Table 6-5. The VA rating of the transformer was calculated to be $1.07P_o$ in Section 3. Taking into account the transformer operating frequency of operation and the cost of magnetic materials, a ferrite core was selected for this design. The relative material constants and properties are listed in Table 6-6.

Table 6-5: Design specifications for high frequency transformer

Parameter	Value
Output Power (P_o)	10 kW
Output Voltage (V_{dc})	560 V_{dc}
Input Voltage ($V_{l\text{-}l}$)	208 V_{rms}
Transformer Operating frequency (f)	20 kHz
Temperature rise (ΔT)	100 °C
Ambient temperature (T_a)	40 °C

Table 6-6: Ferrite material constants and properties

Parameter	Value
Core loss constant α	1.25
Core loss constant β	2.35
Material parameter K_c	16.9
Saturation flux density B_{sat}	0.42 T

Using the design specifications and the material constants, the optimal flux density is calculated to be 0.16 T which is below the saturation flux density. Therefore, the design is not limited by saturation. Using (6.3), the area product is calculated to be 134 cm^4. Using this area product an appropriate core was selected. The characteristics of the selected core are given in Table 6-7. Note that the area product of the selected core is slightly smaller than the calculated value but this is acceptable since the optimal flux is

well below the saturation flux density. The next step in the design process is to determine the number of turns of the transformer winding. From calculation, the number of turns in the primary windings is determined to be 33T. Using the turns-ratio relationship in (3.6), the secondary side windings have 15T, 6T, 15T, 6T respectively. The current density for the selected core is 2.5 x10^6 A/m^2. The primary winding resistance is calculated to be 20 mΩ, the secondary windings with 15T have a resistance of 8mΩ, and the secondary windings with 6T have a resistance of 1mΩ. The rms current through the primary and secondary windings is given by the relation found in Table 3-1. Using (6.13), the copper losses are 27 W. From (6.15), the core losses are calculated to be 20 W. Therefore, the calculated efficiency of the HF transformer is 99.5%.

Table 6-7: Core and windings characteristics for 20 kHz transformer

Parameter	Value
Core cross-sectional area (A_c)	4.4 cm^2
Window Area (W_a)	29.16 cm^2
Area product (A_p)	128 cm^4
Mean length per turn (MLT)	13.72 cm
Core volume (V_c)	362 cm^3
Core stacking factor (k_f)	0.95
Window utilization factor (k_u)	0.4
Conductor resistivity at 20 °C (ρ_{20})	1.72 μΩ-cm
Copper temperature coefficient at 20 °C (α_{20})	0.00393

6.3.3 Line Frequency Transformer Design

For comparison purposes a line frequency transformer is designed. The operating conditions for the line frequency transformer are the same as in Table 6-2 except that the frequency of operation is 60 Hz instead of 600 Hz. Since the proposed three-phase AC to

DC rectifier system is being compared to the conventional 12-pulse rectifier the line frequency transformer's VA rating is $2.06P_o$. The same silicon steel M19 material is chosen for the core. Thus, the same material constants and properties given in Table 6-3 are used.

Using these parameters, the optimum flux density, B_o, is calculated to be 3.94 T. Looking at the B-H curve in Figure 6-1 it is observed that B_o is above the saturation flux density B_{sat}. Thus, the design is limited by saturation and a peak flux density of $0.85B_{sat}$ is chosen. The second iteration for the area product A_p yields 4300 cm^4. The core selected for this design has the characteristics listed in Table 6-5. Other winding specifications are also listed in this table.

Table 6-8: Core and winding characteristics for 60 Hz transformer

Parameter	Value
Core cross-sectional area (A_c)	28.125 cm^2
Window Area (W_a)	157.5 cm^2
Area product (A_p)	4430 cm^4
Mean length per turn (MLT)	34.8 cm
Core volume (V_c)	9045 cm^3
Core stacking factor (k_f)	0.95
Window utilization factor (k_u)	0.4
Conductor resistivity at 20 °C (ρ_{20})	1.72 μΩ-cm
Copper temperature coefficient at 20 °C (α_{20})	0.00393

The number of turns on the primary side is determined to be 204. For 12-pulse operation, the secondary side must have two windings. One winding has the same number of turns and the other has a factor of 1.732. Thus, one secondary winding must have 204 turns while the other secondary winding must have 354 turns. The number of

turns in this design is relatively high compared to the number of turns used in the 600 Hz transformer design. The increase in the number of turns is expected because the frequency of operation has decreased and the same voltage requirements are kept. Thus, the copper losses are expected to increase.

For the selected core, the current density is calculated to be 1.94 $x10^6$ A/m^2. In this design, the core losses are 58W while the copper losses are approximately 139W to achieve 97% transformer efficiency. This is the same efficiency achieved for the 600 Hz transformer design.

6.3.4 Comparison of Transformers

The line frequency, MF and HF transformer designs are compared in Table 6-9. The parameters used for comparison include the output power, core material, area product, core volume, losses and efficiency.

Table 6-9: Comparison of transformer designs

Parameter	Line Frequency Transformer	Medium Frequency Transformer	High Frequency Transformer
Core Material	Silicon Steel	Silicon Steel	Ferrite
Output Power	7 kVA	7 kVA	10 kVA
Area Product (A_p)	4430 cm^4	1750 cm^4	128 cm^4
Core Volume (V_c)	9045 cm^3	2680 cm^3	362 cm^3
Winding Losses	139 W	67 W	27 W
Copper Losses	58 W	164 W	20 W
Efficiency	97%	97%	99%

The area product of the line frequency transformer is approximately three times larger than the area product required for the 600 Hz transformer design. The vast difference in the area product between the 60 Hz and 600 Hz design indicates that the

core chosen for the 60 Hz design must be substantially larger in size/weight. Indeed, for the same output load, input voltage, and transformer efficiency, the line frequency transformer has a core volume of 9.045 L while the MF transformer has a core volume of 2.68 L. The core volume of the MF three-phase transformer is 30% of the core volume of the line frequency transformer. This is a great size reduction achieved by increasing the frequency of operation by 10 times.

The 20 kHz transformer which is rated for 10 kW operation has an area product that is almost 14 times smaller compared to the MF transformer's area product. This indicates that the transformer size is further reduced by operating at HF. The HF transformer has a higher power handling capacity and its core volume is 14% of the MF transformer's core volume. In other words, the HF transformer is seven times smaller than the MF transformer. Remarkably, the HF transformer is twenty-five times smaller than the line frequency transformer. This reduction in core volume is extremely useful in applications where power density is a priority.

6.4 Maxwell Modelling of Transformer Designs

The transformers designed in the previous sub-section are modelled using Ansys Maxwell Finite Element Analysis (FEA) software to verify the magnetic behavior of the transformers.

6.4.1 Medium Frequency Transformer Maxwell Design.

For the medium frequency transformer, the 600 Hz B-H curves in Figure 6-1 is used. The core loss versus frequency data for silicon steel M19 material is given in

Figure 6-6. This data is used in the software to estimate core losses when excited at different frequencies. A 2D transformer simulation model is constructed with dimensions 34 cm x 24 cm. The model depth of the transformer is set to 5 cm. The primary windings are excited using the voltage waveforms shown in Figure 6-7; these waveforms correspond to the three-phase MF AC link created by switching S_1/S_2 complementarily at 50% duty cycle as explained in Section 2. Under this excitation, the transformer core exhibits a flux density distribution as shown in Figure 2-16. From this plot it is observed that the core is operating below the saturation region. Figure 6-8 shows the corresponding field intensity distribution and Figure 2-17 shows the flux lines through the core. The simulated core losses as reported in Section 2 are 69 W. The vast difference between the calculated losses occurs because the software does not take into account all the physical effects in a core [56].

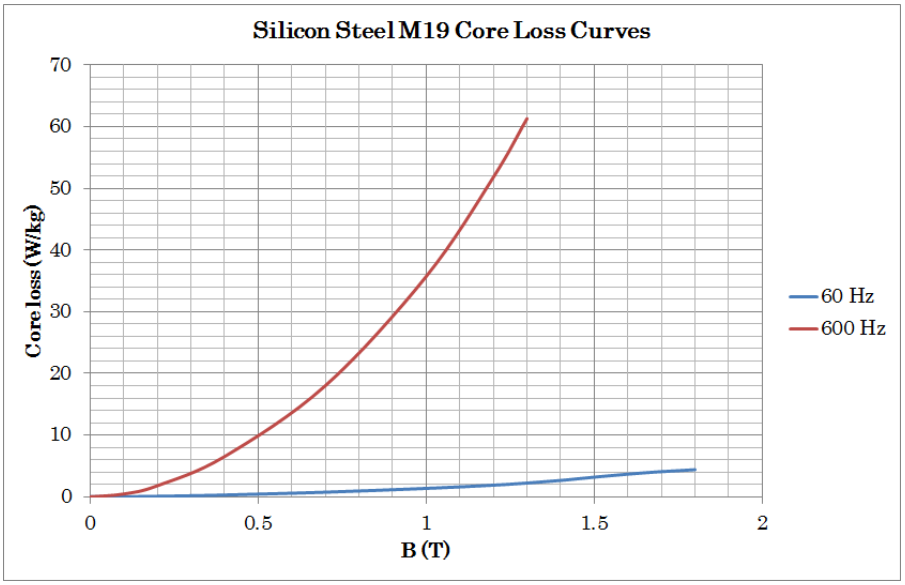

Figure 6-6: Silicon steel M19 core loss curves at 60 Hz and 600 Hz.

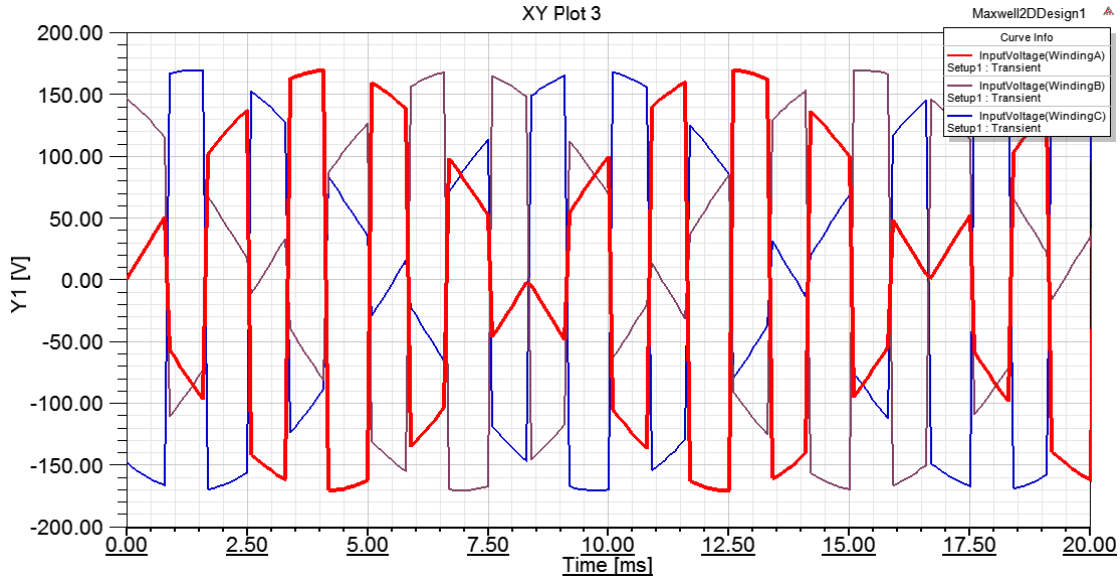

Figure 6-7: Three-phase AC link exciting primary windings of the medium frequency transformer.

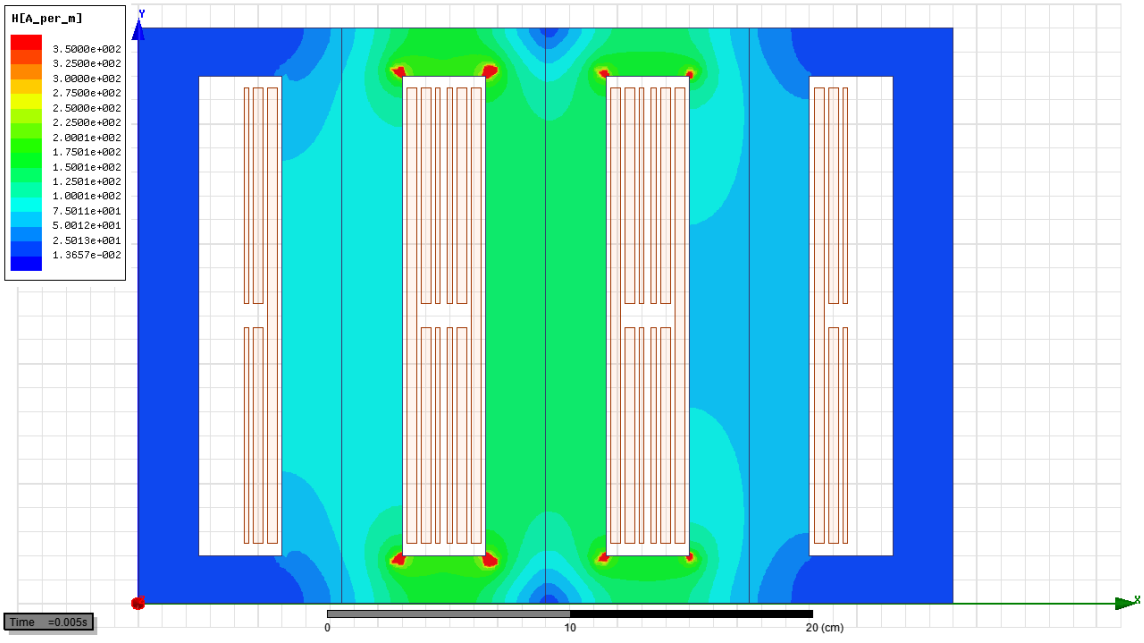

Figure 6-8: Magnetic field intensity of the transformer's core.

6.4.2 High Frequency Transformer Maxwell Design

A 2D model is also built in Ansys Maxwell for the HF transformer. The core material selected is ferrite 3C94. The B-H curve for this particular material is given in Figure 6-3. The volumetric power loss curve for this material is given in Figure 6-9. The 2D model has width of 17.6 cm and a height of 12.32 cm. The depth of the transformer is set to 3 cm resulting in a transformer volume of 0.65L. The primary windings of the transformer are excited with a three-phase HF AC link as shown in Figure 6-10. These voltages represent the output voltage produced by the AC-AC converters in Section 3. Figure 3-12 shows the flux density distribution of the transformer; the transformer operates at 0.34 T which is below the saturating region. The corresponding magnetic field intensity distribution of the transformer is plotted in Figure 6-11 confirming proper operation. The simulated core losses as reported in Section 3 are 3W. Thus it can be concluded that FEA simulations do not give a precise indication of core losses. However, these simulations aid in determining whether the transformer size is appropriate for the given excitation. In other words, the simulations confirm whether or not a transformer will saturate.

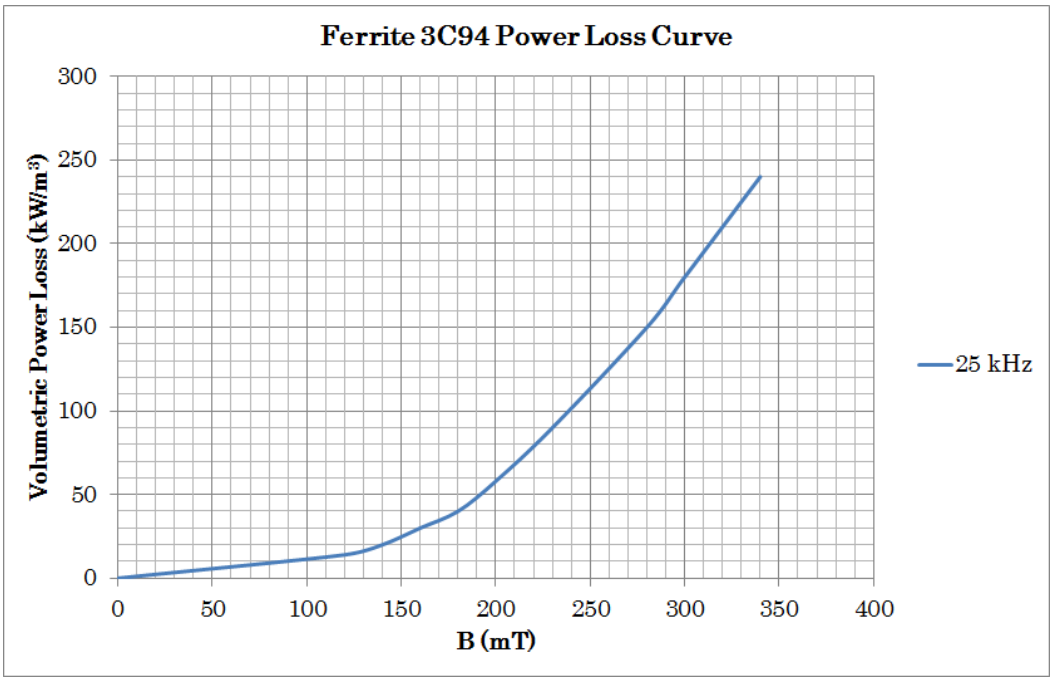

Figure 6-9: Volumetric power loss for ferrite 3C94 as a function of flux density

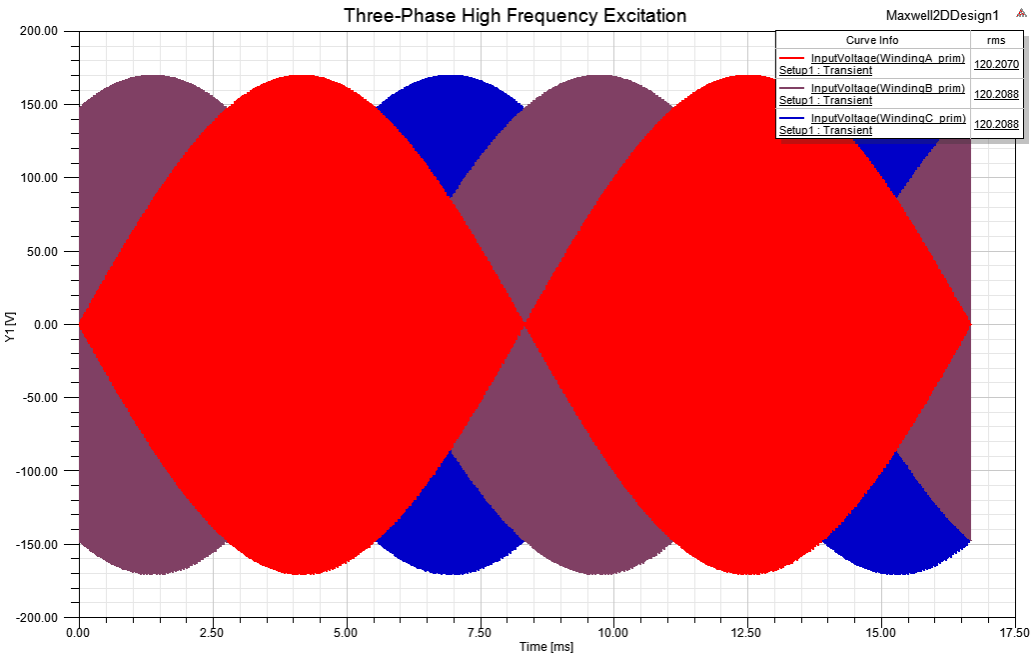

Figure 6-10: Three-phase excitation for HF transformer.

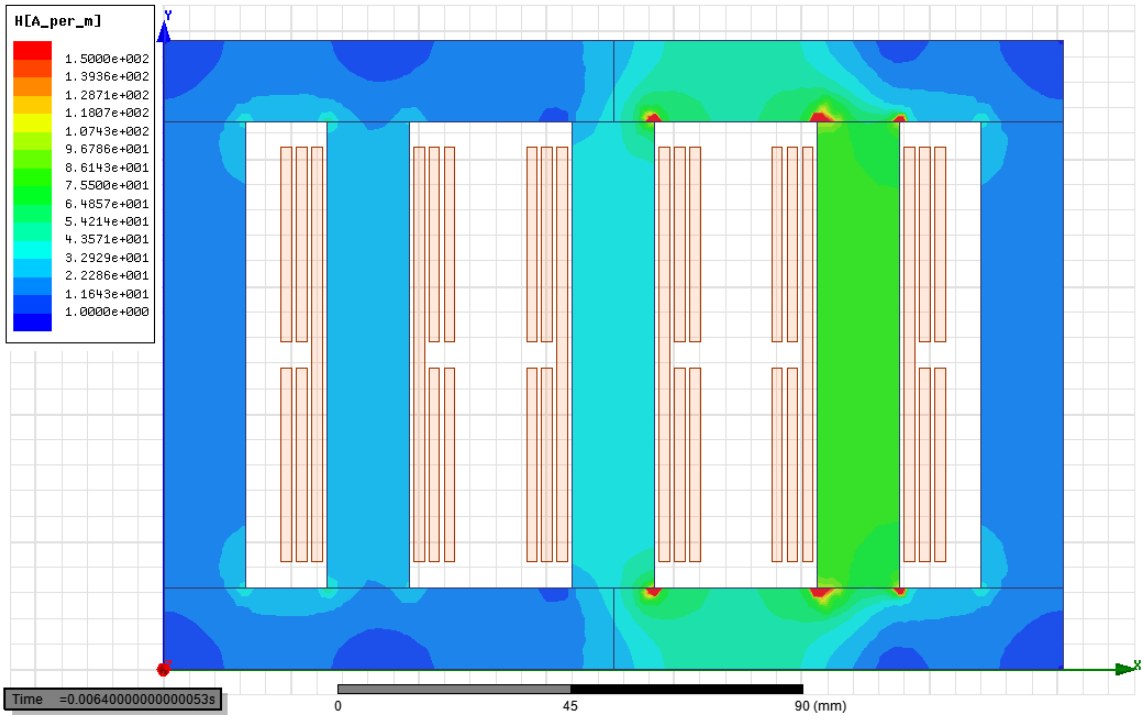

Figure 6-11: Magnetic field intensity. One limb operates at approximately 85 A/m which is below the saturation region.

6.4.3 Line Frequency Transformer Maxwell Design

The transformer designed in sub-section 6.3.2 is also modelled using Ansys Maxwell FEA software. The 2D transformer model has a width of 51 cm and a height of 36 cm. The depth of the transformer is 7.5 cm resulting in a transformer volume of 13.7 L. These dimensions are in accordance with the core specifications given in Table 6-5. The windings in the primary side are excited with sinusoidal voltages as shown in Figure 6-12. A plot of the magnetic field density (at t = 20 ms) under sinusoidal excitation is given in Figure 6-13. At this particular time, the peak flux density on the core is around 1 T which is below the saturation region. This shows that the core size is adequate for the given operating conditions. The corresponding magnetic field intensity plot is shown

in Figure 6-14 and flux lines through the core are shown in Figure 6-15. The simulated core losses are shown in Figure 6-16 and amount to 59 W which is really close to the calculated value.

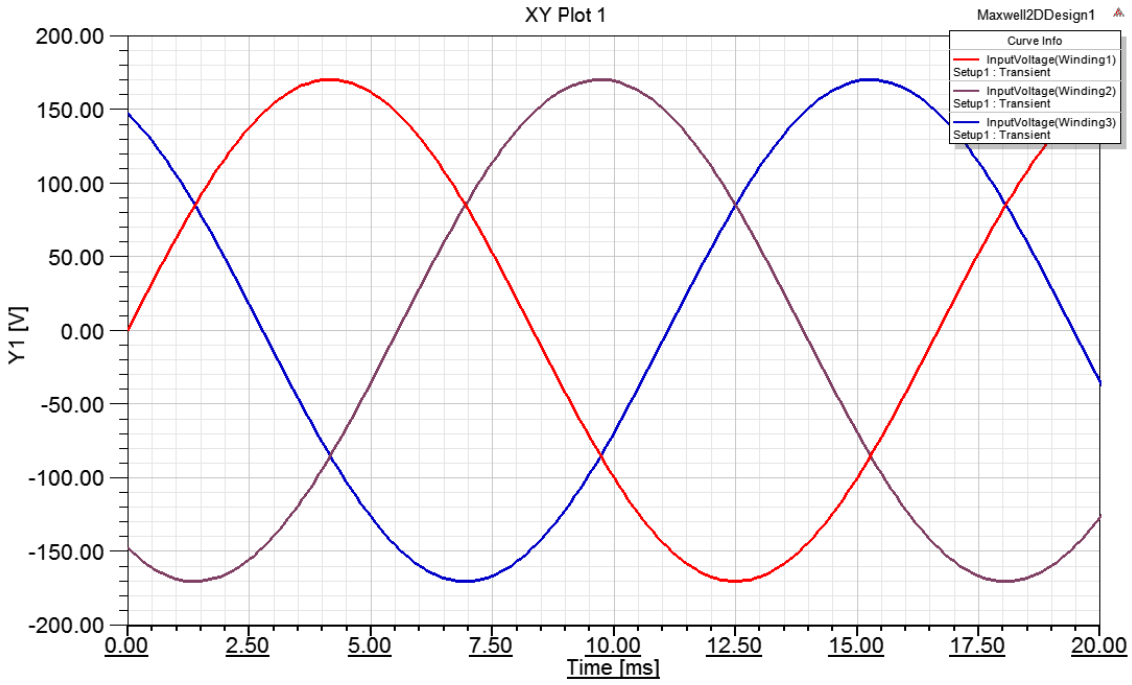

Figure 6-12: Three-phase sinusoidal excitation (120 V_{rms}) for primary windings of the line frequency transformer.

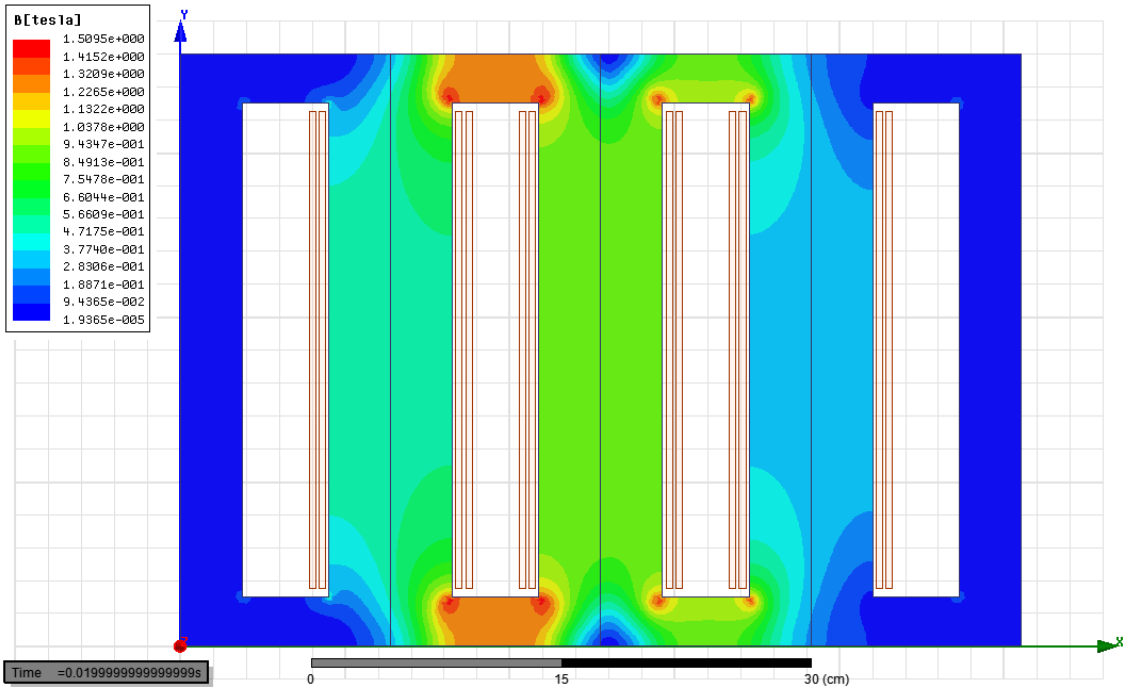

Figure 6-13: Flux density distribution of line frequency transformer.

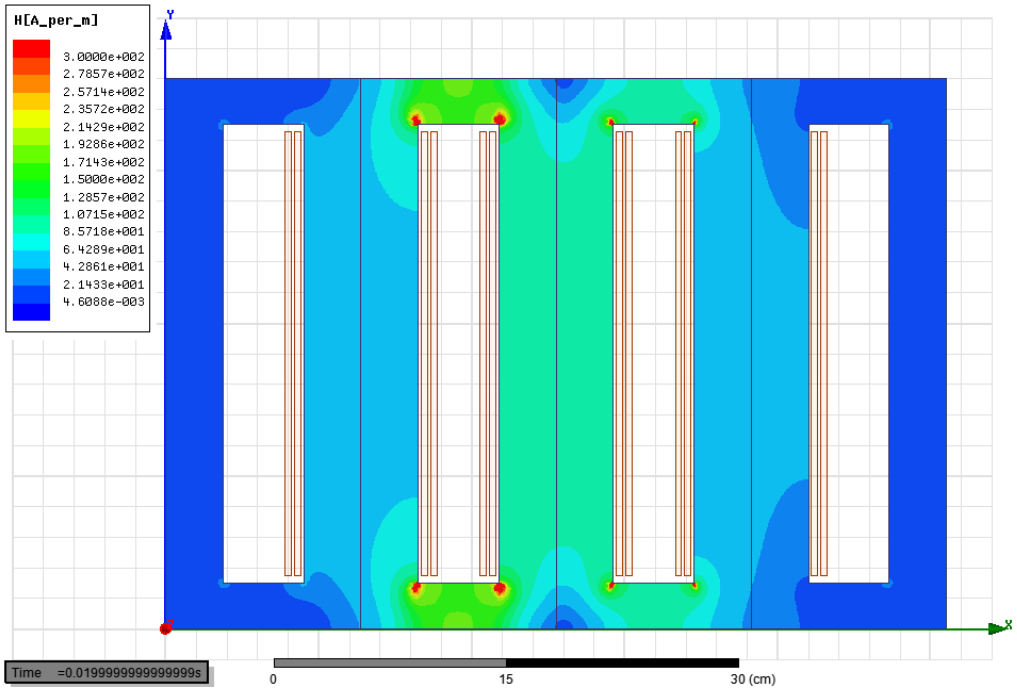

Figure 6-14: Magnetic field intensity distribution of line frequency transformer.

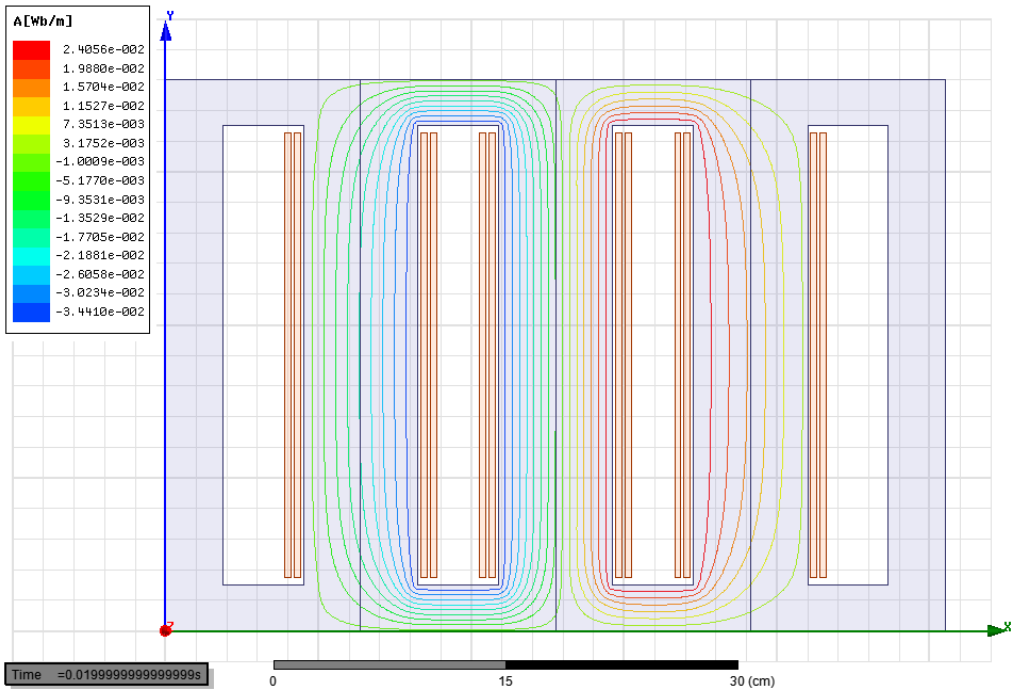

Figure 6-15: Flux lines through the core. At this particular time, the flux concentrates in the interior three limbs.

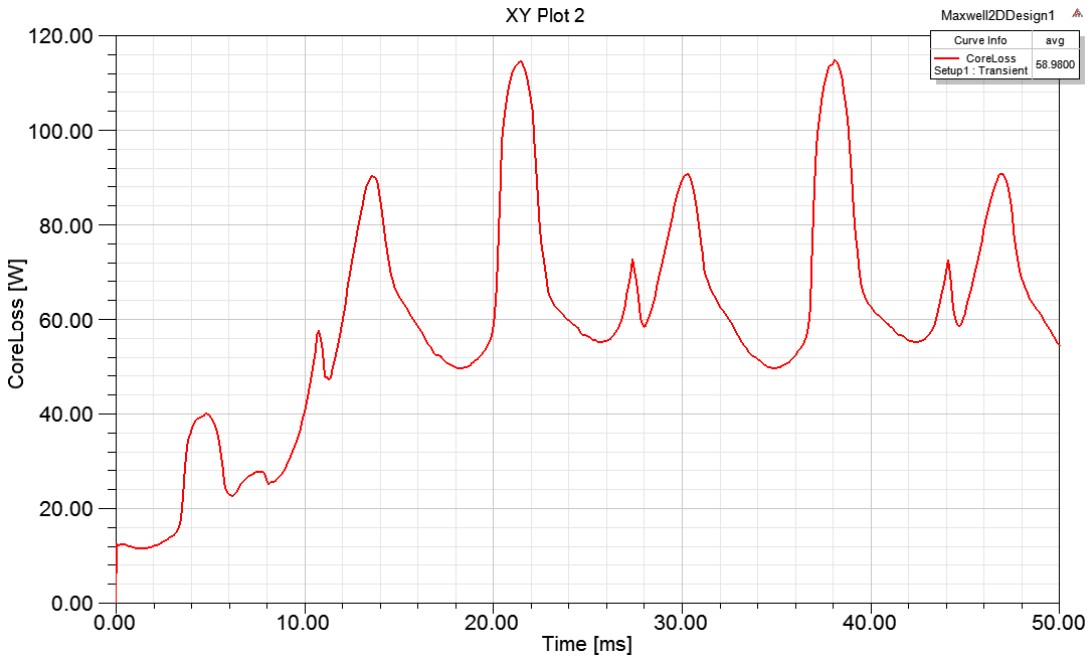

Figure 6-16: Simulated core losses of line frequency transformer. The average losses are 59 W.

6.5 Conclusion

This section explained the benefits of operating a transformer at medium or high frequency. A transformer design procedure based on the area product method was explained in detail. Using this design procedure, three transformer design examples were investigated. It is determined that operating the transformer at 600 Hz results in a core volume that is three times smaller than its line frequency counterpart. Moreover, it was shown that the 20 kHz transformer is seven times smaller than the MF transformer. The magnetic operation of these transformers was confirmed through Ansys Maxwell FEA simulations.

7. CONCLUSION

7.1 Summary

In this dissertation, four novel three-phase AC-DC rectifier systems with higher frequency isolation were proposed. The conventional and state of the art three-phase rectifier systems were discussed and their shortcomings identified. The proposed system in Section 2 is a push-pull based three-phase rectifier employing MF (600 Hz) isolation. Operating the transformer at 600 Hz reduces its size three times compared to the equivalent 60 Hz design. It is shown that the utility input current has 12-pulse performance. Experimental results on a 3.15 kW prototype validate the operation of the system. This topology is best suited for applications where output voltage regulation is not required such as the front-end of adjustable speed drives.

A three-phase AC-DC rectifier with HF (20 kHz) isolation is presented in Section 3. Remarkably, the HF transformer employed for isolation is twenty five times smaller compared to a line frequency transformer. A design example and detailed analysis were presented to explain the operation of the proposed system. It is shown that the utility input current exhibits 12-pulse performance over a wide range of output voltage control. Experimental results on 1 kW prototype validate the operation of the HF 12-pulse rectifier. The HF 12-pulse rectifier is well suited for applications such as electric vehicle charging. The feasibility of various embodiments of the proposed system was explored and their operation was demonstrated through simulation results.

In section 4, a three-phase PWM rectifier is presented. The operation of the PWM rectifier with programmed unipolar switching functions is explained. It is shown

that the utility input current waveforms are essentially the same as the programmed unipolar switching function. Thus, the harmonic content of the current can be programed as desired. A design example eliminating the 5^{th}, 7^{th}, 11^{th}, and 13^{th} harmonic from the utility input current is explained. Detailed analysis and extended simulation results validate the operation of the proposed PWM rectifier. Output voltage control is achieved by varying the modulation index.

A bidirectional three-phase AC-DC rectifier was presented in Section 5. The converter operates in soft-switching conditions in both the rectifier and inverter mode. Extended simulation results are shown for both modes. The input current exhibits sinusoidal performance at unity power factor. Galvanic isolation is achieved through a single-phase HF transformer. Experimental results on a 500 W prototype validate the operation of the resonant tank and HF transformer.

Finally, a design procedure for medium and high frequency transformers was presented in Section 6. Design examples were provided for a line frequency transformer, a medium frequency transformer, and a high frequency transformer. The design of the transformers was validated using Ansys Maxwell FEA software.

7.2 Future Research Opportunities

As in any research topic there is room for future study with regards to the proposed three-phase AC-DC rectifier systems. With respect to the push-pull based rectifier in Section 2 an area to be investigated is the design of an active clamp to recover the energy stored in the leakage inductance of the transformer windings. This

would improve the system's efficiency. Currently, the proposed scheme employs a passive clamp (R_{cl}, C_{cl}) leading to power losses. A possible alternative to the passive clamp is to connect a high efficient flyback converter at the output of the diode clamp circuit and feed the recovered energy to the output. The improvement in efficiency versus the added cost is a trade-off that would have to be considered.

The proposed HF 12-pulse rectifier in Section 3 is very attractive due to its simplicity, high power density, and good current quality. An area of further investigation would be the implementation of this topology using wide-bandgap semiconductor devices such as GaN. Using these kinds of devices would improve the system's efficiencies because the switching losses and conduction losses would reduce. The cost of the topology would have to be considered because wide-bandgap devices are more expensive than regular silicon devices. An alternative to improve the efficiency is to investigate methods for soft switching operation. An LC resonant tank at the output of the AC-AC converters could be explored. Another suitable area for study is an analysis of the optimal number of series stacked AC-AC converters for medium voltage applications.

Another area suitable for future work is the implementation of the proposed PWM rectifier with wide-bandgap devices. The system's efficiency would benefit from using such devices. Soft switching methods can also be studied. The bidirectional capability of the PWM rectifier can also be explored. The indirect AC-AC converter could be replaced by a direct AC-AC converter (i.e. 1x1 matrix converter) and the output six-pulse diode rectifier could be replaced by a six-switch converter. This would increase

the complexity and number of devices but would be attractive for energy storage applications.

In general, the reliability of the proposed three-phase rectifier systems merits future investigation. Future work in the mentioned areas could facilitate the deployment of the proposed systems in the industry sector.

REFERENCES

[1] D. W. Hart, *Power Electronics*. New York, NY: McGraw-Hill, 2011.

[2] F. J. M. d. Seixas and I. Barbi, "A 12 kW Three-Phase Low THD Rectifier With High-Frequency Isolation and Regulated DC Output," *IEEE Transactions on Power Electronics,* vol. 19, pp. 371-377, 2004.

[3] N. Mohan, T. M. Undeland, and W. P. Robbins, *Power Electronics: Converters, Applications, and Design*. United States: John Wiley & Sons, Inc., 1989.

[4] DarnellGroup. (January). *AC-DC Power Supplies: Worlwide Forecasts (Tenth ed.)*. Available: www.darnell.com

[5] T. Soeiro, T. Friedli, and J. W. Kolar, "Three-phase high power factor mains interface concepts for Electric Vehicle battery charging systems," in *Twenty Seventh Annual IEEE Applied Power Electronics Conference and Exposition (APEC)*, Orlando, FL, pp. 2063-2610, 2012.

[6] H. S. Krishnamoorthy, D. Rana, P. Garg, P. N. Enjeti, and I. J. Pitel, "Wind Turbine Generator-Battery Energy Storage Utility Interface Converter Topology with Medium-Frequency Transformer Link," *IEEE Transactions on Power Electronics,* vol. 29, pp. 4146-4155, 2014.

[7] F. Xu, B. Guo, L. M. Tolbert, F. Wang, and B. J. Blalock, "An All-SiC Three-Phase Buck Rectifier for High-Efficiency Data Center Power Supplies," *IEEE Transactions on Industry Applications,* vol. 49, pp. 2662-2673, 2013.

[8] B. T. Patterson, "Defining the Needs for Energy Storage and its Control for Zero-Net-Energy Buildings," presented at the Applied Power Electronics Conference, Fort Worth, TX, 2014.

[9] T. Friedli, M. Hartmann, and J. W. Kolar, "The Essence of Three-Phase PFC Rectifier Systems-Part I," *IEEE Transactions on Power Electronics,* vol. 28, pp. 176-198, 2014.

[10] IEEE, "IEEE Recommende Practice and Requirements for Harmonic Control in Electric Power Systems," in *IEEE Std 519-2014 (Revision of IEEE Std 519-1992)*, ed, pp. 1-29, 2014.

[11] IEC61000-3-4., "Electromagnetic Compatibility (EMC) - Part 3-2: Limitis for Harmonic Current Emmissions (Equipment Inut Current <16A per Phase)," 1.2 ed, 1998.

[12] H. Krishnamoorthy, "Power Electronic Topologies With High Density Power Conversion and Galvanic Isolation for Utility Interface," Doctor of Philosophy, Texas A&M University, 2015.

[13] R. M. Burkart and J. W. Kolar, "Comparative evaluation of SiC and Si PV inverter systems based on power density and efficiency as indicators of initial cost and operating revenue," in *2013 IEEE 14th Workshop on Control and Modeling for Power Electronics (COMPEL)*, pp. 1-6, 2013

[14] M. Smith and S. Atcitty. (2009, Jan 17, 2017). Power Electronics Reliability Analysis.
Available: http://prod.sandia.gov/techlib/access-control.cgi/2009/098377.pdf

[15] Y. Song and B. Wang, "Survey on Reliability of Power Electronic Systems," *IEEE Transactions on Power Electronics,* vol. 28, pp. 591-604, 2013.

[16] G. Ortiz, J. Biela, and J. W. Kolar, "Optimized design of medium frequency transformers with high isolation requirements," in *IECON 2010 - 36th Annual Conference on IEEE Industrial Electronics Society*, pp. 631-638, 2010

[17] C. G. C. Branco, R. P. Torrico-Bascope, C. M. T. Cruz, and F. K. D. A. Lima, "Proposal of Three-Phase High-Frequency Transformer Isolation UPS Topologies for Distributed Generation Applications," *IEEE Transactions on Industrial Electronics,* vol. 60, pp. 1520-1531, 2013.

[18] K. Inagaki, T. Furuhashi, A. Ishiguro, M. Ishida, and S. Okuma, "A new PWM control method for AC to DC converters with high-frequency transformer isolation," *IEEE Transactions on Industry Applications,* vol. 29, pp. 486-492, 1993.

[19] M. Kang, B. O. Woo, P. Enjeti, and I. J. Pitel, "Autoconnected-Electronic-transformer-based multipulse rectifiers for utility interphase of power electronic systems," *IEEE Transactions on Industry Applications,* vol. 35, pp. 646-656, 1999.

[20] A. E. Fitzgerald, J. Charles Kingsley, and S. D. Umans, *Electric Machinery*, 6th ed. New York, NY: McGraw-Hill, 2003.

[21] G. Ortiz, M. Leibl, J. W. Kolar, and O. Apeldoorn, "Medium frequency transformers for solid-state-transformer applications - design and experimental verification," in *2013 IEEE 10th International Conference on Power Electronics and Drive Systems (PEDS)*, pp. 1285-1290, 2013.

[22] T. Hatakeyama and K. Onda, "Core Loss Estimation of Various Materials Magnetized With the Symmetrical/Asymmetrical Rectangular Voltage," *IEEE Transactions on Power Electronics,* vol. 29, pp. 6628-6635, 2014.

[23] X. She, A. Q. Huang, and R. Burgos, "Review of Solid-State Transformer Technologies and Their Application in Power Distribution Systems," *IEEE Journal of Emerging and Selected Topics in Power Electronics,* vol. 1, pp. 186-198, 2013.

[24] W. M. Colonel and T. Mclyman, *Transformer and Inductor Design Handbook* vol. 3rd ed. Boca Raton, FL USA: CRC Press, 2004.

[25] Toshiba. (April 20). *Toshiba MV Drives*. Available: http://www.toshiba.com/ind/data/tag_files/MTX_NEMA_3R_MV_Brochure_3002.pdf

[26] M. M. Swamy, "Uncontrolled and Controlled Rectifiers," in *Power Systems*, 3rd ed: CRC Press, 2012.

[27] S. Choi, P. N. Enjeti, and I. J. Pitel, "Polyphase transformer arrangements with reduced kVA capacities for harmonic current reduction in rectifier-type utility interface," *IEEE Transactions on Power Electronics,* vol. 11, pp. 680-690, September 1996.

[28] G. R. Kamath, D. Benson, and R. Wood, "A Compact Autotransformer based 12-pulse rectifier circuit," in *The 27th Annual Conference of the IEEE Industrial Electronics Society, 2001. IECON*, Denver, CO, pp. 1344-1349, 2001.

[29] S. Choi, S. L. Bang, and P. Enjeti, "New 24-Pulse Diode Rectifier System for Utility Interface of High-Power AC Motor Drives," *IEEE Transactions on Industry Applications,* vol. 33, pp. pp. 925-931, Mar/Apr 1997.

[30] D. Rana, B. Hafez, P. Garg, S. Essakiappan, and P. Enjeti, "Analysis and Design of active inductor as DC-link reactor for lightweight adjustable speed drive systems," presented at the 2014 IEEE Energy Conversion Congress and Exposition (ECCE), Pittsburgh, PA, 2014.

[31] K. Mino, M. L. Heldwein, and J. W. Kolar, "Ultra compact three-phase rectifier with electronic smoothing inductor," in *Twentieth Annual IEEE Applied Power Electronics Conference and Exposition*, pp. pp. 522-528, 2005

[32] H. Ertl and J. W. Kolar, "A constant output current three-phase diode bridge rectifier employing a novel "Electronic Smoothing Inductor"," *IEEE Transactions on Industrial Electronics,* vol. 52, pp. 454-461, 2005.

[33] J. Biela, D. Hassler, J. Sch, x00F, nberger, and J. W. Kolar, "Closed-Loop Sinusoidal Input-Current Shaping of 12-Pulse Autotransformer Rectifier Unit With Impressed Output Voltage," *IEEE Transactions on Power Electronics,* vol. 26, pp. 249-259, 2011.

[34] Y. K. E. Ho, S. Y. R. Hui, and Y.-S. Lee, "Characterization of single-stage three-phase power-factor-correction circuits using modular single-phase PWM DC-to-DC converters," *IEEE Transactions on Power Electronics,* vol. 15, pp. 62-71, Jan 2000.

[35] G. Spiazzi and F. C. Lee, "Implementation of single-phase boost power-factor-correction circuits in three-phase applications," *IEEE Transactions on Industrial Electronics,* vol. 44, pp. 365-371, 1997.

[36] M. M. Swamy, "An Electronically Isolated 12-Pulse Autotransformer Rectification Scheme to Improve Input Power Factor and Lower Harmonic Distortion in Variable-Frequency Drives," *IEEE Transactions on Industry Applications,* vol. 51, pp. 3986-3994, Sept.-Oct. 2015.

[37] J. W. Kolar and F. C. Zach, "A novel three-phase utility interface minimizing line current harmonics of high-power telecommunications rectifier modules," *IEEE Transactions on Industrial Electronics,* vol. 44, pp. 456-467, 1997.

[38] J. R. Rodriguez, J. W. Dixon, J. R. Espinoza, J. Pontt, and P. Lezana, "PWM regenerative rectifiers: state of the art," *IEEE Transactions on Industrial Electronics,* vol. 52, pp. 5-22, 2005.

[39] R. A. Hanna and S. Prabhu, "Medium-voltage adjustable speed drives-users' and manufacturer's experience," *IEEE Transactions on Industry Applications,* vol. 33, pp. 1407-1415, 1997.

[40] G. Song, M. Heldwein, U. Drofenik, J. Minibock, K. Mino, and J. W. Kolar, "Comparative Evaluation of Three-Phase High-Power-Factor AC-DC Converter Concepts for Application in Future More Electric Aircraft," *IEEE Transactions on Industrial Electronics,* vol. 52, pp. 727-73, June 2005.

[41] GE. (2015, April 20). *TM-GE MV Drives*.
Available:
http://www.wmea.net/Technical%20Papers/GE%20Medium%20Voltage%20Drives.pdf

[42] M. Swamy, T. Kume, and N. Takada, "A Hybrid 18-Pulse Rectification Scheme for Diode Front-End Rectifiers With Large DC Bus Capacitors," *IEEE Transactions on Industry Applications,* vol. 46, pp. 2484-2494, Nov-Dec. 2010.

[43] S. Choi, "A three-phase unity-power-factor diode rectifier with active input current shaping," *IEEE Transactions on Industrial Electronics,* vol. 52, pp. 1711-1714, Dec. 2005.

[44] M. Swamy and A. Balakrishnan, "Three, single-phase power factor correction (PFC) boost converters for use with three-phase, 3-wire variable frequency drive systems," in *2015 IEEE Energy Conversion Congress and Exposition*, pp. 6993-7000, 2015.

[45] H. S. Kim, W. Baek, M. H. Ryu, J. H. Kim, and J. H. Jung, "The High-Efficiency Isolated AC-DC Converter Using the Three-Phase Interleaved LLC Resonant Converter Employing the Y-Connected Rectifier," *IEEE Transactions on Power Electronics,* vol. 29, pp. pp. 4017-4028, August 2014.

[46] M. Kang, P. N. Enjeti, and I. J. Pitel, "Analysis and design of electronic transformers for electric power distribution sytem," *IEEE Transactions on Power Electronics,* vol. 14, pp. 1133-1141, Nov. 1999.

[47] H. Krishnamoorthy, P. Garg, and P. Enjeti, "Simplified medium/high frequency transformer isolation approach for multi-pulse diode rectifier front-end adjustable speed drives," in *2015 IEEE Applied Power Electronics Conference and Exposition (APEC)*, pp. 527-534, 2015.

[48] ABB. (June 10). *ABB drives for marine medium voltage drives for reliable and efficient operations at sea*.
Available:
https://library.e.abb.com/public/2e7b508ea530471ac125785b00446c95/Marine%20brochure%20RevB_lowres.pdf

[49] T. Ericsen, N. Hingorani, and Y. Khersonsky, "Power electronics and future marine electrical systems," *IEEE Transactions on Industry Applications,* vol. 42, pp. 155-163, Jan.-Feb. 2006.

[50] R. Gupta, K. K. Mohapatra, N. Mohan, G. Castelino, K. Basu, and N. Weise, "Soft switching power electronic transformer," United States Patent 8,446,743, May 21, 2013.

[51] S. Xu, A. Q. Huang, and R. Burgos, "Review of Solid-State Transformer Technologies and Their Application in Power Distribution Systems," *IEEE Journal of Emerging and Selected Topics in Power Electronics,* vol. 1, pp. 186-198, 2013.

[52] C.-k. Leung, D. S., S. Baek, and B. S., "Design considerations of high voltage and high frequency three phase transformer for Solid State Transformer

application," in *2010 IEEE Energy Conversion Congress and Exposition (ECCE)*, pp. 1551-1558, 2010

[53] International Rectifier. (2008). *Insulated Gate Bipolar Transistor, IRG4PH50SPbF datasheet*.
Available:
http://www.infineon.com/dgdl/irg4ph50spbf.pdf?fileId=5546d462533600a40153564869102325

[54] CREE. (2016). *Silicon Carbide Schottky Diode, C4D40120D datasheet*. Available: http://www.wolfspeed.com/media/downloads/109/C4D40120D.pdf

[55] CREE, "Silicon Carbide Schottky Diode, C3D20060D datasheet," 2016.

[56] ANSYSMaxwellTutorial. Example (2D/3D) Transient - Core loss.

[57] J. Sandoval, H. Krishnamoorthy, P. Enjeti, and S. Choi, "Reduced Active Switch Front End Multi-Pulse Rectifier with Medium Frequency Transformer Isolation," *IEEE Transactions on Power Electronics,* vol. PP, pp. 1-1, 2016.

[58] A. Van den Bossche, and V. Cekov Valchev "Soft Magnetic Materials," in *Inductors and Transformers for Power Electronics*, ed: CRC Press, 2005.

[59] P. N. Enjeti, P. D. Ziogas, and J. F. Lindsay, "Programmed PWM techniques to eliminate harmonics: a critical evaluation," *IEEE Transactions on Industry Applications,* vol. 26, pp. 302-316, 1990.

[60] P. N. Enjeti, P. D. Ziogas, J. F. Lindsay, and M. H. Rashid, "A new PWM speed control system for high-performance AC motor drives," *IEEE Transactions on Industrial Electronics,* vol. 37, pp. 143-151, 1990.

[61] P. N. Enjeti, P. D. Ziogas, and J. F. Lindsay, "A current source PWM inverter with instantaneous current control capability," *IEEE Transactions on Industry Applications,* vol. 27, pp. 582-588, 1991.

[62] N. R. Zargari, G. Joos, and P. D. Ziogas, "Input Filter Design for PWM Current-Source Rectifiers," *IEEE Transactions on Industry Applications,* vol. 30, p. 1573, 1994.

[63] S. B. Dewan and E. B. Shahrodi, "Design of an Input Filter for the Six-Pulse Bridge Rectifier," *IEEE Transactions on Industry Applications,* vol. IA-21, pp. 1168-1175, 1985.

[64] T. Nussbaumer, M. L. Heldwein, and J. W. Kolar, "Differential Mode Input Filter Design for a Three-Phase Buck-Type PWM Rectifier Based on Modeling

of the EMC Test Receiver," *IEEE Transactions on Industrial Electronics,* vol. 53, pp. 1649-1661, 2006.

[65] U. S. D. o. Energy. (2014, March 20). EV everywhere Grand Challenge. 1-16. Available: http://energy.gov/sites/prod/files/2014/02/f8/eveverywhere_road_to_success.pdf

[66] S. Wang, C. R., and Y. Chu, "Investigating the power architectures and circuit topologies for megawatt superfast electric vehicle charging stations with enhanced grid support functionality," presented at the 2012 IEEE International Electric Vehicle Conference (IEVC), 2012.

[67] M. Yilmaz and P. T. Krein, "Review of Battery Charger Topologies, Charging Power Levels, and Infrastructure for Plug-In Electric and Hybrid Vehicles," *IEEE Transactions on Power Electronics,* vol. 28, pp. 2151-2169, 2013.

[68] A. G. Boulanger, A. C. Chu, S. Max, and D. L. Waltz, "Vehicle Electrification: Status and Issues," in *Proceedings of the IEEE*, vol.99, no.6, pp.1116-1138, 2011.

[69] A. Briones, J. Francfort, P. Heitmann, M. Schey, S. Schey, and J. Mart. (2012, Vehicle-to-Grid (V2G) Power Flow Regulations and Building Codes Review by the AVTA.
Available: http://energy.gov/sites/prod/files/2014/02/f8/v2g_power_flow_rpt.pdf

[70] H. Chaudhry and T. Bohn, "A V2G application using DC fast charging and its impact on the grid," in *2012 IEEE Transportation Electrification Conference and Expo (ITEC)*, pp. 1-6, 2012.

[71] Y. Liu and S. C. Mitchem, "Implementation of V2G technology using DC Fast Charging," presented at the 2013 International Conference on Connected Vehicles and Expo (ICCVE), 2013.

[72] Y. Ota, H. Taniguchi, J. Baba, and A. Yokoyama, "Implementation of autonomous distributed V2G to electric vehicle and DC charging system," *Electric Power Systems Research,* pp. 177-183, 2014.

[73] M. Kane. (2014, November 14). *Real World Test of V2G Now Underway in Spain*. Available: http://insideevs.com/real-world-test-of-v2g-now-underway-in-spain-wvideos/

[74] A. S. Yilmaz, M. Badawi, Y. Sozer, and I. Husain, "A fast battery charger topology for charging of electric vehicles," presented at the 2012 IEEE International Electric Vehicle Conference (IEVC), 2012.

[75] Z. Zhang, H. Xu, L. Shi, D. Li, and Y. Han, "A unit power factor DC fast charger for electric vehicle charging station," presented at the 2012 7th Power Electronics and Motion Control Conference, 2012.

[76] S. Harb and R. S. Balog, "Reliability of Candidate Photovoltaic Module-Integrated-Inverter (PV-MII) Topologies - A Usage Model Approach," *IEEE Transactions on Power Electronics,* vol. 28, pp. 3019-3027, 2013.

[77] H. S. Krishnamoorthy, P. Garg, and P. N. Enjeti, "A matrix converter-based topology for high power electric vehicle battery charging and V2G application," in *38th Annual Conference on IEEE Industrial Electronics Society*, pp. 2866-2871, 2012.

[78] S. Manias and P. D. Ziogas, "A Novel Sinewave in AC to DC Converter with High-Frequency Transformer Isolation," *IEEE Transactions on Industrial Electronics,* vol. IE-32, pp. 430-438, 1985.

[79] S. Ratanapanachote, C. H. Ju, and P. Enjeti, "A digitally controlled switch mode power supply based on matrix converter," *IEEE Transactions on Power Electronics,* vol. 21, pp. 124-130, 2006.

[80] V. Vlatkovic, D. Borojevic, and F. C. Lee, "A zero-voltage switched, three-phase isolated PWM buck rectifier," *IEEE Transactions on Power Electronics,* vol. 10, pp. 148-157, 1995.

[81] G. Ortiz, M. Leibl, J. W. Kolar, and O. Apeldoorn, "Medium frequency transformers for solid-state-transformer applications: Design and experimental verification," in *2013 IEEE 10th International Conference on Power Electronics and Drive Systems (PEDS)*, pp. 1285-1290, 2013.

[82] W. G. Hurley and W. H. Ifle, *Transformers and Inductors for Power Electronics: Theory, Design and Applications*: Wiley, 2013.

[83] Hitachi. (2005, Oct. 17). *Nanocrystalline soft magnetic material FINEMET*. Available: http://www.hilltech.com/pdf/hl-fm10-cFinemetIntro.pdf

[84] Hitachi. (2011, October 14, 2016). *Amorphous Alloys for Trasnsformer Cores*. Available: http://www.metglas.com/assets/pdf/2605sa1.pdf

[85] M. Ferch. (2003, Oct. 10, 2016). *Nanocrystalline core materials for modern power electronic design*.
Available: http://www.magnetec.de/fileadmin/pdf/np_powerelectronic_e.pdf

[86] Ferroxcube. (2008, October 14, 2016). *Datasheet 3C94 Material Specification*. Available: http://www.ferroxcube.com/FerroxcubeCorporateReception/datasheet/3c94.pdf

[87] M. S. Rylko, B. J. Lyons, J. G. Hayes, and M. G. Egan, "Revised Magnetics Performance Factors and Experimental Comparison of High-Flux Materials for High-Current DC–DC Inductors," *IEEE Transactions on Power Electronics,* vol. 26, pp. 2112-2126, 2011.

APPENDIX A

This appendix shows the semiconductor curves used in PLECS thermal models to calculate the efficiency of the systems proposed in Section 3 and Section 4. Figure A-1 shows the conduction loss data for device VUE 75-06NO7. The voltage drop as a function of the device current is shown for three different temperatures. This semiconductor device was used to obtain the conduction losses for the single-phase diode rectifiers in the AC-AC converters and for the output six-pulse diode rectifiers.

Similarly, Figure A-2 shows the turn-on loss data used in the thermal model for device IXXH50N60C3D1. The turn-off loss data for this device is given in Figure A-3.

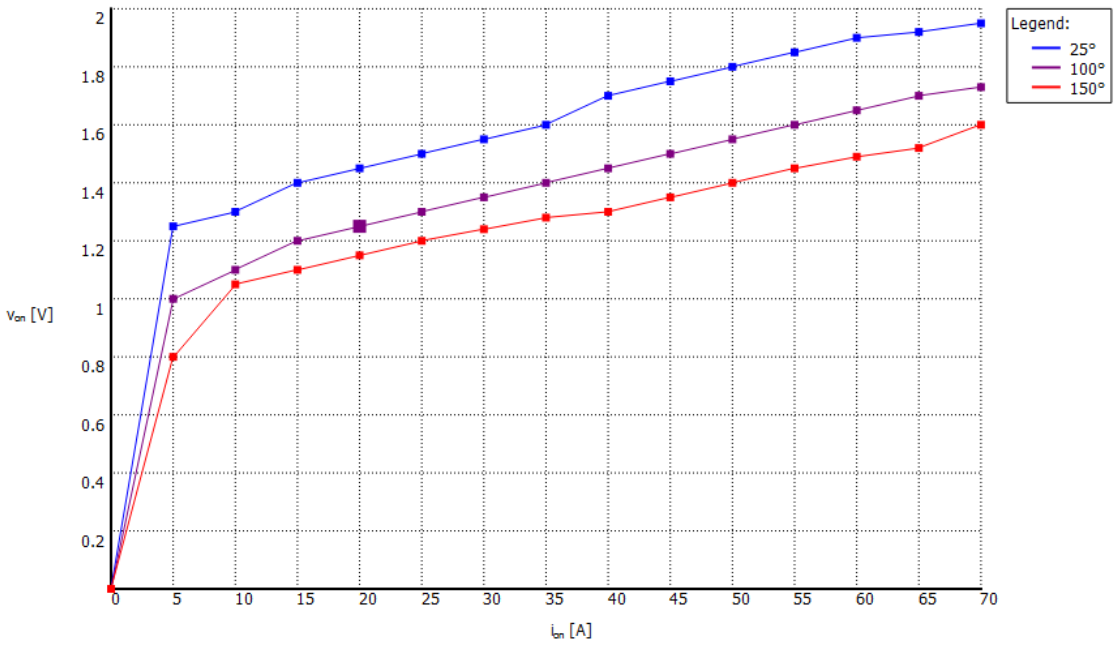

Figure A-1: Conduction loss data for device VUE 75-06NO7. This is used to calculate conduction losses.

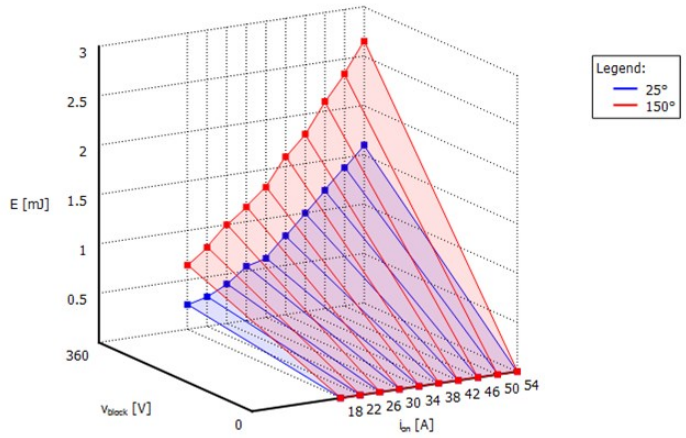

25° 150°

	18 A	22 A	26 A	30 A	34 A	38 A	42 A	46 A	50 A	54 A
0 V	0 mJ	0 mJ	0 mJ	0 mJ	0 mJ	0 mJ	0 mJ	0 mJ	0 mJ	0 mJ
360 V	0.25 mJ	0.3 mJ	0.4 mJ	0.55 mJ	0.6 mJ	0.8 mJ	1 mJ	1.2 mJ	1.4 mJ	1.6 mJ

Figure A-2: Turn-on loss data for device IXXH50N60C3D1. This is used to calculate switching losses.

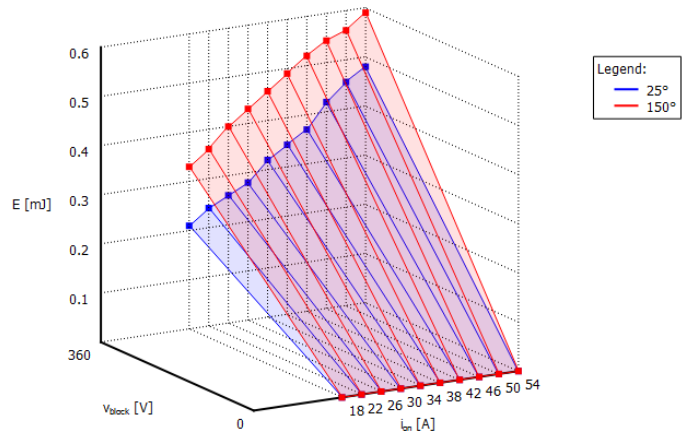

25° 150°

	18 A	22 A	26 A	30 A	34 A	38 A	42 A	46 A	50 A	54 A
0 V	0 mJ	0 mJ	0 mJ	0 mJ	0 mJ	0 mJ	0 mJ	0 mJ	0 mJ	0 mJ
360 V	0.21 mJ	0.24 mJ	0.26 mJ	0.28 mJ	0.32 mJ	0.345 mJ	0.37 mJ	0.42 mJ	0.455 mJ	0.48 mJ

Figure A-3: Turn-off loss data for device IXXH50N60C3D1. This is used to calculate switching losses.